Synthesis, Characterization and Versatile Applications of Metal-Organic Clusters, Extended Frameworks and Related Composites

A Thesis Submitted for the Degree of

Doctor of Philosophy

By

Anindita Chakraborty

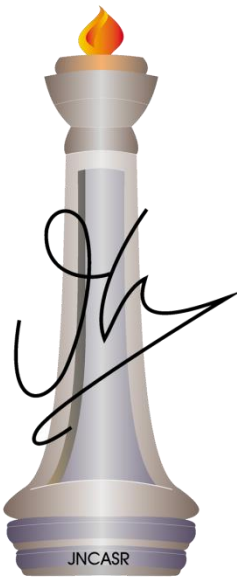

Chemistry and Physics of Materials Unit (CPMU)

Jawaharlal Nehru Centre for Advanced Scientific Research

(A Deemed University)

Bangalore – 560064

Dedicated
to My Family

DECLARATION

I hereby declare that the matter embodied in the thesis entitled "***Synthesis, Characterization and Versatile Applications of Metal-Organic Clusters, Extended Frameworks and Related Composites***" is the result of investigations carried out by me at the Chemistry and Physics of Materials Unit, Jawaharlal Nehru Centre for Advanced Scientific Research, India under the supervision of Prof. Tapas Kumar Maji and that it has not been submitted elsewhere for the award of any degree or diploma.

In keeping with the general practice in reporting the scientific observations, due acknowledgement has been made whenever the work described is based on the findings of other investigators. Any omission that might have occurred due to oversight or error in judgement is regretted.

Anindita Chakraborty

CERTIFICATE

I hereby certify that the work described in this thesis entitled "***Synthesis, Characterization and Versatile Applications of Metal-Organic Clusters, Extended Frameworks and Related Composites***" has been carried out by Anindita Chakraborty under my supervision at the Chemistry and Physics of Materials Unit, Jawaharlal Nehru Centre for Advanced Scientific Research, India and that it has not been submitted elsewhere for the award of any degree or diploma.

Dr. Tapas Kumar Maji

Associate Professor

CPMU, JNCASR

(Research Supervisor)

ACKNOWLEDGEMENT

I wish to express my sincere gratitude to my research supervisor Prof. Tapas Kumar Maji for his kind support, criticism and suggestions, which I have been experienced all through the course of these investigations. I have had enough freedom to work on my own area of interest, and I am grateful to him for that.

Prof. C. N. R. Rao has always been a true source of inspiration, with all his extraordinary enthusiasm and energy. It is really a great opportunity to be in the same institute, to listen to his wonderful motivating speeches and to watch him every day.

I thank the past and present chairmen of CPMU for allowing me to use the facilities of the centre.

I would like to sincerely thank Prof. M. Eswaramoorthy, Prof. Swapan. K. Pati, Dr. S. Dutta, Dr. A. K. Manna and Dr. A. Achari of JNCASR and Prof. Joan Ribas of University of Barcelona for fruitful collaborations.

I am thankful to the faculty members of JNCASR and IISc for the informative courses. In particular, I would like to thank Prof. S. Balasubramanian, Prof. S. K. Pati, Prof. C. Narayana, Prof. H. Ila, Prof. S. Narasimhan and Prof. T. K. Maji of JNCASR and Prof. T. N. Guru Row of IISc for their courses.

I am thankful to the technical staffs Mr. Anil, Mr. Vasu, Mr. Mahesh, Mrs. Usha. Ms. Selvi of JNCASR for their assistance during various experiments.

I would like to thank Prof. A. Sundaresan, Dr. Pranab Mandal, Dr. Nitesh Kumar and Mr. Rana Saha, for the magnetic measurements. It has also been a great experience to have fruitful discussions with them.

I thank JNCASR Library, Complab, Hostel, Health Centre, Academics and Administration staff for providing and maintaining all the wonderful facilities.

I am grateful to my labmates for providing a nice and healthy environment in the lab. My present labmates Dr. Arpan, Nivedita, Papri, Syamantak, Sohini, Deenu and past labmates Dr. Prakash Kanoo, Dr. Sudip Mohapatra, Dr. Ritesh Haldar, Dr. V. Suresh, Ms. Komal and Mr. Krishna Ramachandran always created a vibrant environment inside the lab and outside. It has been a great pleasure to learn many things, by interacting with them. I also acknowledge all the visiting scientists and students (POCE and SRF) for their contributions.

I cordially thank all the Integrated Ph. D. students of CPMU and NCU. It has been really nice and a lot of fun to be part of the Integrated Ph. D. family. My sincere thanks to all my seniors, batchmates and juniors. I sincerely acknowledge my batchmates, Ajmala, Darshana, Dibyajyoti and Prashant for the wonderful times we have had in the past years.

I have been fortunate to have a number of really nice friends. They made all these years truly memorable. I sincerely acknowledge Ajmala, Darshana, Dibyajyoti, Papri, Sunita, Deboshree, Saheli, Bhaswati, Ananya, Prashant, Gayatri, Dhanya, Moumita, Tarak, Amrit, Nitesh, Urmi, Piyush, Josena, Rana and many more for their support and encouragement.

My family has been the greatest strength for me. I sincerely thank my parents, my husband, my brother and all my family members who always have been very supportive. Whenever things in my life did not go the right way, I have been fortunate enough to have them, to be with me with all their care and love. It is all their supports which have always pushed me forward.

PREFACE

The thesis consists of six chapters and articulates the synthesis and fascinating properties of some magnetic coordination compounds and metal-organic framework (MOF) composite materials. **Chapter 1** gives a brief overview of different types of coordination compounds with special focus on molecular magnetic coordination compounds MOF composites.

Chapter 2 discusses synthesis, structural characterization and magneto-structural correlation of five new homo/heterometallic metal-organic coordination compounds synthesized using suitable blocking ligands and multidentate bridging linkers. Assembly of $Cu_3(\mu_3–O)$ cores with bridging NO_3^- ion and $[N(CN)_2^-]$ ligand resulted in a hexanuclear compound and an 1D compound respectively, while a Cu(II) 1D coordination chain has been synthesized containing $[Cu_4(pdmH)_2(pdm)_2(H_2O)_2]$ [$pdmH_2$ = pyridine–2,6–dimethanol] building units. To synthesize the heterometallic compounds, the polytopic ligand, di(2–pyridyl)ketone, has been exploited and a decanuclear Ni_4Cu_6 cluster and a 3D framework with Mn_2Cu_4 secondary building units (SBUs)] have been synthesized. The diverse magnetic properties of compounds **1-5** are rationalized by magneto-structural correlation.

Chapter 3 deals with versatile Cu(II)-azide compounds based on two different types of coligands; N,N′–dimethylethylenediamine (Me_2en) and imidazole/substituted imidazole. By controlling the relative concentration of the blocking Me_2en ligand, a discrete dinuclear complex and an extended 2D compound have been synthesized. On the other hand, by changing the substitution on the imidazolate linker four new compounds (one 0D and three 2D) with different azide binding modes were realized. Change in the structural parameters such as Cu-N(end-on azide)-Cu bond angle, Cu-azide coordination mode, substitution on imidazole ring etc. dramatically alter the magnetic properties in these compounds.

Chapter 4 describes anisotropic 2D/3D magnetic coordination compounds and divided into two chapters. **Part A** discusses isostructural 2D metal-organic coordination compounds which exhibits metamagnetic behavior. In the compounds, anisotropic Co^{II}/Ni^{II} ions are doubly bridged by $\mu_{1,1}$-N_3 ligand to afford 1D linear chains which are further bridged through pyrazine linkers resulting in the 2D rectangular network.

Competition of ferromagnetic (FM) interaction through $\mu_{1,1}$-N_3 bridge and antiferromagnetic (AFM) interaction through pyrazine linker ensue metamagnetic behaviour which was supported by detail magnetic measurements. Presence of magneto-crystalline anisotropy in one of the compounds has been successfully demonstrated by measuring magnetization on a single-crystal by applying external magnetic field along different directions. **Part B** presents four isomorphous 3D frameworks with dual functionalities like porosity and magnetism. Structure determination revealed that all compounds have α-polonium type topology where $Ag(CN)_2^-$ metallo-ligand has been used to generate 2D -M(II)-CN-Ag(I)-CN-M(II)- layers which are further linked by different organic pillars to construct 3D porous structure. The properties of these compounds have been tuned by systematic variation of the pillars (piperazine, pyrazine and dabco). Compounds with aliphatic linkers show spin canting behaviour but use of the aromatic pyrazine linker results in dominant antiferromagnetic interaction.

Chapter 5 describes stabilization of rigid and flexible different MOF nanoparticles (NPs) on two-dimensional aminoclay (AC) template towards new MOF composite materials. In **Chapter 5A**, AC has been used as a water dispersible template having functional amine groups acting as nucleating and anchoring sites for stabilization of ultra-small (2-3 nm) rigid $\{[Cu_3(BTC)_2(H_2O)_2].xH_2O\}$ (CuBTC) MOF NPs. The resulting composite is highly water dispersible and shows significant CO_2 uptake at ambient condition, superior gas separation [CO_2/N_2 and CO_2/CH_4] and improved catalytic efficiency for the chemical fixation of CO_2 to cyclic carbonates in comparison to pristine CuBTC. **Chapter 5B** presents miniaturization of two different flexible MOFs, $\{[Cu(pyrdc)(bpp)](5H_2O)\}_n$ (**F-MOF1**) and$\{[Cu(dhbc)_2(4,4'\text{-bpy})]\cdot 5H_2O\}$ (**F-MOF2**), using AC which acts as the functional template to grow and stabilize F-MOF nanocrystals. Several **F-MOF1@AC** composites were synthesized where the gate/step pressure for specific adsorbate molecule could be tuned by varying the AC content. One of the **F-MOF2@AC** composites shows enhanced CO_2 uptake at ambient condition and also exhibits its CO_2 separation ability from CO_2/N_2 and CO_2/CH_4 gas mixture as realized from breakthrough column experiments.

Chapter 6 is divided into two parts. **Part A** highlights water-dispersible ZIF-8–aminoclay nanocomposites which have been synthesized *in situ* by the self-assembly of ZIF-8 precursors and aminoclay (AC). The formation of the composites is driven by the favourable interaction between NH_2 group of aminoclay and unsaturated Zn(II) sites of

ZIF-8 NPs. In the composites, the ZIF-8 NPs are assembled together by AC. Such assembly increase the effective number of neighbouring frameworks atoms in the composite which eventually facilitates higher adsorption capacity and higher surface area compared to that of ZIF-8 NPs. **Part B** presents post-synthetic surface coating of ZIF-8 NPs with laponite, a highly water dispersible nanoclay material towards hydrogel composite for controlled drug delivery. The hydrogel composite is formed due to the spontaneous electrostatic interaction between ZIF-8 particles having surface positive charge and laponite particles having negatively charged surface. In the hydrogel composite, hexagonal ZIF-8 NPs are wrapped with the laponite clay. Small molecule anti-cancer drug 5-fluorouracil (5-FU) was loaded into the ZIF-8 NP and then further gelation was performed between FU@ZIF-8 and laponite. In the resulting composite, coating of the ZIF-8 NPs by laponite inhibits release of encapsulated drug molecules under physiological conditions. The undesired drug release at physiological condition (pH = 7.4) from the hydrogel composite is significantly less compared to that from uncoated FU@ZIF-8 particles.

TABLE OF CONTENTS

Chapter 1

Introduction

1.1 Coordination Compounds

The pioneering work by Alfred Werner in 1893 described the structure of octahedral transition metal complexes and the coordination number of metal ions. This work was the origin of modern coordination chemistry and thereafter there has been a tremendous development in this field. The extensive study over the years has now made it possible for the chemist to adopt rational synthetic methodologies to obtain desired coordination compounds with novel properties. On the most basic level, the coordination compounds can be described as compounds containing metal nodes linked by inorganic/organic ligands through metal-ligand coordination bond. Depending on their dimensionality, such compounds can be broadly classified into two classes, discrete coordination complexes and coordination polymers (CPs).[1] The former include zero-dimensional (0D) polynuclear complexes (Figure 1) which are formed driven by the spontaneous self-assembly of selected metal ions with suitable ligands containing multiple binding sites. Among the zero-dimensional (0D) discrete complexes, synthesis and study of magnetic polynuclear coordination clusters are highly motivated due to the structural novelty as well as the potential applications in the field of molecular magnetism.[3]

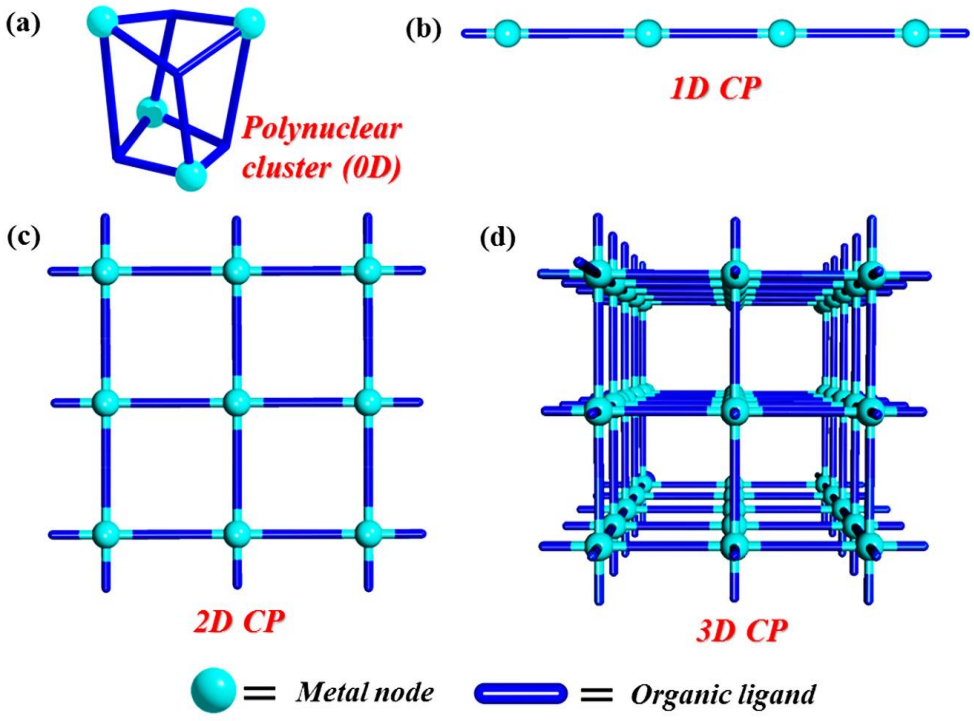

Figure 1. An illustration of metal-organic coordination compounds of different dimensionality; (a) polynuclear cluster; (b) 1D CP; (c) 2D CP and (d) 3D CP.

On the other hand, the phrase coordination polymer (CP) has been traced back to a 1964 review by J. C. Bailar.[2a] CPs are comprised of infinite networks of metal centers or inorganic clusters connected by different bridging ligands and can grow in one-, two or three-dimensions (1D, 2D and 3D) (Figure 1). The bridging ligand can be inorganic (like N_3^-, CN^-, SCN^-, CNO^- etc.) or a metallo-ligand (like $[Ag/Au(CN)_2]^-$, $[M(CN)_6]^{3-/4-}$ etc.) or organic such as different aromatic or aliphatic polycarboxylates, or pyridyl based exo-bidentate linkers. When porosity is introduced into the CPs, the compounds can be termed as porous coordination polymers (PCPs) and if the framework is solely built up by metal ions/metal–oxygen clusters with organic linkers, it is termed as metal–organic frameworks (MOFs).[4] The periodicity in MOFs creates well-defined 'coordination nanospace' which provides unique platform to study various properties like gas storage, separation, catalysis, magnetism, luminescence and drug delivery etc.[2b, 4] By rationally controlling the properties of the organic struts, the coordination nanospaces of MOFs can be modulated and such tunability give MOFs an edge over the traditional porous materials like zeolites and porous carbon.[4] Although extensive studies have been carried out on the synthesis and study of MOFs over the past few decades, there is still room for improvement of the properties of MOFs and thus research on MOFs having novel structural topology, functionality and applications have been continued.[4] Recently, a new class of composite materials have emerged by the integration of MOFs with other functional materials.[5] In such MOF composites, the integration of different functional components has been successful to mitigate the drawbacks of the individual components and provide synergistic effects to accomplish enhanced and novel properties.[5] The succeeding discussion of this thesis would try to describe and understand the fabrication and fascinating behaviours some of the magnetic coordination compounds, MOFs and their composites.

1.2 Magnetism in Coordination Compounds

Over the past few decades, magnetic coordination compounds have been well-explored due to their importance in the field of molecular magnetism which deals with the magnetic properties of materials consisting discrete molecules or assemblies of molecules.[3,6-31] Molecular magnets have attracted significant research interests because of their structural novelty as well as promising applications in high density data storage, quantum calculation, signal processing, thermal displays, optical devices, and pressure sensors.[6] Molecular magnets can be 0D clusters[10-20] or extended networks.[21-31] The

molecular magnets based on metal-organic coordination compounds straddle two different classes; conventional inorganic compounds and organic magnetic materials.[7] The advantages of such materials are their easy synthesis and tunability. These compounds are fabricated in mild conditions, mostly in room temperature and atmospheric pressure, in contrast to the high temperature synthetic conditions required for the conventional inorganic compounds.[10-20] Moreover, the extraordinary flexibility of molecular chemistry allows modulation of the structures with tunable properties. The succeeding discussions will highlight some of important reports of magnetic 0D clusters, extended network and further incorporation of other functionalities into these molecular magnets.

1.2.1 Magnetism in Discrete Clusters

Homo- or heterometallic clusters are zero dimensional (0D) compounds which have drawn immense interests as they can serve as model compounds to understand magnetism in low-dimensional systems and the typical behaviour of magnetically frustrated compounds.[10] Different kind of magnetic exchange interactions can be established in these clusters, depending on the structural parameters, such as metal-ligand bridging mode, bond angle and bond distances etc. The mechanism of magnetic interactions between the paramagnetic metal centres in such clusters has been described by the superexchange mechanism.[8-9] This superexchange mechanism is summarized on the basis of the Goodenough–Kanamori rules,[8] which was a breakthrough discovery during the 1950s. This rule includes consideration of the bond angle and the symmetry of the metal and ligand orbitals concerned. There are two mechanisms for superexchange interactions: the kinetic exchange mechanism (J_{KE}) and the potential exchange mechanism (J_{PE}).[9] Kinetic exchange is mediated by a direct pathway of the overlapping orbitals, which connects the two interacting magnetic orbitals. It is antiferromagnetic in nature as a consequence of the Pauli principle, leading to an antiparallel spin ordering via a common covalent bond. On the other hand, potential exchange is effective between orthogonal magnetic orbitals with comparable orbital energy. The mechanism producing ferromagnetic interaction is indeed the exchange energy that gives rise to Hund's rules leading to a parallel spin alignment, i.e. ferromagnetic interaction. In this case, the exchange energy is minimized if all the electrons have the same spin alignment. A large number of diverse 0D magnetic clusters have been synthesized over the past few decades exploiting different types of bridging ligands like hydroxide, alkoxide or phenoxide and

pseudohalides etc.[10-20] As discussed above, the concerned bond angles of the bridging ligands play a pivotal role to determine the nature of superexchange interaction in these compounds and in general orthogonality of the magnetic orbitals results into ferromagnetic behaviour. Extensive study has been carried out on hydroxido, alkoxido or phenoxido bridged Cu(II) clusters[11] and the results show that ferromagnetic behaviour is observed with and a triplet ground state when the ∠Cu–O–Cu < 97.5°. Orthogonality is realized for larger value of Cu–X–Cu angle when X is less electronegative. Pseudohalides have been proved to be very proficient bridging ligands to design novel structures that exhibit interesting magnetic properties and the azide based clusters have attracted special attentio.[12] Different kind of exchange interaction can be achieved depending on the diverse binding modes of azide. The most commonly observed bridging modes are the end-to-end (EE) and end-on (EO). The EE mode mainly exhibit antiferromagnetic interaction with a few exceptions while the EO mode can mediate both ferro and antiferromagnetic interactions depending on the metal–N–metal bond angle.[13] Calculations based on density functional theory (DFT) predicted that EO mode can exhibit antiferromagnetic behaviour if the metal–N_{EO}–metal angle is above the critical angle 104°.[13] Spin polarization through the π_g orbital of azide group is believed to another important factor to control the nature of exchange interaction in Cu-azide systems.[14] Figure 2 illustrates this mechanism. For the EO binding mode, the electron on the bridging nitrogen (with the α spin, as shown in Figure 2a) is partially delocalized toward the d_{xy} orbitals of metals resulting each unpaired electron localized in its magnetic orbital to have a probability of ß spin higher than 0.5. This favours the ferromagnetic interaction. In case of EE mode, if an α spin is delocalised toward $(d_{xy})_{\mathbf{A}}$, a ß electron would be symmetrically delocalized toward $(d_{xy})_{\mathbf{B}}$ (Figure 2b). Thus, the unpaired electron around **A** will have a probability of ß spin higher than 0.5 and the unpaired electron around **B** will have a probability of α spin higher than 0.5, resulting the antiferromagnetic interaction. A large number of metal-azide cluster of different nuclearity have been reported by various research groups and their magnetic behaviour depends on the above discussed factors.[12] However, there are cases where exceptional behaviour has been exhibited by certain compounds and the general rules are not always satisfied. A dimer $[Cu_2L_2(N_3)_2]$ (L = 1-(*N*-salicylideneamino)-2-aminoethane), shows antiferromagnetic interaction which has a Cu-N_{EO}-Cu angle of 89.1°,[12a] where antiferromagnetism generally arise only when the Cu-N_{EO}-Cu angle is greater than 104°.

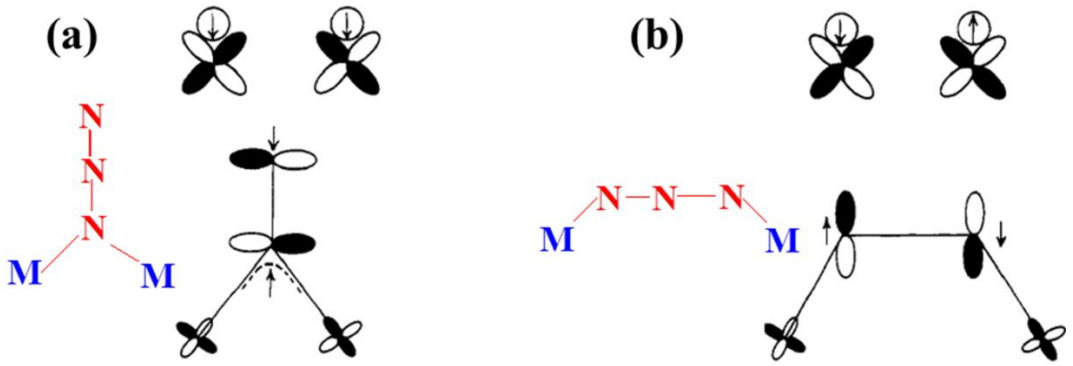

Figure 2. Spin polarization through the π_g orbital of azide in (a) EO and (b) EE mode.

In this compound, Cu centres are connected through an end-on bridge where the N_{EO} occupies the basal plane of one Cu centre but occupies apical position of the other Cu. Moreover, the Cu–N_{EO} distance is quite higher than the critical Cu–N distance for the interaction being ferromagnetic. These factors cumulatively result in the observed weak antiferromagnetic behaviour. Ghosh *et al.* have reported another interesting Ni-azide complex $[Ni_4(\mu_2\text{-}N_3)_4(\mu_3\text{-}N_3)_2(N_3)_2(enbzpy)_2]\cdot 2H_2O$ (enbzpy = [*N*,*N*-bis(pyridin-2-yl)benzylidene]ethane-1,2-diamine), which contains a tetranuclear double-open dicubane structure (Figure 3a).[12c] In this compound, doubly and triply bridged EO azide groups result in a global ferromagnetic behaviour (Figure 3b).

Antiferromagnetic compounds with a frustrated lattice have been of a long term interest to understand the spin frustration mechanism. Trinuclear or tetranuclear cluster based hybrid compound can exhibit geometric frustration. For a triangular antiferromagnetic lattice, it is evident that only two of the three spin constrains can be satisfied simultaneously, leading to spin frustration (Figure 4a). In Figure 4b, the tetrahedron comprised of four edge-sharing equilateral triangles is also a geometrically frustrated system, as only two of the four equivalent nearest neighbour interactions can be satisfied simultaneously. A number of compounds have been reported with a trinuclear and tetranuclear core. Special attentions have been devoted to construct S=½ triangular lattice with the pursuit of magnetic frustration.[15] Ghosh *et al.* have reported two trinuclear complexes $[(CuL_3)_3\text{-}(\mu_3\text{-}OH)](ClO_4)_2\cdot H_2O$ and $[(CuL_4)_3(\mu_3\text{-}OH)](ClO_4)_2\cdot H_2O$ where HL_3 = 7-(ethylamino)-4-methyl-5-azahept-3-en-2-one, and HL_4 = 4-methyl-7-(methylamino)-5-azahept-3-en-2-one, which were derived from tridentate Schiff bases (HL_3 and HL_4).[15b] At low temperature, these compounds exist in spin frustrated doublet state, as evidenced from the EPR spectra at 4 K.

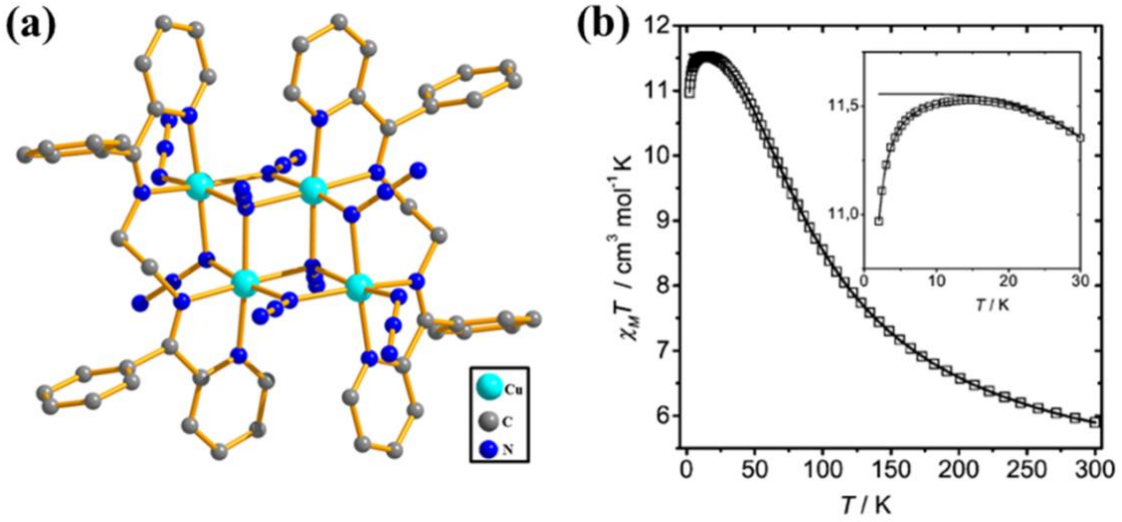

Figure 3. (a)Tetranuclear dicubane Ni-azide complex and (b) the plot of $\chi_M T$ *vs.* T for this compound. The line represents the best fit and the points the experimental data. The theoretical behaviour of a fully isotropic ferromagnetic Ni_4 cluster is included as a dotted line in the inset. Reproduced from reference 12c, by permission of The Royal Society of Chemistry.

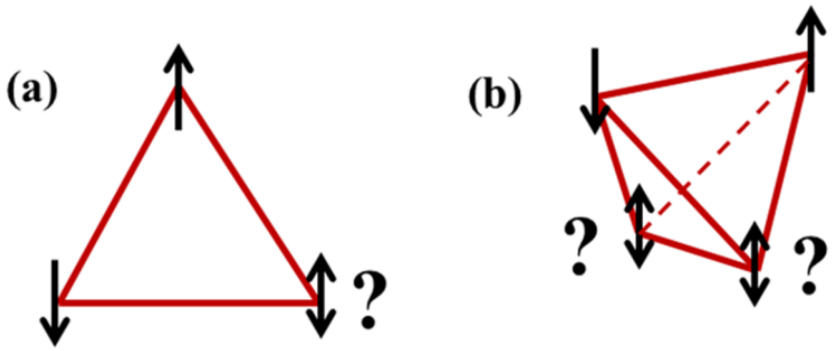

Figure 4. Spin frustration in (a) equilateral triangle and (b) tetrahedron.

Study on the magnetic clusters have been boosted after the discovery of single molecule magnets (SMMs).[16,17] These are isolated or discrete molecules which have a large ground state spin and a high negative magnetic anisotropy. These features give rise to a high barrier for switching from total spin up to total spin down at low temperatures (specifically below the 'blocking temperature', T_B, below which relaxation is slow). These compounds are promising for high density information storage and quantum computation, as the magnetic information is being stored at a molecular level and potentially the density of information being stored could be increased by several orders of magnitude. The first compound to exhibit SMM is the "Mn_{12}" cluster, which was discovered by Gatteschi and co-workers (S =10 ground state; T_B = 10 K).[16a] The last two

decades have witnessed synthesis and study of a large numbers of SMMs.[16,17] Special attentions have been dedicated to synthesize SMMs based on bigger clusters of transition metal ions to achieve large ground state spin while high anisotropy were realized for SMMs based on lanthanide metal ions. To achieve both of the desired properties (large ground state spin and large anisotropy), heterometallic 3d-4f SMMs have also been investigated.[17b]

1.2.2 Magnetism in Higher Dimensional Networks

Higher dimensional compounds such as 1D chains, 2D networks and 3D frameworks are of particular interest because of their novel topology, interesting magnetic behaviours and enhancement of bulk magnetic properties. One interesting class of 1D compounds are "Single Chain Magnets" (SCMs).[18] In these compounds, significant magnetic anisotropy is present and the 1D chains are well separated from each other, which result in the slow relaxation of magnetization. With the quest of theoretical understanding of the SCM behaviour, the study of SCMs has attained significant importance.

There have been continuous efforts to design higher dimensional compounds, especially 3D frameworks. This is because of the fact that bulk magnetism is intrinsically a three-dimensional (3D) property and thus to achieve spontaneous magnetization beyond a certain temperature (T_c), it is necessary to develop a 3D lattice of interacting magnetic centres. However, construction of such systems is not always straightforward. Different strategies have been perceived by the synthetic chemists to solve this problem. Higher dimensional Cu-azide systems have been widely investigated[12] and still remains as a fascinating research topic with the opportunity of exploring interesting magnetic properties. Further extension of metal-azide assemblies have been carried out by using neutral organic linkers with a few examples where ionic organic linkers have also been used.[19] Alternatively, the use of more azide anion by addition of a countercation, such as $N(CH_3)_4^+$ has also been established.[20] Several oxygen-bridged magnetic frameworks have been constructed based on oxides, hydroxides, phosphates, phosphites, sulfates, and carboxylates ligand to invoke magnetic interaction.[21] In such systems, organic molecules are either small or extended polytopic ligands, but the magnetic properties are governed by the M–O–C–O–M or M–O–M structural motifs, which lead to strong interactions compared to the magnetic pathways defined by bridged metal ions through multitopic ligands. Different magnetic properties have been observed by different compounds and those which exhibit ferromagnetic properties have attained considerable interest. A chiral

3D nickel glutarate, $[Ni_{20}(H_2O)_8(C_5H_6O_4)_{20}\cdot 40H_2O]$ shows pure co-operative ferromagnetic behaviour ($Tc \approx 4$ K), without any spin frustration.[22a] The low T_c value is due to the weakening of the ferromagnetic interaction for a Ni–O–Ni bridge angle significantly larger than 90°. A 3D framework $Co_5(OH)_6(SO_4)_2(H_2O)_4$ which consists of M^{II}-OH layers of edge-sharing octahedra, which are pillared by $O_3SO\text{-}Co(H_2O)_4\text{-}OSO_3$, shows ferromagnetic behaviour with a Curie temperature of 14 K.[22b] A strong magnetic exchange is provided via Co-O-Co pathways on a triangular lattice and weak Co-O-S-O-Co interlayer exchange through the pillar. Neutron diffraction data suggests long-range ordering of only the moments within the layer, while the one between the layers is random.

Ferrimagnetic and canted behaviour have also been observed in a large number hybrid compounds. Kurmoo *et al*. reported a cobalt 1,4-cyclohexane dicarboxylate, $[Co_5(OH)_8(CHDC)\cdot 4H_2O]$, (chdc = *trans*-1,4-cyclohexanedicarboxylate),[23] that contains metal–hydroxide octahedral–tetrahedral layers pillared by chdc. 1-D channels situated between the chdc pillars are occupied by noncoordinated water molecules. Single crystalline nature of the material retains during dehydration from $[Co_5(OH)_8(CHDC)\cdot 4H_2O]$ to $Co_5(OH)_8(CHDC)$ via an intermediate $[Co_5(OH)_8(CHDC)\cdot 2H_2O]$ upon heating or evacuation. The magnetic susceptibility data of both the hydrated and dehydrated compound indicates ferrimagnetic behaviour with a T_c of 60 K (Figure 5a). The value of the saturation magnetization at 2 K is explained by a model of two sublattices, one containing three octahedral cobalt atoms and another comprising two tetrahedral cobalt atoms (Figure 5b).

Spin canting in hybrid material can arise from magnetic anisotropy and antisymmetric Dzyaloshinsky–Moriya (DM) interaction.[24] The DM term arises from the spin-orbit coupling resulting the antisymmetric interaction and the Hamiltonain is $H = D_{ij}\cdot[S_i \times S_j]$, while the Hamiltonian used to describe a symmetric exchange between normal antiferromagnetically coupled spins S_i and S_j is given as $H = -2J\sum S_i\cdot S_j$. This anisotropy and the antisymmetric interaction are indeed intrinsic effects due to the particular crystal symmetry. Judicious choice of appropriate system satisfying these factors thus can lead to spin canting behaviour. In this regard, two isomorphous compounds, $[M_2(L)_2(H_2O)_2]_n$ (M= Co, Ni; L = 2,1,3-thiadiazole- 4,5-dicarboxylate) were reported by Batten *et. al*.[25]

The Co^{II} compound shows spin-canted antiferromagnetism while simple antiferromagnetic coupling is observed for the Ni^{II} analogue. Below 6 K, the $\chi_M T$ *vs. T*

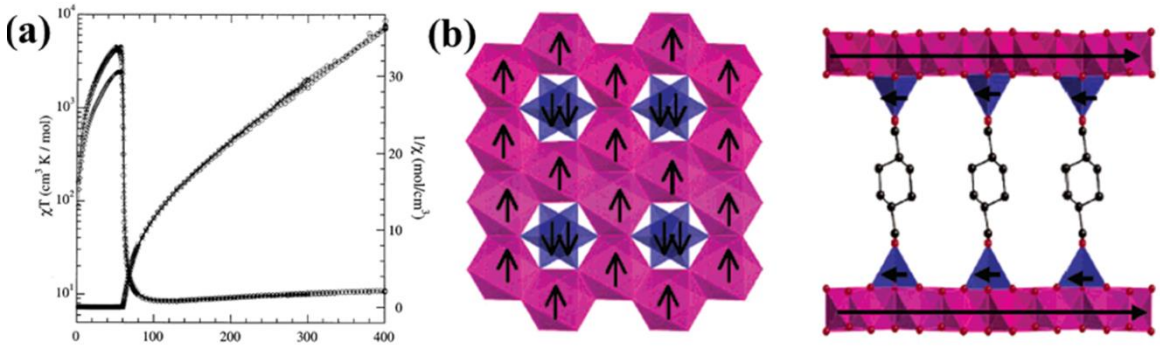

Figure 5. (a) temperature dependence of the inverse magnetic susceptibility and of the product of susceptibility and temperature: virgin (O), dehydrated (X) and rehydrated (♦) and (b) Diagrammatic representation of the proposed magnetic ordering at the tetrahedral and octahedral cobalt(II) sites in $[Co_5(OH)_8(CHDC)\cdot 4H_2O]$ Reprinted with permission from reference 23.

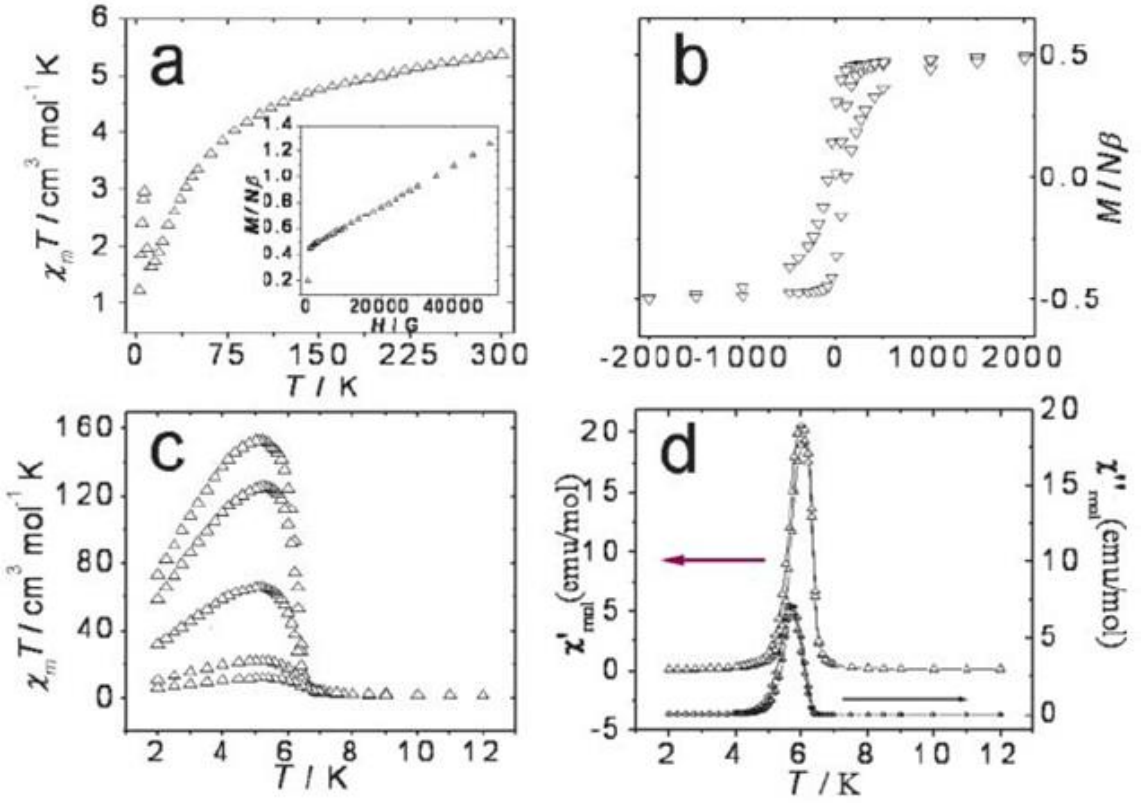

Figure 6. Magnetic behaviour of the Co^{II} compound. (a) $\chi_M T$ *vs.* T plot (insert: plot of the reduced magnetization at 2 K). (b) Hysteresis loop. (c) $\chi_M T$ *vs.* T plots at different fields (from 1000 to 50 G) in the low temperature region. (d) Plot of the ac susceptibility. From reference 25. Reproduced by permission of The Royal Society of Chemistry.

plot of Co^{II} compound exhibits a rapid increase (Figure 6a), which is due to the long range ordering. The plot of reduced magnetization *vs*. temperature, the field dependence of $\chi_M T$ and the ac susceptibility data also confirm the spin canted behaviour (Figure 6). In

contrast, the Ni^{II} analogue shows simple antiferromagnetic behaviour. Despite the structural similarity, the different behaviour of these compounds originates from the difference in anisotropy of the two metal ions. Antisymmetric exchange interaction being of the same order for these isomorphous compounds, the much higher single ion anisotropy of Co^{II} than the Ni^{II} ions results in spin canting in the Co^{II} compound.

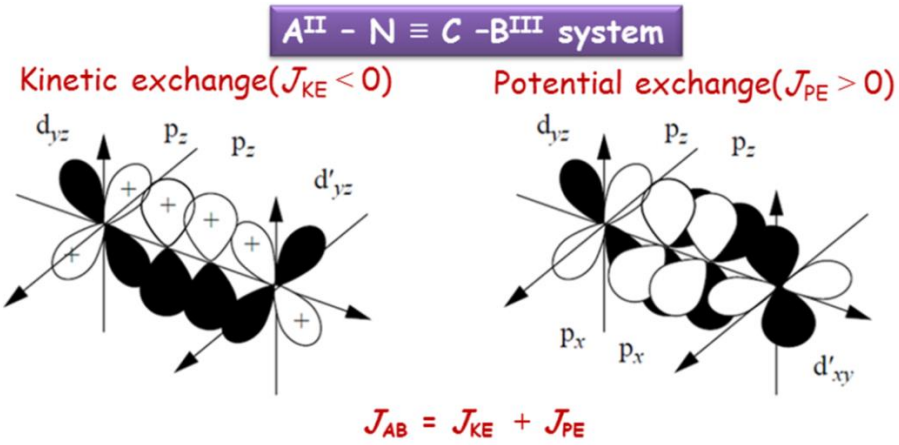

Figure 7. The two basic mechanisms for the isotropic exchange in the magnetic coupling between the A^{II} and B^{III} ions in the CN-bridged complex. Kinetic exchange (J_{KE}) pathways ($d_{yz}\| \pi_z \| d_{yz'}$) dominate in the left one, while on the right is one of significant potential exchange (J_{PE}) pathways ($d_{yz}\| \pi_z \perp \pi_x \| d_{xy'}$). The superexchange coupling between A^{II} and B^{III} (J_{AB}) involves a superposition of J_{PE} and J_{KE}.

The Prussian blue analogues are well-studied 3D compounds[30a] which have exhibited interesting magnetic properties like tunable T_c or T_n, guest induced magnetic phase transition etc.[30b-e] Interestingly, the type of the magnetic exchange interactions in such compounds can be predicted by the superexchange mechanism and a rational design approach may be adopted to realize the desired magnetic interactions. To understand the superexchange mechanism in such compounds, let us take the example of Prussian blue ($Fe^{III}_4[Fe^{II}(CN)_6]_3 \cdot nH_2O$) and its analogues. In this case, the metal *d*-orbitals split into t_{2g} and e_g set by the CN ligands. Therefore, based on magnetic orbital symmetry, we can understand whether the orbital superexchange among each of the orbitals on metal ions is J_{KE} or J_{PE}. When the magnetic orbital symmetries of the metals are the same, the superexchange interaction is J_{KE}. Conversely, when the magnetic orbital symmetries of the metals are different, the superexchange interaction is J_{PE}. The total superexchange interaction is given by the sum of all of the orbital exchange contributions between the transition metal ions (Figure 7). For example, let us consider the case of the

hexacyanochromate cyanide $A^{II}_{y}[Cr^{III}(CN)_6]$, with Cr^{III} being $(t_{2g})^3$ and S_{Cr}= 3/2 . There is no overlap between Cr^{III} and A^{II} magnetic orbitals, if all of the magnetic orbitals of A^{II} have e_g symmetry. In this situation, the potential exchange mechanism becomes dominant, leading to a ferromagnetic interaction between Cr^{III} and A^{II}. In case of $Cs^{I}Ni^{II}[Cr^{III}(CN)_6]$, a high-spin state exists for $Ni^{II}((t_{2g})^6(e_g)^2$, S_{Ni} = 1), and ferromagnetic interaction operates between Cr^{III} and Ni^{II}. In contrast, when all of the A^{II} magnetic orbitals have t_{2g} symmetry, the overlap between the t_{2g} (A) and t_{2g} (Cr) orbitals gives rise to kinetic exchange, leading to an antiferromagnetic interaction. In $Cs^{I}Mn^{II}[Cr^{III}(CN)_6]$, with a high-spin state for $Mn^{II}((t_{2g})^3(e_g)^2$, S_{Mn}= 5/2), the interaction between Cr^{III} and Mn^{II} is antiferromagnetic, and the compound is a ferrimagnet.

1.3 3D Porous Coordination Polymers (PCPs)/Metal-organic Frameworks (MOFs)

Until mid 1990s, only two types of porous materials, namely, inorganic and carbon-based materials were known. At that time, zeolites and porous carbons were considered as the classical porous solids. The last two decades have witnessed the development of design of the hybrid inorganic-organic porous materials, which are well known as metal-organic frameworks (MOFs) or porous coordination polymers (PCPs). In 1990, Robson and co-workers first reported a 3D coordination polymer using suitable molecular building blocks and metal ions.[32] The pioneering works on MOFs were carried out by Yaghi and co-worker.[35] He has introduced the concept of secondary building unit (SBU) and isoreticular synthetic strategy, which allows a sequential increase of surface area by tuning the length of the organic linker based on the same node, i.e., a oxo-centered $\{Zn_4O(CO_2)_6\}$ cluster.[35] The parent structure is MOF-5(IRMOF 1), which exhibits very high specific surface area. Several other research groups have also contributed significantly, in particular to the design principle for construction of MOFs.[33-35] The node (simple metal ions or metal clusters) and spacer (bridging organic ligands) approach has been remarkably successful in producing well-ordered crystalline solids with predictable network architectures.[36] The pioneer work on methane adsorption of porous coordination polymers (PCPs) was reported by Kitagawa and co-workers, which showed that PCPs could be promising for capturing gas molecules.[37] This ensue enormous excitement on the use of MOFs/PCPs for storage of several gases such as hydrogen, carbon dioxide and methane.[4] MOFs having permanent porosity and large surface areas are of special

interests as they exhibit ultralow densities and the availability of uniformly structured cavities allows gas storage, while flexible MOFs (FMOFs, the 3rd generation MOFs as classified by Kitagawa)[39] are important for selective gas adsorption, separation and molecular recognition. MOFs have also shown potential applications in diverse fields, such as catalysis, luminescence, drug delivery, sensing, proton conduction and magnetism. Details of the synthetic strategies, structural features, structure-property relationship and versatile applications of some benchmark MOFs have been highlighted in a number of reviews.[4]

Incorporation of different functionalities such as magnetism, ferroelasticity,[26] non-linear optical effects,[27] chemical storage[28] into in the same MOF towards a multifunctional material have always been an attractive goal. Development of such material requires the combination of properties within the same material. Among these multifunctional MOFs, designs of porous magnet have attracted special attention.[29] It is a real challenge to construct a material where two opposing properties, porosity and long range magnetic ordering are present because of the fact that magnetic exchange generally requires short bridges between the spin carriers, whereas porosity usually rely on the use of long connecting ligands. To synthesize such MOFs having both porosity and magnetism, a rational approach have been adopted by Hazra *et al.*[30d,e] They have used hexacyanometallate ($[M(CN)_6]^{y-}$) as metalloligand which can further connect to other

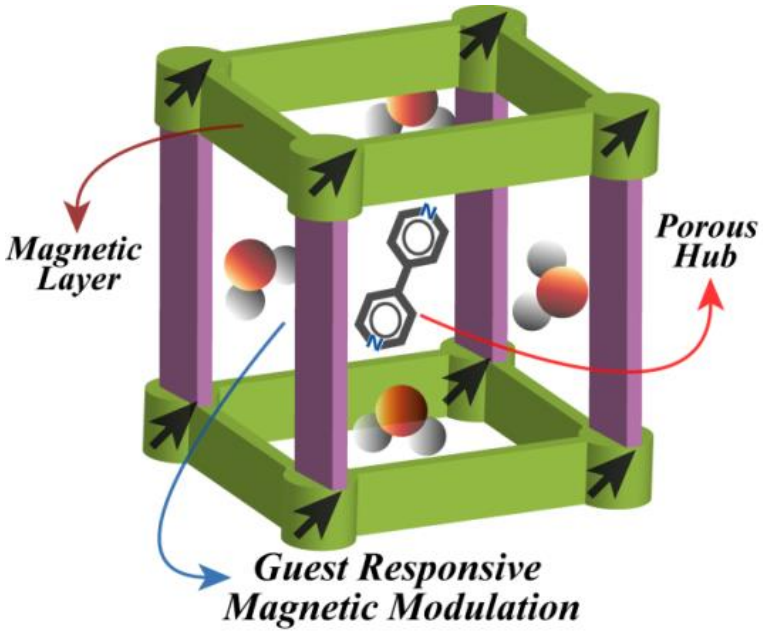

Figure 8. Bimodal functionality (porosity and magnetism) in a framework material. From reference 30d. Reproduced by permission of The Royal Society of Chemistry.

metal centers to form 2D magnetic layers, which are further linked through different exo-bidentate linkers to invoke porosity (Figure 8). Following this approach, the authors reported a hexacyanometallate 3D porous framework $\{[Mn_3(bipy)_3(H_2O)_4][Cr(CN)_6]_2 \cdot 2(bipy) \cdot 4(H_2O)\}_n$ (bipy= 4.4′-bipyridyl).[30d] In this compound, cyanometallate anion $[Cr(CN)_6]_3^-$ is used as magnetic hub while use of long linker 4,4′-bipyridyl helps to invoke porosity (Figure 8). The compound provides high heat of hydrogen adsorption (~11.5 kJ/ mol) and shows guest dependent magnetic modulation. The same group also reported another interesting report of simultaneous tuning of permanent porosity and modulation of magnetic properties by postsynthetic modification (PSM) with light in a 3D porous MOF.[30e] A 3D pillared–layer framework $\{[Co_3(bpee)_3(H_2O)_4][Cr(CN)_6]_2 \cdot 2(bpee) \cdot 2(C_2H_5OH) \cdot 2(H_2O)\}_n$ (MOF1; bpee = 1,2-bis(4-pyridyl)ethylene) is reported where guest and pillared bpee molecules undergo a [2+2]

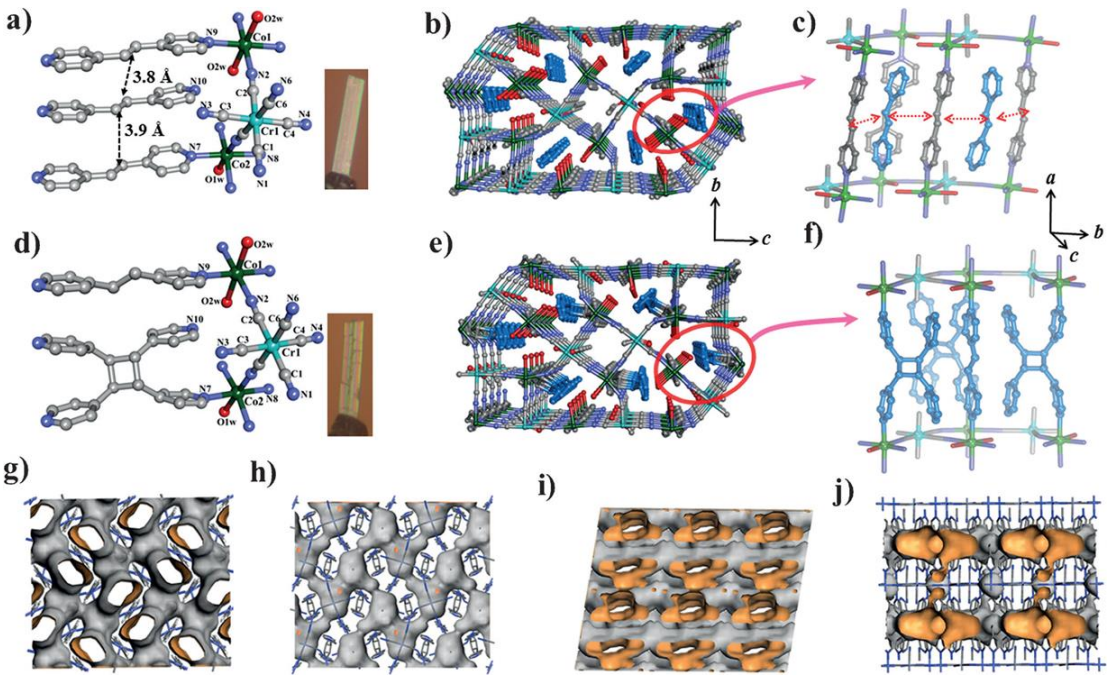

Figure 9. (a) The coordination environment of Co1 and Co2 in MOF1. (b) 3D view of MOF1 along the *a* direction, showing a 1D channel occupied by the guest bpee molecules. (c) Expanded view of the parallel arrangement of coordinated and guest bpee molecules. (d) View of MOF2, showing the formation of *rctt*-tpcb and coordination around the Co1 and Co2 centers. (e) The 3D framework of MOF2 along the *a* axis, showing that the guest bpee is fused with the host framework. f) Expanded view showing the new pillar *rctt*-tpcb in MOF2. Connolly surface of the 1D channel of MOF1 along *a* (g) and *b* (i) directions. (h) Connolly surface of MOF2 showing the continuous 1D channels along the a direction have been blocked after host–guest covalent fusion. (j) Connolly surface of MOF2a along the *b* direction. Insets in (a) and (d) Single crystals of MOF1 before and after irradiation; the linear dimensions of the crystal are 1.2 mm×0.3 mm. Reproduced with permission from reference 30e.

cycloaddition reaction induced by UV irradiation to result in $\{[Co_3(rctt\text{-}tpcb)_2(bpee)(H_2O)_4][Cr(CN)_6]_2\cdot 2(C_2H_5OH)\cdot 2(H_2O)\}_n$ (MOF2; *rctt*-tpcb=*regio-cis,trans,trans*-tetrakis(4-pyridyl)cyclobutane) (Figure 9).

MOF2 demonstrates superior CO_2 selectivity over N_2 than that of MOF1, as the discrete cages of MOF2a are more accessible for CO_2 molecules through narrow channels (Figure 9). Such increase in the CO_2 selectivity was also supported from theoretical calculations. Both MOF1 and MOF2 show similar ferromagnetic behaviour but MOF2 is magnetically reversible upon dehydration and rehydration. Such solvent-assisted reversible changes in magnetic properties were not observed for MOF1. Thus porous magnets can exhibit striking features like unique change in the magnetic properties with response to the adsorption/desorption of guest molecules. Kurmoo *et al.* have reported a reversible crystal-to-crystal transformation accompanied by change from ferromagnetic to antiferromagnetic ground states at 8 K, upon dehydration-rehydration in a nanoporous MOF $[Co^{II}_3(OH)_2(C_4O_4)_2]\cdot 3H_2O$.[31] The later compound sustains its void volume without structural destruction and exhibit transformations between different magnetic ground states following water adsorption–desorption.

1.4 MOF Composites

The last few decades have witnessed a rapid growth in the field of MOF chemistry where efforts have mostly been dedicated to the synthesis of new MOF structures and exploring their various applications. However, MOFs have certain limitations such as poor thermal, chemical and mechanical stability and poor processability which limit the applications of MOFs. To enhance the properties and to further introduce new functionalities, a contemporary approach is the fabrication of new high-performance MOF composites. MOF composites are synthesized by blending MOFs with a variety of functional materials like metal nanoparticles/nanorods (NPs/NRs), oxides, quantum dots (QDs), polyoxometalates (POMs), polymers, silica, graphene, carbon nanotubes, biomolecules and so on (Scheme 1).[5] A large number MOF composite have been reported where MOFs act as the host materials incorporating other functional components. Different functional materials like metal NP, metal oxides, QDs, POMs and various polymers have been incorporated into MOFs by various techniques.[41] The above functional materials@MOF composites find their applications in versatile fields such as adsorption, catalysis and energy transfer etc. Some illustrative examples will be discussed in the following section.

MOFs have also been incorporated into other suitable functional materials (polymers, porous silica, alumina or other inorganic materials etc.) which act as the host materials and have good mechanical, thermal and chemical stability.[41] MOFs are often grown on a two-dimensional planar or curved substrate to form thin films for applications such as small molecule separation, purification and catalysis.[42] *In situ* growth of MOFs in different functional templates have been reported by immersing solutions of MOF precursors into the matrices followed by subsequent growth of MOFs on the internal/external surface of the matrices.[41] Various polymers, carbon materials (graphene, and graphene oxide), silica and alumina microspheres are the widely used functional templates. Template assisted *in situ* growth of MOF nanoparticles (NPs) towards a novel composite is of special interests and some of the important literature reports will be discussed in the following section. Adopting similar strategy, use of a highly water dispersible nanoclay template to assist growth of MOF NPs with better functions has been explored for the first time in this thesis.

MOFs are often coated with another component like thin silica or bio-polymer shells to overcome the cytotoxicity and intrinsic instability of MOFs under physiological conditions.[5] The surface coating of MOFs can enhance the properties of MOFs as well optimize the *in vivo* performance which will be exemplified through some reports in the

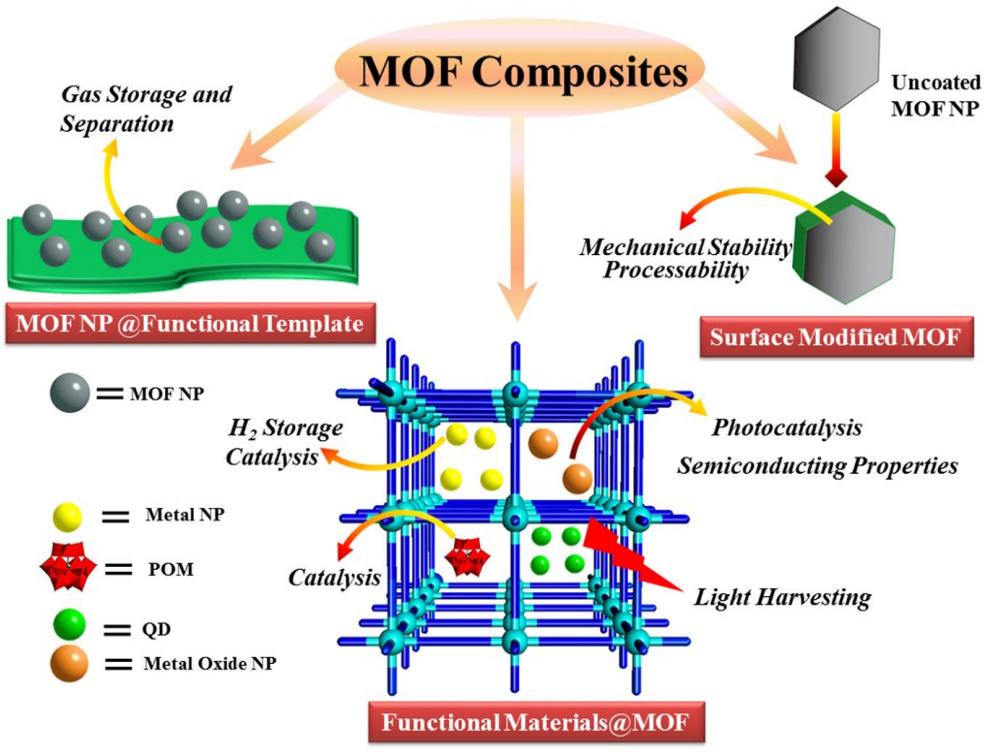

Scheme 1. Different types of MOF composites and their applications.

succeeding section. Some works documented in this thesis will demonstrate that significant enhancement in gas adsorption uptake and controlled release of drug molecules from MOF particles can be realized by coating MOF particles with suitable nanoclay.

1.4.1 MOF as Host Materials Incorporating Functional Species

MOFs offer unique properties that make them ideal as host materials to incorporate various functional materials. Firstly, the nanochannels of MOFs can be accessed by reactants from the exterior environment which allow direct reaction and formation of active species inside the porous frameworks. Furthermore, the pore surfaces of the MOFs are chemically tuneable and different types of functional materials can be incorporated efficiently. Encapsulation of metal nanoparticles into MOFs has been extensively investigated to improve the gas storage and separation by the composites.[5] Particularly, efforts have been dedicated to improve hydrogen storage capacity by using the high surface area of MOFs and the "spillover effect"; which involves the dissociative chemisorption of hydrogen on the surface of metal NPs to atomic hydrogen and its subsequent migration onto adjacent surfaces via diffusion. Following such strategy, MOF-5 was impregnated with Pd NP to result in the increase of reversible hydrogen storage from 1.15 to 1.86 wt% at 1 bar and 77 K.[43a] Suh and co-worker reported an increase of hydrogen storage from 1.03 to 1.48 wt% at 1 bar and 77 K for the redox-

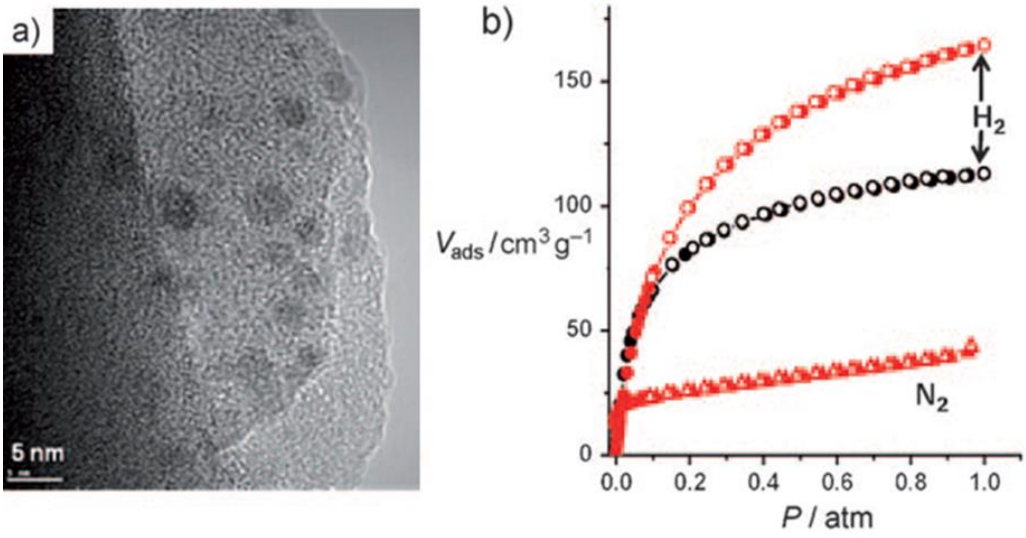

Figure 10. (a) 3 wt% PdNPs@$[SNU\text{-}3]^{0.54+}(NO_3^-)_{0.54}$ sonicated in a methanol solution of potassium hexadecylxantate at room temperature for 1 h. (b) H_2 gas at 77 K (circles) for 3 wt% PdNPs@$[SNU\text{-}3]^{0.54+}(NO_3^-)_{0.54}$ (red) and for the apohost SNU-3 (black). Reproduced by permission from reference 43b.

active MOF $\{[Zn_3(ntb)_2(EtOH)_2]\cdot 4EtOH\}_n$ [ntb = 4,4′,4″-nitrilotrisbenzoate; $[\{Zn_3(ntb)_2\}_n$ denoted as SNU-3] incorporating Pd NPs (~3 nm) (Figure 10).[43b] The enhanced H_2 storage capacity was ascribed to the spillover effect of Pd NPs and the MOFs acting as a spillover receptor. Encapsulation of metal NPs into MOFs have also shown improved catalytic activity for a number of catalytic reactions including catalytic hydrogen generation from chemical hydrides, hydrogenation reaction, C-C coupling reactions and various organic reactions.[44]

Polyoxometalates (POMs), which are discrete anionic metal–oxygen clusters, have been immobilized into porous MOFs to stabilize the POMs and optimize their catalytic performance. Sun and co-worker synthesized a series of POM@HKUST-1 composites based on $H_nXM_{12}O_{40}$ (X = Si, Ge, P, As; M = W, Mo) using one-pot hydrothermal reactions (Figure 11).[45] Single-crystal X-ray diffraction analysis revealed that the guests Keggin polyanions were alternately arranged in the cages of HKUST-1. The catalytic performance of PW12O40@HKUST-1 was evaluated by the hydrolysis of esters in excess water, which showed high catalytic activity, size selectivity and the catalyst can be recycled 15 times without activity loss and leaching.

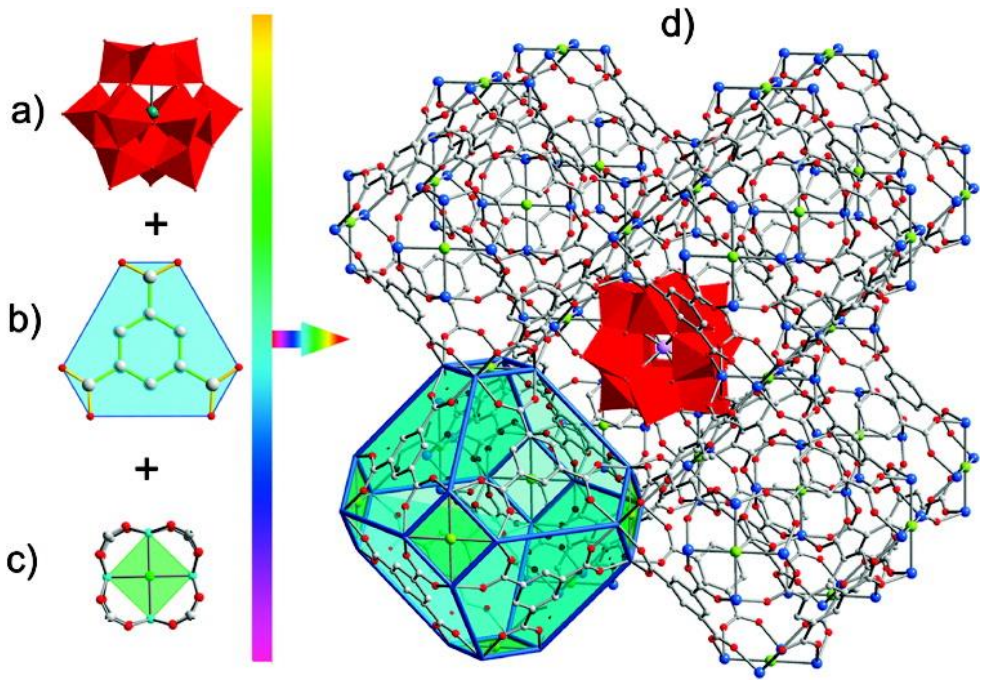

Figure 11. Templated self-assembly of POM@HKUST-1 composites by mixing MOF precursors and polyanions. (a) Keggin polyanion. (b) Three-connected node and hexagonal face (blue) defined by a BTC ligand linked to six adjacent Cu^{2+} ions. (c) SBU and square face (green) defined by four Cu^{2+} ions. (d) Cube of eight sodalite-like truncated-octahedral cages sharing square faces. Reprinted with permission from reference 45.

To obtain composites with unique optical and electrical properties, MOFs have also been functionalized with QDs, which are high quality quantum scale semiconducting materials. An interesting work on MOF-QD composites is reported by Hupp and co-workers.[46] The absorption bands of porphyrin-based MOFs provide limited coverage in the visible spectral range for solar energy conversion. To overcome this problem, porphyrin-based MOFs were modified with CdSe/ZnS core–shell QDs for the enhancement of light harvesting via energy transfer from the QDs to the MOFs (Figure 12). The QDs were coated with a monolayer of an amphiphilic polymer having amine functional groups and a monolayer of PEG. Then they were sensitized on the surface of two zinc-centered porphyrin-based MOFs through the amine–Zn coordination. The photon-generated excitons in the QDs transfer to the MOFs through resonance energy transfer, and the broad absorption band of the QDs in the visible region offered greater coverage of the solar spectrum by the MOF–QD composites. Such sensitization approach can result in a >50% increase in the number of photons harvested by a single monolayer MOF structure with a monolayer of QDs.

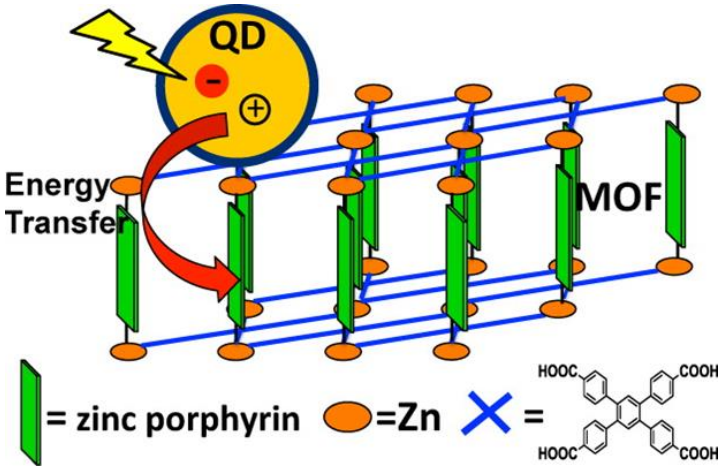

Figure 12. Schematic diagram of enhanced light harvesting in MOF-QD composites through energy transfer from the QDs to the porphyrin-based MOFs. Reproduced by permission from reference 46.

1.4.2 *In situ* Growth of MOF Nanoparticles on a Functional Template

Recently, MOF NPs have been in the spotlight owing to their high surface properties, efficient mass transfer kinetics and easy accessibility resulting in enhanced gas uptake and catalytic efficiency.[47] Furthermore, the enhanced processability at nanoscale also facilitates ease of fabrication of different devices. Template assisted synthesis has been

explored as a technique to grow MOF NPs on different functional scaffolds. The resulting nanocomposites can be of special interest as a synergistic combination of the functional template and MOF can result in novel properties that are not possible in the single component. Graphene oxide (GO) has been employed as functional template to assist the growth of MOF nanocrystals as the presence of oxygen functionalities on either side of GO layer allows it to act as a structure-directing agent in MOF assembly. Liu *et al*. reported the role of GO inducing nanocrystals of Cu-BTC MOF.[48a] It was demonstrated that epoxy groups on the GO layers can act as seed sites to prevent aggregation of crystallites and increase dispersion, which result in the formation of nanosized and well-dispersed Cu-BTC crystallites on the GO layers (Figure 13). The preparation of composites was perfomed by adding MOF precursors to dispersions of GO. The added GO consisted of 3, 9 and 15 wt% of the material weight and the composites are referred to as CG-3, CG-9 and CG-15 respectively. The composites with lesser GO content exhibited significantly enhanced CO_2 and H_2 storage capacity (from 6.39 mmol/g of Cu-BTC to 8.26 mmol/g of CG-9 at 273 K and 1 atm for CO_2; from 2.81 wt% of Cu-BTC to 3.58 wt% of CG-9 at 77 K and 42 atm for H_2). Such improved adsorption uptake by the composites was attributed to the well-dispersed MOF nanoparticles which improve the accessibility of the MOF network for the adsorbent molecules.

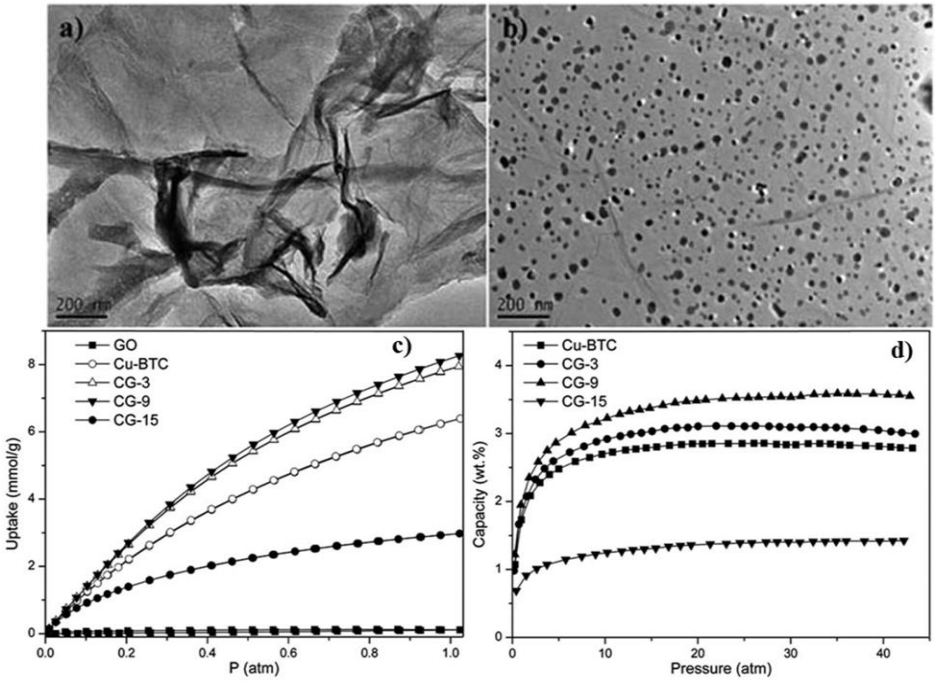

Figure 13. TEM images of the (a) wrinkled GO layers and (b) CG-9. Adsorption isotherms of Cu-BTC, CG-3, CG-9 and CG-15: (c) CO_2 at 273 K and 1 bar and (d) H_2 at 77 K and 42 atm. Reproduced by permission from reference 48a.

A recent report shows the modulation of the shape and particle size of ZIF-8 by changing the concentration of GO in ZIF-8/GO composites, where the ZIF-8 NPs were stabilized on the GO surfaces through functional groups.[48b] The composites exhibited remarkably increased CO_2 storage capacity compared to the parent ZIF-8 and can be used as precursors to prepare GO@ZnS nanocomposites. The enhanced CO_2 uptake was attributed to the cumulative effect of ZIF-8 and GO as the latter provides specific interaction sites based on different polar functional groups for CO_2.

1.4.3 Coating of MOFs with a Functional Component

Nanoscale MOFs (NMOFs) often suffer from poor water dispersibility, biocompatibility. Surface modifications of NMOFs with a suitable biocompatible component are performed to optimize the *in vivo* performance, by improving the water dispersibility and affinity to target specific cells or tissues.[49] This strategy can also slow down the degradation of NMOFs preventing the premature release of the encapsulated molecules. Lin and co-workers first stabilized NMOF particles by encapsulating them within a silica shell.[50] These composites are generally prepared by first modifying NMOFs with a hydrophilic polymer (e.g. PVP) to keep the NMOF particles well dispersed, and then coating with a silica shell in a silica precursor solution. An interesting report documented the coating of an amino-functionalized nanoscale NH_2-MIL-101(Fe) with silica by using sodium silicate to overcome instability of the NH_2-MIL-101(Fe) particles under basic conditions.[51] The amino functionalization of the NMOFs allowed facile loading of the BODIPY fluorophore and an anticancer drug (ESCP) via covalent modifications (Figure 14). The composites were used as a nano-vehicle for imaging contrast agents and anticancer drugs by slow release of the cargoes via NMOF degradation.

In addition to the use of silica, coating NMOFs with organic polymers has also been explored to enhance biocompatibility and retard framework dissolution. Boyes and co-workers modified the surface of a Gd-based NMOF, $[Gd(bdc)_{1.5}(H_2O)_2]$, with different types of polymers through the thiol end groups of polymers which can potentially bind to the vacant orbitals of the Gd^{3+} ions.[52] The polymer coatings slowed down the release of Gd^{3+} ions and the polymer modified Gd-MOF nanoparticles can be utilized as a positive contrast agent in magnetic resonance imaging. Zhou *et al*. have reported a Cu(II)-based coordination nanocage covered with alkyne groups and its surface functionalization by grafting with azide-terminated PEG through click chemistry.[53] The surface functionalization of the hydrophobic nanocage with hydrophilic polymers enhance the

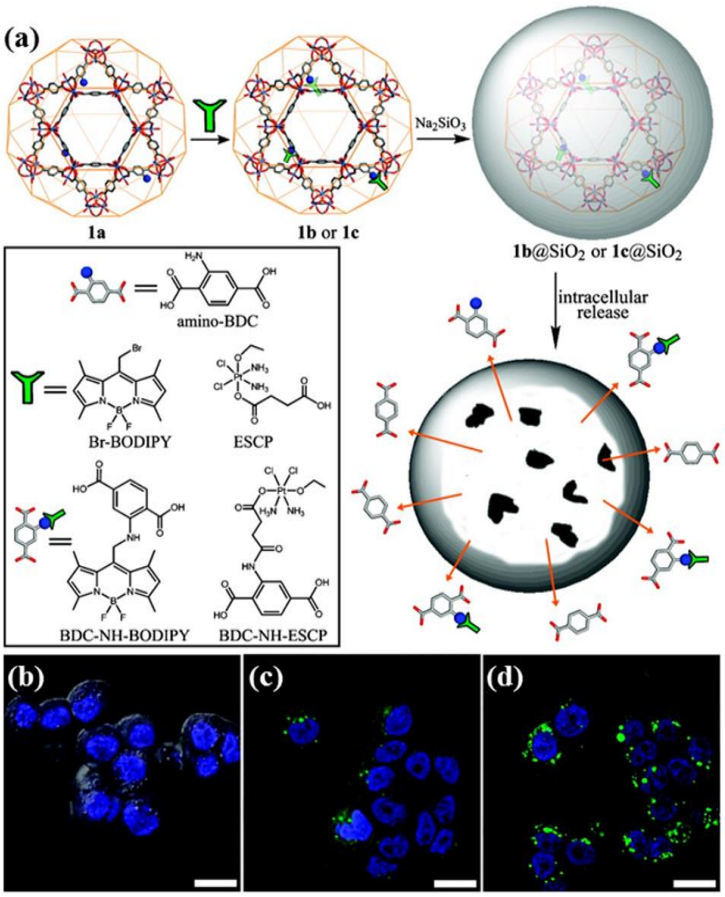

Figure 14. (a) Scheme showing the covalent grafting of BODIPY or ESCP, and the surface functionalization with a thin shell of silica on the NMOF of NH_2-MIL-101(Fe). Confocal fluorescence images of HT-29 cells incubated with (b) no particles, (c) 0.19 mg/ mL and (d) 0.38 mg/mL of BODIPY-NMOF@silica particles. The bars represent 25 mm. Reprinted with permission from reference 51.

water stability and the PEG-modified nanocages were used as a nanocarrier for drug release of 5-fluorouracil (5-FU). In a control experiment, 5-FU was dialyzed and nearly 90% of the total drug was released within 7 hours. In contrast, around 20% of the loaded drug was released in the initial 2 hours from the nanocarrier and beyond that a flatter release curve was obtained up to 24 h.

The surface coating strategy is not only beneficial for controlled delivery of bio-molecules, but can also enhance the thermal stability and mechanical strength of MOF particles. Zeng and co-workers have adopted a synthetic approach to coat microporous MOFs with an enforcing shell of mesoporous silica (*m*SiO_2) (Figure 15). Four well-known MOFs (ZIF-8, ZIF-7, UiO-66, and HKUST-1), have served as a core phase in the nanocomposites where *m*SiO_2 component acts as the shell. The authors have shown that significant enhancement in mechanical properties such as hardness and toughness can be achieved with such "armoring approach". Good accessibility of the *m*SiO_2-wrapped

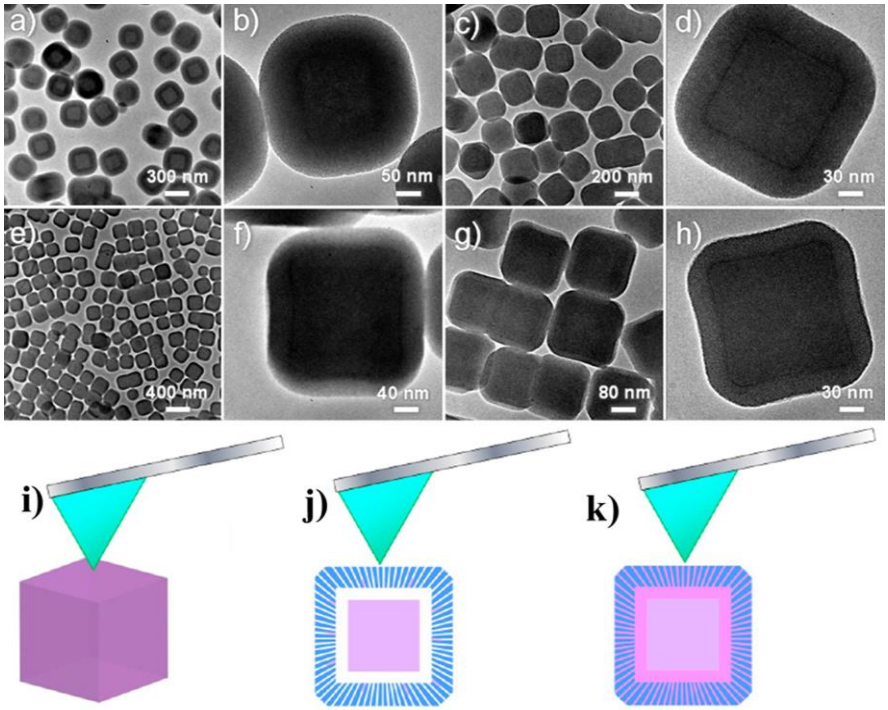

Figure 15. TEM images of ZIF-8@mSiO2 with the different thicknesses for the $mSiO_2$ shell: (a,b) ZIF-8@$mSiO_2$−20, with thickness ∼75 nm; (c,d) ZIF-8@$mSiO_2$−30, with thickness ∼46 nm; (e,f) ZIF-8@$mSiO_2$−40, with thickness ∼36 nm; (g,h) ZIF-8@$mSiO_2$−50 with the thickness ∼26 nm. The numbers (20, 30, 40 and 50) denote the weight (mg) of ZIF-8 nanocubes used in synthesis. Illustrations for the AFM nanoindentation on different nanostructures: (i) ZIF-8 cubes, (j) ZIF-8@mSiO2 (after calcination), and (k) ZIF-8@mSiO2@ZIF-8. Reprinted with permission from reference 54.

MOFs and their metal-containing nanocomposites has also been demonstrated with successful catalytic reduction of 4-nitrophenol.

1.5 Outlook

Major advances have been made in the field of diverse functional coordination compounds over the last two decades and a large number of reports have appeared on both the description and applications of such materials. Improvement of their properties such as increasing the T_c of the magnetic compounds, potential gas adsorption and small gas molecule separation under ambient condition by the porous compounds, superior catalytic activity towards the synthesis of industrially important and medicinal compounds, chemical fixation of hazardous greenhouse gases, controlled drug delivery etc. are the present challenges to the material scientists. Proper understandings of the formation, elemental magnetic exchange/gas adsorption behaviour and chemical nature of these compounds still require further investigations. Scientists will continue to use their perception, backed to the fundamental theories to predict and furnish new materials with versatile properties.

This thesis has tried to describe the fabrication and fascinating behaviours of some of such coordination compounds. Among the 0D discrete complexes, this thesis will focus on the synthesis, structural and magnetic diversity of polynuclear coordination clusters. Extended networks of CPs containing paramagnetic metal ions, their magnetic behavior and further incorporation of other functionalities (like porosity) into such magnetic materials will also be discussed. New composites of MOFs have also been explored in this thesis by blending MOFs with functional nanoclay materials which are introduced to MOF chemistry for the first time. In particular, the succeeding discussions of this thesis will focus on the magneto-structural correlation of homo/hetero-metallic clusters and extended networks consisting of polynuclear building blocks, long-range ordering in three-dimensional frameworks and incorporation of porosity into such magnetic materials. Template (aminoclay) assisted fabrication of rigid/flexible MOF nanocrystals towards novel composites and *in situ*/ post-synthetic surface coating of MOF NPs with suitable nanoclay materials (aminoclay/laponite) have also been explored in this thesis.

1.6 REFERENCES

1. T. R. Cook, Y.-R. Zheng and P. J. Stang, *Chem. Rev*., 2013, **113**, 734.
2. (*a*) J. C. Bailar, *Prep. Inorg. React*., 1964, **1**, 1; (*b*) R. Haldar and T. K. Maji, *CrystEngComm*., 2013, **15**, 9276.
3. (*a*) M. Kurmoo, *Chem. Soc. Rev.*, 2009, **38**, 1353; (*b*) D. Maspoch, D. Ruiz-Molina and J. Veciana, *J. Mater. Chem.*, 2004, **14**, 2713.
4. Themed Issue:Metal-organic Frameworks, *Chem. Rev.*, 2012, **112**, 673.
5. Q-L. Zhu and Q. Xu, *Chem. Soc. Rev*., 2014, **43**, 5468.
6. J. S. Miller, *Adv. Mater*., 1990, **2**, 98.
7. J. S. Miller and A. J. Epstein, *Angew. Chem. Int. Ed.*, 1994, **33**, 385.
8. (*a*) J. B. Goodenough, *Phys. Rev.*, 1959, **100**, 564; (*b*) J. B. Goodenough, *J. Phys. Chem. Solids*, 1958, **6**, 287; (*c*) J. Kanamori, *J. Phys. Chem. Solids*, 1959, **10**, 87.
9. (*a*) A.P. Ginsberg, *Inorg. Chim. Acta. Rev.*, 1971, **5**, 45; (*b*) S. Ohkoshi and K. Kasimoto, *J. Photochem. Photobiol. C*, 2001, 71.
10. John E. Greedan, *J. Mater. Chem.*, 2001, **11**, 37.
11. (*a*) M. P. Suh, M.Y. Han, J. H. Lee, K. S. Min and C. Hyeon, *J. Am. Chem. Soc*., 1998, **120**, 3819; (*b*) E. Ruiz, P. Alemany, S. Alvarez and J. Cano, *J. Am. Chem. Soc*., 1997, **119**, 1297.

12. (*a*) A. Escuer and G. Aromi, *Eur. J. Inorg. Chem*., 2006, 4721; (*b*) Y. Song, S. Ohkoshi, Y. Arimoto, H. Seino, Y. Mizobe and K. Hashimoto, *Inorg*. *Chem.*, 2003, **42**, 1848; (*c*) T. K. Karmakar, S. K. Chandra, J. Ribas, G. Mostafa, T. H. Lu and B. K. Ghosh, *Chem. Commun.*, 2002, 2364.
13. E. Ruiz, J. Cano, S. Alvarez and P. Alemany, *J. Am. Chem. Soc*. 1998, **120**, 11122.
14. (*a*) P. de Loth, P. Cassoux, J. P. Daudey and J. P. Malrieu, *J. Am. Chem. Soc.* 1981, **103**, 4007; (*b*) O. Kahn, S. Sikorav, J. Gouteron, S. Jeannin and Y. Jeannin, *Inorg. Chem.*, 1983, **22**, 2877.
15. (*a*) P. Kanoo, C. Madhu, G. Mostafa, T. K. Maji, A. Sundaresan, S. K. Pati and C. N. R. Rao, *dalton Trans.*, 2009, 5062; (*b*) M. Ray, S. Chattopadhyay, M. G. B. Drew, A. Figuerola, J. Ribas, C. Diaz and A. Ghosh, *Eur*. *J*. *Inorg*. *Chem*., 2005, 4562.
16. (*a*) A. Caneschi, D.Gatteschi, R. Sessoli, A. L. Barra, L. C. Brunel and M. Guillot, *J. Am. Chem. Soc.*, 1991, **113**, 5873; (*b*) R. Sessoli, H. L. Tsai, A. R. Schake, S. Wang, J. B. Vincent, K. Folting, D. Gatteschi, G. Christou and D. N. Hendrickson, *J*. *Am*. *Chem*. *Soc*., 1993, **115**, 1804.
17. (*a*) R. Sessoli, D. Gatteschi, A. Caneschi and M. A. Novak, *Nature*, 1993, **365**, 141; (*d*) W. Wernsdorfer and R. Sessoli, *Science*, 1999, **383**, 145; (*b*) A. Mishra, A. J. Tasiopoulos, W. Wernsdorfer, E. E. Moushi, B. Moulton, M. J. Zaworotko, K. A. Abboud and G. Christou *Inorg. Chem*., 2008, **47**, 4832.
18. (*a*) H. Miyasaka, K. Nakata, L. Lecren, C. Coulon, Y. Nakazawa, T. Fujisaki, K. Sugiura, M. Yamashita and R. Clerac, *J*. *Am*. *Chem*. *Soc*., 2006, **128**, 3770; (*b*) L. Bogani, A. Vindigni, R. Sessoli and D. Gatteschi, *J. Mater. Chem.*, 2008, **18**, 4750; (*c*) D. Gatteschi, L. Bogani, A. Cornia, M. Mannini, L. Sorace and R. Sessoli, *Solid State Sci.*, 2008, **10**, 1701.
19. (*a*) F.-C. Liu, Y.-F. Zeng, J. R. Li, X.-H. Bu, H. J. Zhang and J. Ribas, *Inorg. Chem.* 2005, **44**, 7298; (b) F. C. Liu, Y. –F. Zeng, J. Jiao, J. R. Li, X.-H. Bu, J. Ribas and S. R. Batten, *Inorg. Chem*., 2006, **45**, 6129.
20. M. A. S. Goher, J. Cano, Y. Journaux, M. A.M. Abu-Youssef, F. A. Mautner, A. Escuer and R. Vicente, *Chem. Eur. J*., 2000, **6**, 778.
21. H. Kumagai, M. A.-Tanaka, K. Inoue and M. Kurmoo, *J. Mater. Chem*., 2001, **11**, 2146.

22. (*a*) N. Guillou, C. Livage, M. Drillon and G. Ferey, *Angew.Chem. Int. Ed*, 2003, **42**, 5314; (*b*) M. B. Salah, S. Vilminot, G. André, M. Richard-Plouet, T. Mhiri, S. Takagi, and M. Kurmoo, *J. Am. Chem. Soc.*, 2006, **128**, 7972.
23. M. Kurmoo, H. Kumagai, S.M. Hughes and C. J. Kepert, *Inorg. Chem.*, 2003, **42**, 6709.
24. (*a*) I. Dzyaloshinsky, *J. Phys. Chem. Solids*, 1958, **4**, 241; (*b*) T. Moriya, *Phys. Rev.*, 1960, **120**, 91; (*c*) T. Moriya, *Phys. Rev.*, 1960, **117**, 635.
25. J. Li, Q. Yu, Y. Tao, X.Bu, J. Ribas and S. R. Batten, *Chem. Commun.*, 2007, 2290.
26. M. E. Brown and M. D. Hollingsworth, *Nature,* 1995, **376**, 323.
27. V. Ramamurthy and D. F. Eaton, *Chem. Mater*., 1994, **6**, 1128.
28. F. Toda, S. Hyoda, K. Okada and K. Hirotsu, *J. Chem. Soc., Chem. Commun*., 1995, 1531.
29. (*a*) R. J. Kuppler, D. J. Timmons, Q.-R. Fang, J.-R. Li, T. A. Makal, M. D. Young, D. Yuan, D. Zhao, W. Zhuang and H.-C. Zhou, *Coord. Chem. Rev.*, 2009, **253**, 3042; (*b*) P. Dechambenoit and Jeffrey R. Long, *Chem. Soc. Rev.*, 2011, **40**, 3249.
30. (*a*) H. Tokoro and S.-i. Ohkoshi, *Dalton Trans.*, 2011, **40**, 6825; (*b*) W. Kaneko, M. Ohba and S. Kitagawa, *J. Am. Chem. Soc.*, 2007, **129**, 13706; (*c*) N. Yanai, W. Kaneko, K. Yoneda, M. Ohba and S. Kitagawa, *J. Am. Chem. Soc.*, 2007, **129**, 3496; (*d*) A. Hazra, P. Kanoo and T. K. Maji, *Chem. Commun.*, 2011, **47**, 538; (e) A. Hazra, S. Bonakala, K. K. Bejagam, S.Balasubramanian and T. K. Maji, *Chem. Eur. J*., 2016, **22**, 7792.
31. M. Kurmoo, H. Kumagai, K. W. Chapman and C. J. Kepert, *Chem. Commun*., 2005, 3012.
32. B. F. Hoskins and R. Robson, *J. Am. Chem. Soc.* 1990, **112**, 1546.
33. K. Biradha, C. Seward and M. J. Zaworotko, *Angew. Chem. Int. Ed.*, 1990, **38**, 492.
34. M. J. Zaworotko, *Angew*. *Chem*. *Int. Ed*., 2000, **39**, 3052.
35. (*a*) O. M. Yaghi, G. Li and H. Li, *Nature*, 1995, **378**, 703; (*b*) O. M. Yaghi, G. Li and H. Li, *Nature*, 1995, **378**, 703; (*c*) M. Eddaoudi, J. Kim, N. L. Rosi, D. T. Vodak, J. Wachter, M. O'Keeffe and O. M. Yaghi, Science, 2002, **295**, 469; (c) N. L. Rosi, J. Eckert, M. Eddaoudi, D. T. Vodak, J. Kim, M. O'Keeffe and O. M. Yaghi, *Science*, 2003, **300**, 1127 (*d*) O. M. Yaghi, H. Li, C. Davis and D. Richardson, T. L. Groy, *Acc. Chem. Res.*, 1998, **31**, 474.

36. Z. Wang, V. C. Kravtsov and M. J. Zaworotko, *Angew. Chem. Int. Ed*., 2005, **44**, 2877.
37. M. Kondo, T. Yoshitomi, H. Matsuzaka, S. Kitagawa and K. Seki, *Angew. Chem., Int. Ed. Engl*., 1997, **36**, 1725.
38. H. Li, M. Eddaoudi, T. L. Groy and O. M. Yaghi, *J. Am. Chem. Soc*., 1998, **120**, 8571.
39. S. Kitagawa and M. Kondo, *Bull. Chem. Soc. Jpn.* **1998**, *71*, 1739.
40. A. Karmakar, A.V. Desai and S. K. Ghosh, *Coord. Chem. Rev*., 2016, **307**, 313.
41. S. Li and F. Huo, *Nanoscale*, 2015, **7**, 7482.
42. S. Li, K. Yang, C. Tan, X. Huang, W. Huang and H. Zhang, ***Chem. Commun.,*** 2016, 52, 1555.
43. (*a*) M. Sabo, A. Henschel, H. Frode, E. Klemm and S. Kaskel, *J. Mater. Chem*., 2007, **17**, 3827; (*b*) Y. E. Cheon and M. P. Suh, *Angew. Chem., Int. Ed*., 2009, **48**, 2899.
44. (*a*) X. Gu, Z.-H. Lu, H.-L. Jiang, T. Akita and Q. Xu, *J. Am. Chem. Soc*., 2011, **133**, 11822; (*b*) A. Aijaz, A. Karkamkar, Y. J. Choi, N. Tsumori, E. Ronnebro, T. Autrey, H. Shioyama and Q. Xu, *J. Am. Chem. Soc*., 2012, **134**, 13926; (c) P.-Z. Li, K. Aranishi and Q. Xu, *Chem. Commun*., 2012, **48**, 3173.
45. F.-J. Ma, S.-X. Liu, C.-Y. Sun, D.-D. Liang, G.-J. Ren, F. Wei, Y.-G. Chen and Z.-M. Su, *J. Am. Chem. Soc*., 2011, **133**, 4178.
46. S. Jin, H.-J. Son, O. K. Farha, G. P. Wiederrecht and J. T. Hupp, *J. Am. Chem. Soc*., 2013, **135**, 955.
47. (*a*) D. Tanaka, A. Henke, K. Albrecht, M. Moeller, K. Nakagawa, S. Kitagawa and J. Groll, *Nat. Chem.*, 2010, **2**, 410; (*b*) S. Diring, S. Furukawa, Y. Takashima, T. Tsuruoka and S. Kitagawa, *Chem. Mater*., 2010, **22**, 4531.
48. (*a*) S. Liu, L. Sun, F. Xu, J. Zhang, C. Jiao, F. Li, Z. Li, S. Wang, Z. Wang, X. Jiang, H. Zhou, L. Yang and C. Schick, *Energy Environ. Sci*., 2013, **6**, 818; (*b*) R. Kumar, K. Jayaramulu, T. K. Maji and C. N. R. Rao, *Chem. Commun*., 2013, **49**, 4947.
49. C. He, D. Liu and W. Lin, *Chem. Rev.*, 2015, **115**, 11079.
50. W. J. Rieter, K. M. Taylor and W. Lin, *J. Am. Chem. Soc*., 2007, **129**, 9852.
51. K. M. Taylor-Pashow, J. D. Rocca, Z. Xie, S. Tran and W. Lin, *J. Am. Chem. Soc*., 2009, **131**, 14261.

52. (*a*) M. D. Rowe, C.-C. Chang, D. H. Thamm, S. L. Kraft, J. F. Harmon Jr, A. P. Vogt, B. S. Sumerlin and S. G. Boyes, *Langmuir*, 2009, **25**, 9487; (b) M. D. Rowe, D. H. Thamm, S. L. Kraft and S. G. Boyes, *Biomacromolecules*, 2009, **10**, 983.

53. D. Zhao, S. Tan, D. Yuan, W. Lu, Y. H. Rezenom, H. Jiang, L.-Q. Wang and H.-C. Zhou, *Adv. Mater*., 2011, **23**, 90.

54. Z. Li and H. C. Zheng, *J. Am. Chem. Soc.*, 2014, **136**, 5631.

Chapter 2

Homo/Heterometallic Clusters and Cluster Based Extended Networks: Synthesis, Structure and Magnetic Properties

Abstract

This chapter describes the synthesis, structural characterization and magneto-structural correlation of five new homo/heterometallic metal-organic coordination compounds synthesized using suitable blocking ligands and multidentate bridging anions. The compounds are $\{Cu_6(\mu_3\text{-}OH)_2(ppk)_6(H_2O)_2(NO_3)_4\}$ (**1**) [ppk = phenyl-2-pyridylketoxime], $[Cu_3(\mu_3\text{–}OH)(ppk)_3(\mu\text{–}N(CN)_2)(OAc)]_n$ (**2**), $\{[Cu_4(pdmH)_2(pdm)_2(\mu_2\text{–}OH)(H_2O)]\cdot ClO_4\}_n$ (**3**) [$pdmH_2$ = pyridine–2,6–dimethanol], $[Ni_4Cu_6(\mu\text{–}OH_2)_2(dpkO_2)_8(OAc)_4(H_2O)_4]\cdot 2CH_3OH\cdot 17H_2O\}$ (**4**) [dpk = di(2–pyridyl)ketone, $dpkO_2^{2-}$ = $(C_5NH_4)_2CO_2$] and $[\{MnCu_2(dpkO_2H)_2(dpkO_2)N_3\}.(NO_3).H_2O]_n$ **(5)**. Trinuclear $[Cu_3(\mu_3\text{–}OH)(ppk)_3]$ units are bridged by NO_3^- and $[N(CN)_2^-]$ anions to result in the hexanuclear compound **1** and the 1D coordination compound **2**, respectively. Compound **3** is a 1D coordination compound containing tetranuclear $[Cu_4(pdmH)_2(pdm)_2(H_2O)]^{2+}$ cores which are connected by OH^- groups. The dpk ligand has been exploited to furnish heterometallic compounds **4** and **5**. Compound **4** represents the first example of a heterometallic Ni_4Cu_6 cluster which consists of two symmetry related Ni_2Cu_3 cores. In compound **5**, $\{MnCu_2(dpkO_2H)_2(dpkO_2)^{2+}$ units are connected through azide ligand to result in a 3D framework. The magnetic properties of **1-5** are studied in detail.

Paper based on this study:

A. Chakraborty, B. K. Ghosh, J.R Arino, J. Ribas, T. K. Maji, *Inorg. Chem*., 2012, **51**, 6440.

A. Chakraborty, K. L. Gurunatha, A. Muthulakshmi, S. Dutta, S. K. Pati, T. K. Maji, *Dalton Trans*., 2012, **41**, 5879.

A. Chakraborty, J. Ribas, A. Escuer, T. K. Maji, *Dalton Trans*., 2016, DOI: 10.1039/C6DT03094G.

2.1 INTRODUCTION

Polynuclear coordination clusters have attracted intensive research interest with the contribution to the understanding and application of magnetic properties.[1] This field has become more fascinating after the emergence of single molecule magnets (SMMs) and single chain magnets (SCMs)[1-2] with potential applications including high density information storage and quantum computation.[3] Polynuclear homometallic Cu(II) complexes are of special interests as they are important in several catalytic processes in living organisms.[4] These complexes are also important to study magneto-structural correlations which essentially help to understand the super-exchange phenomenon.[5-11] Trinuclear and tetranuclear Cu(II) complexes are of special interests as geometric frustration is common in the antiferromagnetically coupled compounds which show unusual electronic properties.[5] Furthermore, linking of such polynuclear clusters towards a larger cluster or even higher dimensional network has also received significant interests.[6-8] Oxido, hydroxido, azido, halogenoto groups can act as excellent multidentate bridging ligands in the formation of dinuclear, trinuclear, tetranuclear, hexanuclear[9-11] clusters supported by different organic blocking ligands. There are reports on trinuclear $Cu_3(\mu_3–X)$ compounds (X = O, OH, Cl, Br, I) and tetranuclear oxido bridged copper complexes, but the assembly of trinuclear cores towards a hexanuclear compound[8a] or 1D coordination polymers containing trinuclear[8b] or tetranuclear[10d,e] building units are yet to be properly explored. We envisioned the use of blocking ligands such as phenyl–2–pyridylketoxime (ppk) and pyridine–2,6–dimethanol ($pdmH_2$) (Scheme 1), along with the oxido or hydroxido ligands can lead to the formation of the desired polynuclear cluster. The ligands ppk and $pdmH_2$ have already established themselves as versatile cluster forming agents in different metal systems[12] (Mn(II), Cr(III), Ni(II), Co(II) *etc*.), but there are few reports on the use of these ligands in Cu(II) polynuclear cluster chemistry.[13,17-18] In this chapter, the above ligands have been explored in Cu(II) chemistry to synthesis new Cu(II) magnetic clusters. Efforts were also dedicated to synthesize new heterometallic clusters are which are relatively less explored, despite of their fascinating magnetic properties including SMM behaviour.[14a-c] The synthesis of heterometallic clusters based on different metal ions with different coordination geometries remains a challenge as precise control over the nuclearity of the clusters is very difficult.[14d-g] To achieve the desired heterometallic cluster, it is necessary to conceive a rational approach based on the ligational motifs of organic spacers and the coordination environment of different metal

ions. Polytopic ligands like di(2–pyridyl)ketone (dpk) with well-defined and appropriately separated coordination compartments, in principle, have a better control over the outcome of a self-assembly process.[14e] Moreover, dpk can be translated into a new ligand *in situ* in aqueous or alcoholic medium through nucleophilic attack to the keto group (Scheme 1) in presence of metal ions,[14f] which renders further flexibility towards binding more number of metal centres ensuing the desired cluster. Such clusters can further be bridged by appropriate ligands towards a higher dimensional network.

This chapter articulates the synthesis, single-crystal structure and detailed magnetic study of five new compounds, $\{Cu_6(\mu_3\text{-}OH)_2(ppk)_6(H_2O)_2(NO_3)_4\}$ (**1**), $[Cu_3(\mu_3\text{–}OH)(ppk)_3(\mu\text{–}N(CN)_2)(OAc)]_n$ (**2**), $\{[Cu_4(pdmH)_2(pdm)_2(\mu_2\text{–}OH)(H_2O)]\cdot ClO_4\}_n$ (**3**) [pdmH is the monoanionic ligand and pdm is the dianionic ligand of $pdmH_2$], $[Ni_4Cu_6(\mu\text{–}OH_2)_2(dpkO_2)_8(OAc)_4(H_2O)_4]\cdot 2CH_3OH\cdot 17H_2O\}$ (**4**) [$dpkO_2^{2-}$ = $(C_5NH_4)_2CO_2$] and $[\{MnCu_2(dpkO_2H)_2(dpkO_2)N_3\}.(NO_3).H_2O]_n$ **(5)**. The ppk ligand was chosen to generate Cu_3 cores and exploited suitable anion (NO_3^-) and bridging ligand [$N(CN)_2^-$] to bridge the trinuclear building units towards hexanuclear compound **1** and 1D coordination compound **2**, respectively. In compound **3**, tetranuclear cores are connected by hydroxido (OH^-) groups resulting in a 1D chain. On the other hand, spontaneous self-assembly of dpk with Cu(II) and Ni(II) results in the formation of decanuclear cluster **4**, while employing azide ligand in the self-assembly of dpk with Cu(II) and Mn(II) ions produces the 3D framework of **5** containing Mn_2Cu_4 cores. The magnetic properties of **1-5** are studied in detail.

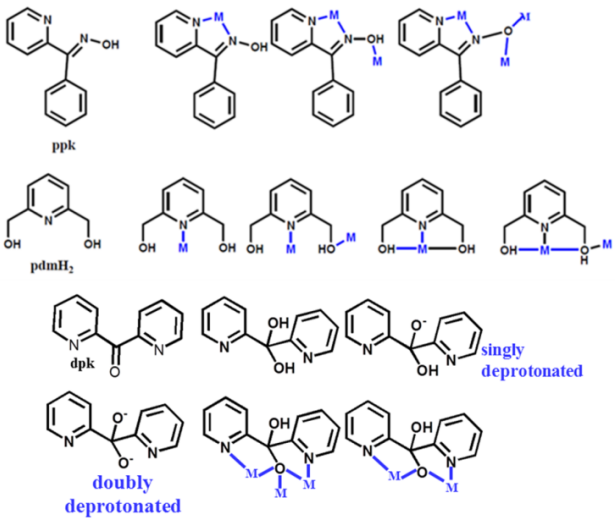

Scheme 1. Structure and different binding modes for phenyl-2-pyridylketoxime (ppk), pyridine-2,6-dimethanol ($pdmH_2$) and di(2–pyridyl)ketone (dpk). *In-situ* formation of new ligands from dpk and their binding modes are also shown.

2.2 EXPERIMENTAL SECTION

2.2.1 Materials

All the reagents and solvents employed are commercially available and used as supplied without further purification. $Cu(OAc)_2 \cdot H_2O$, $Cu(NO_3)_2 \cdot 3H_2O$, $Cu(ClO_4)_2 \cdot 6H_2O$, $Ni(OAc)_2 \cdot H_2O$, $Mn(NO_3)_2 \cdot 4H_2O$, sodium dicyanamide, phenyl–2–pyridylketoxime, pyridine–2,6–dimethanol, sodium azide and di(2-pyridyl)ketone were obtained from the Aldrich chemical Co.

2.2.2 Synthesis

$\{Cu_6(\mu_3\text{-}OH)_2(ppk)_6(H_2O)_2(NO_3)_4\}$ (1): $Cu(NO_3)_2 \cdot 3H_2O$ (0.5 mmol, 0.121 g) was dissolved in 20 mL H_2O and then methanolic solution (20 mL) of phenyl–2–pyridylketoxime (0.5 mmol, 0.099 g) was dropwise added to the above solution with constant stirring. The resulting green coloured solution was stirred for three hours. The reaction mixture was kept for slow evaporation at room temperature. Dark green coloured single crystals suitable for single crystal X-ray analysis were isolated after ten days. Yield, 62%, relative to Cu(II). Selected IR data (KBr, cm^{-1}); 3447 br, 3063 w, 3028 w, 1594 sh, 1537 sh, 1492 sh, 1428 sh, 1403 sh, 1342 sh, 1304 m, 1289 sh, 1267 sh, 1204 sh, 1154 w, 119 sh, 1053 w, 1026 w, 972 m, 823 m, 800 m, 786 m (Figure 1). Anal. calc. for $C_{72}H_{60}Cu_6N_{16}O_{22}$: C, 42.93; H, 3.21; N,11.9. Found: C, 43.06; H, 3.26; N, 12.21. The good correspondence of the PXRD patterns of the simulated and as-synthesized bulk sample indicates high purity of the sample (Figure 2).

$[Cu_3(\mu_3\text{–}OH)(ppk)_3(\mu\text{–}N(CN)_2)(OAc)]_n$ (2): $Cu(OAc)_2 \cdot H_2O$ (0.5 mmol, 0.099 g) was dissolved in 40 mL CH_3CN and then methanolic solution (20 mL) of phenyl–2–pyridylketoxime (0.5 mmol, 0.099 g) was dropwise added to the above solution with constant stirring. The resulting green coloured solution was stirred for ten minutes. Then aqueous solution (20 mL) of $NaN(CN)_2$ (0.33 mmol, 0.029 g) was dropwise added to the above mixture and then the mixture was stirred for overnight. Then the reaction mixture was filtered and kept for slow evaporation at room temperature. Green coloured single-crystals suitable for X-ray analysis were isolated after one week and washed with H_2O and CH_3CN. Yield, 75%, relative to Cu(II). Selected IR data (KBr, cm^{-1}); 3424 br, 3151 w, 3070 w, 2279 s, 2223 s, 1658 m, 1604 m, 1556 m, 1416 m, 1392 s, 1091 sh, 890 sh (Figure 1). Anal. calc. for $C_{40}H_{31}Cu_3N_9O_6$: C, 51.97; H, 3.38; N,13.64. Found: C, 51.67;

H, 3.31; N, 13.96. The phase purity was checked by comparing the PXRD pattern of the bulk powder sample with the simulated data from single-crystal (Figure 3).

$\{[Cu_4(pdmH)_2(pdm)_2(\mu_2\text{–}OH)(H_2O)_2]\cdot(ClO_4)\}_n$ (3): $Cu(ClO_4)_2\cdot 6H_2O$ (1 mmol, 0.370 g) was dissolved in 10 mL water and 10 mL methanolic solution of pyridine–2,6–dimethanol (1mmol, 0.139 g) was dropwise added to the above metal solution. Then the resulting green solution was stirred for four hours and filtered. The filtrate was kept for slow evaporation at room temperature and after one week blue crystals were isolated. The crystals were washed with water and methanol. Yield, 69%, relative to Cu(II). Selected IR data (KBr, cm^{-1}) 3097 w, 2829 w,1606 m, 1471 m, 1268 m, 1093 s, 781 m, 625 m (Figure 1). Anal. calc. for $C_{28}H_{35}Cu_4N_4O_{15}Cl$: C, 35.13; H, 3.68; N,5.85. Found: C, 35.09; H, 3.62; N, 5.88%. The phase purity was checked by comparing the PXRD pattern of the bulk powder sample with the simulated data from single-crystal (Figure 4).

$\{[Ni_4Cu_6(\mu\text{-}OH_2)_2(dpkO_2)_8(OAc)_4(H_2O)_2]\cdot 2CH_3OH\cdot 17H_2O\}$(4): $Cu(OAc)_2\cdot H_2O$ (1 mmol, 0.199 g) was dissolved in 10 mL H_2O; methanolic solution (5 mL) of dpk (1 mmol, 0.184 g) was added dropwise to it with constant stirring. The resulting solution was stirred for 15 minutes. An aqueous solution (10 mL) of $Ni(OAc)_2\cdot H_2O$ (1 mmol, 0.249 g) was added slowly to the above reaction mixture which turned green. After stirring for 1 hour, the reaction mixture was filtered and kept for slow evaporation at room temperature. Green single crystals suitable for X-ray analysis were obtained after two weeks. The crystals were separated and washed with H_2O and CH_3OH. Yield: 53% relative to Cu(II). Selected IR data (KBr, cm^{-1}); 3424 br, 1604s, 1583 s, 1375 s, 1046 m, 665 m (Figure 1). Compound purity was verified by PXRD (Figure 5) and elemental analysis result. Anal. calc. for **4**: C, 40.14; H, 4.47; N,7.64. Found: C, 40.07; H, 4.12; N, 7.94%.

$[\{MnCu_2(dpkO_2H)_2(dpkO_2)N_3\}.(NO_3).H_2O]_n$ (5): $Mn(NO_3)_2\cdot 4H_2O$ (0.5 mmol, 0.126 g) was dissolved in 10 mL H_2O; methanolic solution (5 mL) of dpk (1 mmol, 0.184 g) was added dropwise to it with constant stirring. The resulting solution was stirred for 10 minutes. An aqueous solution (5 mL) containing $Cu(OAc)_2\cdot H_2O$ (1 mmol, 0.199 g) and NaN_3 (0.5 mmol, 0.0325 g) was added slowly to the above reaction mixture which turned green. After stirring for 1 hour, the reaction mixture was filtered and kept for slow evaporation at room temperature. Green single crystals suitable for X-ray analysis were obtained after three weeks. The crystals were separated and washed with CH_3OH. Yield: 53% relative to Cu(II). Selected IR data (KBr, cm^{-1}); 3462 br, 3389 m, 3066 m, 2821 m,

2050 sh, 1562 m, 1478 m, 1432 m, 1383 sh, 1353 sh, 1294 m, 1242 m, 1215 m, 1156 m, 1070 sh, 1057 sh, 975 m, 937 m, 906 m, 806 sh, 783 sh, 703 m, 678 m, 645 m, 631 m, 587 m, 458 m (Figure 1). Compound purity was verified by PXRD (Figure 6) and elemental analysis result. Anal. calc. for **5**: C, 43.71; H, 3.11; N,15.45. Found: C, 43.27; H, 3.12; N, 15.54%.

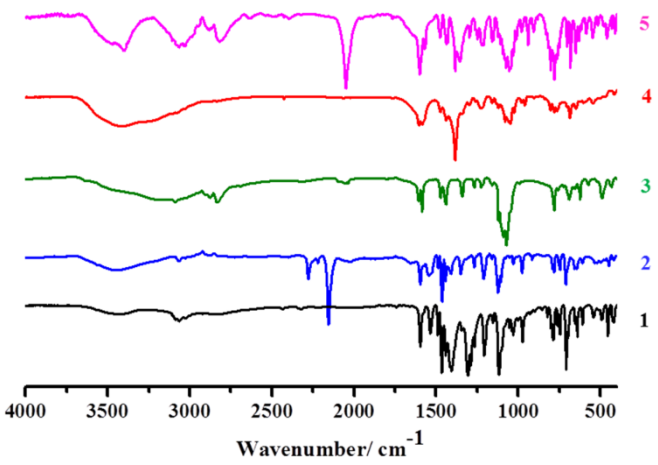

Figure 1. FT-IR spectra for **1-5**.

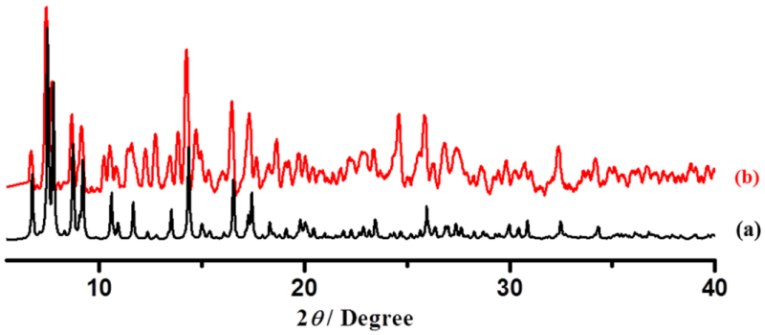

Figure 2. PXRD patterns of compound **1**: (a) simulated; (b) bulk as-synthesized. Similarity in simulated and as-synthesized pattern indicates high purity of the compound.

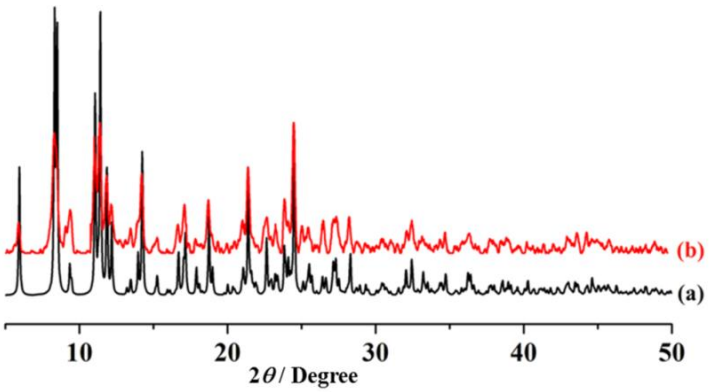

Figure 3. PXRD patterns of compound **2:** (a) simulated; (b) bulk as-synthesized.

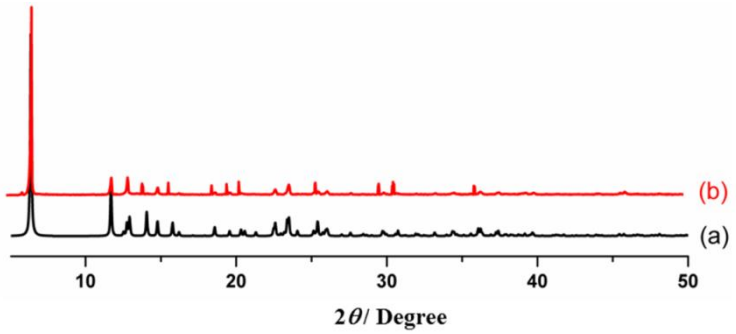

Figure 4. PXRD patterns of compound **3**: (a) simulated; (b) bulk as-synthesized.

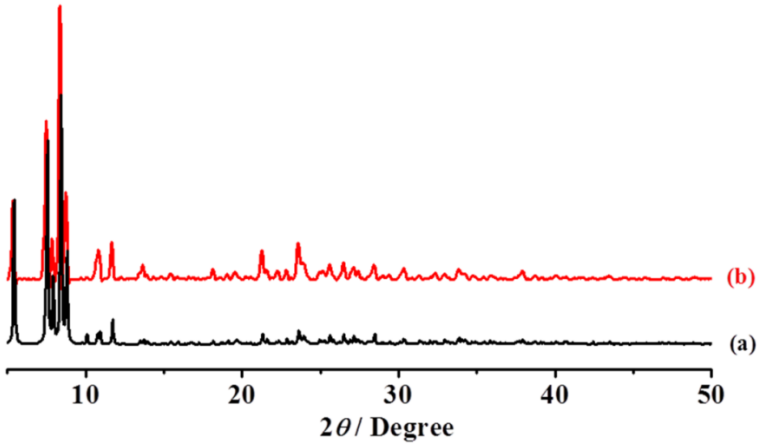

Figure 5. PXRD patterns of compound **4**: (a) simulated; (b) bulk as-synthesized.

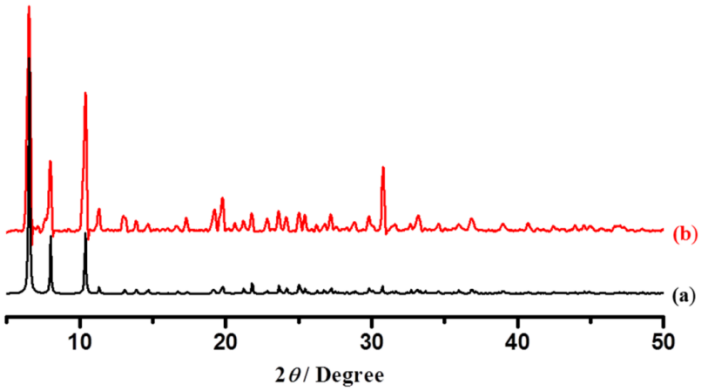

Figure 6. PXRD patterns of compound **5**: (a) simulated; (b) bulk as-synthesized.

2.2.3 Single-crystal X-ray Diffraction

X-ray single-crystal structural data of **1-5** were collected on a Bruker Smart–CCD diffractometer equipped with a normal focus, 2.4 kW sealed tube X-ray source with graphite monochromated Mo–$K\alpha$ radiation (λ = 0.71073 Å) operating at 50 kV and 30 mA. The SAINT program[15a] was used for integration of diffraction profiles and absorption correction was made with SADABS[15b] program. Both the structures were solved by SIR 92[15c] and refined by full matrix least square method using SHELXL 97.[15d]

All the non-hydrogen atoms (except the guest water molecules and O12W atom in **4** and the nitrate ions in **5**) were refined anisotropically and all the hydrogen atoms were fixed by HFIX and placed in ideal positions. All calculations were carried out using SHELXL 97, PLATON[15e] and WinGX system, Ver 1.70.01.[15f] All the crystallographic and structure refinement data of **1**-**5** are summarized in Table 1. Selected bond lengths and angles are displayed in Tables 2–6.

2.2.4 Physical Measurements

Elemental analyses were carried out on a Perkin Elmer 2400 CHN analyser. Energy dispersive analysis of X-rays (EDX) was carried out using field emission scanning electron microscope. Inductively coupled plasma atomic emission spectroscopy (ICP-AES) study was carried out using a Perkin-Elmer Optima 2100 DV spectrometer. IR spectra were recorded in KBr pellets on a Bruker IFS 66v/S spectrophotometer in the region of 4000 – 400 cm^{-1}. The temperature dependent magnetic measurements (300 K–3 K) for polycrystalline powder sample of **1**-**5** were carried out using Vibrating Sample Magnetometer in physical property measurement system (PPMS, Quantum Design, USA). Susceptibility data were collected using an external magnetic field of 500 Oe.

2.3 RESULTS AND DISCUSSION

2.3.1 Crystal Structure Description

2.3.1.1 Structural description of $\{Cu_6(\mu_3\text{-}OH)_2(ppk)_6(H_2O)_2(NO_3)_4\}$ (1)

Compound **1** crystallizes in triclinic *P*$\bar{1}$ space group. Single crystal X–ray diffraction study reveals that cyclic trinuclear Cu(II) units (Figure 7) of formula $[Cu_3(\mu_3\text{–}OH)(ppk)_3(H_2O)(NO_3)]^+$ are bridged by NO_3^- (nitrate) anions resulting in a hexanuclear cluster. There are two crystallographically independent hexanuclear clusters. The first one consists of a triangular Cu_3 skeleton where the Cu(II) centres are present in different coordination geometries. Cu1 is penta-coordinated (4+1) and exhibits square pyramidal geometry (Figure 7). The degree of distortion from the ideal square pyramidal geometry can be understood from the Addison parameter (τ)[16], which is 0.0275 for Cu1, reflecting that the geometry is close to ideal square pyramidal one. Cu1 is chelated to one ppk ligand (N1, N4) and coordinated to another ppk ligand by O9 oxygen atom and forms the equatorial plane involving the bridging μ_3–O1 oxygen atom. The axial position is occupied by the O4 atom from the bridging NO_3^- ligand which bridges two trinuclear

cores. Cu2 locates itself in a distorted octahedral geometry. The equatorial plane is occupied by two chelated nitrogen atoms (N2, N6) from one ppk ligand, O3 from another ppk ligand and μ_3–O1. O14 oxygen atom from the bridging NO_3^- ligand (connects Cu2 and Cu3) and one water molecule (O1w) occupies the axial coordination sites. Cu3 also exhibits distorted (4+2) octahedral geometry. Chelated nitrogen atoms (N3, N15) from one ppk ligand, O8 from the another ppk ligand and μ_3–O1 furnish the equatorial coordination sites; while O2 and O6 atoms of two different bridging nitrate occupy the axial positions. Selected bond length and angles are given in Table 2.

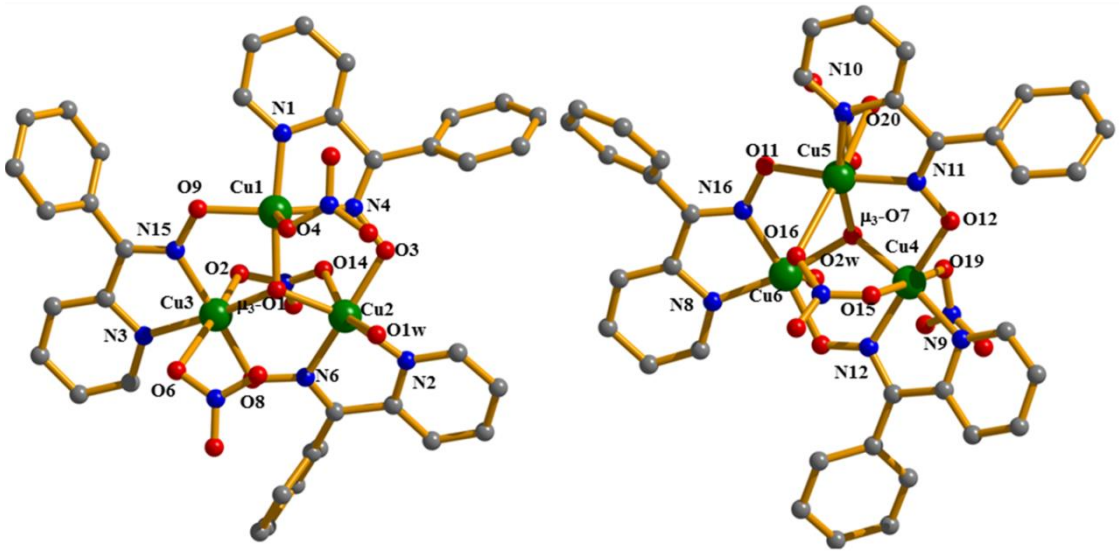

Figure 7. View of the two crystallographically independent trinuclear building unit [$Cu_3(\mu_3$–OH)$(ppk)_3(H_2O)(NO_3)$] of **1** and the coordination environment of each Cu(II) ion. Colour code: C:green; N:blue; O:red; C:grey.

The degree of distortion from the ideal square pyramidal/octahedral geometry is reflected in the angles of the basal plane of the Cu(II) ions. In the trinuclear [$Cu_3(\mu_3$–OH)$(ppk)_3(NO_3)]^+$ core, the copper atoms are held together by three different types of bridging; (i) the μ_3–OH oxygen atom (O1) bridging three Cu(II) centres; (ii) the N–O group from the ppk ligand bridging two Cu(II) centres and (iii) the nitrate ligand bridging Cu2 and Cu3. The μ_3–OH oxygen atom (O1) is located above the mean plane defined by the three copper atoms by 0.601 Å. The trinulcear core is further connected to its symmetry-related counter-part through the bridging nitrate groups ensuing the formation of the hexanuclear cluster (Cu1 atom of one trinuclear core is connected to the Cu3 atom of another trinuclear core through the O4, O6 atoms of the NO_3^- ligand). The distance between Cu1 and Cu3 via NO_3^- bridging is about 5.814 Å. Similarly, the second hexanuclear cluster is formed through the union of two symmetry related trinuclear cores

assembled *via* nitrate bridging (Figure 8). Each trinuclear core contains three crystallographically independent Cu(II) centres. Cu4 is present in distorted octahedral geometry. Two chelated nitrogen atoms (N9, N12) from one ppk ligand, O12 from another ppk ligand and μ_3–O7 atoms fulfil the basal coordination sites; while O15 and O19 oxygen atoms from two different bridging NO_3^- ligands occupy the axial sites.

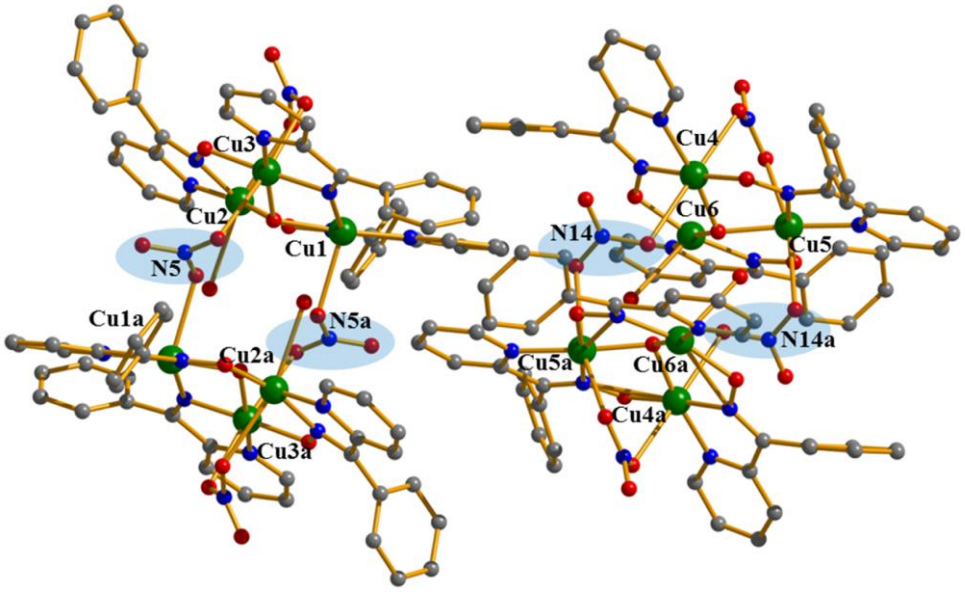

Figure 8. Formation of the hexanuclear clusters from the symmetry-related trinuclear cores through the nitrate (highlighted) bridging. Colour code: C:green; N:blue; O:red; C:grey.

Cu5 adopts distorted octahedral geometry and the coordination sites (O11, O16, N10, N11, O7, O20 atoms) are occupied in a similar fashion like Cu4. Cu6 is located in square pyramidal geometry with Addison parameter of 0.08. N8, N16, O7, O10 atoms furnish equatorial coordination sites of Cu6 while apical position is occupied by a water molecule (O2w). Cu4 atom of one trinuclear core is connected to the Cu5 atom of another trinuclear core through the O19, O20 atoms of the NO_3^- ligand). The distance between Cu4 and Cu5 via NO_3^- bridging is about 6.013 Å.

2.3.1.2 Structural description of $[Cu_3(\mu_3\text{–}OH)(ppk)_3(\mu\text{–}N(CN)_2)(OAc)]_n$ (2)

Compound **2** crystallizes in the monoclinic $P2_1/n$ space group. The structure determination of **2** shows that cyclic trinuclear Cu(II) units (Figure 9) of formula $[Cu_3(\mu_3\text{–}OH)(ppk)_3(OAc)]^+$ are bridged by $N(CN)_2^-$ (dicyanamide) anions resulting in an one dimensional coordination chain (Figure 10). In the asymmetric unit each trinuclear core contains a triangular Cu_3 skeleton where each Cu(II) centre is present in a distorted square pyramidal (4+1) geometry (Figure 9).

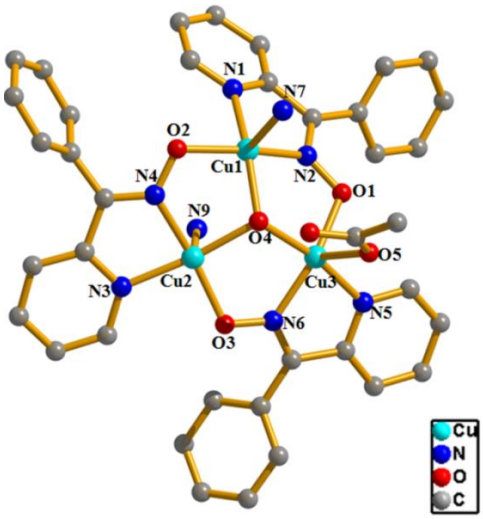

Figure 9. View of the trinuclear building unit $[Cu_3(\mu_3–OH)(ppk)_3(OAc)]$ of **2** showing the square pyramidal coordination environment of each Cu(II) ion.

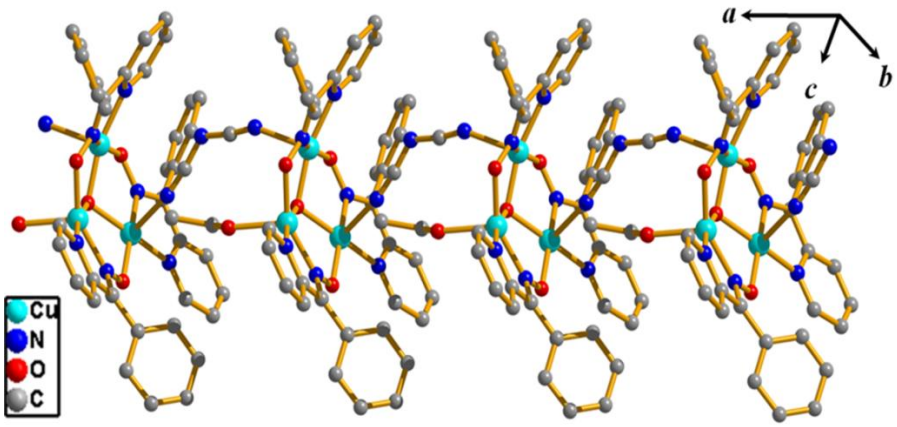

Figure 10. View of the 1D coordination chain of **2** showing trinuclear $\{Cu_3(\mu_3–OH)\}$ core connected by the $N(CN)_2^-$ anions.

Cu1 is chelated to one ppk ligand (N1, N2) and connected to another ppk ligand by O2 oxygen atom and forms the equatorial plane involving the bridging μ_3–O4 atom. The axial position is occupied by the N7 nitrogen atom from the bridging $N(CN)_2^-$ ligand. For Cu2, the basal plane is occupied by two chelated nitrogen atoms (N3, N4) from one ppk ligand, O3 from another ppk ligand and μ_3–O4 and the axial position is ligated through N9 from the bridging $N(CN)_2^-$ ligand. The oxygen atom (O5) from the pendent acetate group is attached in the axial position around Cu3 and the equatorial positions are occupied by the chelated nitrogen atoms (N5, N6) from one ppk ligand, O1 from the another ppk ligand and μ_3–O4. The Cu–O and Cu–N bond lengths are in the range of 1.928(4)–2.146(4) Å and 1.955(4)–2.261(6) Å respectively (Table 3). The degree of distortion from the ideal square pyramidal geometry is reflected in the angles of the basal

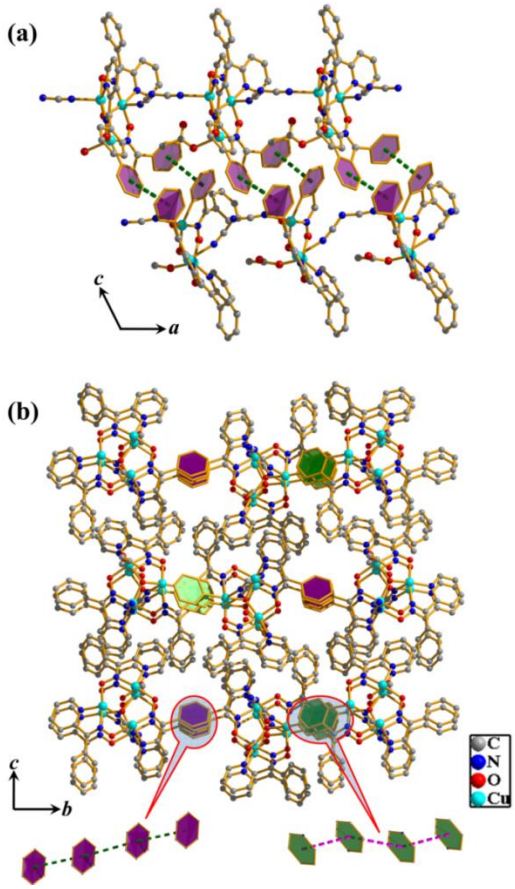

Figure 11. (a) View of the 2D supramolecular sheet formed by π–π interactions between the 1D coordination chains lying in the crystallographic *ac* plane and (b) View of the 3D supramolecular framework formed by the π–π interactions between the 2D supramolecular sheets of compound **2**.

plane of the Cu atoms (Table 3). The Addison parameter (τ)[16] have been calculated and the values are 0.06, 0.05 and 0.33 for Cu1, Cu2 and Cu3, respectively. In the trinuclear $[Cu_3(\mu_3\text{–}OH)(ppk)_3(OAc)]^+$ core the copper atoms are held together by two kind of bridging; (i) the μ_3–OH oxygen atom (O4) bridging three Cu(II) centres (Cu1–O4, 1.949(4); Cu2–O4, 1.961(3) and Cu3–O4, 1.962(4) Å) and (ii) the N–O group from the ppk ligand bridging two Cu(II) centres. In the tricnuclear core, Cu–O4–Cu bond angles are in the range 105.98(17)°–114.99(17)° and the Cu1–Cu2, Cu1–Cu3 and Cu2–Cu3 distances are 3.122(1), 3.298(1) and 3.225(1) Å, respectively. The average Cu–N–O–Cu torsion angle is 19.8°. The μ_3–OH oxygen atom (O4) is located above the mean plane defined by the three copper atoms by 0.616 Å. The dihedral angles between the adjacent basal planes of Cu(II) ions are 50.23°, 33.69°, and 32.46°. The Cu1 atom of one trinuclear core is connected to the Cu2 atom of another trinuclear core through the N7, N9 atoms of the $N(CN)_2^-$ ligand resulting in a 1D coordination polymer (Figure 10). The distance between Cu1 and Cu2 via $N(CN)_2^-$ bridging is about 8.210 Å. Each 1D coordination

chain undergoes π–π interactions through the phenyl and pyridyl rings of the ppk ligands (cg–cg distances are 3.836(4) Å and 4.529(4) Å, respectively) forming a 2D supramolecular network in the crystallographic *ac* plane (Figure 11a). The 2D networks are further assembled by π–π interactions mediated through phenyl–phenyl and pyridyl–pyridyl rings of ppk ligands with cg–cg distances 4.040(4) Å and 3.976(3) Å, respectively, resulting in a 3D supramolecular framework (Figure 11b).

2.3.1.3 Structural description of $\{[Cu_4(pdmH)_2(pdm)_2(\mu_2\text{–}OH)(H_2O)_2]\cdot(ClO_4)\}_n$ (3)

Compound **3** crystallizes in the orthorhombic $Pbn2_1$ space group with formula $\{[Cu_4(pdmH)_2(pdm)_2(\mu_2\text{–}OH)(H_2O)_2]\cdot(ClO_4)\}_n$. Single-crystal X–ray diffraction study reveals that asymmetric unit of **3** contains four Cu(II) centres, four pyridine–2,6–dimethanol ligands [two act as monoanionic ligand (pdmH) and two act as dianionic ligand (pdm)], two coordinated H_2O molecules, one μ_2–OH group and a non-coordinated ClO_4^- anion (Figure 12). In the tetranuclear $[Cu_4(pdmH)_2(pdm)_2(H_2O)_2]^{2+}$ core, Cu1 locates itself in a distorted square pyramidal (4+1) geometry and the equatorial coordination sites are furnished by one tridentate chelated pdmH ligand (O7, O8, N4 atoms) and one bridging pdm ligand (O4 atom). The apical position is occupied by O13 atom coming from bridging μ_2–OH group. Cu2 adopts distorted square pyramidal geometry with coordinations coming from N3, O5, O6 atoms from one tridentate chelated pdm ligand, O2 atom from a pdmH ligand and O13 atom from the μ_2-OH group.

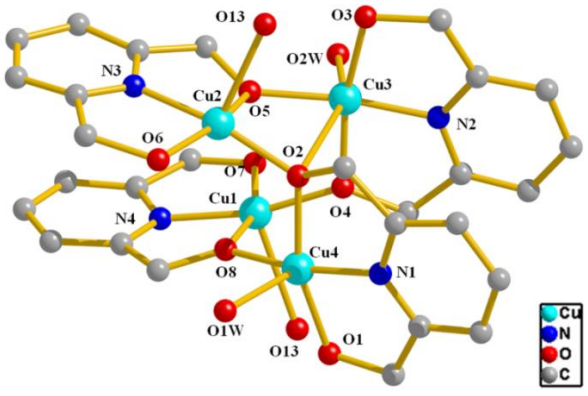

Figure 12. View of the tetranuclear building unit $[Cu_4(pdmH)_2(pdm)_2(H_2O)]^{2+}$ of **3** showing the different coordination environment around Cu(II) ion.

Cu3 is present in a distorted octahedral (4+2) coordination environment where the equatorial positions are occupied by one tridentate chelated pdm ligand (O3, O4 and N2

atoms) and O5 oxygen atom from another pdm ligand. The axial positions are occupied by O2 and O2w oxygen atoms. Cu4 adopts a distorted square pyramidal geometry where O1, N1, O2, O8 atoms define the square plane and O1w atom from a water molecule occupies the apical position. The equatorial Cu–O and Cu–N bond distances for all the Cu(II) centres are in the range of 1.885(6) – 2.007(6) Å and 1.881(6) – 1.943(8) Å, respectively. However, the apical bonds are elongated (2.425(5) – 2.791(5) Å) due to Jahn–Teller distortion. In all cases the degree of distortion is reflected in the bond lengths and bond angles around the Cu(II) centres (Table 4). The τ values are for Cu1, Cu2 and Cu4 are 0.05, 0.08 and 0.12 respectively. In the tetranuclear core Cu(II) ions are held together by different alkoxido oxygen atoms where μ_2–O4, μ_2–O8 and μ_2–O5 atoms bridge Cu1, Cu3; Cu1, Cu4 and Cu2 and Cu3 atoms respectively, while Cu2, Cu3 and Cu4 atoms are connected by μ_3–O2 atom.

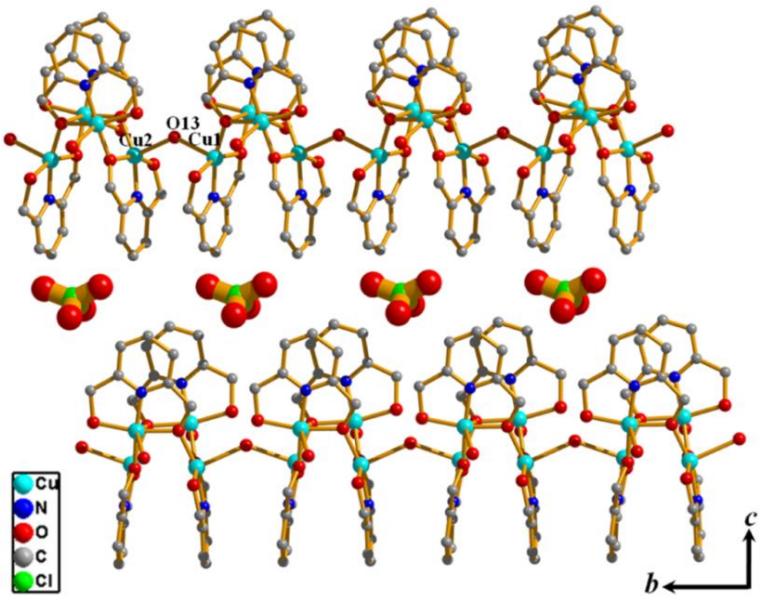

Figure 13. View of the 1D chain formed by the linking of $[Cu_4(pdmH)_2(pdm)_2(H_2O)]^{2+}$ cores by μ-OH where ClO_4^- anions are intercalated between the chains.

2.3.1.4 Structural description of {[$Ni_4Cu_6(\mu$–$OH_2)_2(dpkO_2)_8(OAc)_4(H_2O)_4$]·$2CH_3OH·17H_2O$} (4)

Single crystal X–ray diffraction study reveals that compound **4** crystallizes in monoclinic $P2_1/c$ space group and contains a decanuclear cluster comprised of two symmetry related pentanuclear cores with formula $[Ni_2Cu_3(\mu$–$OH_2)(dpkO_2)_4(OAc)_2(H_2O)_2]$ (Figure 15b). The formulation and composition of Cu(II) and Ni(II) in **4** is confirmed from the ICP-AES and EDX results (Figure 14). The positions of the metal atoms were assigned on the basis of coordination geometry and structure refinement parameters. The pentanuclear

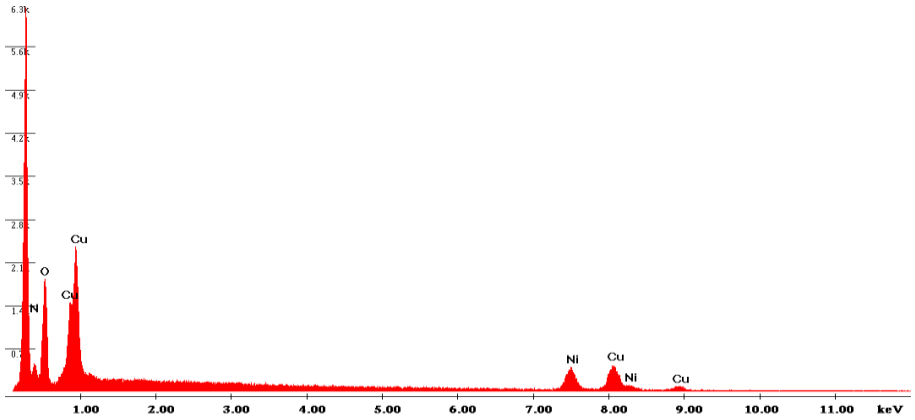

Figure 14. EDX analysis for 4 confirming the presence of both Cu(II) and Ni(II).

core (Figure 15) contains two crystallographically independent Ni(II) centres and three crystallographically independent Cu(II) centres with different coordination environments. The metal centres are bridged by three $dpkO_2$, doubly deprotonated anions of the gem-diol form $(C_5NH_4)_2C(OH)_2$, formed by *in situ* reaction in presence of the metal ions. Ni1 and Ni2 display octahedral coordination as preferred by virtue of the high octahedral site stabilzation energy (OSSE) of Ni(II). Ni1 adopts distorted octahedral geometry and chelated to two different $dpkO_2$ ligands (O1, N1; O3, N3 atoms), the other two coordination sites are furnished by O7 atom of another $dpkO_2$ ligand and O14 atom of a coordinated water molecule. Ni2 also locates itself in a distorted octahedral geometry. Three different $dpkO_2$ ligands (O3, N4; O5, N6; and O7, N8 atoms) chelate Ni2 centre (Figure 15). The Ni–O bond lengths vary from 2.001(8) to 2.199(7) Å whereas the Ni–N bond lengths are in the range of 2.052(10)–2.114(10) Å. All the copper centres adopt distorted square pyramidal (4+1) geometry. Cu1 is coordinated to three different $dpkO_2$ ligands (ligated through N5, O5; O2; O3) and one acetate ligand (O9 atom). Similarly for Cu2, three different $dpkO_2$ ligands and one acetate ligand furnish the coordination sites (O7, N7; O1; O5 and O11atoms). Cu3 is ligated to one $dpkO_2$ ligand (O2, N2), two bridging μ–OH_2 (O13, O13_a) and one coordinated water molecule (O12W atom). The Cu–O/N equatorial bond lengths are in the range of 1.905(7)–2.035(10) Å and the Cu–O axial bond lengths vary from 2.312(7) to 2.73(2) Å. Ni1, Ni2, Cu1 and Cu2 form a distorted cubane like structure with a missing one edge (Figure 15b). In the cubane core, μ_3–O5, μ_3–O3 and μ_3–O7 atoms coming from three different $dpkO_2$ ligands bridge Cu1, Cu2, Ni2; Cu1, Ni1, Ni2 and Ni1, Ni2, Cu2 respectively, while Cu2 and Ni1 atoms are doubly bridged by μ_2–O1 atom. The μ_2–O2 atom bridges Cu1 and Cu3 which result in the

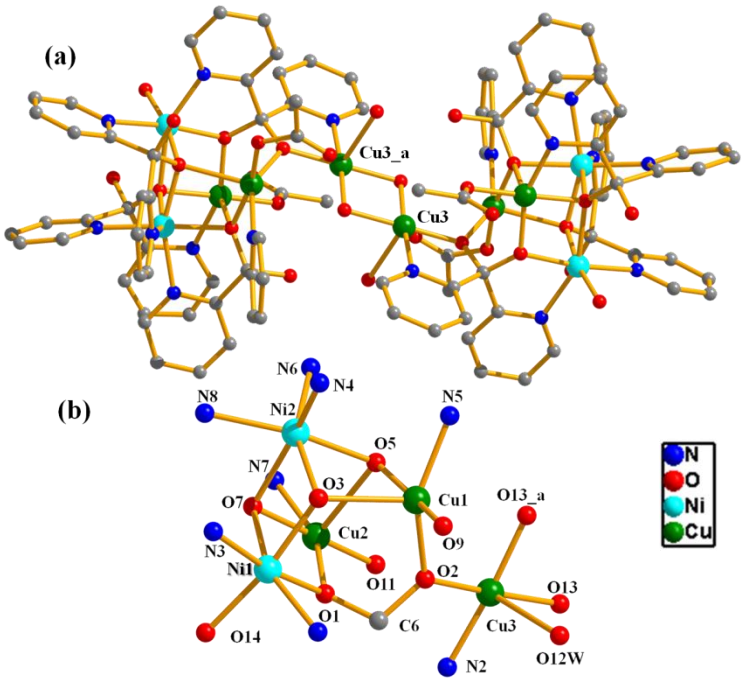

Figure 15. (a) View of the heterometallic Ni(II)–Cu(II) decanuclear core of **4**. (b) The pentanuclear core showing the metal–ligand bridging. Non-bonding atoms are omitted for clarity.

extension of this cubane to the pentanuclear core (Figure 15b). Two pentanuclear cores are further bridged by two water molecules (μ_2–O13 and μ_2–O13_a) to form the novel decanuclear cluster (Figure 15a).

2.3.1.5 Structural description of [{$MnCu_2(dpkO_2H)_2(dpkO_2)N_3$}.($NO_3$).$H_2O$]$_n$ (5)

Compound **5** crystallizes in tetragonal $P4_12_12$ space group. The composition of Cu(II) and Mn(II) in **5** is confirmed from ICP-AES and EDX results (Figure 16). The positions of the metal atoms were assigned on the basis of the coordination geometry and structure refinement parameters. Single crystal X–ray diffraction study reveals that the asymmetric unit contains two crystallographically different Cu(II) centres and one Mn(II) centre. There are three crystallographically different ligands [anions of the *gem*-diol form $(C_5NH_4)_2C(OH)_2$] generated *in situ* from the dpk ligand, two of which are singly deprotonated $dpkO_2H$ anions (see Scheme 1). The other one is doubly deprotonated $dpkO_2$ dianion (its corresponding pyridyl rings contain N1 and N2 atoms). Cu1 adopts a distorted (4+2) octahedral geometry. In the basal plane, Cu1 is coordinated to one $dpkO_2H$ ligand (N3 atom) and symmetry-related $dpkO_2$ ligands (O1, O1a and N1 atoms); while the two axial coordination sites are furnished by O3 atom of the $dpkO_2H$ ligand and the N9 atom of $\mu_{1,3}$ azide ligand. Cu2 locates itself in a penta-coordinated geometry (Figure 17). The degree of distortion from the ideal square pyramidal geometry can be

understood from the Addison parameter (τ)[16], which is 0.295 for Cu2, reflecting the distortion from square pyramidal geometry. The coordination sites are furnished by the $dpkO_2$ ligand (N2 and O2 atoms), $dpkO_2H$ ligand (N6, O5 atoms) and N7 atom from the $\mu_{1,3}$ azide ligand. The Cu-O and Cu-N bond distances are in the range of 1.913(5)–2.523(4) Å and 1.972(8)–2.595(8) Å respectively (Table 6). The Mn(II) centre is hexa-coordinated and ligated to the $dpkO_2H$ ligands (O3, O3a, O5, N4, N5 atoms) and the $dpkO_2$ ligand (O2 atom). Mn-O and Mn-N bond distances are in the range of 2.074(4)–2.334(5) Å and 2.253(6)–2.311(6) Å respectively.

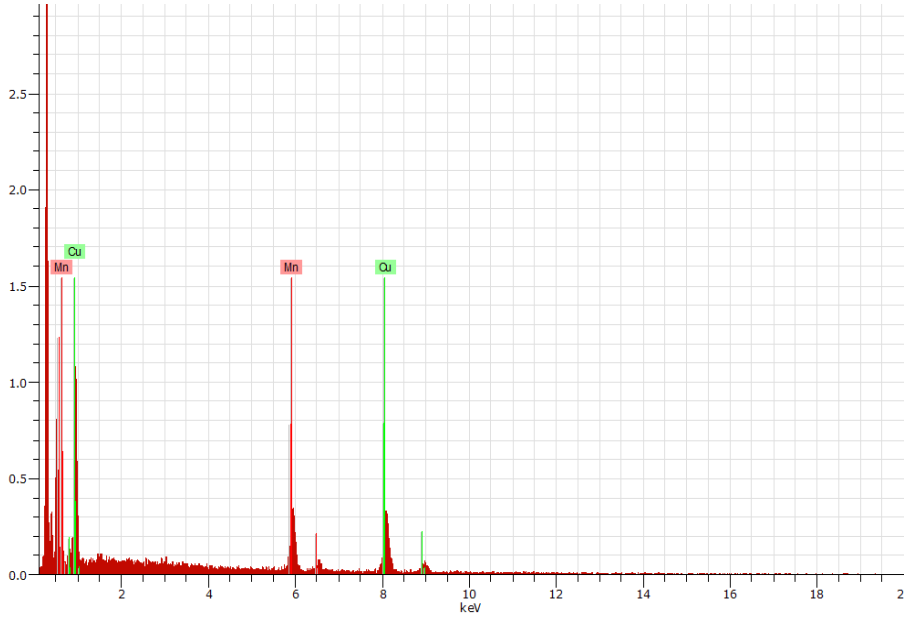

Figure 16. EDX analysis for **5** confirming the presence of both Cu(II) and Mn(II).

The metal centres are bridged together by dpkO2H/dpkO2 ligands to form a hexanuclear $Mn^{II}_2Cu^{II}_4$ core which acts as the secondary building unit (SBU). In the hexanuclear core, two symmetry related μ_2-O2 oxygen atoms (O2 and O2a) from one $dpkO_2$ ligand bind the symmetry related Cu1 atoms in μ_2-oxo fashion. This results in the formation of one Cu_2O_2 moiety (Figure 17b). In a similar fashion, μ_2-O3 oxygen atoms from $dpkO_2$ ligand connect Mn1 and its symmetry related counterpart (Figure 17b). The symmetry related Cu_2O_2 moiety and the Mn_2O_2 moiety can be considered to form a $Cu_2Mn_2O_4$ cubane core, of which two edges are missing (Figure 17b). Cu1 and Mn1 atoms are bridged together in μ_2-oxo fashion by the O3 atom of one $dpkO_2H$ ligand. Cu2 and Mn1 are doubly bridged by O2 and O5 atoms (Figure 17b). The symmetry related atoms of Cu2 and Mn1 are also bridged in a similar fashion. Such bridging between Mn1 and Cu2 centres extends the $Cu_2Mn_2O_4$ cubane core to a Mn_2Cu_4 core resulting in a hexanuclear SBU.

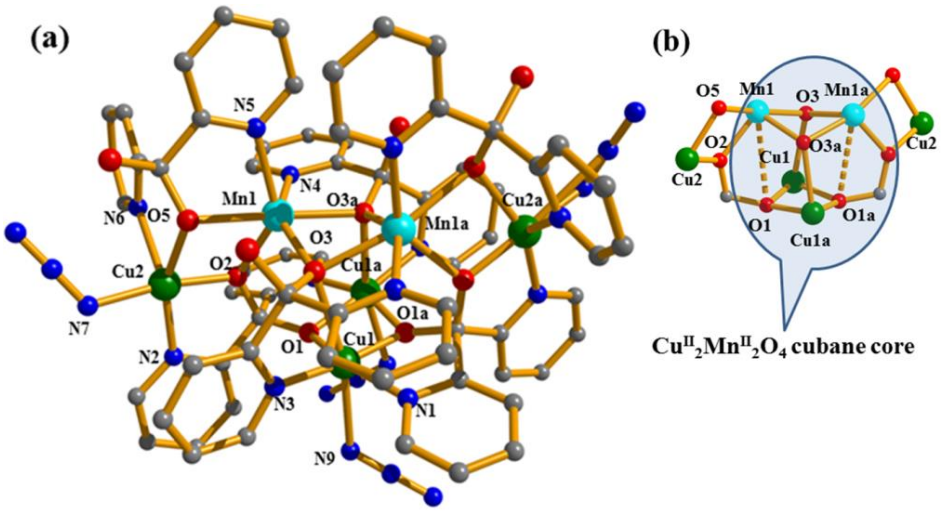

Figure 17. (a) The coordination environments around Cu(II) and Mn(II) centres in **5**. (b) The hexanuclear Mn_2Cu_4 core of **5** containing the $Cu_2Mn_2O_2$ cubane core. Color code: Cu: green; Mn: cyan; C: grey; O: red; N: blue.

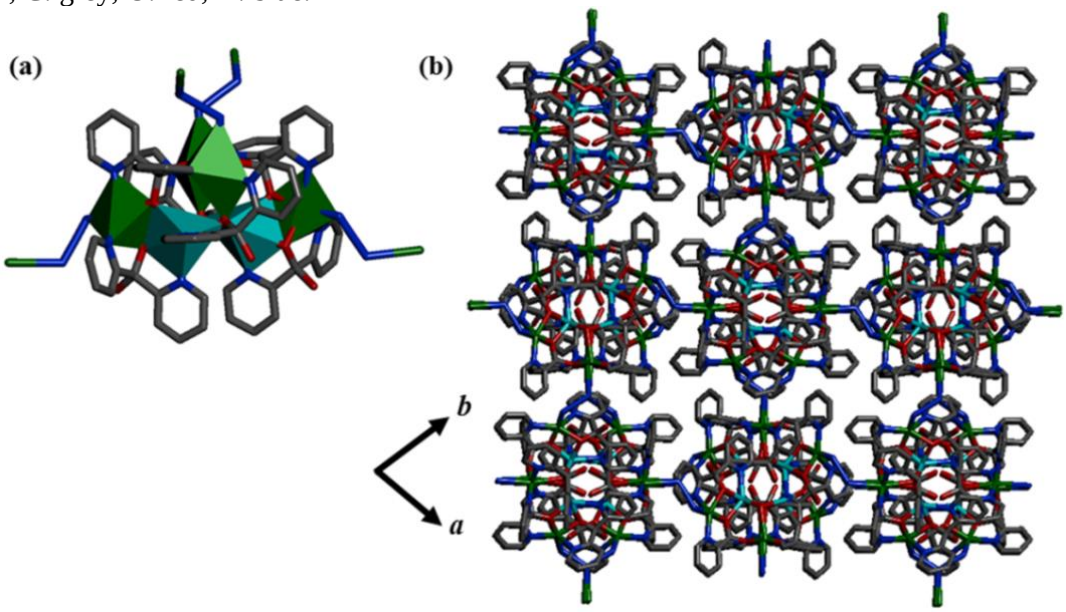

Figure 18. (a) Polyhedral view of the hexanuclear Mn_2Cu_4 core with azide nails (b) The 3D framework of **5** constructed from the hexanuclear cores connected through azide groups. Color code: Cu: green; Mn: cyan; C: grey; O: red; N: blue.

Cu1 of one hexanuclear core is connected to the Cu2 centre of other hexanuclear core by the $\mu_{1,3}$ azido bridging. The hexanuclear $Mn^{II}_2Cu^{II}_4$ core acts as the SBU with four azide ligands acting as "nails" of the SBU (Figure 18a). Along crystallographic *ab* plane, the SBUs are connected through the azido ligand forming a 2D network. The angular disposition of azide nails also connects the SBUs along *c* direction, resulting in a complex 3D framework (Figure 18b). The simplified 3D nets along different directions are shown in Figure 19. As can be seen in Figure 19, in the extended net of **2** the diagonal SBUs are connected with each other through azide nails in a zigzag fashion. The distance between

Cu1 and Cu2 through $\mu_{1,3}$ azide bridging is 5.795 Å. The cationic charge of the framework is neutralized by the nitrate anions.

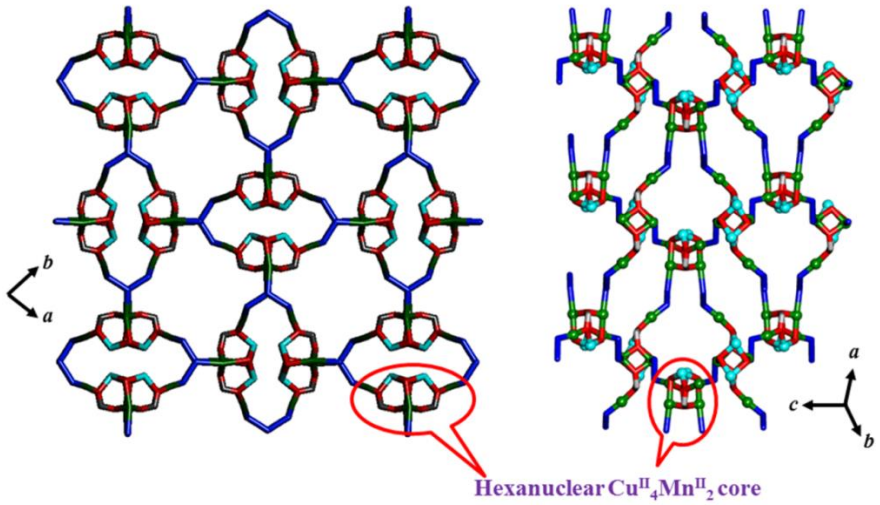

Figure 19. The simplified 3D net of **5** in two different directions. Color code: Cu: green; Mn: cyan; C: grey; O: red; N: blue.

Table 1. Crystal data and structure refinement parameters for **1-5.**

parameters	**1**	**2**	**3**	**4**	**5**
empirical formula	$C_{72}H_{60}Cu_6N_{16}O_{22}$	$C_{40}H_{31}Cu_3N_9O_6$	$C_{28}H_{35}Cu_4N_4O_{15}Cl$	$C_{98}H_{130}Cu_6Ni_4O_{49}$	$C_{33}H_{28}Cu_2MnN_{10}O_{10}$
formula weight	1882.61	924.36	957.21	2931.04	906.68
crystal system	triclinic	monoclinic	orthorhombic	monoclinic	tetragonal
space group	$P\bar{1}$	$P2_1/n$	$Pbn2_1$	$P2_1/c$	$P4_12_12$
a, Å	13.8873(2)	8.4798(3)	7.9039(2)	11.8151(6)	19.165(5)
b, Å	16.1982(3)	20.8033(7)	15.7253(4)	23.7558(16)	19.165(5)
c, Å	17.5410(3)	21.2503(8)	27.7552(8)	22.5320(14)	18.967(5)
α, deg	90.499(1)	90	90	90	90
β, deg	108.881(1)	92.601(2)	90	98.698(4)	90
γ, deg	94.530(1)	90	90	90	90
V, Å^3	3719.40(11)	3744.9(2)	3449.73(16)	6251.5(7)	6967(4)
Z	2	4	4	2	8
T, K	298	298	298	298	298
D_{calcd}, g/cm^3	1.676	1.640	1.843	1.529	1.725
F (000)	1896	1876	1936	2908	3656
reflections [$I>2\sigma(I)$]	9555	4036	5295	4426	5572
R_{int}	0.050	0.106	0.054	0.193	0.088
GOF on F^2	1.02	0.97	1.08	0.97	1.10
$R_1{}^a$	0.0404	0.0648	0.0635	0.0767	0.0413
$R_w{}^b$	0.1348	0.1464	0.1762	0.2471	0.1289

$^a R_1[I>2\sigma(I)] = \sum||F_o|-|F_c||/\sum|F_o|$; $^b R_w$[all data] $= [\sum\{w(F_o^2-F_c^2)^2\}/\sum\{w(F_o^2)^2\}]^{1/2}$

Table 2. Selected bond distances (Å) and bond angles (°) for **1**.

Cu1-O9	1.929(2)	Cu1-O1	1.947(3)
Cu1-N4	1.973(4)	Cu1-N1	1.962(3)
Cu1-O4	2.423(3)	Cu2-O1	1.947(3)
Cu2-O1W	2.572(4)	Cu2-O3	1.958(3)
Cu2-O14	2.546(4)	Cu2-N2	1.961(4)
Cu2-N6	2.002(3)	Cu3-O1	1.967(3)
Cu3-O2	2.406(5)	Cu3-O8	1.926(3)
Cu3-N3	1.971(3)	Cu3-N15	1.971(4)
Cu3-O6	2.763(4)	Cu4-N9	1.986(3)
Cu4-N12	1.966(4)	Cu4-O7	1.962(3)
Cu4-O12	1.930(3)	Cu4-O15	2.472(5)
Cu4-O19	2.550(3)	Cu5-N11	1.978(4)
Cu5-O16	2.537(5)	Cu5-N10	1.979(3)
Cu5-O20	2.673(4)	Cu5-O7	1.963(3)
Cu5-O11	1.924(3)	Cu6-O7	1.941(3)
Cu6-O2W	2.577(4)	Cu6-O10	1.940(3)
Cu6-N8	1.958(4)	Cu6-N16	1.976(3)
Cu1-Cu2	3.223(7)	Cu1-Cu3	3.191(2)
Cu2-Cu3	3.245(3)		
O1-Cu1-N1	172.01(16)	O2-Cu3-O8	88.96(15)
O2-Cu3-N3	92.99(16)	O2-Cu3-N15	90.40(16)
O2-Cu3-O6	170.98(14)	O8-Cu3-N3	96.58(14)
O4-Cu1-N1	101.72(13)	O8-Cu3-N15	177.10(13)
O4-Cu1-N4	92.09(13)	O6a -Cu3-O8	88.89(12)
N1-Cu1-N4	81.62(15)	N3-Cu3-N15	80.64(15)
O1-Cu2-O1W	90.23(13)	O6a-Cu3-N3	78.56(13)
O1-Cu2-O3	95.63(12)	O6a-Cu3-N15	91.31(14)
O1-Cu2-O14	88.06(13)	O15-Cu4-N12	88.47(16)
O1-Cu2-N2	165.27(13)	O19-Cu4-N9	99.00(13)
O1-Cu2-N6	88.45(14)	O19-Cu4-N12	89.83(13)
O1W-Cu2-O3	79.42(12)	N9-Cu4-N12	81.11(15)
O1W-Cu2-O14	163.02(13)	O7-Cu4-N12	90.26(13)
O1W-Cu2-N2	84.76(14)	O10-Cu4-O12	159.91(10)
O1W-Cu2-N6	114.01(13)	O10-Cu4-O15	91.90(13)
O3-Cu2-O14	83.94(14)	O10-Cu4-O19	85.60(9)
O3-Cu2-N2	97.05(13)	O10-Cu4-N9	103.56(13)
O3-Cu2-N6	166.01(14)	O14-Cu2-N2	100.70(14)
O12-Cu4-O15	89.25(14)	O14-Cu2-N6	82.83(15)
O12-Cu4-O19	92.55(12)	N2-Cu2-N6	81.01(15)
O12-Cu4-N9	96.49(14)	O1-Cu3-O2	99.05(14)
O12-Cu4-N12	176.87(14)	O1-Cu3-O8	93.58(12)
O7-Cu4-O10	67.80(10)	O1-Cu3-N3	164.38(15)
O7-Cu4-O12	92.22(12)	O7-Cu4-O15	99.13(12)
N8-Cu6-N16	80.99(15)	O7-Cu4-O19	78.41(11)
O7-Cu4-N9	171.03(14)	O7-Cu6-O11	67.96(10)
O15-Cu4-O19	177.01(12)	O7-Cu6-O16	70.55(12)
O15-Cu4-N9	83.17(14)	O7-Cu6-N8	170.35(13)
O7-Cu5-O16	80.44(14)	O7-Cu6-N16	90.24(14)

O7-Cu5-O11	94.09(12)	O10-Cu6-O11	155.27(11)
O7-Cu5-O12	66.52(10)	O10-Cu6-O16	98.53(13)
O7-Cu5-O20a	88.38(11)	O10-Cu6-N8	95.56(14)
O11-Cu5-O12	160.59(11)	O10-Cu6-N16	165.32(15)
O11-Cu5-O16	81.69(14)	O11-Cu6-O16	60.34(11)
O11-Cu5-N10	95.69(13)	O11-Cu6-N8	103.44(11)
O11-Cu5-N11	174.85(15)	O2W-Cu6-O7	87.93(12)
O7-Cu5-N10	165.79(15)	O2W-Cu6-O10	77.79(12)
O7-Cu5-N11	88.80(13)	O2W-Cu6-O11	116.51(11)
O12-Cu5-O16	95.05(13)	O2W-Cu6-O16	157.98(13)
O12-Cu5-N10	103.28(12)	O2W-Cu6-N8	92.40(14)
O12-Cu5-N11	22.56(11)	O2W-Cu6-N16	116.47(14)
O12-Cu5-O20	90.09(9)	O7-Cu6-O10	93.94(12)
O16-Cu5-N10	111.17(17)	Cu1-O1-Cu2	111.71(14)
O16-Cu5-N11	103.02(16)	Cu1-O1-Cu3	109.23(14)
O16-Cu5-O20	164.61(14)	Cu2-O1-Cu3	111.99(14)
N10-Cu5-N11	80.73(14)	O20a-Cu5-N10	81.57(14)
O11-Cu6-N16	22.51(12)	O16-Cu6-N16	69.63(14)
Cu4-O7-Cu5	107.05(13)	Cu4-O7-Cu6	112.46(14)
Cu5-O7-Cu6	110.02(13)	Cu1-Cu2-Cu3	59.12(11)
Cu1-Cu3-Cu2	60.11(11)	Cu2-Cu1-Cu3	60.77(7)

Table 3. Selected bond distances (Å) and bond angles (°) for **2**.

Cu1-O2	1.985(4)	Cu1-O4	1.949 (4)
Cu1-N1	1.997(4)	Cu1-N2	1.994(4)
Cu1-N7	2.213(6)	Cu2-O3	1.928(4)
Cu2-O4	1.961(3)	Cu2-N3	1.998(4)
Cu2-N4	1.955(4)	Cu2-N9_a	2.261(6)
Cu3-O1	1.979(4)	Cu3-O4	1.962(4)
Cu3-O5	2.146(4)	Cu3-N5	2.001(4)
Cu3-N6	1.989(4)		
O1-Cu1-O2	158.29(14)	N3-Cu2-N9_a	100.8(2)
O1-Cu1-O4	68.70(13)	N4-Cu2-N9_a	89.1(2)
O1-Cu1-N1	102.30(15)	O1-Cu3-O3	144.98(15)
O1-Cu3-O4	93.86(16)	O1-Cu1-N7	98.89(16)
O1-Cu3-O5	94.01(17)	O2-Cu1-O4	91.94(15)
O1-Cu3-N5	92.77(17)	O2 -Cu1-N1	92.82(17)
O1-Cu3-N6	149.00(19)	O2-Cu1-N2	163.41(18)
O3-Cu3-O4	67.57(13)	O2 –Cu1-N7	93.50(18)
O3-Cu3-O5	116.55(14)	O4-Cu1-N1	160.04(16)
O3-Cu3-N5	101.99(15)	O4-Cu1-N2	89.65(16)
O4-Cu1-N7	98.58(19)	O4-Cu3-O5	96.21(15)
N1-Cu1-N2	80.43(17)	O4 -Cu3-N5	168.67(17)
N1-Cu1-N7	100.5(2)	O4-Cu3-N6	89.69(16)
N2-Cu1-N7	102.60(17)	O5-Cu3-N5	92.49(18)
O2-Cu2-O3	162.42(14)	O5-Cu3-N6	116.23(18)
O2-Cu2-O4	68.30(13)	N5-Cu3-N6	79.93(18)

O2-Cu2-N3	103.43(14)	Cu1-O1-Cu3	81.63(13)
O2-Cu2-N9_a	82.81(18)	Cu3-O1-N2	112.9(3)
O3-Cu2-O4	94.32(16)	Cu1-O2-Cu2	77.25(12)
O3-Cu2-N3	93.21(17)	Cu1-O2-N4	111.4(3)
O3-Cu2-N4	170.05(17)	O3-Cu2-N9_a	99.8(2)
Cu2-O3-Cu3	79.79(12)	O4-Cu2-N3	167.31(16)
Cu2-O3-N6	111.9(3)	O4-Cu2-N4	90.41(16)
O4-Cu2-N9_a	87.96(19)	Cu1-O4-Cu2	105.98(17)
N3-Cu2-N4	80.66(19)	Cu1-O4-Cu3	114.99(17)
Cu2-O4-Cu3	110.60(17)		

Symmetry code: a = −1+x, y, z

Table 4. Selected bond distances (Å) and bond angles (°) for **3**.

Cu1-O4	1.922(5)	Cu1-O7	1.956(6)
Cu1-O8	1.989(5)	Cu1-N4	1.917(8)
Cu1-O13_b	2.506(5)	Cu2-O2	1.916(5)
Cu2-O5	1.961(5)	Cu2-O6	1.987(7)
Cu2-O13	2.425(5)	Cu2-N3	1.943(8)
Cu3-O2	2.791(5)	Cu3-O2W	2.768(5)
Cu3-O3	2.007(6)	Cu3-O4	1.954(5)
Cu3-O5	1.895(6)	Cu3-N2	1.881(6)
Cu4-O1	2.004(6)	Cu4-O1W	2.418(5)
Cu4-O2	1.984(5)	Cu4-O8	1.885(6)
Cu4-N1	1.908(6)		
Cu1-O8-Cu4	113.1(3)	Cu1_a-O13-Cu2	135.8(4)
Cu2-O2-Cu4	115.9(3)	Cu1-O4-Cu3	114.6(3)
Cu3-O2-Cu4	101.59(19)	O2-Cu3-O5	70.63(19)
Cu2-O5-Cu3	109.9(3)	O4-Cu1-O8	93.1(2)
O4-Cu1-O7	100.4(2)	O2W-Cu3-O4	81.31(18)
O2W-Cu3-O3	107.09(18)	O2W-Cu3-O5	88.6(2)
O4-Cu1-O13_b	91.6(2)	O5-Cu1-O8	77.6(2)
O5-Cu1-O7	94.8(2)	O3-Cu3-O5	96.6(2)
O3-Cu3-O4	166.9(2)	O7-Cu1-O8	160.8(2)
O4-Cu3-O5	93.6(2)	O7-Cu1-O13_b	104.7(2)
O1-Cu4-O1W	102.9(2)	O8-Cu1-O13_b	88.5(2)
O1-Cu4-O2	161.2(2)	O1-Cu4-O4	91.2(2)
O2-Cu2-O5	92.7(2)	O1-Cu4-O8	97.1(3)
O2-Cu2-O6	100.8(3)	O2-Cu2-O13	92.9(2)
O1W-Cu4-O2	91.88(19)	O1W-Cu4-O4	159.1(2)
O5-Cu2-O6	160.8(3)	O1W-Cu4-O8	93.5(2)
O5-Cu2-O13	91.6(2)	O2-Cu4-O4	78.17(17)
O6-Cu2-O13	101.1(3)	O2-Cu4-O8	93.5(2)
O4-Cu4-O8	69.10(18)	O2-Cu3-O2W	151.93(19)
O2-Cu3-O3	94.21(17)	O2-Cu3-O4	81.42(17)

Symmetry codes: b= 1+x, y, z

Table 5. Selected bond distances (Å) and bond angles (°) for **4.**

Cu1-O2	1.985(7)	Cu1-O3	2.308(7)
Cu1-O5	1.939(7)	Cu1-O9	1.927(7)
Cu1-N5	2.038(9)	Cu2-O1	1.932(7)
Cu2 -O5	2.488(6)	Cu2-O7	1.971(7)
Cu2-O11	1.919(7)	Cu2-N7	2.010(10)
Cu3-O2	1.889(7)	Cu3-O12W	2.78(2)
Cu3-O13	1.947(7)	Cu3-N2	1.968(9)
Cu3-O13_a	1.926(7)	Ni1-O1	1.999(7)
Ni1-O3	2.041(7)	Ni1-O7	2.194(7)
Ni1-O14	2.072(7)	Ni1-N1	2.064(9)
Ni1-N3	2.067(9)	Ni2-O3	2.073(7)
Ni2-O5	2.091(7)	Ni2-O7	2.122(6)
Ni2-N4	2.068(8)	Ni2-N6	2.100(10)
Ni2-N8	2.088(9)	Ni1-Ni2	3.193
Ni1-Cu2	3.139	Ni2-Cu1	3.153
Ni2-Cu2	3.188	Ni1-Cu1	3.664
Cu1-Cu2	3.665	Cu1-Cu3	3.356
Cu2-O7-Ni2	102.3(3)	Ni1-O7-Ni2	95.4(2)
Cu3-O13-Cu3_a	95.6(3)	Cu2-O1-Ni1	106.0(3)
Cu1-O2-Cu3	120.0(4)	Cu1-O3-Ni1	114.7(3)
Cu1-O3-Ni2	91.9(3)	Cu1-O5-Cu2	111.2(3)
Cu1-O5-Ni2	102.9(3)	Cu2-O7-Ni1	97.7(3)
Cu2-O5-Ni2	87.8(2)		

Symmetry code: a = 2-x,-y,-z

Table 6. Selected bond distances (Å) and bond angles (°) for **5.**

Cu1-O1	1.930(4)	Cu1-O3	2.523(4)
Cu1-N1	1.998(6)	Cu1-N3	1.981(6)
Cu1-N9	2.595(8)	Cu1-O1	1.953(4)
Cu2-O2	1.913(5)	Cu2-O5	2.071(6)
Cu2-N2	2.020(6)	Cu2-N6	2.248(6)
Cu2-N7	1.972(8)	Mn1-O2	2.074(4)
Mn1-O3	2.167(4)	Mn1-O5	2.334(5)
Mn1-N4	2.311(6)	Mn1-N5	2.253(6)
Mn1-O3a	2.180(4)		
O1-Cu1-O3	98.22(15)	O2-Mn1-N5	136.14(19)
O1-Cu1-N1	81.0(2)	O2-Mn1-O3a	94.24(17)
O1-Cu1-N3	173.4(2)	O3-Mn1-O5	164.31(18)
O3-Mn1-N4	71.26(18)	O1-Cu1-O1a	79.80(16)
O3-Mn1-N5	105.45(18)	O3-Cu1-N1	105.03(19)
O3-Mn1-O3a	77.08(15)	O3-Cu1-N3	75.18(19)
O5-Mn1-N4	123.01(19)	O5-Cu2-N7	100.2(3)
O3-Cu1-N9a	167.96(19)	O5-Mn1-N5	71.6(2)
O1a-Cu1-O3	88.14(14)	O3a-Mn1-O5	89.66(16)
N1-Cu1-N3	100.7(2)	N4-Mn1-N5	85.7(2)
N1-Cu1-N9a	83.9(2)	O3a-Mn1-N4	146.90(18)
O1a -Cu1-N1	158.1(2)	O3a-Mn1-N5	112.30(18)
N3-Cu1-N9a	95.4(2)	O1a -Cu1-N3	99.5(2)
Cu1-O1-Cu1a	98.91(17)	O1a -Cu1-N9a	86.0(2)

O2-Cu2-O5	84.20(18)	Cu2-O2-Mn1	107.7(2)
O2-Cu2-N2	81.0(2)	O2-Cu2-N6	93.1(2)
O2-Cu2-N7	171.0(3)	Cu1-O3-Mn1	98.72(15)
O5-Cu2-N2	153.3(2)	O5-Cu2-N6	74.2(2)
Cu1-O3-Mn1a	111.67(16)	N2-Cu2-N6	128.6(2)
Mn1-O3-Mn1a	95.92(15)	N2-Cu2-N7	91.9(3)
N6-Cu2-N7	95.7(3)	Cu2-O5-Mn	93.73(19)
O2-Mn1-O3	114.43(16)	O2-Mn1-O5	74.41(19)

Symmetry code: a = y, x, -z

2.3.2 Magnetic properties

2.3.2.1 Magnetic properties of 1

Variable temperature magnetic susceptibility measurements of complex **1** were measured in the temperature range 300 -3 K. The temperature dependence of $\chi_M T$ (χ_M being the magnetic susceptibility per trinuclear unit) is shown in Figure 20a. At room temperature, $\chi_M T$ per three Cu^{II} centres is equal to 0.48 cm^3 mol^{-1} K which is much lower than the expected for the sum of three non-interacting S = 1/2 spin (~1.2 cm^3 mol^{-1} K) and provides evidence of strong antiferromagnetic interactions. The $\chi_M T$ product rapidly decreases with decreasing the temperature reaching a value of 0.26 at 2 K. The *M vs H* curve at 3 K reaches a maximum value of 1.49 Nβ, being markedly below from the expected 3 Nβ (Figure 20b), corroborating strong antiferromagnetic interactions operating within the Cu(II) ions.

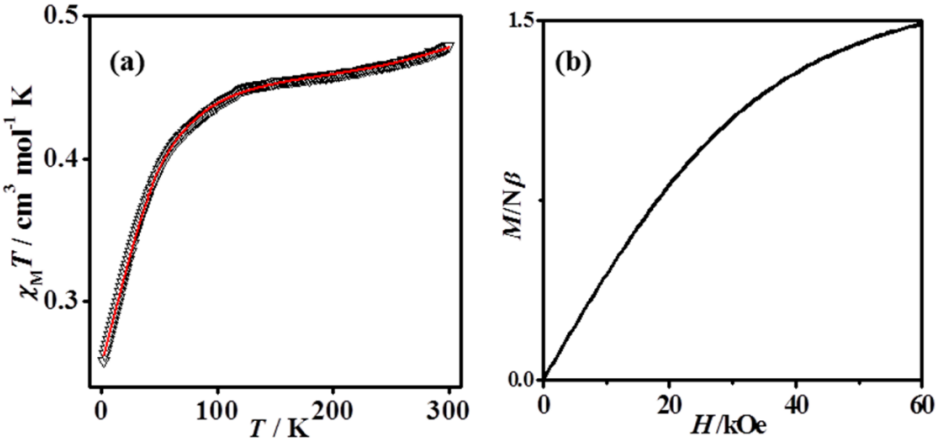

Figure 20. (a) The plot of $\chi_M T$ *vs. T* for **1**. The red line indicates the possible best fit obtained. (b) The M *vs. H* curve for **1** at 3 K.

As discussed in the structural description, complex **1** can be considered as a hexanuclear compound where two trinuclear cores are linked by nitrate anions present in axial coordination sites with very long Cu-O distances (2.5-2.7 Å). Thus from magnetic point of view, it is better to consider **1** as a trinuclear one with small intermolecular interactions

due to nitrato bridges between trinuclear entities. It might be noted that the two triangles (Figure 7) were assumed to be magnetically equivalent for simplification. The typical plateau, at low temperatures, corresponding to isolated trinuclear Cu(II) complexes with antiferromagnetic coupling between the metal ions (spin doublet state, $\chi_M T \approx 0.4$ emu mol^{-1} K, and reasonable g value) does not appear. Furthermore, the use of the isotropic Heisenberg-Dirac-van Vleck (HDVV) Hamiltonian formalism: $H = -J_{12}S_1S_2 - J_{23}S_2S_3 - J_{13}S_1S_3$ (Scheme 2), assuming a small J' (intermolecular) interaction considered to analyze the experimental variation of $\chi_M T$ at low temperatures was failed in all the attempts. The results obtained considering one, two or three coupling constants give serious discrepancies between the theoretical and the experimental data in the low temperature region in all the cases.

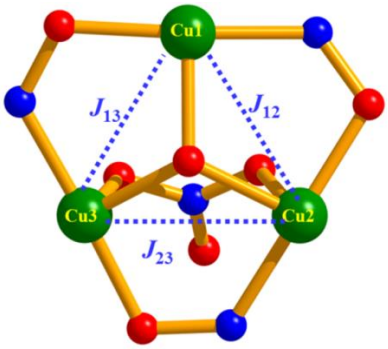

Scheme 2. Magnetic exchange interaction in the trinuclear core of **1**.

It is well known that in triangular complexes that show intramolecular antiferromagnetic coupling give rise to spin frustration effects;[5] as it is impossible for all possible pairing of spins to be simultaneously antiferromagnetic. As is pointed in the literature,[8b,17,18] to interpret the magnetic properties of this kind of systems it is necessary to introduce an antisymmetric exchange interaction (ASE) in the isotropic exchange model. The Hamiltonian used to investigate the magnetic interaction between the metal centres assuming isosceles character of the triangle (J and j) is:

$$\boldsymbol{H = -J(S_1.S_2 + S_2.S_3) - j(S_1.S_3) + G_z[(S_1 \times S_2) + (S_2 \times S_3) + (S_1 \times S_3)}$$

Where $J = J_{1,2} = J_{2,3}$, $j = J_{1,3}$ and G_z is the antisymmetric exchange vector parameter.

For an equilateral triangle (C_3) the isotropic exchange yields two degenerated spin doublets, ^{2}E, as ground state and a spin quadruplet, ^{4}A, which are separated by the gap $3J_{av}/2$.[18b,c] Within the framework of the isotropic HDVV model, the two doublets in the ^{2}E state are non-interacting and the degeneracy is accidental.[18b,c] Thus splitting of the two degenerated doublets is only possible via distortion of the C_3 symmetry, which makes

non-equivalent two (C_2) or three (C_i) J_{ij} parameters. The ASE acts within the ^2E term giving rise to two spin doublets separated by a $\sqrt{3}G_z$ gap. This energy gap increases to $\Delta = (\delta + 3G_z^2)^{1/2}$ by a distortion of the equilateral triangle (C_3) to an isosceles (C_2), where $\delta = J - j$.[18b,c] The expression of the magnetic susceptibility from this Hamiltonian, derived by Lloret and coworkers,[18b,c] in which the parallel and the perpendicular susceptibility components must be considered separately, because they are affected differently by the G_z vector is:

$$\chi_M^{||} = \frac{N\beta^2 g_{||}^2}{4kT}\left[\frac{\cosh(x)+5\exp(3J_{av}/2kT)}{\cosh(x)+\exp(3J_{av}/2kT)}\right]$$

$$\chi_M^{\perp} = \frac{N\beta^2 g_{\perp}^2}{4kT}\left[\frac{\rho^2\cosh(x)+5\exp(3J_{av}/2kT)+(1-\rho^2 senh(x)/x}{\cosh(x)+\exp(3J_{av}/2kT}\right]$$

$$\chi_M^{av} = \frac{\chi_M^{||}+2\chi_M^{\perp}}{3}$$

where $x = \Delta/2kT$ and $\rho = \delta/\Delta$

In the trinuclear cores of **1**, the Cu(II) ions can be considered to be in an isosceles arrangement (Scheme 2) where J_{12} and J_{23} can be approximated to be similar considering the bond distances and bond angles involved in this Cu_3 core (Table 2). The best fit obtained, introducing the Weiss parameter θ to take into account the additional antiferromagnetic interactions between the trinuclear units, are: J_{av} = -655 cm^{-1}, $g_{||}$ = 2.25, $g_{\perp}$ = 2.22 , Δ = 92.2 cm^{-1}, δ = 51.9 cm^{-1}, θ = -0.18 K and R = 1.25 x 10^{-6} ($R = \Sigma_i(\chi T_{icalc} - \chi T_{iexp})^2 / \Sigma_i(\chi T_{iexp})^2$). Introducing these parameters to the equation $G_z = ((\Delta^2-\delta^2)/3)^{1/2}$, a G_z value of 44.0 cm^{-1} was obtained for the antisymmmetric interaction. The exchange interaction between the Cu(II) ions in the trinuclear unit considering an isosceles arrangement can be deduced from the equations $J_{av} = (2J+j)/3$ and $\delta = J-j$ that give values of J = -671.8 cm^{-1} and j = -620.0 cm^{-1}. All these results are in good agreement with those reported in the literature for other trinuclear Cu(II) complexes in which the antisymmetric interaction was taking into account; the observed values are in the ranges of 17.7-63 cm^{-1}, 15-47 cm^{-1} and 39.7-103 cm^{-1} for δ, G_z and Δ respectively.[5c, 17-18] The large J_{av} value of -655 cm^{-1} found in complex **1** is consistent with the observed N,O oximato and μ_3-O bridges between the Cu(II) ions in **1**. Literature works have established relationships

between the magnetic coupling and structural features for trinuclear complexes with [Cu_3O] core (Table 7) based on the following factors:

a) The Cu-O(H)-Cu bridging angle is a major factor controlling the spin coupling between the metal centres in hydroxido, alcoxido or phenoxido bridged compounds. For the larger Cu–O–Cu angles, like greater than ≥97.5°, the antiferromagnetic interactions predominates.[20] In fact, in compound **1** all the Cu–O–Cu angles are in the range of 107.05(13)°–117.71(14)° (Table 2), which fall in the range of similar parameters of trinuclear core showing antiferromagnetic interactions.

b) The deviation of the μ_3-O atom from the centroid of the Cu_3 triangular motif plays a pivotal role on the antiferromagnetic coupling between the Cu centres. This feature is evident from the excellent linear correlation of the coupling constant *J* with this deviation.[18a] Smaller deviation results in strong antiferromagnetic coupling (Table 7).

Furthermore, other parameters like the coplanarity of the coordination planes around each copper atom[21] and the interplanar angle between the equatorial planes of Cu(II) are also important for determining the *J* value. The more flattened is the $Cu_3O(H)$ core, the stronger will be the magnetic interaction.[8b] On the other hand, lower interplanar angle between the equatorial planes of copper(II) gives rise to higher *J* value due to larger overlap of the $d_{x^2-y^2}$ magnetic orbital.[11b] For trinuclear $Cu_3O(H)$ systems, the highest *J* value of −1000 cm^{-1} was reported for an oximate compound, $[Cu_3(O)L'_3(ClO_4)]_2$ (**A**), HL'= 1,2–diphenyl–2–(methylimino)ethanone–1–oxime[21] which has an average interplanar angle of 20.5° and a distance of 0.352 Å of μ_3–OH from the mean Cu_3 plane. A comparison of important structural parameters and the corresponding *J* values of copper compounds containing a $Cu_3O(H)$ core is given in Table 7**.**

2.3.2.2 Magnetic properties of 2

The temperature dependence of the χ_M and $\chi_M T$ (χ_M being the magnetic susceptibility per Cu_3 entity) of **2** are shown in Figure 21a. At room temperature the $\chi_M T$ value is much lower (0.47 cm^3 mol^{-1} K) compared to the value expected for three uncoupled S = ½ spins (ca. 1.12 cm^3 mol^{-1} K) and it decreases steadily with decreasing temperature and becomes 0.34 cm^3 mol^{-1} K at temperature 2.5 K. This behaviour indicates that a strong antiferromagnetic coupling operates between the Cu(II) ions. In order to investigate the magnetic coupling in this compound, an isotropic Heisenberg–Dirac–van Vleck (HDVV) Hamiltonian formalism (eq 1) was used.

$\hat{H}_{HDVV} = -J_{12}\hat{S}_1\,\hat{S}_2 - J_{13}\hat{S}_1\,\hat{S}_3 - J_{23}\hat{S}_2\,\hat{S}_3$ …….(1)

Since the three copper atoms of the $Cu_3(\mu_3–OH)$ unit resemble a quasi-equilateral triangle (Table 3), the three exchanges (Cu1–Cu2, Cu2–Cu3 and Cu3–Cu1) can be considered equivalent and so $J_{12} = J_{13} = J_{23} = J$. From this Hamiltonian, a solution of the magnetic susceptibility may be derived as follows:

$(\chi_M)_{tri} = (N\beta^2g^2/4kT)[1 + 5\exp(3J/2kT)]/[1 + \exp(3J/2kT)]$…….. (2)

Where N, g, β, k and T have their usual meanings.

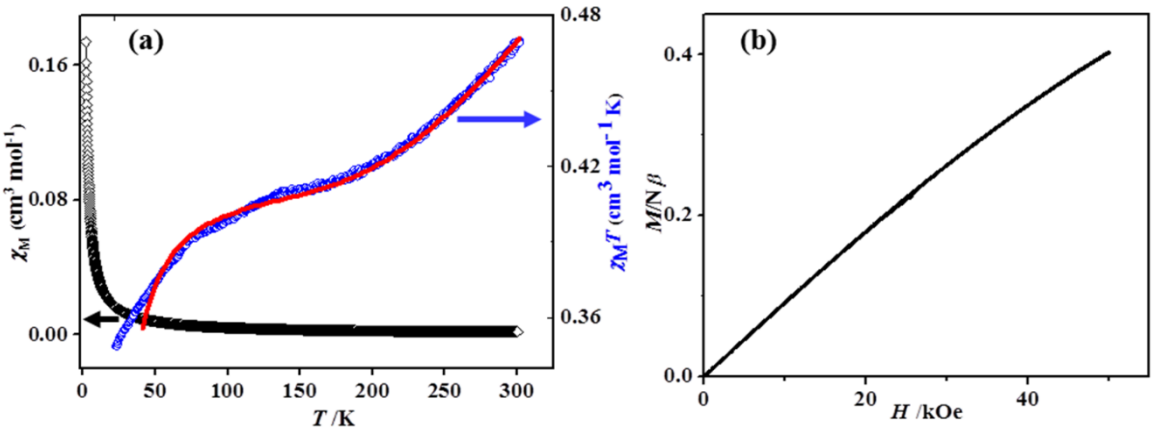

Figure 21. (a) The plots of χ_M *vs.* T and χ_MT *vs.* T of **2**. The solid red line indicates the best fit obtained. (b) The M *vs.* H curve of **2** at 5 K.

The trinuclear $Cu_3(\mu_3–OH)$ cores are further connected by the $N(CN)_2^-$ anions, therefore, the exchange interaction between the trinuclear units cannot be ignored. The interaction between trinuclear cores was considered and the overall equation is

$\chi_M = (\chi_M)_{tri}/[1-(2zj'/N\beta^2g^2)(\chi_M)_{tri}]$……..(3) where zj' is the inter-trinuclear coupling. Using equation 3, the experimental data were fitted satisfactorily in the temperature range 300 K–20 K and the best fit parameter are $J = -459.7$ cm^{-1}, g = 2.11, $zj' = -5.25$ cm^{-1} and $R = 3.4\times10^{-6}$ $\{R = \sum[(\chi_M)^{obs} - (\chi_M)^{calc}]^2/[(\chi_M)^{obs}]^2\}$ (Figure 21a). It is worth mentioning that antisymmetric exchange was not considered in the analysis which is expected to be present in such systems and could also influence low temperature data. The observed deviation of the fitted curve from the experimental curve in the low temperature region is probably due to the antisymmetric exchange interaction.[17,18] The values of the coupling constant J and zj' indicate the existence of a strong antiferromagnetic coupling within the trinuclear core and a weak antiferromagnetic coupling between the trinuclear core through the $N(CN)_2^-$ bridges. The M *vs* H curve at 5 K reaches a maximum value of 0.4 Nβ, being markedly below from the expected 3 Nβ (Figure 21b), corroborating strong antiferromagnetic interactions operating within the

{Cu(II)}$_3$ triangle. For a detailed understanding of the exact magnetic exchange pathways towards antiferromagnetic interactions, computational study based on density functional theory (DFT) was performed within the broken symmetry (BS) formalism[19a] using GAUSSIAN 03 package.[19b] The trinuclear Cu$_3$(μ_3–OH) core was considered to find the sign and magnitude of the magnetic coupling, considering B3LYP exchange and correlation functional LANL2DZ basis set.[19b] The calculations show that, for the trinuclear core, the doublet state is stable than the quartet state by 0.2028 eV. The predominant antiferromagnetic interactions can further be confirmed by spin density plot, showing delocalization of opposite spins through O atom of μ_3–OH group (Figure 22).

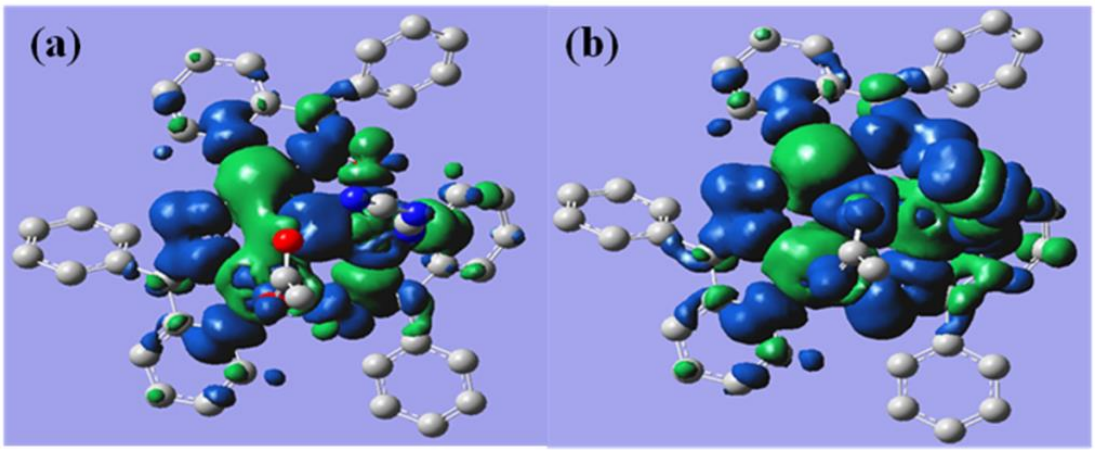

Figure 22. The spin density plot for **2:** (a) doublet and (b) quartet spin state.

Afrati *et al.*[17a,18a] have reported a trinuclear Cu$_3$-OH core similar to **2**, using phenyl–2–pyridylketoxime ligand with $J \geq -400$ cm^{-1} obtained experimentally as well as theoretically. The average Cu···Cu distance (3.22 Å) and the deviation of μ_3–OH (0.59 Å) from the mean Cu$_3$ plane in [Cu$_3$(PhPyCNO)$_3$(OH)(CH$_3$OH)$_2$(ClO$_4$)$_2$] (PhPyCNO = phenyl–2–pyridylketoxime)[18] is similar to compound **2,** which are 3.21 Å and 0.616 Å, respectively (Table 7). Therefore, the *J* value (−457.9 cm^{-1}) obtained in **2** is reasonable which also corresponds well with the *J* value for above compound (J = −456.5 cm^{-1}). A comparison of important structural parameters and the corresponding *J* values of copper compounds containing a Cu$_3$O(H) core is given in Table 7**.**

2.3.2.3 Magnetic properties of 3

The obtained magnetic data for **3** is plotted as $\chi_M T$ and χ_M *vs. T* as shown in Figure 23a. The $\chi_M T$ value at 300 K is 1.56 cm^3 mol^{-1} K which is slightly higher than the spin only

value expected for a cluster comprising four Cu(II) non-interacting ions (1.50 cm^3 mol^{-1} K with g = 2).

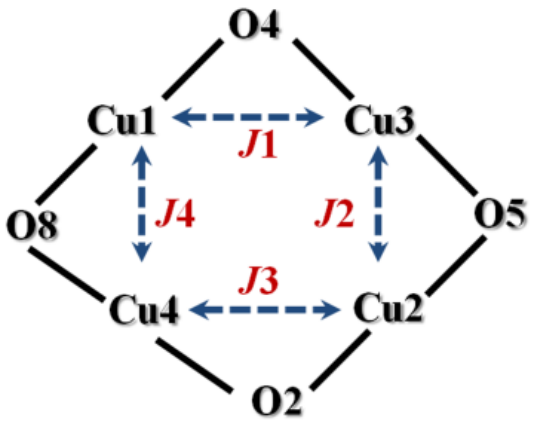

Scheme 3. Simplified coupling scheme between the Cu(II) centres for **3**.

Table 7. Comparison of structural parameters concerning the μ_3–OH in Cu_3O trinuclear clusters.

Compounds	**O(H)….Cu_3 plane/Å**	**Cu-O(H) /Å (av)**	**Cu-Cu'/Å (av)**	**-*J*/cm^{-1}**	**References**
A	0.352	1.868	3.177	1000	21
B	0.695	1.964	3.194	122	21
C	0.816	1.973	3.111	109	25
D	0.92	2.003	3.101	400	17a
E	0.66	1.942	3.166	220	18a
F	-	1.891	3.275	500	8b
G	-	1.992	3.251	140	22
H	0.576	2.013	3.341	191.2	23
I	0.478	1.99	3.351	200	24
J	0.473	1.991	3.355	197.7	5c
K	0.564	2.000	3.341	190.9	5c
L	0.433	2.007	3.371	198.2	5c
1	0.62	1.987	3.321	655	This work
2	0.616	1.957	3.215	459.7	This work

A=$[Cu_3(O)L'_3(ClO_4)]_2$, HL'= 1,2-diphenyl–2–(methylimino)ethanone–1–oxime; B=$[Cu_3(OH)L''_3(ClO_4)]^+$, HL''= 3–(phenylimino)butanone-2-oxime;C=$[Cu_3(amox)_3(\mu_3–OH)(\mu_3–Cl)]ClO_4$, amoxH= 4–amino–4–methylpentan–2–one oxime; D=$[Cu_3(PhPyCNO)_3(OMe)(Cl)(ClO_4)]$, PhPyCNO= phenyl–2-pyridyl ketooxime; E=$[Cu_3(PhPyCNO)_3(\mu_3\text{-}OH)(2,4,5–T)_2]$, 2,4,5–T= 2,4,5–trichlorophenoxyacetate; pz=pyrazole; F=$[PPN]_2[Cu_3(\mu_3–O)(\mu–pz)_3Cl_3]$, G=$Cu_3(\mu–OH)(\mu–Cl)(pz)_3(py)_2Cl_2$; H=$[Cu_3(\mu_3–OH)(hppt)_3(NO_3)_2](H_2O)_4$; hppt=3–(2–hydroxyphenyl)–4–phenyl–1,2,4–triazole; I=$[Cu_3(\mu_3\text{-}OH)(pz)_3(NO_3)(Hpz)_2](NO_3)$. H_2O, J=$[Cu_3(OH)(aat)_3(CF_3SO_3)(H_2O)_2](CF_3SO_3)$, K=$[Cu_3(OH)(aat)_3(NO_3)(H_2O)_2](NO_3).(H_2O)_2$; L=$[Cu_3(OH)(aat)_3(ClO_4)(H_2O)_2](ClO_4)$.

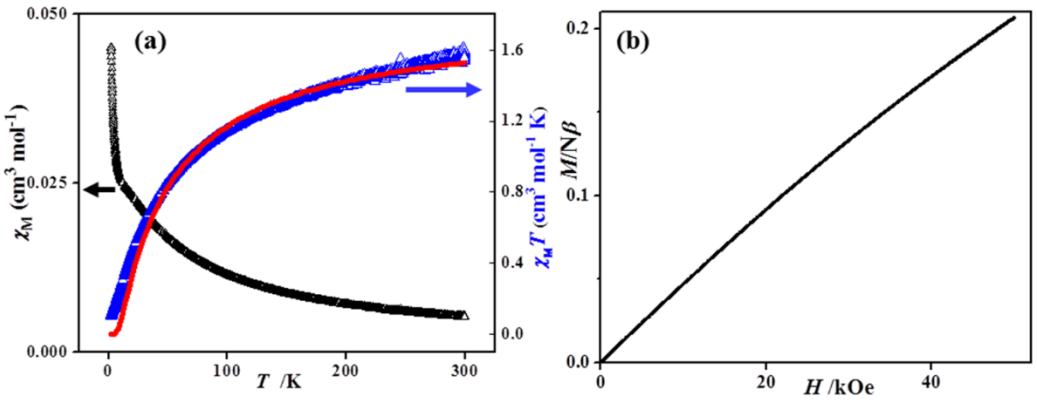

Figure 23. (a) The plots of χ_M *vs. T* and $\chi_M T$ *vs. T* for **3**. The red line indicates the possible best fit obtained. (b) The M *vs. H* curve for **3** at 5 K

The $\chi_M T$ product continuously decreases with decreasing temperature and becomes 0.112 cm^3 mol^{-1} K at temperature 3 K. This indicates antiferromagnetic interactions operating in **3**. The *M vs H* curve at 5 K reaches a maximum value of 0.21 Nβ, which is well below from the expected 4 Nβ (Figure 23b), suggesting the antiferromagnetic interactions operating within the tetranuclear core. In order to avoid over parameterization, only the significant interactions (i.e. Cu1–O4–Cu3, Cu3–O5–Cu2, Cu2–O2–Cu4, and Cu4–O8–Cu1) (Scheme 3) in the tetranuclear core were considered. Since the apical Cu–O bond distances are quite large (Table 4), all other interactions except above four mentioned ones (the bridges involved in these four interactions are in the equatorial positions) can be approximated to be negligible. Now the bond distances and bond angles involved in these four interactions are similar (Table 4) and the exchange interactions can be considered to be equivalent, and therefore *J1 = J2 = J3 = J4= J*. Hence for the interactions in the tetranuclear core an isotropic Heisenberg Hamiltonian formalism (eq 4) is adopted as:

$$H = -J(\hat{S}_1 \hat{S}_3 + \hat{S}_2 \hat{S}_3 + \hat{S}_2 \hat{S}_4 + \hat{S}_4 \hat{S}_1) \quad \text{.....(4)}$$

Now the general relation between $\chi_M T$ and T is

$$\chi_M T = (N\beta^2 g^2/kT)[_{i=16}\Sigma(S_z)^2 e^{-Ei(J)/KT}]/[\Sigma e^{-Ei(J)/KT}] \quad \text{.....(5)}$$

For compound **3**, 16 spin states (six states with S_z = 0, eight with S_z = 1 and two states with S_z = 2) are possible. Now from equations 4 and 5, the equation of the temperature dependence of the magnetic susceptibility can be derived as:

$$(\chi_M)_{tetra} = (N\beta^2 g^2/kT)[4 + 2\exp(J/kT) + 10\exp(-J/kT)]/[7 + \exp(2J/kT) + 3\exp(J/kT) + 5\exp(-J/kT)] \quad \text{.....(6)}$$

As it has been mentioned earlier that the tetranuclear cores are further connected by the hydroxido groups forming a 1D coordination chain, therefore an intertetramer *zj'* term

was introduced which results to the final expression as:

$\chi_M = (\chi_M)_{tetra}/[1-(2zj'/N\beta^2g^2)(\chi_M)_{tetra}]$ ……(7)

The best fit parameters obtained based on equation 7 are $J = -27.09$ cm^{-1}, $zj' = -9.65$ cm^{-1} with g= 2.17 and $R = 2.67\times10^{-3}$ where $R = \sum[(\chi_M)^{obs} - \chi_M)^{calc}]^2/[(\chi_M)^{obs}]^2\}$ (Figure 23a). As it has been mentioned previously, for oxido-bridged Cu(II) complexes the spin-coupling between the Cu(II) ions depend strongly on the geometry of the Cu(II) centres and the Cu–O–Cu bridging angles and distances. In the tetranuclear core of **3** all the Cu–O–Cu angles involved in the important magnetic exchange pathways are in the range of 109°–115° which falls under the range of antiferromagnetic interaction. To gain insight into the magnetic exchange mechanism, spin-unrestricted calculations were performed using the Gaussian 03 package at the B3LYP level employing the LANL2DZ basis set. A $\{[Cu_4(pdmH)_2(pdm)_2(\mu_2\text{–}OH)(H_2O)]\cdot ClO_4\}$ unit was considered for calculating ground state energy of the singlet, triplet and the quintet states. The triplet state was found to be the most stable one, followed by the quintet and singlet states, respectively. The triplet state is more stable than the quintet state by 0.1069 eV suggesting the dominant antiferromagnetic exchange coupling among the Cu(II) centres within the tetranuclear core. This fact is further proved by the spin density plots (Figure 24).

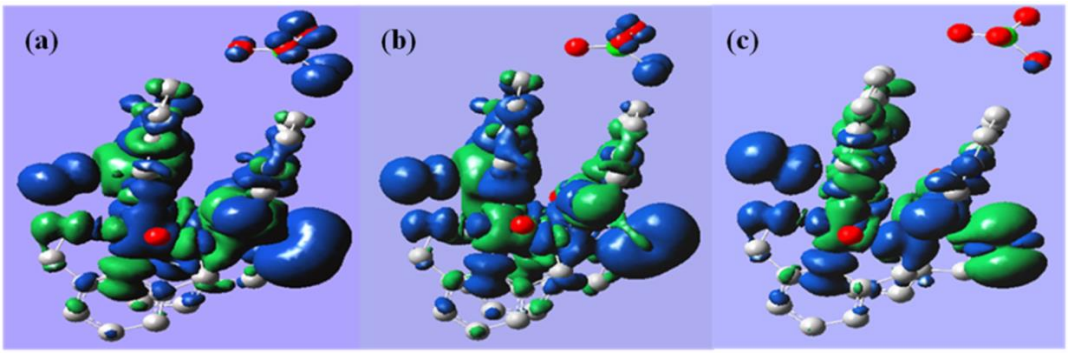

Figure 24. The spin density plot for **3:** (a) quintet, (b) triplet and (c) singlet spin state.

2.3.2.4 Magnetic properties of 4

The temperature dependent magnetic studies have been performed for compound **4** in the temperature range 300–3 K (Figure 25). At room temperature the $\chi_M T$ value is 7.3 cm^3 mol^{-1} K, which is consistent with four quasi-isolated Ni(II) ions and six quasi-isolated Cu(II) ions; the corresponding theoretical value would be 6.25 assuming the lower theoretical limit of g = 2.00. The $\chi_M T$ value decreases monotonically up to 30 K; after that there is a small increase of $\chi_M T$ value which finally shows a small decrease beyond 5 K with a value of 3.6 cm^3 mol^{-1} K presumably due to the *D* parameter [zero field splitting of

the Ni(II) ions]. The decanuclear structure is formed by the union of two symmetry related pentanuclear cores via diaqua bridging ligands. DFT calculations (see below) have demonstrated that this coupling interaction is ferromagnetic. Indeed, from qualitative point of view this *J* parameter cannot be negative (antiferromagnetism, with $H = -J\sum S_i S_j$), as in that case, the $\chi_M T$ of both pentanuclear moieties would be cancelled due to the presence of inversion centre and the final $\chi_M T$ would be zero, which is not the case here. For the decanuclear entity, the reduced magnetization at 3 K (Figure 25b) tends to 6 $M/N\beta$, corresponding to six unpaired electrons. This feature is consistent with the following assumption: the presence of the antiferromagnetism in the $\chi_M T$ *vs T* plot is due to the antiferromagnetic character of the Ni–O–Ni pathway, which is well documented in the literature with such kind of geometries.[26a] Thus, once being cancelled the spins of Ni(II) ions, it seems there are six unpaired electrons arising from the six Cu(II) ions, which may be in isolated form or ferromagnetically coupled. The fitting of the magnetic data for the decanuclear core has been performed using the MAGPACK program[27] with or without the *D* parameter. The spin part of the Hamiltonian in this program is $H = -2J\sum S_i S_j$. The magnetic pathways of the pentanuclear core is shown in Scheme 4 and the calculated *J* values with or without *D* are presented in Table 8.

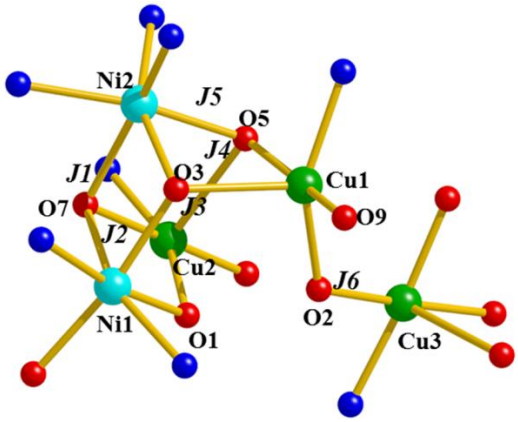

Scheme 4. Different magnetic exchange interactions in the pentanuclear core of **4**.

It is worth-mentioning that there are only small differences in the calculations of *J* parameters, if *D* is considered or not. In both cases, the magnetic pathway between Cu1–Cu3 remains antiferromagnetic with very small *J* value (<–1 cm^{-1}). Although a strong interaction is expected because of the Cu−O−Cu angle of magnitude 119.7(4)°,[20] the trigonal bipyramidal distortion of Cu1 coordination would reduce the magnitude of the interaction.

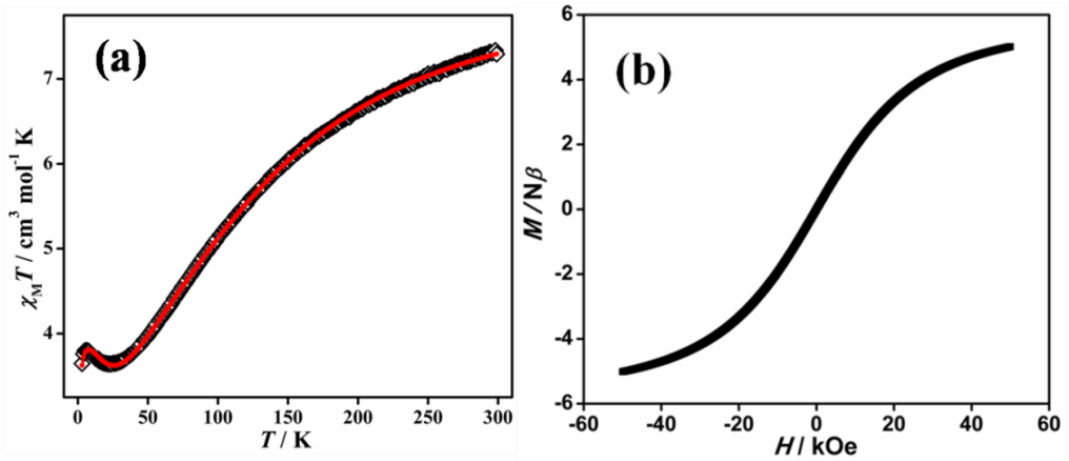

Figure 25. (a) Experimental (black points) $\chi_M T$ *vs* *T* plot for **4**. The red line indicates best fit obtained considering *D* (For *J* and *D* values see Table 1). (b) The *M vs H* curve for **4** at 3 K.

The best fit obtained considering *D* can be seen in Figure 25a. With or without *D* (Figure 26a), the result is practically the same with the R value nearly equal; however invoking *D* the result is slightly better. It is also logical to assume that the *D* parameter is not zero for Ni(II) ions (Table 8) with S = 1. The *D* parameter obtained with the fit is too high for standard Ni(II) ions[26] which may be a simple mathematical artifact arising from other antiferromagnetic pathways. The intricate structure may result in some spin-frustrations among Cu(II) and Ni(II) ions (Table 8). These findings indicate that the system has several analytical solutions and the most reliable value should be assumed as the calculated ones with an average of those with appreciable *D* or with *D* = 0. Some of the coupling constants have been assumed as negligible (Table 8) to minimize the number of variables in the fitting process. The assumption of six unpaired electrons in the ground state, accounting the saturation of the magnetization curve at 3 K, which corresponds to six quasi-isolated Cu(II) ions, is corroborated by the calculations with $J_{Cu1–Cu2}$ and $J_{Cu2–Cu3}$ to be negligible (Table 8) and $J_{Cu1–Cu3}$ almost to be zero. The central magnetic pathway Cu_2O_2 should be ferromagnetic, as anticipated from the Cu3–O–Cu3_a angle of 95.4(3)°.[20] To understand the interaction between the pentanuclear cores, DFT study has been performed (Figure 26b,c). The water bridged cluster comprising of two Cu(II) centres has been considered to calculate ground state energy of the singlet and triplet states. The results show that the triplet state is more stable than the singlet state by 0.003371 eV (27.2 cm^{-1}) suggesting the dominant ferromagnetic exchange interaction between the two pentanuclear cores.

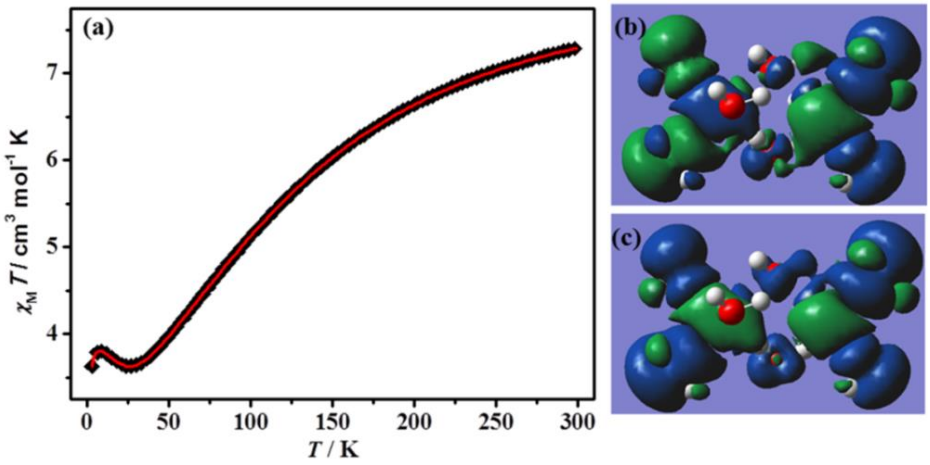

Figure 26. (a) Experimental (black points) $\chi_M T$ *vs T* for the decanuclear compound **4**. The red line shows the best fit obtained by considering D = 0; Spin density plot for (b) singlet state and (c) triplet state for the water bridged two Cu atoms connecting two pentanuclear cores. Calculations have been performed within the broken symmetry (BS) formalism using GAUSSIAN 03 package at the B3LYP level employing the LANL2DZ basis set.

Table 8. *J* and *D* values for the decanuclear cluster based on Figure 15b.

Magnetic pathway	*J* (cm^{-1})	*D*= 0	*D* variable (cm^{-1})
Ni1–Ni2	*J*1	–49.2	–49.7
Ni1–Cu2	*J*2	29.5	28.9
Ni1–Cu1	*J*3	62.1	62.8
Ni2–Cu2	*J*4	26.1	26.7
Ni2–Cu1	*J*5	–13.3	–11.7
Cu1–Cu3	*J*6	–0.45	–0.28
Cu3-Cu3_a	*J7*	13.6[a]	13.6[a]
	g	2.29	2.29
	D	0	29.6
	R[b]	7.4 x 10^{-6}	6.9 x 10^{-6}
Cu1–Cu2		Negligible d(Cu2–O) = 2.5 Å	
Ni1–Cu3		Negligible (*syn–anti* quasi perpendicular)	
Cu2–Cu3		Negligible (*syn–anti* quasi perpendicular)	

[a]fixed from value of the DFT calculations.

[b]*R* factor is the agreement factor defined as $\sum_i[(\chi_M T)_{obs}-(\chi_M T)_{calc}]^2/\sum_i[(\chi_M T)_{obs}]^2$.

2.3.2.5 Magnetic properties of 5

The temperature dependence (300 -3 K) of the $\chi_M T$ product (χ_M being the magnetic susceptibility per Mn_2Cu_4 unit) for compound **5** is shown in Figure 27. At room temperature, the $\chi_M T$ value is 9.6 cm^3 mol^{-1} K, which is slightly lower than that expected

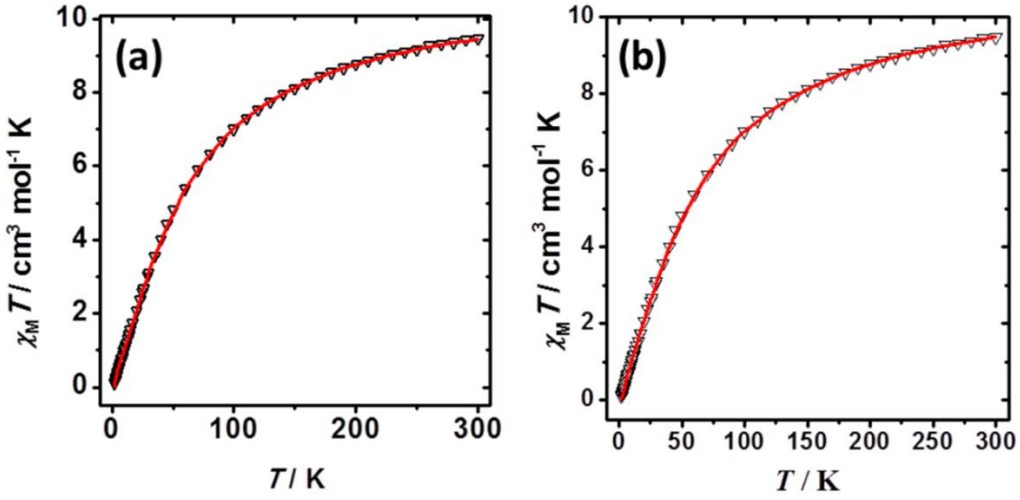

Figure 27. The plot of $\chi_M T$ *vs.* T for **5**. The solid red line indicates the best fit obtained (a) considering five "*J*" and (b) considering four "*J*" parameters (see text).

for four isolated Cu(II) ions and two Mn(II) ions (10.1 cm^3 mol^{-1} K). The $\chi_M T$ product continuously decreases with decreasing temperature and becomes 0.11 cm^3 mol^{-1} K at temperature 3 K. This indicates a dominant antiferromagnetic interactions operating in **5**. The 3D framework of **5** consists of repeating hexanuclear Mn_2Cu_4 cores connected through the end-to-end azido ($\mu_{1,3}$) bridging between Cu(II) centres of different hexanuclear cores. However, one of Cu(II)-N (Cu1-N9) bond distance involved in such linking is 2.6 Å and magnetic interaction through this pathway can be negligible and thus we can model the system to a simplified hexanculear one. In the hexanuclear core, there are several possible interactions between Cu(II)-Mn(II), Mn(II)-Mn(II) and Cu(II)- Cu(II) ions as shown in Scheme 5. No formula to reproduce the magnetic susceptibility of such a complex system is available in literature. Nevertheless, fitting of the experimental data was attempted to rationalize the results. The different exchange coupling interactions in the hexanuclear core are *J1*: Cu2-Mn1 and Cu2a-Mn1a interaction through oxo-like bridges (O5 and O2 atoms); *J2*: Mn1-Mn1a interaction (O3 and O3a atoms); *J3*: Cu1-Cu1a interaction (O1 and O1a atoms); *J4*:Cu2-Cu1a and Cu2a-Cu1a interactions through carboxylate-like bridging (O2-C6-O1 atoms); *J5*: Cu2-Cu1 and Cu1-Cu2a interactions (O2-C6-O1 atoms). The exchange interaction through Mn1-O3a-Cu1a and its symmetry-related counterparts Mn1a-O3a-Cu1a have been neglected due the long bond distance Cu1a-O3a (2.524 Å). Only one g value (average between Mn and Cu) has been considered and an intermolecular term ($z'J'$) is also considered to account for the inter-hexanuclear interaction through the azido ligands. The best fit parameters with MAGPACK program (using $H = -2J\Sigma S_{ij}$) are shown in Table 9.

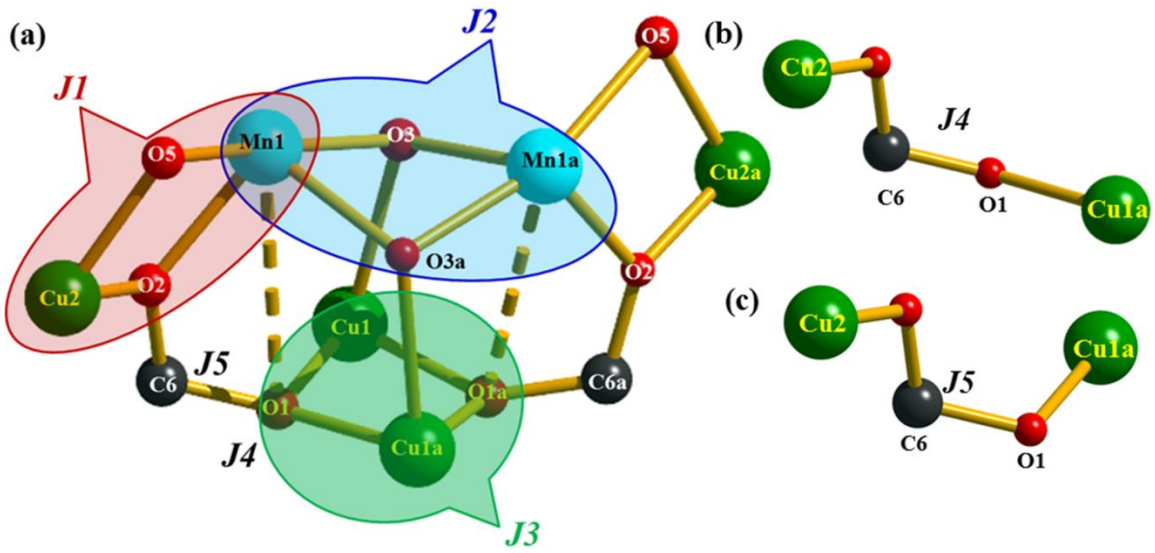

Scheme 5. (a) Different magnetic exchange pathways in the hexanuclear $Mn^{II}_2Cu^{II}_4$ core of **2.** The interactions *J*1, *J*2 and *J*3 are highlighted. The weaker interactions (through *syn-anti* carboxylate bridge) involving *J*4 (b) and *J*5 (c) are shown separately.

Table 9. Results of the fitting of magnetic data for the $\{Mn_2Cu_4\}$ unit of compound **5** based on Scheme 5.

Magnetic pathway	*J* (four *J* values + *z'J'*)/ cm^{-1}	*J* (five *J* values + *z'J'*)/cm^{-1}
Cu2-Mn1 and Cu2a-Mn1a	*J1* = 0.41	*J1* = 0.41
Mn1-Mn1a	*J2* = -18.64	*J2* = -18.44
Cu1-Cu1a	*J3* = -0.39	*J3* = -0.39
Cu2-Cu1a and Cu2a-Cu1a	*J4* = -0.46	*J4* = -0.43
Cu2-Cu1 and Cu1-Cu2a		*J5* = -0.41
$g_{average}$	g = 2.07	g = 2.07
z'J'	*z'J'* = -0 .586	*z'J'* = -0.587
R	5.31 x 10^{-5}	5.36 x 10^{-5}

Fitting were also performed without considering *J5* pathway (four *J* and *z'J'*). The results are similar for both the calculations (Table 9). However, this result could be overparametrized with many *J* parameters. Consequently, the solution may not be very accurate and there might be some discrepancies. For e.g.; we suppose that *J3* [interaction between Cu(II) ions through oxo bridge] should be stronger than *J4* [interaction between Cu(II) ions through *syn-anti* carboxylate bridge] although we did not realize it in the above fitting results. Therefore, we looked at the structural details further to simplify the model system and to obtain more reliable fitting. It is noteworthy that *J4* and *J5* involve interactions through *syn-anti* like carboxylate bridges; which are generally poor in magnitude. Therefore *J4* and *J5* parameters were neglected and then fitting using MAGPACK program yielded the following best-fit parameters: *J1* (Cu2-Mn1 and Cu2a-Mn1a) = 5.0 cm^{-1}, *J2* (Mn1-Mn1a) = -31.8 cm^{-1}, *J3* (Cu1-Cu1a) = -3.13 cm^{-1}, *g* (average)

= 2.11, *z'J'* (intermolecular) = -3.31 cm^{-1}, R = 6.66 x 10^{-5} (Figure 27b). To understand the magneto-structural correlation, different bridging pathways were considered. As discussed earlier, the Cu-O-Cu bridging angle is a major factor controlling the coupling interaction and antiferromagnetic interactions predominates for ∠Cu–OH–Cu ≥97.5°. In **5**, the ∠Cu1–O1–Cu1a angle (98.88°) involved in the exchange pathway (*J3*) is only slightly larger than the crossover angle (97°) proposed in the related systems and results in an weak antiferromagnetic interaction (-3.13 cm^{-1}). Literature reports show that in similar systems with $(py)_2CO$-based ligands, the coupling between Mn(II) ions should be antiferromagnetic when the ∠Mn-O-Mn angle is in the range of 80-110°.[28] This is consistent with the value of *J2* (-31.8 cm^{-1}). Finally, it is difficult to comment on the coupling interaction between Cu(II) and Mn(II), as such systems are infrequently investigated.[29]

2.4 SUMMARY

Judicious self-assembly approach has been adopted by using suitable blocking ligands and multidentate bridging linkers to synthesize five new metal-organic coordination compounds. Assembly of $Cu_3(\mu_3–O)$ cores with bridging NO_3^- ion and $[N(CN)_2^-]$ ligand resulted in a hexanuclear compound and an 1D compound respectively, while a Cu(II) 1D coordination chain has been synthesized containing tetranuclear $[Cu_4(pdmH)_2(pdm)_2(H_2O)_2]$ building units connected by OH^- groups. On the other hand, to synthesize novel heterometallic clusters, polytopic dpk ligand with suitable coordination compartments has been exploited. A cluster containing two symmetry related pentanuclear Ni_2Cu_3 cores has been synthesized and this represents the first example of a heterometallic decanuclear cluster based on Ni(II) and Cu(II). Assembly of $\{MnCu_2(dpkO_2H)_2(dpkO_2)^{2+}$ cores connected through azide ligand towards a new 3D framework is also reported in this chapter. The different complex magnetic interactions operating in compounds **1**-**5** were analyzed. Proper understandings of the chemical nature and magnetic behaviour such compounds will shed some light into the fundamental aspects of molecular magnetism.

2.5 REFERENCES

1. (*a*) R. Sessoli, H. L. Tsai, A. R. Schake, S. Wang, J. B. Vincent, K. Folting, D. Gatteschi, G. Christou and D. N. Hendrickson, *J. Am. Chem. Soc.*, 1993, **115**, 1804; (*b*) R. Sessoli, D. Gatteschi, A. Caneschi and M. A. Novak, *Nature*, 1993, **365**, 141.

2. (*a*) H. Miyasaka, K. Nakata, L. Lecren, C. Coulon, Y. Nakazawa, T. Fujisaki, K. Sugiura, M. Yamashita and R. Clerac, *J. Am. Chem. Soc*., 2006, **128**, 3770; (*b*) M. Murugesu, W. Wernsdorfer, K. A. Abboud, E. K. Brechin and G. Christou, *Dalton Trans*., 2006, 2285.
3. (*a*) H. Miyasaka and M. Yamashita, *Dalton Trans*., 2007, 399; (*b*) G. Christou, D. Gatteschi, D. N. Hendrickson and R. Sessoli, *MRS Bull*., 2000, **25**, 66.
4. (*a*) E. I. Solomon, U. M. Sundaram and T. E. Machonkin, *Chem. Rev*., 1996, **96**, 2563; (*b*) R. H. Holm, P. Kennepohl and E. I. Solomon, *Chem. Rev*., 1996, **96**, 2239.
5. (*a*) L. Gutierrez, G. Alzuet, J. A. Real, J. Cano, J. Borras and A. Castineiras, *Inorg. Chem*., 2000, **39**, 3608; (*b*) O. Kahn, *Chem. Phys. Lett*., 1997, **265**, 109; (*c*) S. Ferrer, J. G. Haasnoot, J. Reedijk, E. Muller, M.B. Cingi, M. Lanfranchi, A. M. M. Lanfredi and J. Ribas, *Inorg. Chem*., 2000, **39**, 1859.
6. (*a*) W. Wernsderfer, N. Aliaga-Alcalde, D. N. Hendricson and G. Christou, *Nature*, 2002, **416**, 406; (*b*) E. E. Moushi, T. C. Stamatatos, W. Wernsdorfer, V. Nastopoulos, G. Christou and A. J. Tasiopoulos, *Angew. Chem. Int. Ed.*, 2006, **45**, 7722.
7. (*a*) J. Kim, M. L. Jin and Y. Do, *Eur. J. Inorg. Chem*., 2003, **14**, 2563; (*b*) Y. Z. Zheng, M. L. Tong, W. Xue, W. Zhang, X. M. Chen, F. Grandjean and G.J. Long, *Angew. Chem. Int. Ed*., 2007, **46**, 6076; (*c*) P. Albores and E. Rentschler, *Inorg. Chem*., 2008, **47**, 7960.
8. (*a*) A. Escuer, B. Cordero, M. Font-Bardia and T. Calvet, *Inorg. Chem*., 2010, **49**, 9752; (*b*) S. Ferrer, F. Lloret, I. Bertomeu, G. Alzuet, J. Borrás, S. García-Granda, M. Liu-González and J. G. Hassnoot, *Inorg. Chem*., 2002, **41**, 5821; (*c*) P.A. Angaridis, P. Baran, R. Boèa, F. Cervantes-Lee, W. Haase, G. Mezei, R. G. Raptis and R. Werner, *Inorg. Chem*., 2002, **41**, 2219.
9. (*a*) C. D. Nicola, Y. Y. Karabach, A. M. Kirillov, M. Monari, L. Pandolfo, C. Pettinari, and A. J. L. Pombeiro, *Inorg. Chem*., 2007, **46**, 221; (*b*) S. J, Seo, D. Whang, H. Lee, S. I. Jun, J. Oh, Y. J. Jeon and K. Kim, *Nature*, 2000, **404**, 982; (*c*) G. Férey, C. Mellot-Draznieks, C. Serre, F. Millange, J. Dutour, S. Surble and I. Margiolaki, *Science*, 2005, **309**, 2040; (*d*) Q. Fang, G. Zhu, M. Xue, J. Sun, Y. Wei, S. Qiu and R. Xu, *Angew. Chem. Int. Ed*., 2005, **44**, 3845; (*e*) A. Biswas, M. G. B. Drew, J. Ribas, C. Diaz and A. Ghosh, *Eur. J. Inorg. Chem*., 2011, 2405.

10. (*a*) S. R. Breeze, S. N. Wang and L.Q. Chen, *J. Chem. Soc. Dalton Trans*., 1996, 1341; (*b*) A. Fragoso, M. L. Kahn, A. Castineiras, J. P. Sutter, O. Kahn and R. Cao, *Chem. Commun*., 2000, **24**, 1547; (*c*) S. Mukherjee, B. Gole, Y. Song and P. S. Mukherjee, *Inorg. Chem*., 2011, **50,** 3621; (*d*) X. Zhang, Y. Wang and E. Gao, *Eur. J. Inorg. Chem*., 2010, 1249; (*e***)** J. Zhao, D. Shi, H. Cheng, L. Chen, P. Ma and J. Niu, *Inorg. Chem. Commun*., 2010, **13**, 822.
11. (*a*) S. Mukherjee, B. Gole, R. Chakrabarty and P. S. Mukherjee, *Inorg. Chem*., 2009, **48**, 11325; (*b*) S. Karmakar, O. Das, S. Ghosh, E. Zangrando, M. Johann, E. Rentschler, T. Weyhermüller, S. Khanra and T. K. Paine, *Dalton Trans*., 2010, **39**, 10920.
12. (*a*) P. Chaudhuri, *Coord. Chem. Rev*., 2003, **243**, 143; (*b*) C. J. Milios, P. Kyritsis, C. P. Raptopoulou, A. Terzis, R. Vicente, A. Escuer and S. P. Perlepes, *Dalton Trans*., 2005, 501; (*c*) Th. C. Stamatatos, A. K. Boudalis, Y. Sanakis and C. P. Raptopoulou, *Inorg. Chem*., 2006, **45**, 7372.
13. (*a*) S. Winter, W. Seichter and E. Z. Weber, *Anorg. Allg. Chem*., 2004, **630**, 434; (*b*) Th. C. Stamatatos, G. C. Vlahopoulou, C. P. Raptopoulou, A. Terzis, A. Escuer and S. P. Perlepes, *Inorg. Chem*., 2009, **48**, 4610.
14. (*a*) H. Oshio, M. Nihei, A. Yoshida, H. Nojiri, M. Nakano, A. Yamaguchi, Y. Karaki and H. Ishimoto, *Chem. Eur. J*., 2005, **11**, 843; (*b*) V. Chandrasekhar, B. Pandian, R. Azhakar, J. Vittal and R. Clerac, *Inorg. Chem*., 2007, **46**, 5140; (*c*) L. Zou, L. Zhao, Y. Guo, G. Yu, Y. Guo, J. Tang and Y. Li, *Chem. Commun*. 2011, **47**, 8659; (*d*) J. Zhao, B. Hu, F. Lloret, J. Tao, Q. Yang, X. Zhang and X. Bu, *Inorg. Chem*., 2010, **49**, 10390; (*e*) D. Wu, W. Huang, W. Hua, Y. Song, C. Duan, S. Li and Q. Meng, *Dalton Trans*., 2007, 1838; (*f*) N. Lalioti, C. Raptopoulou, A. Terzis, A. Aliev, I. Gerothanassis, E. Manessi-Zoupa and S. Perlepes, *Angew. Chem. Int. Ed*. 2001, **40**, 3211; (*g*) S. Biswas, S. Naiya, C. Gomez-Garcia and A. Ghosh, *Dalton Trans*. 2012, **41**, 462.
15. (*a*) SMART (V 5.628), SAINT (V 6.45a), XPREP, SHELXTL; Bruker AXS Inc. Madison, Wisconsin, USA, 2004; (*b*) G. M. Sheldrick, Siemens Area Detector Absorption Correction Program, University of Göttingen, Göttingen, Germany, 1994; (*c*) A. Altomare, G. Cascarano, C. Giacovazzo, A. Gualaradi, *J. Appl. Cryst*., 1993, **26**, 343; (*d*) G. M. Sheldrick, SHELXL-97, Program for Crystal Structure Solution and Refinement; University of Göttingen, Göttingen, Germany, 1997; (*e*)

A. L. Spek, *J. Appl. Cryst*., 2003, **36**, 7; (*f*) L. J. Farrugia, WinGX–A Windows Program for Crystal Structure Analysis, *J. Appl. Crystallogr*., 1999, **32**, 837.

16. A. W. Addison, T. N. Rao, J. Reedijk, J. van Rijn and G. C. Verschoor, ***J. Chem. Soc., Dalton Trans***., 1984, 1349.
17. (*a*) T. Afrati, C. Dendrinou-Samara, C. Raptopoulou, A. Terzis, V. Tangoulis and D. P. Kessissoglou, *Dalton Trans*., 2007, 5156; (*b*) T. Moriya, *Phys. Rev. Lett*. 1960, **4**, 228; (*c*) B. Tsukerblat, *Inorg. Chim. Acta* 2008, **361**, 3746; (*d*) X. Liu, M. P. de Miranda, E. J. L. McInnes, C. A. Kilner and M. A. Halcrow, *Dalton, Trans.* 2004, 59.
18. (*a*) T. Afrati, C. Dendrinou-Samara, C. Raptopoulou, A. Terzis, V. Tangoulis, A. Tsipis and D. P. Kessissoglou, *Inorg. Chem*., 2008, **47**, 7545; (*b*) S. Ferrer, F. Lloret, E. Pardo, J. M. Clemente-Juan, M. Liu-González and S. García-Granada, *Inorg. Chem*. 2012, **51**, 984; (*c*) A. Escuer. G. Vlahopoulou, F. Lloret, F.A. Mautner, *Eur. J. Inorg. Chem*. 2014, 83.
19. (*a*) L. Noodleman, *J. Chem. Phys*., 1981, **74**, 5737; (*b*) M. J. Frisch *et al*. GAUSSIAN 03, Revision C.02, Gaussian Inc., Wallingford, CT, 2004.
20. (*a*) M. P. Suh, M.Y. Han, J. H. Lee, K. S. Min and C. Hyeon, *J. Am. Chem. Soc*., 1998, **120**, 3819; (*b*) E. Ruiz, P. Alemany, S. Alvarez and J. Cano, *J. Am. Chem. Soc*., 1997, **119**, 1297; (*c*) D. Venegas–Yazigi, D. Aravena, E. Spodine, E. Ruiz and S. Alvarez, *Coord. Chem. Rev*. 2010, **254**, 2086 and references cited there.
21. R. J. Butcher, C. J. O'Connor and E. Sinn, *Inorg. Chem*., 1981, **20**, 537.
22. M. Angaroni, G. A. Ardizzoia, T. Beringhelli, G. L. Monica, D. Gatteschi, N. Masciocchi and M. Moret, *J. Chem. Soc. Dalton Trans*., 1990, 3305.
23. W. Vreugdenhil, Ph.D. Thesis, Leiden University, The Netherlands, 1987.
24. F. B. Hulsbergen, R. W. M. Hoedt, J. Verschoor, J. Reedijk and A. L. J. Spek, *J. Chem. Soc., Dalton Trans*., 1983, 539.
25. Y. Jiang, H. Kou, R. Wang, A. Cui and J. Ribas, *Inorg. Chem*., 2005, **44**, 709.
26. (*a*) M. A. Palacios, A.J. Mota, J.E. Perea-Buceta, F.J. White, E.K. Brechin and E.Colacio, *Inorg. Chem*. 2010, **49**, 10156; (*b*) R. Boca, *Coord. Chem. Review*, 2004, **248**, 757; (c) R. Boca, *Structure and Bonding*, 2006, **117**, 1.
27. MAGPACK (Magnetic Properties Analysis Package for Spin Clusters) (*a*) employed with a nonlinear least-squares curve fitting program, DSTEPIT (*b*);
(*a*) J.J. Borrás-Almenar, J. Clemente, E. Coronado and B.S. Tsukerblat, *Inorg. Chem*., 1999, **38**, 6081and J.J. Borrás-Almenar, J. Clemente, E. Coronado and B.S.

Tsukerblat, *J. Comput. Chem*., 2001, **22**, 985; (*b*) Program 66, Quantum Chemistry Program Exchange. Indiana University, Bloomington, IN (USA), 1965.

28. *(a)* C. J. Milios, E. Kefalloniti, C. P. Raptopoulou, A. Terzis, A. Escuer, R. Vicente and S. P. Perlepes, *Polyhedron*, 2004, **23**, 83; (*b*) M.-L. Tong, S.-L. Zheng, J.-X. Shi, Y.-X. Tong, H. K. Lee and X.-M. Chen, *J. Chem. Soc*., *Dalton Trans*., 2002, 1727; (*c*) G.S. Papaefstathiou, A. Escuer, C. P. Raptopoulou, A. Terzis, S. P. Perlepes and R.Vicente, *Eur. J. Inorg. Chem.* 2001, 1567.
29. *(a)* L. N. Dawe, K. V. Shuvaev and L. K. Thompson, *Inorg. Chem.*, 2009, **48**, 3323; (*b*) H. Oshio, M. Nihei, A. Yoshida, H. Nojiri, M. Nakano, A. Yamaguchi, Y. Karaki and H. Ishimoto, *Chem. Eur. J.*, 2005, **11**, 843; (*c*) M. Nayak, R. Koner, H.-H. Lin, U. Flo1rke, H.-H. Wei and S. Mohanta, *Inorg. Chem*., 2006, **45**, 10764.

Chapter 3

New Cu(II)-azido Coordination Compounds and Their Magnetic Properties

Abstract

This chapter describes syntheses, single-crystal structure and magnetic studies of six Cu(II)-azide compounds with different types of coligands; N,N′–dimethylethylenediamine (Me_2en) and imidazole/substituted imidazole ligands. The compounds, $[Cu(\mu_{1,1}–N_3)(N_3)(Me_2en)]_2$ **(1)**, **[**$Cu_3(\mu_{1,1,1}–N_3)_2(\mu_{1,1,3}–N_3)(\mu_{1,1}–N_3)_2(\mu_{1,3}–N_3)(Me_2en)]_n$ **(2),** $[Cu_2(\mu_{1,1}\text{-}N_3)_2(EtimiH)_4(ClO_4)_2]$ (**3**) (EtimiH = 2-ethylimidazole), $[Cu_2(\mu\text{-}Meimi^-)(MeimiH)_2(\mu_{1,1}\text{-}N_3)_2(\mu_{1,3}\text{-}N_3)]_n$ (**4**) (MeimiH = 2-methylimidazole), $[Cu_2(\mu\text{-}imi^-)(imiH)_2(\mu_{1,1}\text{-}N_3)_2(\mu_{1,3}\text{-}N_3)]_n$ (**5**) and $[\{Cu_2(\mu_{1,1}–N_3)_2(\mu_{1,3}–N_3)(\mu\text{-}imi^-)(imiH)_3\}.H_2O]_n$ (**6**) (imiH = imidazole) are synthesized by the self-assembly of Cu(II) ion, azide ion and the corresponding coligand. The dinuclear compounds **1** and **3** are formed by doubly asymmetric $\mu_{1,1}–N_3$ bridging ligand. Compound **2** contains hexanuclear secondary building units where the Cu(II) centers are connected to each other by $\mu_{1,1,1}$, $\mu_{1,1}$ and $\mu_{1,1,3}$ bridging azide ligands. Compound **4** and **5** contain 1D chain with alternate $\mu_{1,1}\text{-}N_3$ and $\mu\text{-}Meimi^-$ bridging and the chains are further connected through $\mu_{1,3}\text{-}N_3$ bridge resulting in the formation of 2D networks. 2D network of compound **6** consists of zigzag 1D coordination chain having $\mu_{1,1}\text{-}N_3$, $\mu\text{-}imi^-$ and $\mu_{1,3}\text{-}N_3$ bridging ligands and the chains are bridged together through $\mu_{1,3}\text{-}N_3$ group. Temperature dependent magnetic measurements show diverse magnetic properties of **1-6**, which have been correlated to the structures resulted by the different bridging modes of azide supported by the coligands.

Papers based on this study:

A. Chakraborty, S. R. Lingampalli, A. K. Manna, S. K. Pati, J. Ribas, T. K. Maji, *Dalton Trans*., 2013, **42**, 10707.

A. Chakraborty, S. R. Lingampalli, A. Kumari, J. Ribas, T. K. Maji, *Inorg. Chem*., 2014, **53**, 11991.

3.1 INTRODUCTION

Discrete polynuclear clusters and extended networks of coordination polymers containing paramagnetic metal ions have been a fascinating research topic to the inorganic chemists in the recent past. Their studies are highly motivated due to the structural novelty as well as the potential applications in the field of molecular magnetism.[1] The magnetic exchange in these materials is mediated via suitable bridging ligands and various factors like appropriate bridging modes, strict and accidental orthogonality of magnetic orbitals,[2] spin polarization,[3] delocalization of unpaired electrons[3c] etc. influence the type of magnetic coupling between the paramagnetic centers. Pseudohalogens are found to be versatile and efficient bridging ligands to construct molecular magnets.[4a] Among them, azide ion has been extensively studied and still is in the current focus due to its excellent ability to propagate different kinds of magnetic properties. In particular, a rich diversity of structures is possible with copper coordination compounds as Cu(II) can adopt different kinds of geometries with the different binding modes of azide.[4-7] Synthesis of such structurally diverse compounds having different topologies and dimensionalities using same set of metal-ligand system would be highly demanding, as it can provide better insight into the observed properties through proper structure-property relationship. With the motivation of synthesis and study of such compounds, in this chapter different types of coligands were exploited in Cu(II)-azide chemistry; N,N′–dimethylethylenediamine (Me_2en) and imidazole/substituted imidazole.

Literature reports show that it is possible to control dimensionality of the Cu-azide compounds by changing coligand stoichiometry,[7] as decrease of coligand concentration provides more available coordination sites for azide leading to the formation of higher dimensional structure. Similar synthetic strategy has been employed here in this chapter using Me_2en ligand to envisage the diverse binding modes of azide (Scheme 1, 2) in two new compounds having different dimensionality. On the other hand, we have also explored the use of imidazole or similar substituted imidazole ligand as a second linker in Cu-azide chemistry (Scheme 2). The imidazolate (imi^-) ion, the deprotonated form of imidazole (imiH), is an efficient heterocyclic bridging ligand which provides a three-atom magnetic pathway between the paramagnetic metal centers.[8] Being able to provide a stronger three-atom bridge in an aromatic heterocyle, the magnetic interaction would be much stronger than many other longer bridging ligands like 4,4′-bipyridine.[5a]

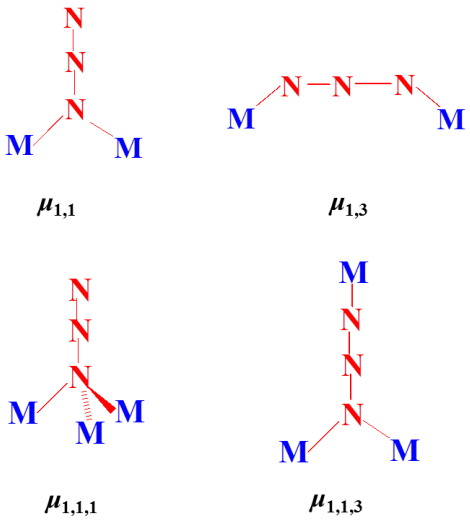

Scheme 1. The observed binding modes for azide ligand in **1** and **2**.

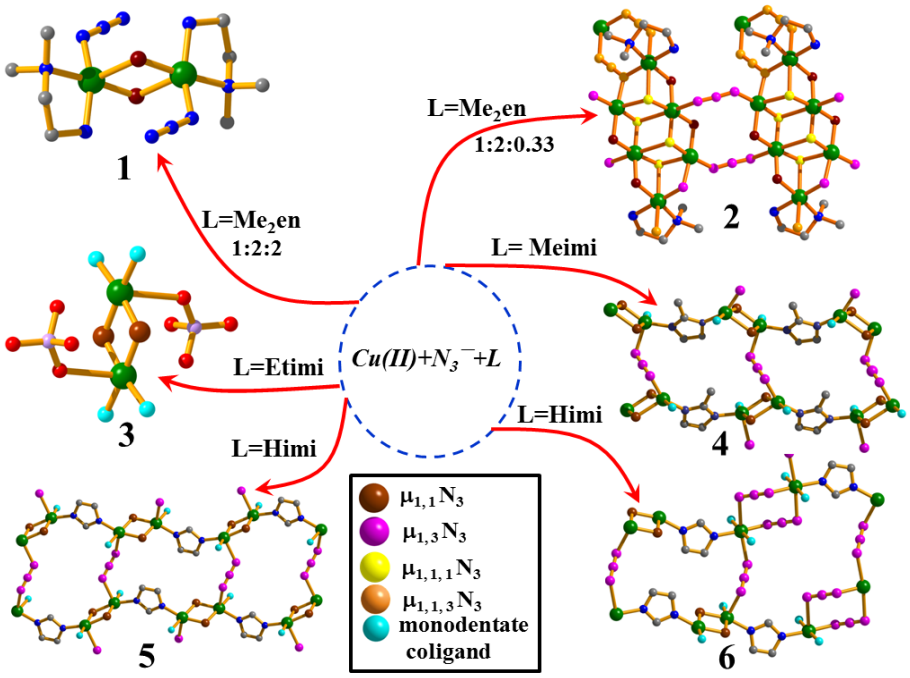

Scheme 2. Formation of versatile Cu-azide coordination compounds (**1-6**) by changing different types of coligands (with or without bridging capability) and their stoichiometry. Color code: Cu: green, C: grey, N: blue, Cl: yellow, O: red.

It will be further interesting to synthesize different compounds by changing the substitution (for e.g., $-CH_3$, $-CH_2CH_3$ etc.) on imidazole ring and study the structural and magnetic diversity. In this chapter, synthesis, structural characterization and magnetic studies of six new coordination compounds; $[Cu(\mu_{1,1}\text{–}N_3)(N_3)(Me_2en)]_2$ **(1)**, **[**$Cu_3(\mu_{1,1,1}\text{–}N_3)_2(\mu_{1,1,3}\text{–}N_3)(\mu_{1,1}\text{–}N_3)_2(\mu_{1,3}\text{–}N_3)(Me_2en)]_n$ **(2),** $[Cu_2(\mu_{1,1}\text{-}N_3)_2(EtimiH)_4(ClO_4)_2]$ **(3)** (EtimiH = 2-ethylimidazole), $[Cu_2(\mu\text{-}Meimi^-)(MeimiH)_2(\mu_{1,1}\text{-}N_3)_2(\mu_{1,3}\text{-}N_3)]_n$ **(4)** (MeimiH = 2-methylimidazole, μ-Meimi$^-$ is the bridging mononegative anion of 2-

methylimidizole), $[Cu_2(\mu\text{-imi}^-)(imiH)_2(\mu_{1,1}\text{-}N_3)_2(\mu_{1,3}\text{-}N_3)]_n$ (**5**) and $[\{Cu_2(\mu_{1,1}\text{–}N_3)_2(\mu_{1,3}\text{–}N_3)(\mu\text{-imi}^-)(imiH)_3\}.H_2O]_n$ (**6**) (imiH = imidazole and μ-imi$^-$ = bridging mononegative anion of imidazole) are presented. It should be noted that judicious choice of the ligands and variation in the molar ratio of different starting compounds steered diverse binding modes and interesting structural features in compounds **1**-**6**.

3.2 EXPERIMENTAL SECTION

3.2.1 Materials

All the reagents and solvents employed are commercially available and used as supplied without further purification. $Cu(OAc)_2{\cdot}H_2O$, $Cu(ClO_4)_2{\cdot}6H_2O$, sodium azide (NaN_3), N,N′-dimethylethylenediamine (Me_2en), imidazole, 2-methylimidazole and 2-ethylimidazole are obtained from the Aldrich chemical Co.

3.2.2 Synthesis

$[Cu(\mu_{1,1}\text{-}N_3)(N_3)(Me_2en)]_2$ (1): $Cu(OAc)_2{\cdot}H_2O$ (1 mmol, 0.199 g) was dissolved in 10 mL water and 2 mmol of Me_2en was dropwise added to the above metal solution. The resulting blue coloured solution was stirred for ten minutes. Then aqueous solution (10 mL) of NaN_3 (2 mmol, 0.13 g) was dropwise added to the above reaction mixture. The resulting green coloured solution was stirred for one hour and filtered. The filtrate was kept for slow evaporation at room temperature and after one weak green crystals were isolated. Yield, 52%, relative to Cu. Selected IR data (KBr, cm^{-1}) 3316 m, 3256 m, 2054 s, 2032 s, 1385 m, 1053 m, 783 m (Figure 1). Anal. calcd. for $C_8H_{24}Cu_2N_{16}$: C, 20.38; H, 5.13; N,47.53. Found: C, 20.49; H, 5.42; N, 47.98%. The phase purity is checked by comparing the PXRD pattern of the bulk powder sample with the simulated data from single-crystal (Figure 2).

$[Cu_3(\mu_{1,1,1}\text{-}N_3)_2(\mu_{1,1,3}\text{-}N_3)(\mu_{1,1}\text{-}N_3)_2(\mu_{1,3}\text{-}N_3)(Me_2en)]_n$ (2): An aqueous solution (20 mL) of NaN_3 (2 mmol, 0.13 g) was mixed with 0.33 mmol (54.6 µL) of Me_2en and the resulting blue solution was stirred for 20 min. to mix well. $Cu(ClO_4)_2{\cdot}6H_2O$ (1 mmol, 0.370 g) was dissolved in 10 mL methanol and 2.5 mL of this metal solution was slowly layered with the above mixed ligand solution using 1 mL buffer (1:1 of water and MeOH) solution in a crystal tube, which was sealed and left undisturbed at room temperature. Slow diffusion yielded green block crystals of **2** after 20 days. Compound purity was verified by PXRD (Figure 3) and elemental analysis result. Yield 51%, relative to Cu(II).

Selected IR data (KBr, cm^{-1}) 3314 m, 3268 m, 2096 s, 2062 sh, 1466 m, 1278 m (Figure 1). Anal. calcd. for $C_4H_{12}Cu_3N_{20}$: C, 9.05; H, 2.28; N,52.76. Found: C, 9.08; H, 2.31; N, 52.68%.

$[Cu_2(\mu_{1,1}\text{-}N_3)_2(EtimiH)_4(ClO_4)_2]$ (3): $Cu(ClO_4)_2{\cdot}6H_2O$ (0.5 mmol, 0.185 g) was dissolved in 10 mL water. 1 mmol (0.048 g) of 2-ethylimidazole was dissolved in 5 mL methanol and was dropwise added to the above metal solution. The resulting blue coloured solution was stirred for ten minutes. Then aqueous solution (5 mL) of NaN_3 (0.5 mmol, 0.0325 g) was dropwise added to the above reaction mixture. The resulting green coloured solution was stirred for one hour and filtered. The filtrate was kept for slow evaporation at room temperature and after one week green crystals were isolated. Yield, 62%, relative to Cu. Selected IR data (KBr, cm^{-1}); 3355 br, 3155 m, 3137 m, 2976 m, 2938 m, 2090 s, 1563 m, 1462 m, 1322 m, 1080 s, 780 m, 713m, 622 m (Figure 1). Anal. calcd. for $C_{20}H_{32}Cu_2N_{14}O_8Cl_2$: C, 30.23; H, 4.06; N, 24.68. Found: C, 30.18; H, 4.12; N, 25.18%. The phase purity was checked by comparing the PXRD pattern of the bulk powder sample with the simulated data from single-crystal (Figure 4).

$[Cu_2(\mu\text{-}Meimi^-)(MeimiH)_2(\mu_{1,1}\text{-}N_3)_2(\mu_{1,3}\text{-}N_3)]_n$ (4): An aqueous solution (10 mL) of $Cu(OAc)_2{\cdot}H_2O$ (0.5 mmol, 0.099 g) was stirred with a methanolic solution (10 mL) of 2-methylimidazole (0.75 mmol, 0.0615 g) to mix well. To this resulting blue solution, aqueous solution (5 mL) of NaN_3 (0.75 mmol, 0.0487 g) was dropwise added to result green coloured turbid solution. The resulting solution was stirred for one hour and filtered. The filtrate was kept for slow evaporation at room temperature and after two weeks block shaped green crystals were isolated. Yield, 51%, relative to Cu. Selected IR data (KBr, cm^{-1}); 3438 br, 2976 m, 2060 s, 1616 m, 1571 m, 1408 m, 1310 m, 1275 m, 1153 m, 762 s, 665 m, 426 m (Figure 1). Anal. calcd. for $C_{12}H_{15}Cu_2N_{15}$: C, 29.03; H, 3.05; N, 42.32. Found: C, 28.98; H, 3.12; N, 42.25%. The phase purity was confirmed from the well correspondence of the PXRD pattern of the bulk powder sample with the simulated data from single-crystal (Figure 5).

$[Cu_2(\mu\text{-}imi^-)(imiH)_2(\mu_{1,1}\text{-}N_3)_2(\mu_{1,3}\text{-}N_3)]_n$ (5): Similar methodology as for **4** was adopted to synthesize compound **5** except that 2-methylimidazole was replaced by imidazole (0.75 mmol, 0.051 g). Green colour block shaped crystals of **5** were isolated after 15 days. Yield 69%, relative to Cu(II). Selected IR data (KBr, cm^{-1}); 3137 br, 2045 s, 1542 m, 1481 m, 1460 m, 1433 m, 1330 m, 1280 s, 1257 m, 1070 s, 950 m, 855 m, 770 m, 658 m (Figure 1). Anal. calcd. for $C_9H_{11}Cu_2N_{15}$: C, 29.69; H, 2.43; N, 46.04. Found: C, 24.57;

H, 2.38; N, 46.68%. The phase purity was checked by comparing the PXRD pattern of the bulk powder sample with the simulated data from single-crystal (Figure 6).

$[\{Cu_2(\mu_{1,1}–N_3)_2(\mu_{1,3}–N_3)(\mu\text{-}imi^-)(imiH)_3\}.H_2O]_n$ (6): $Cu(OAc)_2{\cdot}H_2O$ (0.75 mmol, 0.149 g) was dissolved in 10 mL water, 5 mL methanol and 5 mL acetonitrile. Then 2 mmol of imidazole (0.136 g) was added to the metal solution which results a dark blue coloured solution. After 5 minutes, 2 mmol (0.130 g) of sodium azide was added dropwise and the solution turned dark green. The resulting green solution was stirred for one hour and filtered. The filtrate was kept for slow evaporation at room temperature and after seven days, dark green coloured block shaped crystals appeared. The crystals were isolated. Yield 74%, relative to Cu(II). Selected IR data (KBr, cm^{-1}); 3130 br, 2949 m, 2045 s, 1541 m, 1491 m, 1322 m, 1135 m, 1064 s, 775 s, 652 s, 619 m (Figure 1). Anal. calcd. for $C_{12}H_{17}Cu_2N_{17}$: C, 27.38; H, 3.26; N, 45.23. Found: C, 27.24; H, 3.15; N, 45.72%. The phase purity was checked by comparing the PXRD pattern of the bulk powder sample with the simulated data from single-crystal (Figure 7).

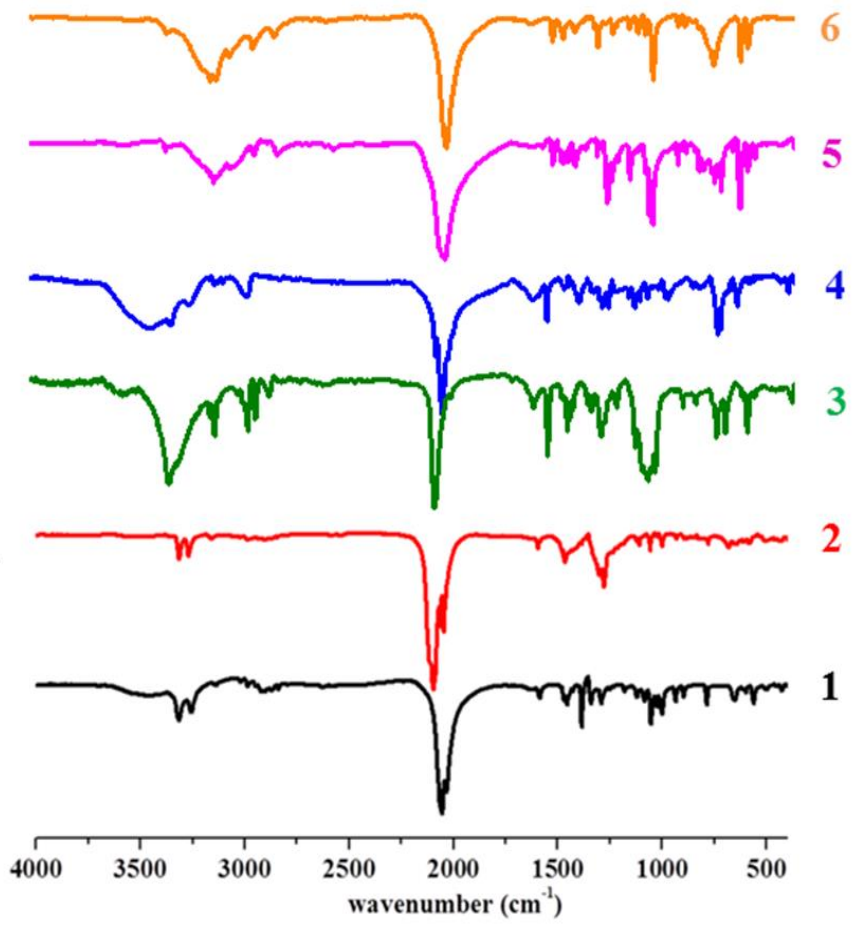

Figure 1. IR spectra of compounds **1-6**.

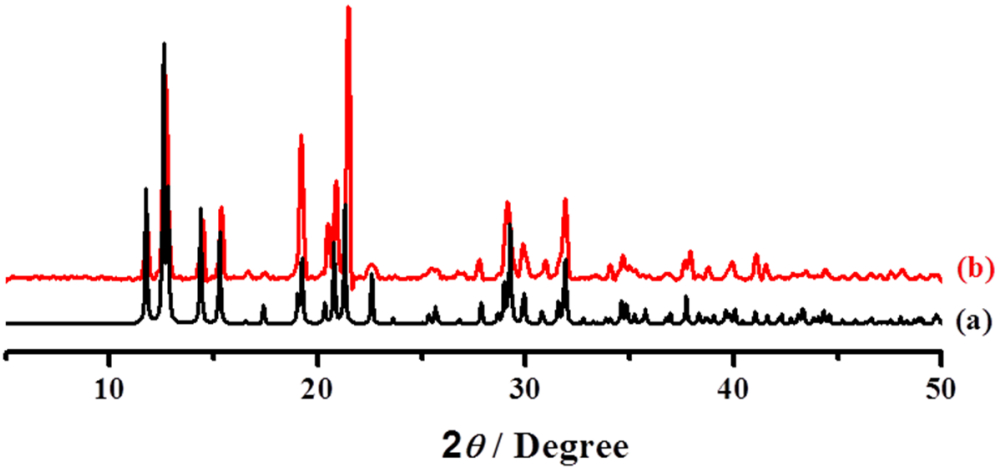

Figure 2. PXRD patterns of compound **1**: (a) simulated; (b) bulk as-synthesized. Similarity in simulated and as-synthesized pattern indicates high purity of the compound.

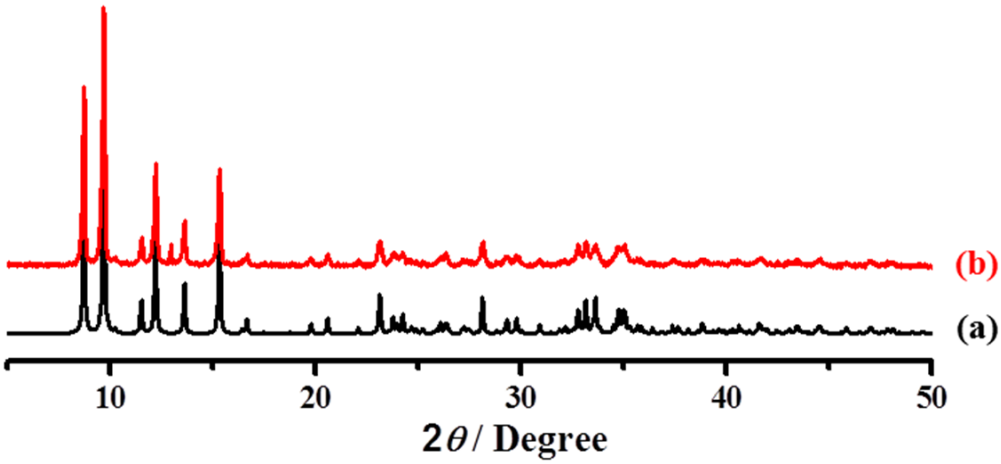

Figure 3. PXRD patterns of compound **2**: (a) simulated; (b) bulk as-synthesized.

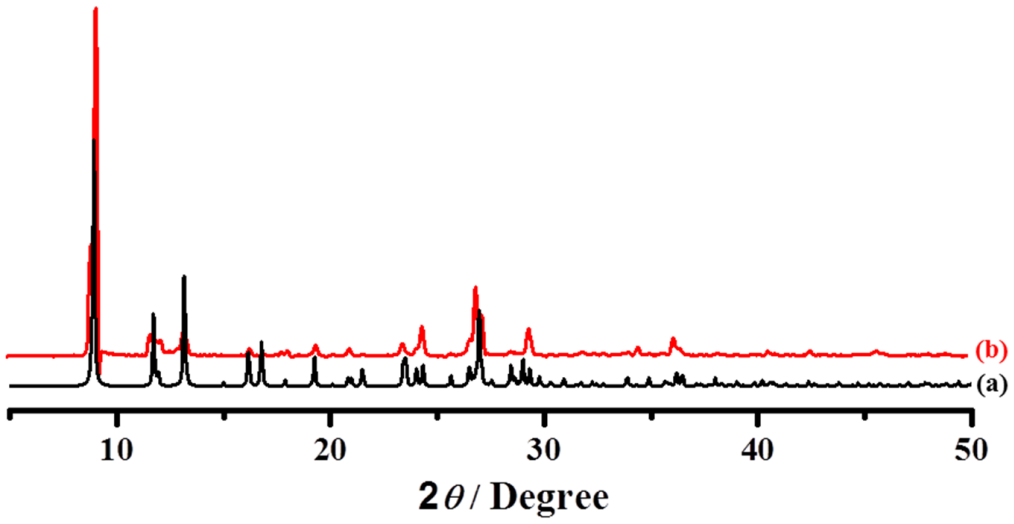

Figure 4. PXRD patterns of compound **3**: (a) simulated; (b) bulk as-synthesized.

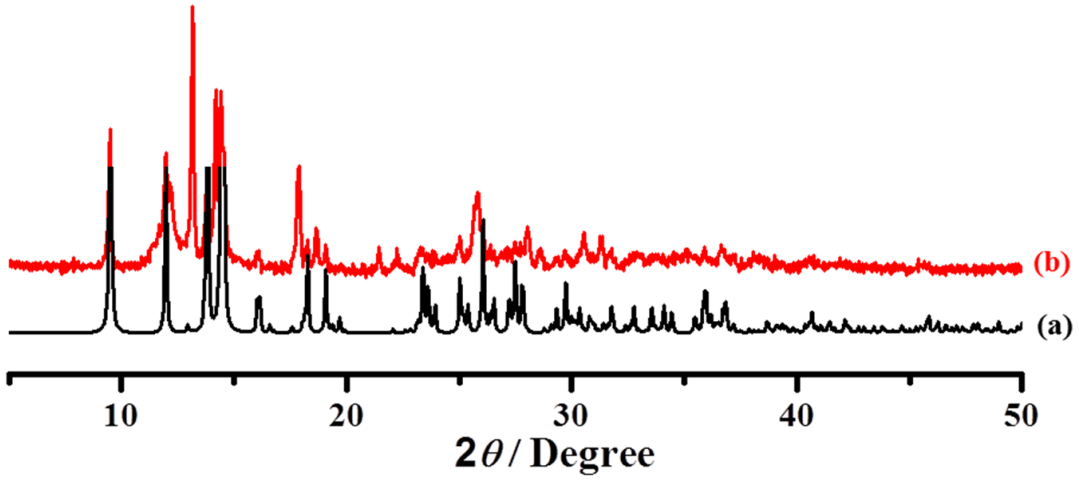

Figure 5. PXRD patterns of compound **4**: (a) simulated; (b) bulk as-synthesized.

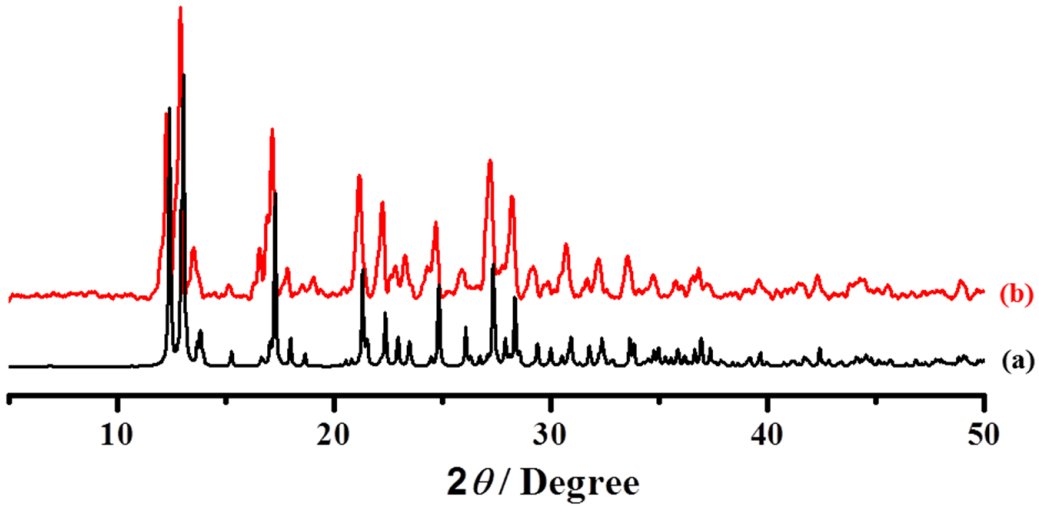

Figure 6. PXRD patterns of compound **5**: (a) simulated; (b) bulk as-synthesized.

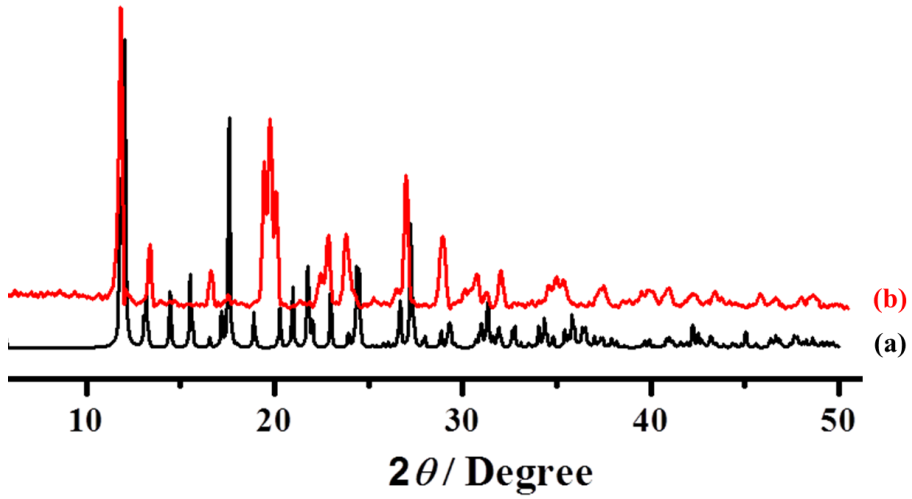

Figure 7. PXRD patterns of compound **6**: (a) simulated; (b) bulk as-synthesized.

3.2.3 Single-crystal X-ray Diffraction

X-ray single-crystal structural data of **1-6** were collected on a Bruker Smart-CCD diffractometer equipped with a normal focus, 2.4 kW sealed tube X-ray source with graphite monochromated Mo–Kα radiation (λ = 0.71073 Å) operating at 50 kV and 30 mA. The program SAINT[9a] was used for integration of diffraction profiles and absorption correction was made with SADABS[9b] program. All the structures were solved by SIR 92[9c] and refined by full matrix least square method using SHELXL-97.[9d] All the non hydrogen atoms were refined anisotropically and all the hydrogen atoms are fixed by HFIX and placed in ideal positions. All calculations were carried out using SHELXL 97, PLATON[9e] and WinGX system, Ver 1.70.01[9f]. Important crystallographic and structure refinement data are summarized in Table 1. Selected bond lengths and angles are displayed in Tables 2-7.

3.2.4 Physical Measurements

Elemental analyses were carried out on a Perkin Elmer 2400 CHN analyzer. IR spectra were recorded in KBr pellets on a Bruker IFS 66v/S spectrophotometer in the region of 4000 – 400 cm^{-1}. Powder X-ray diffraction (PXRD) patterns were recorded on a Bruker D8 Discover instrument using Cu–Kα radiation. The magnetic measurements for polycrystalline powder sample of **1**-**6** were carried out using Vibrating Sample Magnetometer (VSM) in physical property measurement system (PPMS, Quantum Design, USA). Susceptibility data were collected under an external applied magnetic field of 500 Oe.

3.2.5 Computational details:

All the spin-unrestricted DFT calculations were performed using Gaussian03[10] program suits employing hybrid B3LYP[11] exchange and correlation functional and 6-31+g(d,p) basis set for all atoms except for Cu for which an effective core potential with LANL2DZ basis set[12] was used. In previous studies, the usage of B3LYP functional has been proved to give reliable results in predicting the magneto-structural interactions in transition metal complexes.[13a] The magnetic exchange coupling constant (*J*) for the azide-bridged binuclear complex was calculated by making use of the simple 1D Heisenberg Hamiltonian for the interaction of two spins[14] and was estimated as the energy difference (E) between the high spin (HS) and low spin (LS) broken symmetry[15] singlet state using

the following expression: $J = 2\Delta E/S(S+1)$ where S corresponds to the z-component of the total spin (S_z^t) for the HS state.

3.3 RESULTS AND DISCUSSION

3.3.1 Crystal Structure Description

3.3.1.1 Structural description of $[Cu(\mu_{1,1}\text{-}N_3)(N_3)(Me_2en)]_2$ (1)

Compound **1** crystallizes in the monoclinic $P2_1/n$ space group. Single-crystal X-ray structure determination reveals that **1** is a dinuclear complex formed by doubly $\mu_{1,1}$–N_3 bridging ligand. Each Cu(II) locates itself in a distorted square pyramidal geometry with CuN_5 chromophore (Figure 8). The four coordination sites of Cu(II) in the equatorial plane are furnished by N1 and N2 nitrogen atoms from a chelated Me_2en ligand, N6 atom of the monodentate azide and N3 atom of the bridging $\mu_{1,1}$-N_3 ligand. The axial position is occupied by another nitrogen atom (N3_a) of the symmetry related bridging $\mu_{1,1}$-N_3 group, resulting in the formation of doubly $\mu_{1,1}$–N_3 bridged dinuclear complex. Equatorial Cu(II)–N bond distances are in the range of 1.953 (6)–2.048 (5) Å while the axial bond length is 2.356 (6) Å. The Cu1–N3–Cu1_a angle is found to be 101.1(2)° in this complex. The distance between Cu1 and Cu1_a is 3.364 Å. The *cisoid* angles are varying from 78.9(2)° to 100.1 (2)° and the *transoid* angles are 173.6 (2)° and 160.1 (3)° (Table 2) indicating the degree of distortion from ideal square pyramidal geometry. The value of addison parameter (τ)[16] for the Cu(II) center is 0.23. From symmetry point of view, the

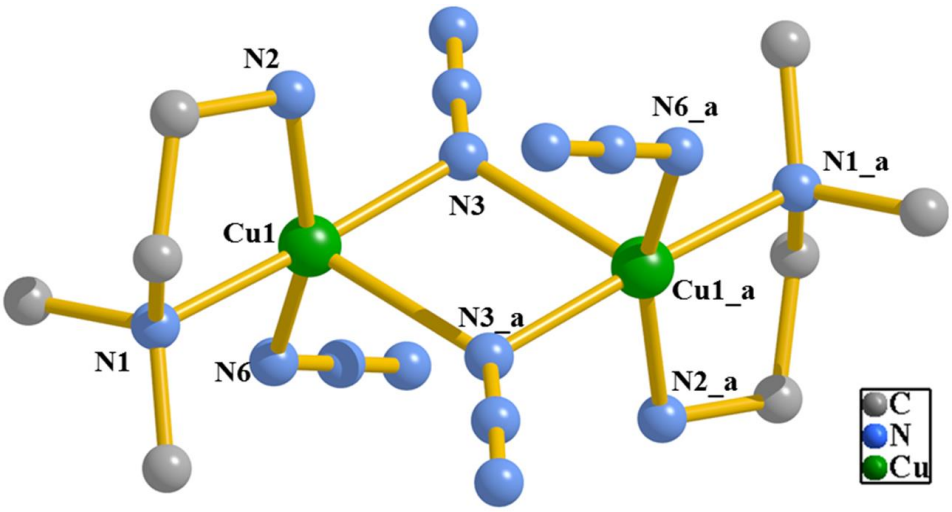

Figure 8. Coordination environment around Cu(II) ions in the dinuclear complex **1**. Symmetry code: a = 1-x, -y, -z.

dimers pack in the lattice with the application of 2_1-screw axis along *b* direction while the two metal centers within the dimer are related by an inversion center.

3.3.1.2 Structural description of $[Cu_3(\mu_{1,1,1}\text{-}N_3)_2(\mu_{1,1,3}\text{-}N_3)(\mu_{1,1}\text{-}N_3)_2(\mu_{1,3}\text{-}N_3)(Me_2en)]_n$ (2)

Compound **2** crystallizes in the triclinic *P*ī space group and the structure determination by single-crystal X-ray diffraction reveals a 2D coordination polymer of Cu(II), construction of which is facilitated by four different types of bridging azide ions. In the asymmetric unit, there are three crystallographically independent Cu(II) centers (Cu1, Cu2 and Cu3) having different coordination environments (Figure 9) and they are connected to each other by $\mu_{1,1,1}$, $\mu_{1,1}$ and $\mu_{1,1,3}$ bridging azide ions (through N7, N10 and N16 nitrogen atoms) forming a trinuclear core. In the trinuclear core, Cu1 is octahedrally coordinated to six different nitrogen atoms (N1, N7, N1_c, N4, N10 and N15_d) from six different azide ions. N1, N4, N10 and N7 are present in the equatorial plane while N1_c and N15_d occupy the axial positions. Cu2 is found in a distorted square pyramidal geometry with coordinations coming from N13, N4, N1, N16 and N7_c atoms of different azide groups ($\mu_{1,3}$, $\mu_{1,1}$, $\mu_{1,1,1}$, $\mu_{1,1,3}$ and $\mu_{1,1,1}$).

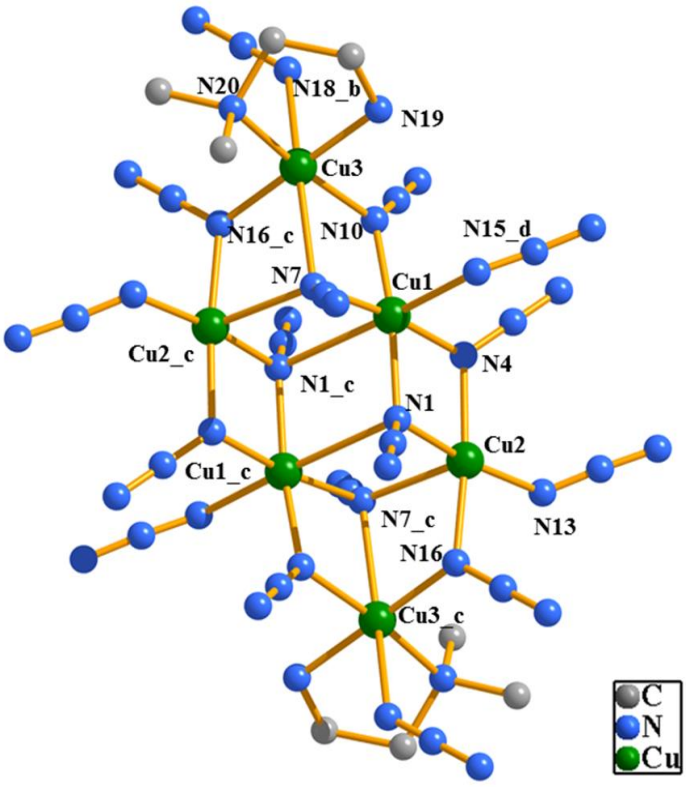

Figure 9. Coordination environment around Cu(II) ions in the hexanuclear core of **2**.

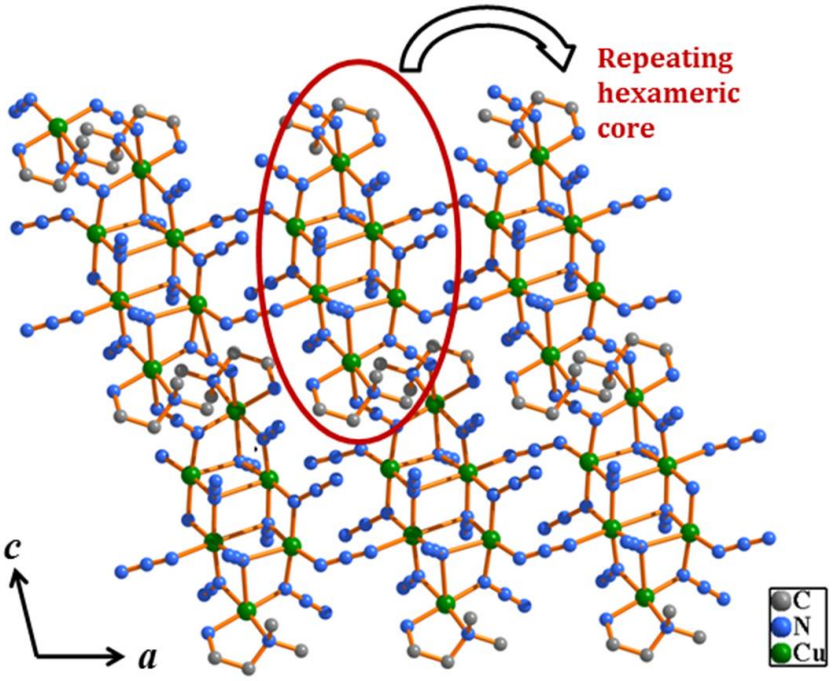

Figure 10. View of the 2D sheet of **2** formed by repeating hexanuclear core lying in the crystallographic *ac* plane.

The value of addison parameter (τ)[16] for the Cu2 center is 0.018. Cu3 adopts a distorted octahedral coordination geometry with coordinations furnished by one chelated Me_2en ligand (through N19, N20 atoms) and three different azide groups having $\mu_{1,1,3}$ and $\mu_{1,1}$ and $\mu_{1,1,1}$ binding modes (N16, N18, N10 and N7). Axial and equatorial coordinations are furnished by N7, N18_b and N19, N20, N10, N16_c nitrogen atoms, respectively. The equatorial and axial Cu(II)–N bond lengths are in the range of 1.937(10)–2.052(9) Å and 2.360(11)–2.670(8) Å, respectively. Selected bond distances and angles for **2** are listed in Table 3. The trinuclear core is linked to its symmetry related counterpart via $\mu_{1,1}$ and $\mu_{1,1,1}$ bridging azide ions (N1 and N4 atoms, respectively) forming a hexanuclear core, which acts as a secondary building block. The hexanuclear building blocks are further connected to each other via $\mu_{1,3}$ and $\mu_{1,1,3}$ azide ions resulting in 2D sheet in the crystallographic *ac* plane (Figure 10).

3.3.1.3 Structural description of $[Cu_2(\mu_{1,1}\text{-}N_3)_2(EtimiH)_4(ClO_4)_2]$ (3)

Single-crystal X-ray diffraction analysis reveals that complex **3** crystallizes in a monoclinic space group $P2_1/n$ and is a dinuclear complex with molecular formula $[Cu_2(\mu_{1,1}\text{-}N_3)_2(EtimiH)_4(ClO_4)_2]$ (Figure 11a). Each of the Cu(II) centers locates itself in a square pyramidal geometry and coordinated to four nitrogen atoms and one oxygen atom. Two of the nitrogen atoms are from 2-ethylimidazole (N4, N6) and two are from azide

ligands (coordinated through N1 and N1_a). Oxygen atom (O2) of the perchlorate anion occupies the apical position, while the remaining three perchlorate oxygen atoms remain uncoordinated. Selected bond lengths and bond angles are given in Table 4. The equatorial bond lengths vary from 1.972 (4) Å to 1.975(4) Å, whereas the apical bond length is 2.639(5) Å. The Cu1–N1–Cu1_a angle through $\mu_{1,1}$-N_3 bridge is found to be 102.4(2)° in this complex. Cisoid angles are in the range from 77.6(2)º to 95.0(1)º and the transoid angles are 170.8(2)º and 171.2(1)º, showing deviation from the ideal square pyramidal structure. The degree of distortion of the coordination polyhedron from square pyramid to trigonal bipyramid can be calculated in terms of the Addison parameter (τ). Addison parameter has been calculated for Cu1, which is 0.007, indicating that geometry around Cu1 is very close to an ideal square pyramidal geometry. The pendant oxygen atom (O2) of the perchlorate anion forms hydrogen bond with the –NH of the 2-ethylimidazole resulting a 2D supramolecular sheet in crystallographic *bc* plane as shown in Figure 11b.

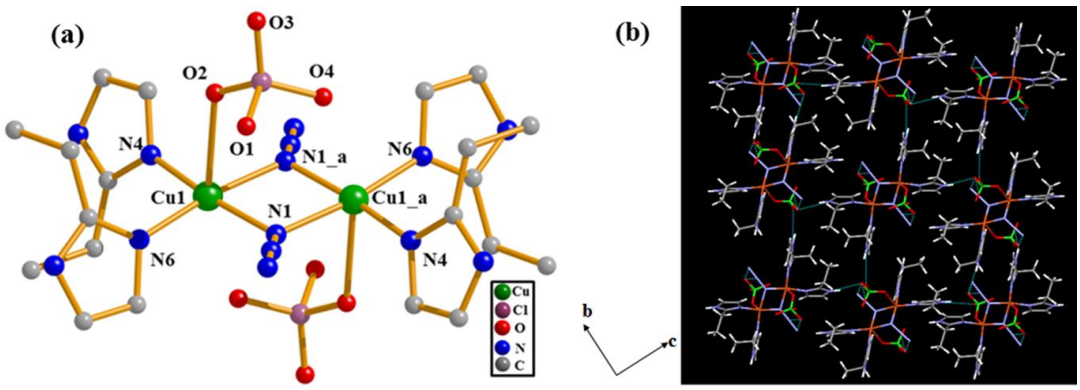

Figure 11. (a) View of the dinuclear complex **3.** Symmetry code: a= 1-x, 1-y, 2-z. (b) 2D H-bonded sheet generated by the (imidazole)N-H…O (ClO_4^-) H-bonding interactions.

3.3.1.4 Structural description of $[Cu_2(\mu\text{-Meimi}^-)(\text{MeimiH})_2(\mu_{1,1}\text{-}N_3)_2(\mu_{1,3}\text{-}N_3)]_n$ (4)

Compound **4** crystallizes in a monoclinic space group $P2_1/c$ and the asymmetric unit consists of two crystallographically independent Cu(II) centers both present in a distorted square pyramidal geometry. For Cu1, equatorial coordination sites are furnished by bridging μ-Meimi$^-$ ligand (N1), one monodentate pendant MeimiH (N3) ligand, bridging $\mu_{1,3}$-azide (N7) and bridging $\mu_{1,1}$-azide ligand (N10) whereas N13 of $\mu_{1,1}$-azide ligand occupies the axial position. Cu2 adopts similar binding modes where N2, N5, N10, N13

and N9 occupy the coordination sites, among which N9 is in the axial position (Figure 12a). Selected bond lengths and bond angles are given in the Table 5. Equatorial Cu-N bond distances are in the range of 1.964(2) Å – 2.037(3) Å and bond distances in the axial positions are 2.290(2) Å and 2.362(3) Å for Cu1 and Cu2, respectively. The Addison parameter for Cu1 and Cu2 are 0.39 and 0.31 respectively, suggesting high distortion of the square pyramid around Cu1 and Cu2. Cisoid angles are in the range from 72.1(1)º to 98.62(1)º and the transoid angles are in the range 148.8(1)º – 172.1(1)º showing deviation from the ideal square pyramidal structure. Cu1 and Cu2 are connected to each other by μ-Meimi$^-$ and asymmetric $(\mu_{1,1}\text{-}N_3)_2$ bridges alternatively resulting into the formation of 1D coordination polymer (Figure 12). The angles Cu1-N13-Cu2 and Cu1-N10-Cu2 are 98.62(1)° and 106.3(1)° respectively, which are important parameters for determining the type and strength of the magnetic exchange. In the 1D chain, distances between Cu1 and Cu2 through $\mu_{1,1}$-azide and μ-Meimi$^-$ bridge are 3.251 Å and 5.965 Å, respectively. Each chain further assembles via $\mu_{1,3}$-azide bridging forming a 2D network lying in the crystallographic *bc* plane and the 2D net can be viewed as an assembly of repeating hexa-

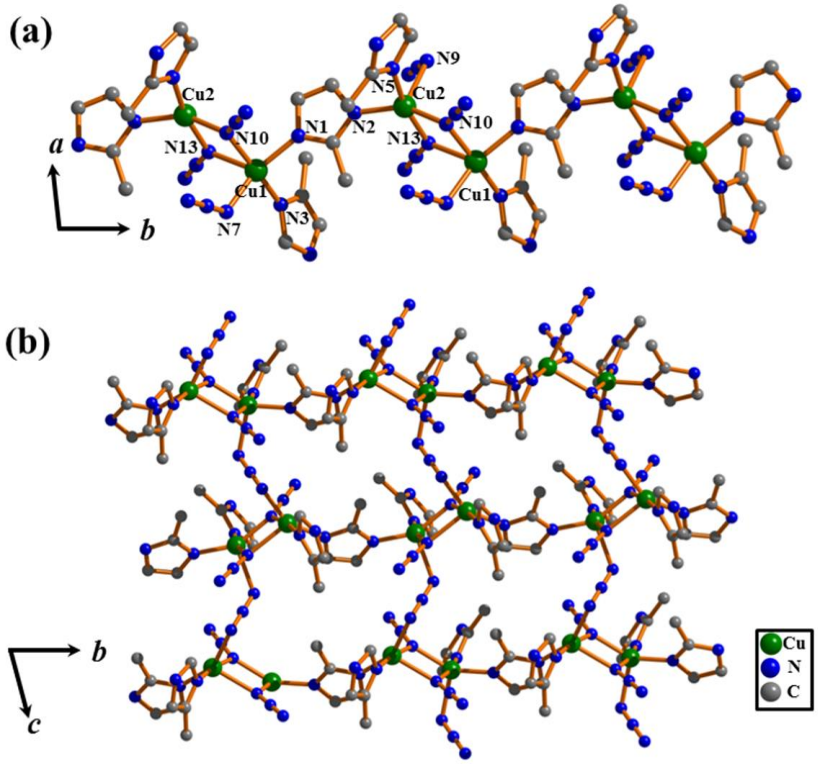

Figure 12. (a) View of the 1D chain of compound **4** with alternate μ-Meimi and $(\mu_{1,1}\text{-}N_3)_2$ bridges. The coordination environments around each Cu(II) ion have also been shown. (b) View of the 2D network of compound **4** constructed by the $\mu_{1,3}$-azide bridging between the 1D chains.

-nuclear units (Figure 12b). Topological analysis of the 2D network using TOPOS 4.0[9e] suggests a 3-connected uninodal net and the simplified 2D net is shown in Figure 13. In the 2D sheet, distance between Cu1 and Cu2 through $\mu_{1,3}$-azide bridging is 5.560 Å.

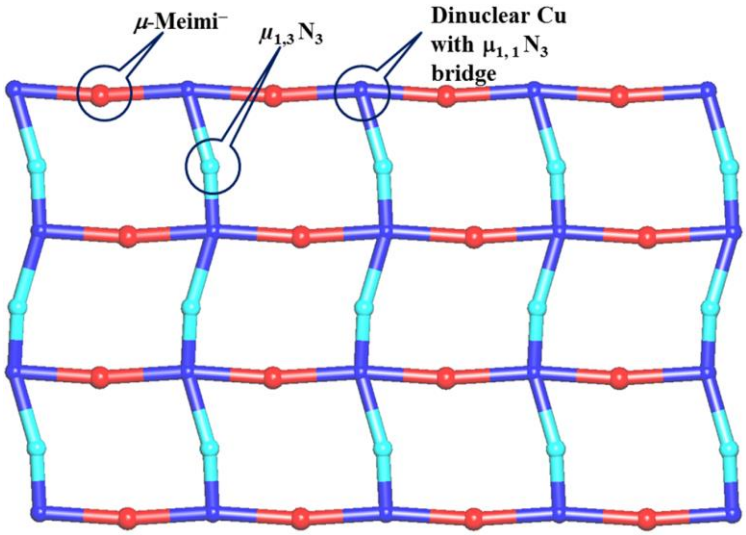

Figure 13. The simplified net of compound **4** (The terminal monodentate ligands are not shown)**.**

3.3.1.5 Structural description of $[Cu_2(\mu\text{-imi}^-)(imiH)_2(\mu_{1,1}\text{-}N_3)_2(\mu_{1,3}\text{-}N_3)]_n$ (5)

Compound **5** crystallizes in a triclinic space group *P*$\bar{1}$. Single crystal X-ray diffraction analysis reveals that **5** is a 2D coordination polymer comprised of 1D coordination chain with alternate imidazole and $\mu_{1,1}$-azide bridging, similar to compound **4**. In compound **5**, there are two crystallographically independent Cu(II) centers in the asymmetric unit, both adopting distorted square pyramidal geometry (Figure 14). For Cu1, equatorial coordination sites are occupied by bridging μ-imi$^-$ ligand (N9), one monodentate imiH (N7) ligand and bridging $\mu_{1,1}$-azide ligand (N1 and its symmetry related counterpart N1_a) whereas N4 of $\mu_{1,3}$-azide ligand occupies the axial position. Similarly Cu2 locates itself in a similar coordination environment as Cu1, where N10, N11, N13, N13_a furnish the equatorial coordination sites while N6 is present at axial position. Equatorial Cu-N bond distances are in the range of 1.972(5) Å – 2.035(6) Å and the axial bond distances are 2.371(8) Å and 2.380(8) Å, for Cu1 and Cu2, respectively. The Addison parameter for Cu1 and Cu2 are 0.06 and 0.10 respectively. Cu1 and its symmetry related counterpart Cu1_a are connected to each other by the symmetrical $(\mu_{1,1}\text{-}N_3)_2$ bridging, through N1 and N1_a atoms. Similarly N13 and N13_a bind Cu2 and its symmetry related counter-

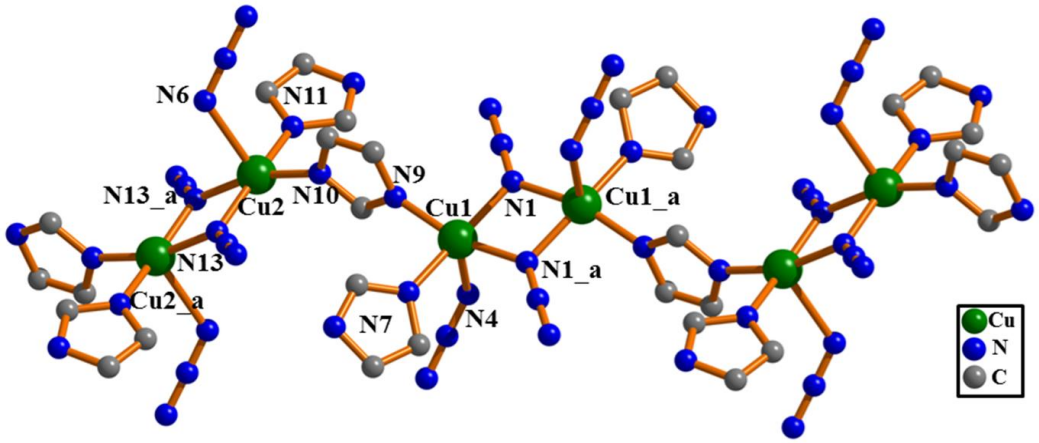

Figure 14. View of the coordination environment around each Cu(II) ion and the 1D chain with alternate μ-imi and $(\mu_{1,1}\text{-}N_3)_2$ bridges in compound **5.** Symmetry code: a = 1-x, 1-y, 1-z.

-part Cu2_a. The angle between Cu1-N1-Cu1_a and Cu2-N13-Cu2_a are 104.0(3)° and 103.5(3)° respectively. The bridging μ-imi$^-$ creates connection between Cu1 and Cu2. The structure can be described as an 1D chain of Cu1 and Cu2 held together by the bridging μ-imi$^-$ and $\mu_{1,1}$-azide ligand alternately (Figure 14). The 1D coordination chain further construct a 2D network via $\mu_{1,3}$-azide bridging through N4 and N6 atoms (Figure 15). The 2D net is composed of two different kinds of hexanuclear building units (Figure 15). In the 2D network, distances between the Cu1 and Cu2 through $\mu_{1,1}$-azide and μ-imi$^-$ bridge are 3.180 Å and 5.981 Å respectively, while distance through $\mu_{1,3}$-azide is 6.183 Å. As it has been previously discussed, both compounds **4** and **5** contain 1D chains with alternate μ-imi$^-$ and $\mu_{1,1}$-azide bridging and the 1D chains are further bridged through $\mu_{1,3}$-azide bridging forming 2D networks. However, there are some distinct differences between the structural aspects of **4** and **5**. First, the degree of distortion of the 5-coordinated Cu(II) centers are different. As evident from the Addison parameters (0.39, 0.31 for **4**; 0.06 and 0.10 for **5**), the Cu(II) centers in **4** are more distorted from ideal square pyramidal geometry than that of **5**. Furthermore, if we consider the hexanuclear building unit in the respective 2D net, **4** contains only one repeating unit while two different units are present in **5** (Figure 12b, 15). The spatial orientations of the μ-Meimi$^-$ or μ-imi$^-$ bridging ligands in the corresponding 2D nets are also different (Scheme 2), which is expected to arise from the variation of the substitution on imidazole ring. The μ-Meimi$^-$ ligand in **4** tries to avoid steric hindrance because of the methyl group and thus could not afford formation of hexanuclear units which are observed in **5**. Indeed, **4** adopts

a more symmetric structure with only one kind of hexanuclear building unit and eventually crystallizes in the more symmetric monoclinic space group $P2_1/c$, while **5** with two different hexanuclear units crystallizes in the triclinic $P\bar{1}$ space group.

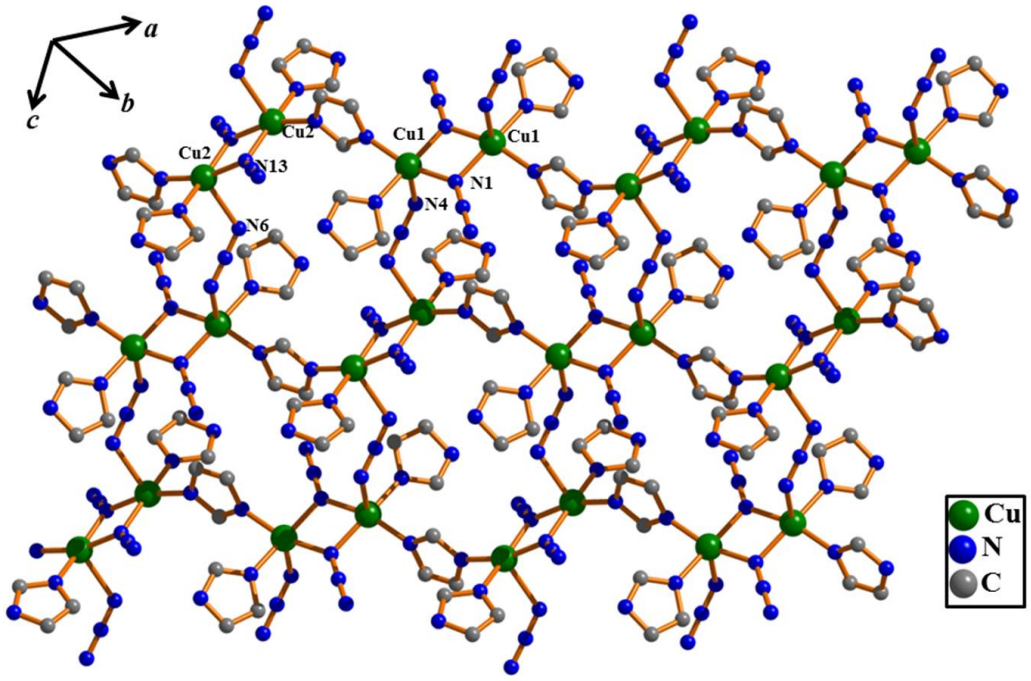

Figure 15. View of the 2D network of compound **5** constructed by the $\mu_{1,3}$-azide bridging between the 1D chains.

3.3.1.6 Structural description of $[\{Cu_2(\mu_{1,1}\text{-}N_3)_2(\mu_{1,3}\text{-}N_3)(\mu\text{-}imi^-)(imiH)_3\}.H_2O]_n$ (6)

Compound **6** crystallizes in triclinic $P\bar{1}$ space group and the structure determination by single-crystal X-ray diffraction reveals a 2D coordination polymer of Cu(II), construction of which is facilitated by different bridging azide ligands along with a bridging imidazole ligand. In the asymmetric unit, there are two crystallographically independent Cu(II) centers (Cu1 and Cu2) having different coordination environments (Figure 16). Cu1 is found in a distorted square pyramidal geometry (4+1). For Cu1 the equatorial plane is occupied by four nitrogen atoms, N1 and N6 of two different imidazole ligands and N8, N8_a nitrogen atoms of the two symmetry related bridging $\mu_{1,1}$-N_3 ligands. The axial position is occupied by N3 nitrogen atom from the bridging azide $\mu_{1,3}$-N_3 ligand. The degree of distortion from the ideal square pyramidal geometry is reflected in the angles of the equatorial plane of the Cu1 atom (Table 7). The equatorial Cu-N bond lengths are in the range of 1.969(3) Å - 2.031(3) Å, while the axial Cu1-N3 distance is 2.323(3) Å. Cu2

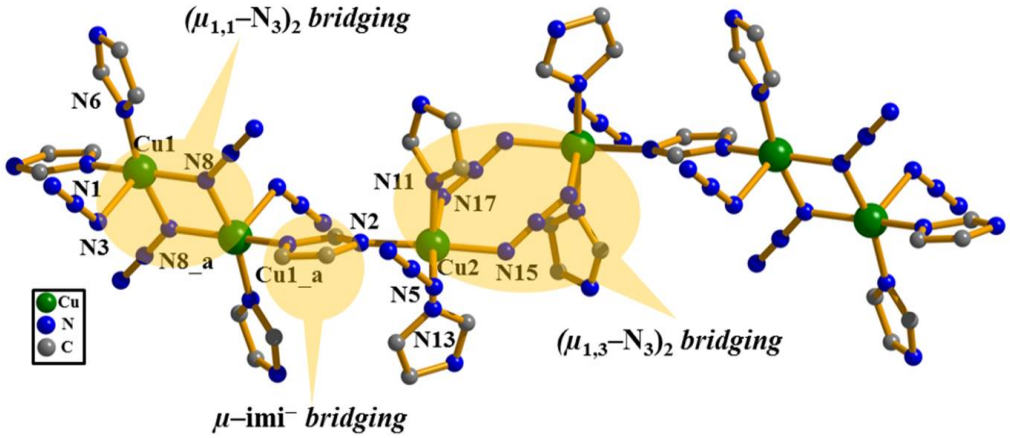

Figure 16. View of the coordination environment around each Cu(II) ion of compound **6.** The different bridging groups have been highlighted. Symmetry code: a = 2-x, -1-y, -z.

is present in a distorted octahedral geometry (4+2) and the equatorial coordination sites are furnished by N2, N11 and N13 nitrogen atoms of the three imidazole ligands and N15 nitrogen atom of the bridging $\mu_{1,3}$-N_3 ligand. The axial positions are occupied by N5 and N17 nitrogen atoms of two different bridging $\mu_{1,3}$-N_3 ligand. The equatorial Cu–N bond lengths are in the range of 1.995(3) Å – 2.019(3) Å, while the axial Cu–N bond lengths are 2.625(4) Å and 2.664(4) Å respectively. The Cu(II) centers form a zigzag one-dimensional coordination chain, formation of which is assisted by consecutive bridging units having $(\mu_{1,1}$-$N_3)_2$- (μ-imi$^-$)-$(\mu_{1,3}$-$N_3)_2$-(μ-imi$^-$) groups (Figure 16, 17). In the 1D coordination chain, Cu1 and its symmetry related counterpart are bridged via symmetric $(\mu_{1,1}$-$N_3)_2$ group, while a symmetric $(\mu_{1,3}$-$N_3)_2$ group bridges Cu2 and its symmetry related counterpart Cu2_a. Finally, Cu1 and Cu2 are bridged by the μ-imi$^-$ group. The distance between Cu1 and Cu1_a through the bridging $\mu_{1,1}$-N_3 ligand is 3.182 Å and the Cu1–N8–

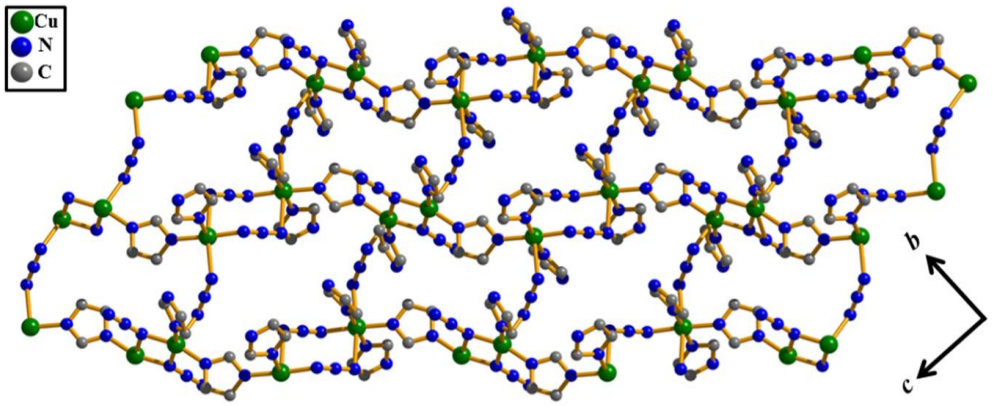

Figure 17. View of the 2D network of **6** lying in the crystallographic *bc* plane.

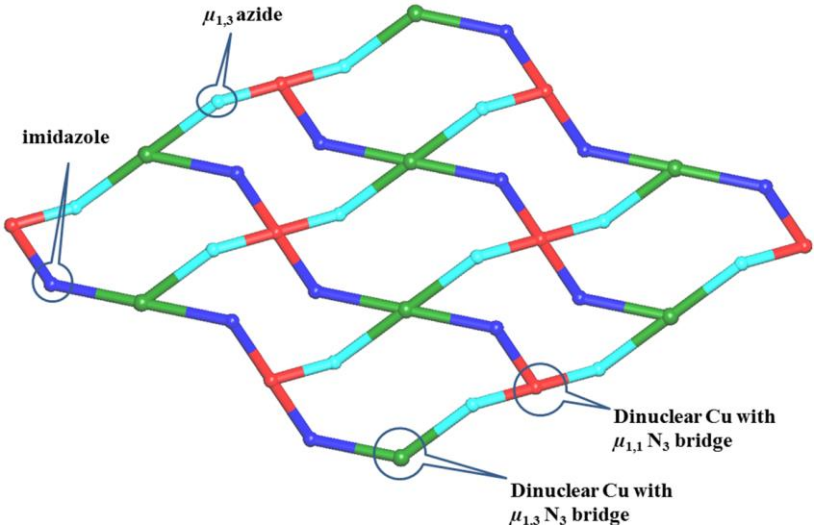

Figure 18. View of the different bridging and simplified net of compound **6** (the terminal monodentate ligands are not shown)**.**

Cu1_a angle is found to be 103.25(2)°. The distance between Cu1 and Cu2 through the bridging μ-imi$^-$ ligand is 5.976 Å. The 1D coordination chains are further connected to each other by the $\mu_{1,3}$ bridging azide group to furnish the 2D network along the crystallographic *bc* plane (Figure 17). The simplified 2D net is shown in Figure 18.The $\mu_{1,3}$ azide group bridges Cu1 of one chain and Cu2 of another chain and the distance between these Cu(II) centers through this $\mu_{1,3}$-N_3 bridging is 6.240 Å.

3.3.1.7 Structural correlation in 3-6

The formation of different Cu(II)-azide compounds (**3-6**) with imidazolate based linkers from the similar reagents is remarkable (Scheme 2). The distinct difference of the compound **3** with respect to the other 2D compounds (**4-6**) in terms of dimensionality should be noted. The reason for the formation of a discrete dinuclear complex **3** is probably due to the larger steric effect of 2-ethylimidazole, which inhibit formation of higher dimensional network. It is noteworthy that attempts were made to synthesize different Cu(II)-EtimiH-azide compounds (other than **3**) by employing several reaction conditions (for e.g., changing the EtimiH: azide concentration, varying solvent etc.), but could not isolate any different single-crystal, which suggests that **3** is probably the most stable structure without any steric crowding. Yu and co-workers have reported a mononuclear Cu(II)-imidazole-azide compound with the formula $Cu(imiH)_4(N_3)_2$, where pendant imidazole and monodentate azide ligands are present.[8e] Our work shows that by using such relatively smaller coligand (imiH and MeimiH), various azide binding modes

and formation of 2D network (in **4-6** see structural descriptions) can be observed. Under similar synthetic reaction condition (stoichiometry Cu(II): MeimiH/imiH: azide = 0.5: 0.75: 0.75), use of MeimiH and imiH resulted **4** and **5** respectively, which are structurally very similar. However, as it has been discussed earlier, as a consequence of the difference in the substitution on the respective imidazole rings, they differ significantly in terms of the spatial orientation of the bridging ligands and the respective 2D nets. By changing the stoichiometry (Cu(II): imiH: azide = 0.75: 2: 2) and employing imidazole as the coligand, compound **6** is furnished which consists even more diverse binding modes of azide ligand than that of **4** and **5**. Thus by varying the reaction condition slightly, higher dimensional networks having various structural motifs could be achieved with a smaller coligand like imidazole. In the effort to furnish such higher dimensional networks, another compound with the formula $[Cu_3(imiH)_4(\mu\text{-}imi^-)_2(N_3)_4]_n$ (**7**) is synthesized by the self-assembly of Cu(II) salt with imiH and azide at room temperature (stoichiometry Cu(II): MeimiH/imiH: azide = 0.75: 1.5: 1). Compound **7** is a 2D compound where linear 1D chains are present with alternating dinuclear units and mononuclear units. There are two different dinuclear units with the formula $[Cu_2(imiH)_2(\mu\text{-}imi^-)_2(\mu_{1,1}\text{-}N_3)_2(\mu_{1,3}\text{-}N_3)_2]^{2-}$ and $[Cu_2(imiH)_2(\mu\text{-}imi^-)_2(\mu_{1,1}\text{-}N_3)_2(N_3)_2]^{2-}$ and a mononuclear unit with the formula $[Cu_2(imiH)_2(\mu\text{-}imi^-)_2(\mu_{1,1}\text{-}N_3)]^-$. Interchain $\mu_{1,3}$-N_3 bridging between the mononuclear unit

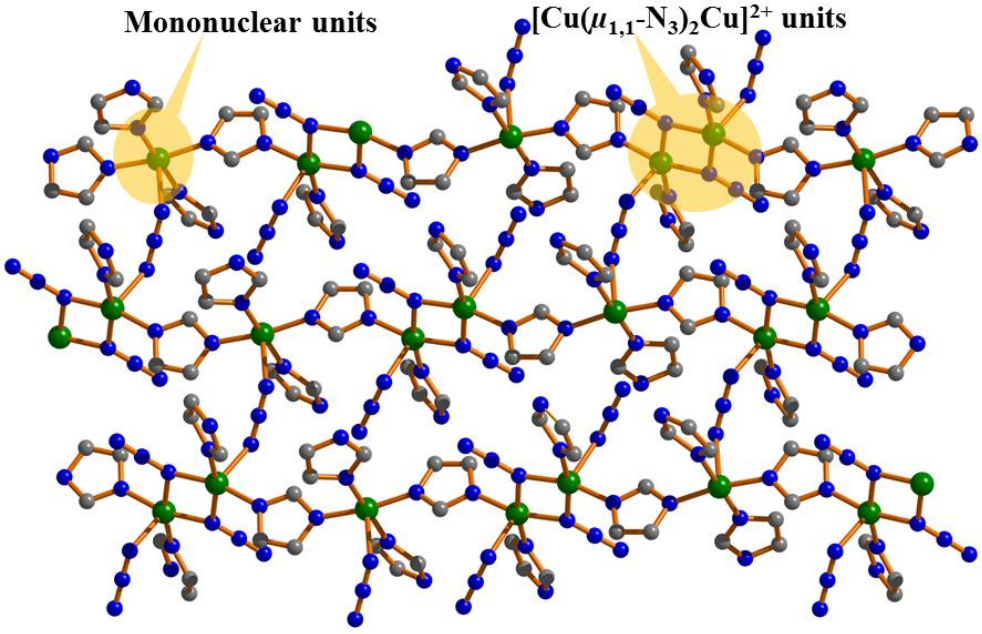

Figure 19. View of the 2D network of compound **7.**

to the nearest neighbouring dinuclear unit of the adjacent chain results a 2D network (Figure 19). Later a literature survey showed that this compound was reported by Nakamura *et al.*[8d] where they observed ferrimagnetic behaviour of the compound. Numerous efforts to isolate methyl imidazole substituted compounds similar to **6** or **7** other than compound **4** were unsuccessful. It is proposed that here steric factor of 2-methyl imidazole plays a role which probably inhibits formation of 2D nets similar to **6** or **7**. Formation of such different compounds by changing the reaction conditions like stoichiometry and substitution on coligand suggests that versatile 2D Cu-azide compounds can indeed be fabricated by the aid imidazole based ligand.

Table 1. Crystallographic data for compounds **1**-**6**.

Parameters	**1**	**2**	**3**	**4**	**5**	**6**
Crystal system	Monoclinic	Triclinic	Monoclinic	Monoclinic	Triclinic	Triclinic
Space group	$P2_1/n$	$P\bar{1}$	$P2_1/n$	$P2_1/c$	$P\bar{1}$	$P\bar{1}$
a (Å)	9.3636(9)	8.5602(2)	7.8665(3)	18.5986(4)	7.6956(3)	7.8482(1)
b (Å)	10.7124(13)	10.6248(3)	14.8088(5)	8.0499(2)	8.7246(4)	8.7740(2)
c (Å)	9.6384(10)	11.4803(5)	13.9124(5)	12.9360(3)	13.1172(6)	15.4669(3)
α (°)	90	103.612(2)	90	90	83.099(3)	90.309(1)
β (°)	104.864(7)	106.749(2)	106.292(2)	90.742(1)	77.457(2)	90.548(1)
γ (°)	90	111.431(1)	90	90	71.479(2)	107.391(1)
V (Å ^{3})	934.44(18)	860.07(5)	1555.62(10)	1936.58(8)	813.91(6)	1016.28(3)
Z	2	2	2	4	2	2
T (K)	298	298	298	298	298	298
D_c (g / cm^3)	1.662	2.043	1.696	1.703	1.862	1.766
F(000)	476	522	812	1000	456	544
Data [$I>2\sigma(I)$]	1010	2460	1855	2968	1948	3230
R^a	0.0539	0.0632	0.0589	0.0294	0.0505	0.0388
$R_w{}^b$	0.1314	0.2116	0.1612	0.0836	0.1468	0.0982
GOF	0.97	1.05	1.01	1.08	1.14	1.13

$^aR = \sum||F_o|-|F_c||/\sum|F_o|$. $^bR_w = [\sum\{w(F_o^2-F_c^2)^2\}/\sum\{w(F_o^2)^2\}]^{1/2}$

Table 2. Selected Bond Distances [Å] and Angles [°] for **1**.

Cu1-N1	2.048(5)	Cu1-N2	2.030(5)
Cu1-N3	1.989(6)	Cu1-N6	1.953(6)
Cu1-N3_a	2.356(6)		
N1-Cu1-N2	84.8(2)	N1-Cu1-N3	173.6(2)
N1-Cu1N6	91.1(2)	N1-Cu1-N3_a	99.9(2)
N2-Cu1-N3	89.3(2)	N2-Cu1-N6	160.1(3)
N2-Cu1-N3_a	99.8(2)	N3-Cu1-N6	95.2(3)
N3-Cu1-N3_a	78.9(2)	N3_a-Cu1-N6	100.1(2)
Cu1-N3-Cu1_a	100.1(2)		

Symmetry code: a = 1−x, −y, −z

Table 3. Selected Bond Distances [Å] and Angles [°] for **2**.

Cu1-N1	2.000(6)	Cu1-N4	2.030(9)
Cu1-N7	2.002(8)	Cu1-N10	1.998(7)
Cu1-N1_c	2.670(8)	Cu1-N15_d	2.360(11)
Cu2-N1	2.007(8)	Cu2-N4	2.016(7)
Cu2-N13	1.937(10)	Cu2-N16	2.034(6)
Cu2-N7_c	2.394(8)	Cu3-N7	2.466(6)
Cu3-N10	2.041(9)	Cu3-N19	2.002(9)
Cu3-N20	2.052(9)	Cu3-N18_b	2.595(8)
Cu3-N16_c	2.018(8)		
N1-Cu1-N4	79.2(3)	N7-Cu3-N18_b	159.4(3)
N1-Cu1-N7	96.2(3)	N7-Cu3-N16_c	79.4(3)
N1-Cu1-N10	168.0(3)	N10-Cu3-N19	87.9(3)
N1-Cu1-N1_c	80.7(3)	N10-Cu3-N20	172.4(4)
N1-Cu1-N15_d	96.0(4)	N10-Cu3-N18_b	89.5(3)
N4-Cu1-N7	173.0(3)	N10-Cu3-N16_c	90.0(3)
N4-Cu-N10	97.2(3)	N19-Cu3-N20	84.8(4)
N1_c-Cu1-N4	92.7(3)	N18_b-Cu3-N19	89.4(3)
N4-Cu1-N15_d	97.8(4)	N16_c-Cu3-N19	176.9(3)
N7-Cu1-N10	86.3(3)	N18_b-Cu3-N20	92.2(3)
N1_c-Cu1-N7	81.3(3)	N16_c-Cu3-N20	97.5(3)
N7-Cu1-N15_d	87.9(4)	N16_c-Cu3-N18_b	88.4(3)
N1_c-Cu1-N10	88.0(3)	Cu1-N1-Cu2	101.3(3)
N10-Cu1-N15_d	95.9(4)	Cu1-N1-N2	127.5(6)
N1_c-Cu1-N15_d	168.2(3)	Cu1-N1-Cu1_c	99.3(3)
N1-Cu2-N4	79.4(3)	Cu2-N1-N2	122.8(6)
N1-Cu2-N13	171.0(4)	Cu1_c-N1-Cu2	90.6(3)
N1-Cu2-N16	92.7(3)	Cu1_c-N1-N2	106.6(6)
N1-Cu2-N7_c	88.6(3)	N1-N2-N3	178.2(11)
N4-Cu2-N13	97.9(4)	Cu1-N4-Cu2	100.0(3)
N4-Cu2-N16	172.1(3)	Cu1-N4-N5	124.6(7)
N4-Cu2-N7_c	98.1(3)	Cu2-N4-N5	126.4(7)
N13-Cu2-N16	90.0(4)	N4-N5-N6	177.9(11)
N7_c-Cu2-N13	100.3(3)	Cu1-N7-Cu3	92.6(3)
N7_c-Cu2-N16	80.8(3)	Cu1-N7-N8	117.5(6)
N7-Cu3-N10	74.1(3)	Cu1-N7-Cu2_c	99.2(3)
N7-Cu3-N19	102.1(3)	Cu3-N7-N8	124.1(6)
N7 -Cu3-N20	105.7(3)	Cu2_c-N7-Cu3	87.5(2)

Symmetry codes: b = x, y, 1+z; c =2−x, 1−y, −z; d = 3−x, 1−y, −z

Table 4. Selected Bond Distances [Å] and Angles [°] for **3**.

Cu1-N1	1.975(4)	Cu1-N4	1.972(4)
Cu1-N6	1.972(4)	Cu1-O2	2.639(5)
N1_a-Cu1-N4	93.7(2)	N1_a-Cu1-N6	171.2(1)
N1-Cu1-N1_a	77.6(2)	N4-Cu1-N6	95.0(1)

N1-Cu1-N4	170.8(2)	N1-Cu1-N6	93.8(2)
Cu1-N1-Cu1_a	102.4(2)		

Symmetry code: a= 1-x, 1-y, 2-z

Table 5. Selected Bond Distances [Å] and Angles [°] for **4**.

Cu1-N1	1.974(2)	Cu1-N3	1.976(2)
Cu1-N7	2.037(3)	Cu1-N10	2.028(2)
Cu1-N13	2.290(2)	Cu2-N2	1.964(2)
Cu2-N5	1.987(2)	Cu2-N13	1.990(3)
Cu2-N10	2.035(2)	Cu2-N9	2.362(3)
N1-Cu1-N3	94.8(1)	N1-Cu1-N7	148.8(1)
N1-Cu1-N10	87.4(1)	N3 -Cu1-N7	92.0(1)
N3 -Cu1-N10	72.1(1)	N7-Cu1-N10	90.10(1)
N2-Cu2 -N5	96.32(1)	N2-Cu2 -N13	96.1(1)
N2-Cu2 -N10	149.3(1)	N5-Cu2 -N13	67.62(1)
N5-Cu2-N10	88.6(1)	N10-Cu2-N13	81.0(1)
N3-Cu1-N10	172.1(1)	N5-Cu2-N13	167.62(1)
Cu1-N10-Cu2	106.3(1)	Cu1-N13-Cu2	98.62(1)

Table 6. Selected Bond Distances [Å] and Angles [°] for **5**.

Cu1-N1	2.016(7)	Cu1-N1_a	2.018(7)
Cu1-N4	2.371(8)	Cu1-N7	1.989(7)
Cu1-N9	1.976(6)	Cu2-N10	1.972(5)
Cu2-N11	1.985(6)	Cu2-N13	2.021(7)
Cu2-N6	2.380(8)	Cu2-N13_a	2.035(6)
N1-Cu1-N4	97.3(3)	N1-Cu1-N7	167.8(3)
N1-Cu1-N9	92.9(3)	N1-Cu1-N1_a	76.0(3)
N7-Cu1-N9	92.2(3)	N1_a-Cu1-N7	96.6(3)
N1_a -Cu1-N9	163.8(2)	N10-Cu2-N11	93.8(3)
N10-Cu2-N13	92.9(3)	N10-Cu2-N13_a	163.8(3)
N11-Cu2-N13_a	95.3(3)	N11-Cu2-N13	170.1(3)
N6 -Cu2-N11	91.3(3)	Cu2-N13-Cu2_a	103.5(3)
Cu1-N1-Cu1_a	104.0 (3)°		

Symmetry code: a = 1-x, 1-y, 1-z

Table 7. Selected Bond Distances [Å] and Angles [°] for **6**.

Cu1-N1	1.969(3)	Cu1-N3	2.323(3)
Cu1-N6	1.983(3)	Cu1-N8_a	2.031(3)
Cu1-N8	2.027(3)	Cu2-N2	1.999(3)
Cu2-N11	1.995(3)	Cu2-N13	1.996(3)
Cu2-N15	2.019(3)	Cu2-N5	2.625(4)
Cu2-N17	2.664(4)		
N1-Cu1-N6	94.0(1)	N1-Cu1-N8_a	91.8(1)

N1-Cu1-N8	163.41(1)	Cu1-N3-N4	118.8(3)
N3-Cu1-N6	96.32(1)	N3-Cu1-N8	93.3(1)
N3-Cu1-N8_a	95.6(1)	N6-Cu1-N8_a	168.7(1)
N6-Cu1-N8	95.30(1)	N8-Cu1-N8_a	76.8(1)
Cu1-N8-Cu1_a	103.3(1)	N2-Cu2-N11	92.0(1)
N2-Cu2-N13	89.4(1)	N2-Cu2-N15	176.0(1)
N2-Cu2-N17_a	90.3(1)	N11-Cu2-N13	178.1(1)
N11-Cu2-N15	92.0(1)	N5-Cu2-N11	87.2(1)
N11-Cu2-N17	88.41(1)	N13-Cu2-N15	86.8(1)
N13-Cu2-N17	90.3(1)	N5-Cu2-N15	85.41(1)

Symmetry code: a = 2-x, -1-y, -z.

3.3.2 Magnetic properties

3.3.2.1 Magnetic properties of Complex 1

The temperature dependence of χ_M and $\chi_M T$ product per Cu2 unit for **1** is shown in Figure 20a. The $\chi_M T$ product at room temperature, 0.82 cm^3 mol^{-1} K, is slightly higher than the spin-only value of 0.75 cm^3 mol^{-1} K expected for two isolated Cu(II) ions (S = ½) assuming g =2.00. As the temperature is lowered, $\chi_M T$ remains almost constant up to 40 K and then decreases to 0.19 cm^3 mol^{-1} K upon cooling to 2 K. Upon cooling, χ_M increases, reaching a maximum value of 0.106 cm^3 mol^{-1} around 3.1 K, and then rapidly decreases with temperature. The magnetic data indicates antiferromagnetic coupling in the dinuclear compound. To estimate the magnitude of the antiferromagnetic coupling, the $\chi_M T$ data (300–2 K) are fitted to the modified Bleaney-Bowers equation for two Cu(II) ions (S = ½) with the Hamiltonian in the form $\hat{H} = -J\hat{S}_1 \hat{S}_2$. The susceptibility equation for such a dimeric system can be written as follows:

$\chi_M = (2N\beta^2g^2/kT)\,[3 + \exp(-J/kT)]^{-1}(1-\rho) + N\beta^2g^2\rho/2kT$ …….. (1) Where N, g,β, k and ρ parameters bear their usual meaning. The best fit parameter shows $J = -4.83$ cm^{-1} with g = 2.12, ρ = 0.02 and $R = 1.039\times10^{-4}$ $\{R = \sum[(\chi_M)^{obs} - (\chi_M)^{calc}]^2/[(\chi_M)^{obs}]^2\}$ (Figure 20a). The values of the coupling constant J indicates the existence of an antiferromagnetic coupling within the dinuclear compound. The *M vs. H* curve at 3 K reaches a maximum value of 0.7Nβ, being markedly below from the expected 2 Nβ (Figure 20b), supporting the antiferromagnetic interactions in **1**. To understand the energetics of magneto-structural interactions, theoretical calculations using first-principles DFT method were carried out. All the calculation details are presented in computational details section.

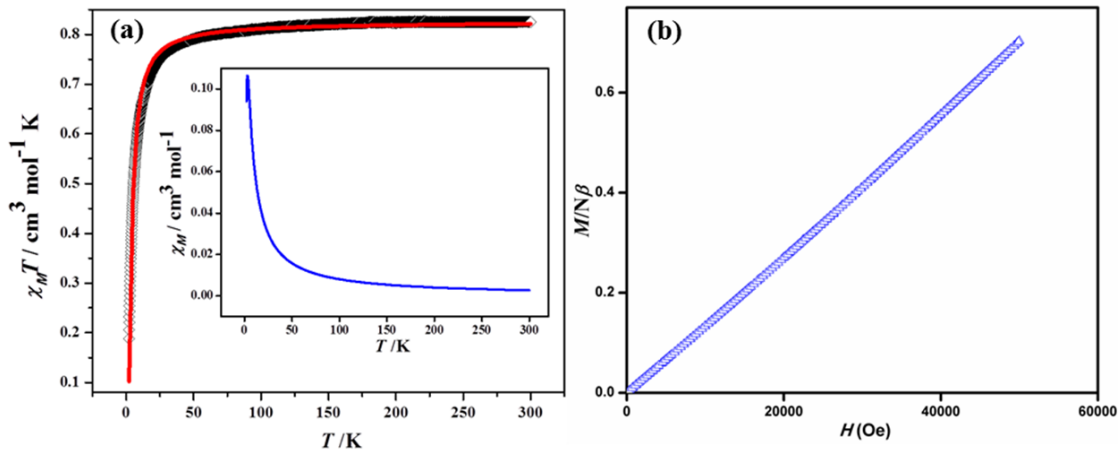

Figure 20. (a) The plots of χ_M *vs. T* and $\chi_M T$ *vs. T* (inset) for **1**. The solid red line indicates the best fit obtained. (b) The M *vs. H* curve for **1** at 3 K.

A dinuclear core for the compound **1** was considered for the calculation and the initial structure modelled from X-ray crystallography was subjected to partial geometry optimization considering only hydrogen position minimization, as X-ray analysis cannot predict the position of hydrogen atoms correctly. Model **A** represents the DFT optimized geometry for the compound **1** (Figure 21). In order to find out the minimum energy magnetic ground state, spin unrestricted DFT calculations are performed considering the two possible spin states. The results show that for the dinuclear model **A**, the LS antiferromagnetic state is more stable than the HS ferromagnetic state with a marginal energy difference and the calculated *J* value is ~3.7 cm^{-1} (Table 8), which corroborates well with the experimental findings. A significant part of the spin density is distributed over the azide bridging ligand, as also can be seen from Figure 21b. Moreover, calculated spin density at the azide bridging ligand shows that the end nitrogen atoms of the two azide groups contribute a significant amount to the overall spin density of the complex. The analysis predicts that the dinuclear complex would show weak antiferromagnetic interaction, which supports the experimental result.

Table 8. Results for the two possible spin states of the model system **A**. (The energy (E) is scaled with respect to the lowest energy magnetic state and the spin density values for all Cu(II) centers are given only for the low energy spin state).

Model	S	E (cm^{-1})	Spin density (e)
A (For compound **1**)	0	0.00	Cu1 (0.48) Cu2 (-0.48)
	1	3.66	

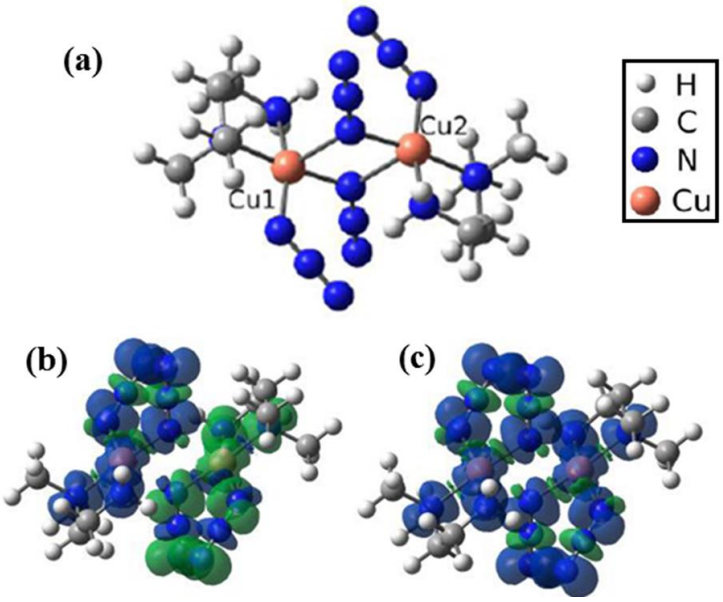

Figure 21. (a) The geometry optimized model structure **A** for binuclear compound **1**. (b) Spin density plot of the S = 0 state and (c) the S = 1 state of model **A**. All the magnetic centers are labelled as Cu1 and Cu2.

An insight into the structure reveals that N3 atom of the azide ligand connecting two Cu(II) centers through an end-on bridge belongs to the equatorial plane of Cu1 but occupies axial position of square pyramidal coordination geometry of Cu1_a. In the dinuclear structure, N3_a also binds Cu1 and Cu1_a in a similar fashion and thus the coordination mode is asymmetric (axial-equatorial). The observed antiferromagnetism can be a consequence of such asymmetric equatorial-axial binding mode of azide. This feature has been theoretically studied by Ruiz *et al.*,[3c] showing that the double asymmetric end-on bridges produce antiferromagnetic coupling. The Addison parameter (τ) for **1** is 0.23 and there is a small electronic density in the z^2 orbital, which overlap with the x^2-y^2 of the neighbour copper. Thus the interaction between the magnetic orbitals is expected to be very small and a weak AF coupling occurs.

3.3.2.2 Magnetic properties of Compound 2

The plot of χ_M and $\chi_M T$ versus T per Cu3 unit for **2** is displayed in Figure 22a. The room temperature $\chi_M T$ value is 1.47 cm^3 mol^{-1} K, which is slightly greater than the spin only value of 1.125 cm^3 mol^{-1} K, expected for three isolated Cu(II) ions (S = ½) assuming g =2.00. Upon cooling, χ_M increases and reaches a maximum value of 0.24 cm^3 mol^{-1} at around 6.8 K, and then decreases with temperature. The $\chi_M T$ product gradually increases giving a maximum value of 2.04 cm^3 mol^{-1} K at 14 K and then decreases to 0.51 cm^3

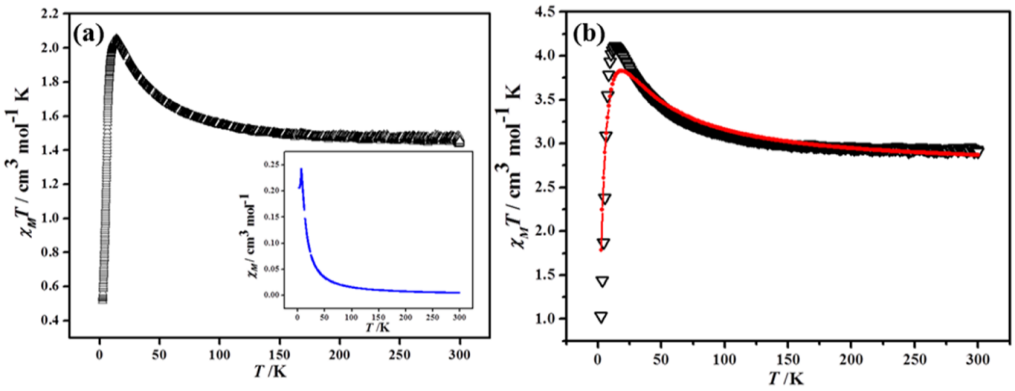

Figure 22. (a) The plots of $\chi_M T$ *vs.* *T* (per Cu3 unit) and χ_M *vs.* *T* (inset) for **2**. (b) The plot of $\chi_M T$ *vs.* *T* for **2** considering a hexanuclear unit. The solid red line indicates the best fit obtained considering one average *J*.

mol^{-1} K upon cooling to 2.5 K. The nature of $\chi_M T$ versus *T* plot indicates a dominant ferromagnetic interaction at higher temperature and antiferromagnetic interaction at low temperature. The geometry around the Cu(II) ions in **2** is either square pyramidal or octahedral with axially elongated bond suggesting that the unpaired electron on each Cu(II) resides in the basal $d_{x^2-y^2}$ orbital, while the d_{z^2} orbital contains the paired electrons. Now the magnetic exchange between the Cu(II) ions is mediated via the different azide bridging ligands as mentioned earlier. As there is no analytical equation to fit the magnetic data of a 2D system, to simplify the problem, the repeating hexanuclear cores are considered to model the data (Scheme 3). In the hexanuclear core, there are four pairs of exchange pathways: two involving Cu1-Cu3 (or Cu1_c-Cu3_c, *J1*), two involving Cu1-Cu2 (or Cu1_c-Cu2_c, *J2*), two involving Cu2_c-Cu3 (or Cu2-Cu3_c, *J3*) and the two involving Cu1-Cu2_c (or Cu1_c-Cu2, *J4*) pathways (Scheme 3). First a simple case

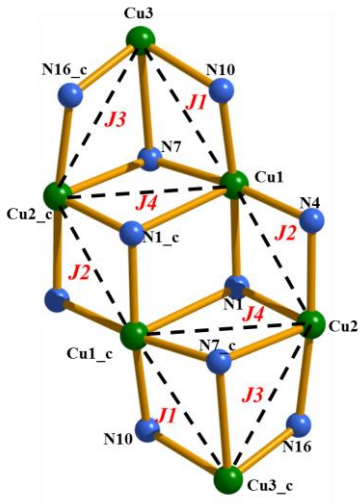

Scheme 3. Simplified coupling scheme between the Cu(II) centers for **2.**

is considered; approximating these interactions to be equivalent as the bond distances and bond angles involved are similar (Table 3). Thus the exchange interactions are considered to be equivalent, and therefore *J1 = J2 = J3 = J4 = J*. As it has been mentioned earlier that the hexanuclear cores are further connected by $\mu_{1,1,3}$-N_3 and $\mu_{1,3}$-N_3 groups forming a 2D network, therefore an interhexamer *zj'* term is introduced and the data (considering a hexanuclear unit) are fitted using MAGPACK program.[17]The values giving best fit (300-2 K) parameters are J = 18.2 cm^{-1} with g = 2.19, zj' = -1.30 cm^{-1} and R = 7.5 x 10^{-3} {$R = \sum[(\chi_M)^{obs} - (\chi_M)^{calc}]^2/[(\chi_M)^{obs}]^2$} (Figure 9b). This result suggests an overall ferromagnetic interaction in the hexanuclear core and an antiferromagnetic interaction operating between the hexanuclear cores. Thus this fitting qualitatively provides some understanding; although approximating all the *J* s to be equal is not appropriate**.** To obtain a more realistic fit, fitting is performed by adopting a four *J* model as mentioned earlier (Figure 23a). To avoid overparametrization, a possible interaction between Cu1-Cu1_c is neglected as one (Cu1-N1_c) of the Cu-N distances is close to 2.7 Å. The best fit (300-2 K) parameters are *J1* = 8.23 cm^{-1}, *J2* = 12.52 cm^{-1}, *J3* = 8.32 cm^{-1}, *J4* = 6.75 cm^{-1}, with g = 2.21, zj' = -1.5 cm^{-1} and R = 7.09×10^{-4} {$R = \sum[(\chi_M)^{obs} - (\chi_M)^{calc}]^2/[(\chi_M)^{obs}]^2$}. The ferromagnetic character of *J1*, *J2* and *J3* can be well-explained as they involve at least one symmetrical end-on azide bridge.[3c] The highest value of *J2* among the four interactions is attributed to the fact that *J2* involves two symmetrical end-on interactions. However, the positive value of *J4* is difficult to explain as both the two interactions are asymmetric and this value can be a mathematical artefact. As expected from the structure, the exchange interaction between the clusters (zj') mediated via end-to-end azide groups

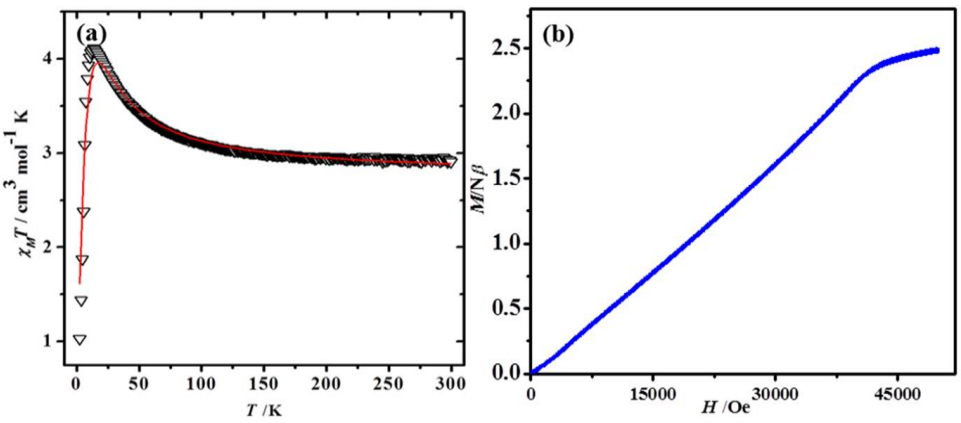

Figure 23. (a) The plot of $\chi_M T$ *vs.* *T* for **2** considering a hexanuclear unit. The solid red line indicates the best fit obtained considering a four *J* model. (b) The M *vs.* *H* curve for **2** at 3 K.

is weakly antiferromagnetic (-1.5 cm^{-1}). These findings indicate that the system may have several analytical solutions and we believe that the most reliable one should be assumed to be the one considering four *J* model. The *M vs H* curve at 3 K reaches a maximum value of 2.5 Nβ, which is slightly less than the expected 3 Nβ (Figure 23b), demonstrating presence of small antiferromagnetic interaction in **2**.

3.3.2.3 Magnetic properties of Complex 3

The magnetic properties of complex **3** as $\chi_M T$ *vs T* plot [χ_M is the molar magnetic susceptibility for two Cu(II) ions] and the reduced magnetization (M/Nβ *vs H*) are shown in Figure 24a. Starting from room temperature, $\chi_M T$ values gradually increase upto 70 K and the value at 70 K is 1.03 cm^3 mol^{-1} K. Below 70 K, the $\chi_M T$ values decrease quickly to 0.52 cm^3 mol^{-1} K at 2 K. This feature is characteristic of an intramolecular ferromagnetic coupling with weak intermolecular antiferromagnetic interactions. Above 70 K, the $1/\chi_M$ *vs T* plot (Figure 24b) plot is well fitted by the Curie-Weiss law ($\chi_M = C/(T - \theta)$), with C = 0.92 cm^3 mol^{-1} K, θ = 10.9 K. The positive Weiss constant indicates ferromagnetic interaction operates in **3**. The reduced molar magnetization at 2 K (Figure 24a inset) also corroborates ferromagnetic coupling and the intermolecular antiferromagnetic interactions as the M/Nβ value at 5 T and 2 K reaches a maximum value of 1.73 Nβ, which is less than the value expected (2 Nβ) for two ferromagnetically coupled Cu(II) ions.

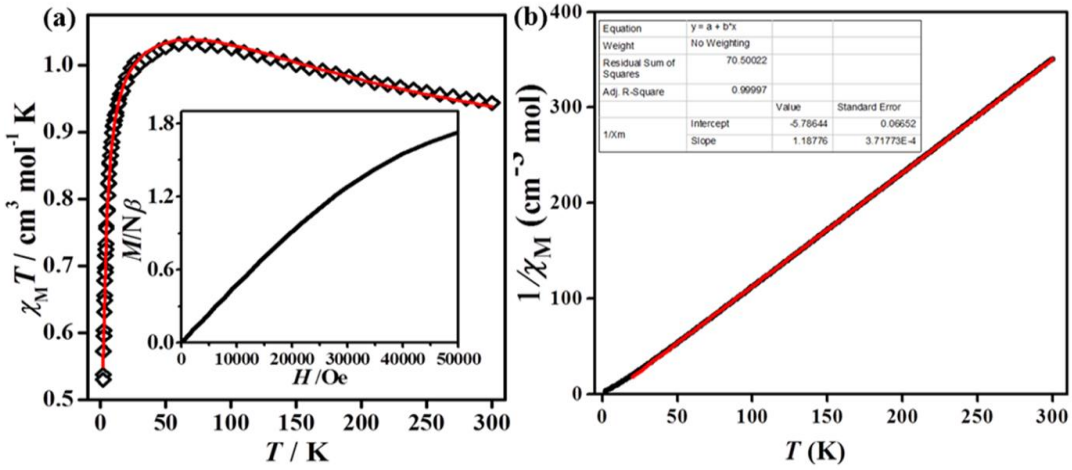

Figure 24. (a) The plots of $\chi_M T$ *vs. T* for **3**. The solid red line indicates the best fit obtained (see text). Inset: Plot of the reduced magnetization ($M/N\beta$) at 2 K. (b) Reciprocal molar susceptibility as function of temperature for **3**; solid red line indicates Curie-Weiss fitting in the range 70-300 K.

Complex **3** is a dinuclear compound with doubly $\mu_{1,1}$–N_3 bridging ligand and the dinuclear entities are assembled through the supramolecular hydrogen bonding interaction (as discussed in the structural discussion). The fit of the susceptibility data has been carried out applying a modified Bleaney-Bowers formula, considering the mean field approach for taking into account the intermolecular interactions.[1e] The best-fit parameters obtained are J = +183.7 ± 3 cm^{-1}, $z'J'$ (intermolecular) = -1.98 ± 0.01 cm^{-1}, g = 2.12 ± 0.01 and R = 1.0 x 10^{-5}. ($R = \sum_i[(\chi_m T)_{obs}–(\chi_m T)_{calc}]^2/\sum_i[(\chi_m T)_{obs}]^2$). The strong ferromagnetic J value can be interpreted as a consequence of the existence of the two azide bridges in *end-on* coordination mode, which gives ferromagnetic coupling. Ruiz *et al*.[3c] have shown from density functional theory (DFT) based calculations that there is a correlation between the calculated J parameter and the Cu-N_3-Cu angle. The theoretical calculation predicted that the J value decreases from a maximum (J ~ +300 cm^{-1}) at about θ = 90º with increasing θ, eventually reaching an antiferromagnetic regime for θ > 104-105º. The Cu1– N1–Cu1_a angle is found to be 102.4° in **1**, which is very common in this kind of complexes and values of J ~ +170 cm^{-1} are reported for such Cu-N_3-Cu angle.[4e] The intermolecular antiferromagnetic interactions derive probably from the H-bonding interaction between the dimers through the perchlorate anions and the NH of the 2-ethylimidazole (Figure 11b).

3.3.2.4 Magnetic properties of Compound 4

The plot of $\chi_M T$ *vs* T for compound **4** starts at 0.4 cm^3 mol^{-1} K (for per one Cu unit) at 300 K (Figure 25a) and with decrease in temperature there is a monotonous decreasing of $\chi_M T$ till 25 K and beyond this temperature the $\chi_M T$ value achieves a value close to 0 cm^3 mol^{-1} K at 2 K. The $1/\chi_M$ *vs* T plot (Figure 26) shows non-linearity suggesting strong magnetic exchange. The $M/N\beta$ value at 5 T and 2 K reaches a maximum value of 0.34 $N\beta$ (Figure 25b), being significantly lower than 2 $N\beta$ (expected for two unpaired electrons) corroborating the presence of an antiferromagnetic interaction. To apprehend the type and magnitude of the magnetic exchange interactions, the magnetic data is correlated to its structure. Compound **4** is indeed a magnetically 2D system formed by $\mu_{1,3}$–N_3 bridging of 1D chains where Cu(II) ions are linked together by alternative $\mu_{1,1}$–N_3 and μ-Meimi$^-$ bridging. So far, neither empirical formula nor computer programs of $\chi_M T$ *vs* T are available for fitting magnetic data of complicated 2D systems. There are two different

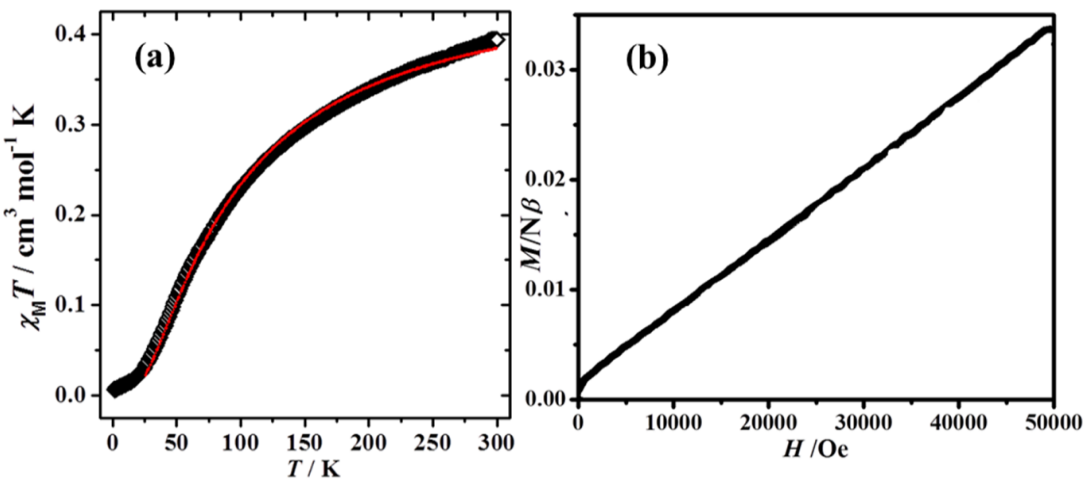

Figure 25. (a) The plot of $\chi_M T$ *vs.* *T* for **4** per one Cu(II) center. The solid red line indicates the best fit obtained (see text). (b) Plot of the reduced magnetization (M/Nβ) (per two Cu centers)*vs.* *H* at 2 K**.**

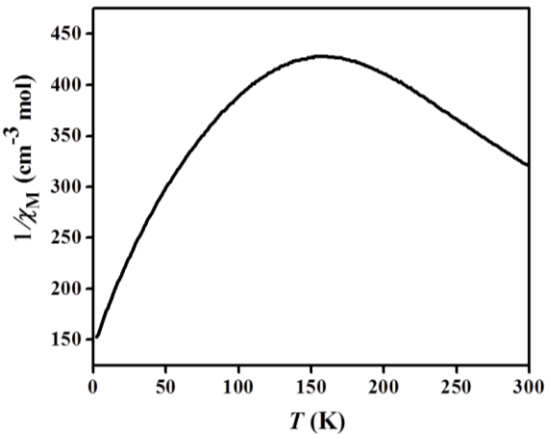

Figure 26. Reciprocal molar susceptibility (considering one Cu center) as function of temperature for **4** showing the non-linear dependence.

Cu-$\mu_{1,3}$-azide bonds (Cu1-N7 and Cu2-N9) of distances 2.037 Å and 2.362 Å respectively. Due to the long distance of the latter one, electron density can be considered as almost zero for the axial position. Thus, for having a rather good approach towards the understanding of exchange interactions, **4** can be considered as a pseudo-1D system, owing to the short intrachain Cu-$\mu_{1,1}$-azide distances and long intrachain Cu-$\mu_{1,3}$-azide distances (considering Cu2-N9 bond distance). The Cu(II) ions are linked by imidazole (AF) and N_3^-(end-on) (F), giving an alternating F-AF one dimensional system. Borras-Almenar and co-workers reported in 1994 an empirical equation for this kind of Cu(II) alternating chains.[18] In this equation, the parameter α (alpha) represents the ratio $J_F/|J_{AF}|$. Indeed, according to the authors, there are two possibilities for the fit: $0 \leq \alpha \leq 2$ and $2 \leq \alpha$

≤ 8. All attempts to fit with the data with later range ($2 \leq \alpha \leq 8$) last values failed. On the contrary, with the first hypothesis, $0 \leq \alpha \leq 2$, a good fit was obtained with the following parameters: J_{AF} = -88.4 ± 2.1 cm^{-1}; J_F = 100.8 ± 2.2 cm^{-1}, g = 2.27± 0.018 and R =1.2 x 10^{-4}. The fitting has been made from 300 K to 25 K since the formula employed here[18] is not perfectly valid at very low temperatures. Furthermore, at low temperatures, the interchain $\mu_{1,3}$-N_3 bridging in **4** would also create a deviation. The values of the fitted parameters agree well with the structural topology of **4**. The coupling through $\mu_{1,1}$-N_3 bridging is ferromagnetic as expected,[3c] whereas the 2-methyl imidazole bridging ligand creates a strong antiferromagnetic coupling (J_{AF} = -88.45 cm^{-1}), which agrees well with the literature reports.[8b,c,19]

3.3.2.5 Magnetic properties of Compound 5

For compound **5**, the magnetic susceptibility has been measured from 300 K to 2 K (Figure 27a) as well as the magnetization (*M vs H*) at 2 K (Figure 27b). At low temperature, the increase in χ_M value is due to paramagnetic impurities is present in the sample. However, the quantity of the impurities must be very small as reflected by the CHN data and also the powder X-ray diffraction of the sample confirms the phase purity. The $1/\chi_M$ *vs T* plot (Figure 28) shows non-linearity suggesting strong magnetic exchange. Figure 27b shows the plot of the reduced magnetization ($M/N\beta$) (per two Cu centers) at 2 K for compound **5.** The $M/N\beta$ value at 5 T and 2 K reaches a maximum value of 0.14 Nβ, being significantly lower than expected 2 Nβ (for ferromagnetically coupled Cu centers) corroborating the presence of an antiferromagnetic interaction. As revealed by

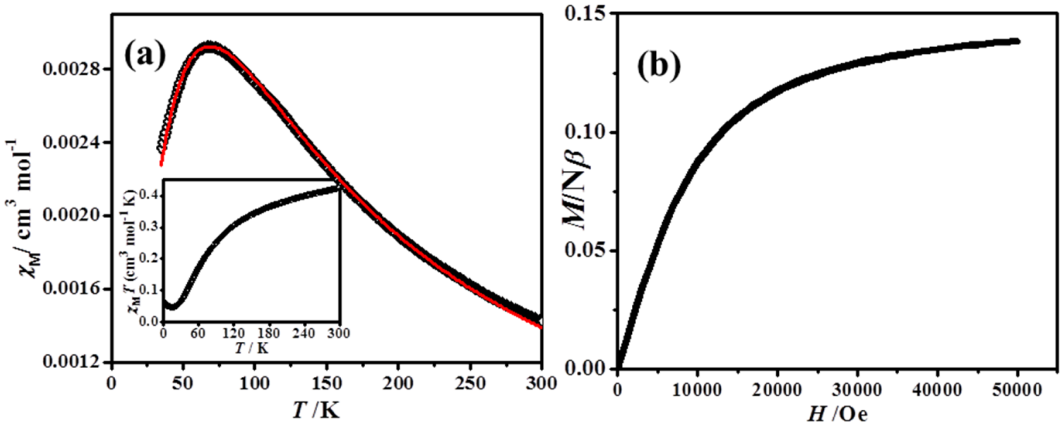

Figure 27. (a) The plot of χ_M *vs. T* for **5** per one Cu center. The solid red line indicates the best fit obtained (see text). Inset shows the plot of $\chi_M T$ *vs. T* for **5** per one Cu center. (b) Plot of the reduced magnetization ($M/N\beta$) (per two Cu centers) *vs. H* at 2 K for compound **5.**

single crystal X-ray diffraction analysis, compound **5** is two-dimensional. However, it is built from one-dimensional alternating chain (similar to compound **4**) linked together by $\mu_{1,3}$–N_3 ligands. The important structural feature is the coordination of the $\mu_{1,3}$-N_3 bridge in the axial position in the square pyramidal geometry of Cu(II) ions (Cu1-N4 and Cu2-N6 bonds). Thus, the unpaired electron is placed in the x^2-y^2 orbital, having an electronic density almost zero in the apical position (z^2 orbital) and eventually **5** can be considered as 1D magnetic system. The chain is an alternating antiferro (imidazole bridge, J_1)-ferro (end-on azide bridges within the chains, J_2). Hence, the previously mentioned mathematical formula[18] which was used for the analysis of compound **4**, can be applied for compound **5** too. However, the mathematical expression is made from the method of closed spin chains of increasing length and is not valid at low temperatures. Furthermore, fitting of the data at low temperature would not be appropriate because of the possible presence of paramagnetic impurities. The presence of a rounded maximum in χ_M close to

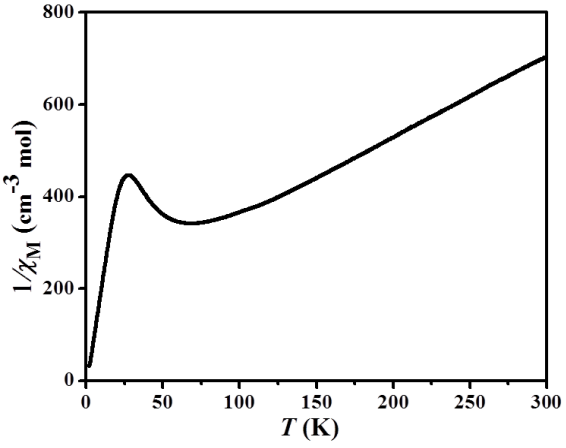

Figure 28. Reciprocal molar susceptibility (considering one Cu center) as function of temperature for **5** showing the non-linear dependence

75 K is indicative of the antiferromagnetic behaviour. In these cases, it is better to fit χ_M than $\chi_M T$. The χ_M *vs.* T data were fitted from 300 K to 35 K. The fit under these conditions is illustrated in Figure 27a. The best values obtained are the following: $|J_1|$ = 63.30, thus, J_1 = -63.30 ± 1.5 cm^{-1}, α = 1.55 ± 0.011, giving, thus, J_2 = 98.12, and g = 2.11 ± 0.021, with very good agreement factor, R = 2.26 x 10^{-10}. The value of the J_1 (antiferromagnetic) must be attributed to the imidazole bridges, which is well reported in the literature.[8b,c, 19] The ferromagnetic interaction (J_2), originates from two azide ligands in end-on conformation. According to the reported experimental and theoretical data, this

kind of geometry with the corresponding Cu-N_{EO}-Cu angles, would give ferromagnetic coupling,[3c] as it occurs in compound **5**.

3.3.2.6 Magnetic properties of Compound 6

The plot of $\chi_M T$ *vs* T for compound **6** is shown in Figure 29 (considering four Cu centres). Starting from 300 K, the $\chi_M T$ values increase upto 16 K exhibiting a maximum and then gradually decreases. Above 25 K, the $1/\chi_M$ *vs* T plot (Figure 30) is well fitted by the Curie-Weiss law ($\chi_M = C/(T - \theta)$), with C = 1.47 cm^3 mol^{-1} K, θ = 11.9 K. The positive Weiss constant indicates ferromagnetic interaction operates in **6**.

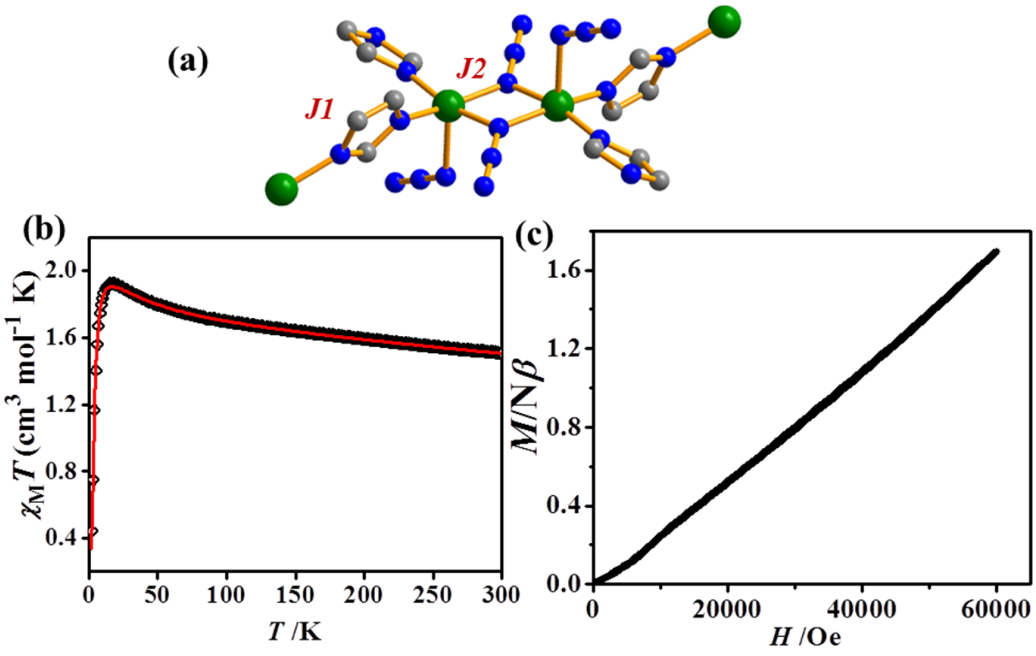

Figure 29. (a) The tetranuclear [Cu-(μ-imi$^-$)-Cu-($\mu_{1,1}$-N_3)$_2$-Cu-(μ-imi$^-$)-Cu] unit considered for modeling the magnetic data. (b) The plot of χ_MT *vs.* T for **6** per four Cu centers. The solid red line indicates the best fit obtained (see text). (c) Plot of the reduced magnetization (M/Nβ) *vs*. H (per two Cu centers) at 2 K for compound **6.**

To understand the nature and value of coupling parameters, an appropriate model is necessary to fit the magnetic data. Due to the long interchain Cu-$\mu_{1,3}$-azide distances, the magnetic interaction between the 1D chains can be ignored. Now further structural insight into **6** reveals that in the 1D chains, interaction through the ($\mu_{1,3}$-N_3)$_2$ bridging can also be neglected due to the axial coordination of N atom to the Cu(II) centre in Cu2-N17 bond. A simplified tetranuclear Cu_4 unit [Cu-(μ-imi$^-$)-Cu-($\mu_{1,1}$-N_3)$_2$-Cu-(μ-imi$^-$)-Cu] (Figure

29a) is considered and such units are linked to the neighboring units by different sets of $\mu_{1,3}$-azide bridging ligands (where J can be ignored due to long bond distances), giving a 2D network (Figure 17). The fitting has been made assuming the tetranuclear unit with intermolecular interactions ($z'J'$), by means of MAGPACK program,[17] which uses the spin Hamiltonian $H = -2J\sum S_i S_j$. The best fit results are the following parameters: J_1 (imidazolate bridge) = -28.37 ± 1.2 cm^{-1}; J_2 [$(\mu_{1,1}\text{-}N_3)_2$ bridge] = 16.17 ± 0.9 cm^{-1}; g = 2.11 ± 0.011; $z'J'$ = 1.65 ± 0.026 cm^{-1}, TIP = 366 x 10^{-6} cm^{-1} mol^{-1} and the R factor is 2.38 x 10^{-5} (Figure 20). The J values agree with those reported in the literature for similar bridging ligand.[8c,19] It should be noted that the best fitting gives a small positive $z'J'$ parameter and thus indicates a ferromagnetic intermolecular interaction. This feature is likely due to the fact that these intermolecular interactions are made between magnetic orbitals with the unpaired electron in the z^2 and x^2-y^2 atomic orbitals respectively (orthogonal each other). The $M/N\beta$ value at 6 T and 2 K does not saturate; it reaches a maximum value of 1.7 Nβ (Figure 29c), which is slightly lesser than expected 2 Nβ (for ferromagnetically coupled two Cu centers). Thus the dominant interaction between the Cu(II) would be ferromagnetic in nature, with a small contribution of an antiferromagnetic interaction, which supports the experimental $\chi_M T$ *vs* T data and our fitting results.

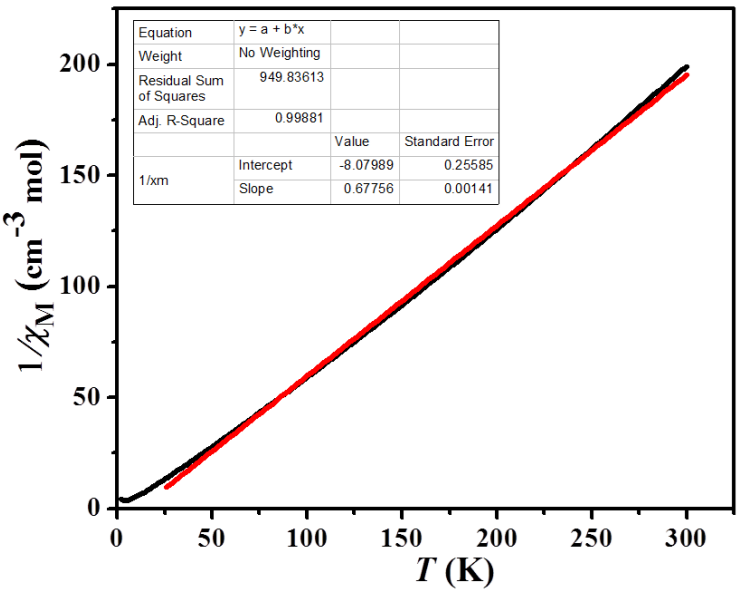

Figure 30. Reciprocal molar susceptibility as function of temperature for **6**; solid red line indicates Curie-Weiss fitting in the range 25-300 K.

3.4 SUMMARY

It has been shown in this chapter that structural diversities and versatile magnetic properties in novel Cu(II)-azide compounds could be realized by changing the coligand (N,N′–dimethylethylenediamine (Me_2en) and imidazole/substituted imidazole) and employing judicious synthetic strategies. Six Cu(II)-azide coordination compounds with novel structural motifs and different binding modes of bridging ligands were furnished and their magnetic studies were studied in detail. By controlling the relative concentration of the blocking Me_2en ligand, a discrete dinuclear complex **1** and an extended 2D compound **2** have been synthesized. On the other hand, by changing the substitution on the imidazolate linker another four new compounds were realized. Structural insight provides explanations to the diverse magnetic behaviours of these compounds.

3.5 REFERENCES

1. (*a*) E. Coronado, P. Delhaes, D. Gatteschi and J. S. Miller, Dordrecht, *Molecular magnetism: From the molecular assemblies to the Devices*, NATO ASI series no. E321, Dordrecht, 1996; (*b*) J. J. Vittal, *Coord. Chem. Rev*., 2007, **251**, 1781; (*c*) J. Yoon and E. I. Solomon, *Coord. Chem. Rev*., 2007, **251**, 379; (*d*) C. F. Lee, D. A. Leigh, R. G. Pritcharg, D. Schults, S. J. Teat, G. A. Timco and R. E. P. Winpenny, *Nature*, 2009, **458**, 314; (*e*) O. Kahn, *Molecular Magnetism*. VCH, New York, 1993.
2. (*a*) O. Kahn, M. F. Charlot, *Nouu. J. Chim.*, 1980, **4**, 567; *(b)* P. J. Hay, J. C. Thibeault and R. J. Hoffmann, *J. Am. Chem. Soc.*, 1975, **97**, 4884; (*c*) V. M. Crawford, H. W. Richardson, J. R. Wasson, D. J. Hcdgson and W. E. Hatfield, *Inorg. Chem.*, 1976, **15**, 2107.
3. (*a*) L. K. Thompson and S. K. Tandon, *Comments Inorg. Chem*., 1996, **18**, 125; (*b*) R. D. Willett, D. Gatteschi and O. Kahn, *Magneto-Structural Correlations in Exchange Coupled Systems*, Dordrecht, The Netherlands, 1985; (*c*) E. Ruiz, J. Cano, S. Alvarez and P. Alemany, *J. Am. Chem. Soc*., 1998, **120**, 11122; (*d*) S. Koner, S. Saha, T. Mallah and K. -I. Okamoto, *Inorg. Chem.*, 2004, **43**, 840.
4. (*a*) Y. Song, S. Ohkoshi, Y. Arimoto, H. Seino, Y. Mizobe and K. Hashimoto, *Inorg. Chem.*, 2003, **42**, 1848; (*b*) M. A. M. Abu-Youssef, A. Escuer, M. A. S. Goher, F. A. Mautner and G. J. Reib and R. Vicente, *Angew. Chem., Int. Ed.*, 2000, **39**, 1624; (*c*) P. S. Mukherjee, T. K. Maji, G. Mostafa, T. Mallah and N. Ray

Chaudhuri, *Inorg. Chem.*, 2000, **39**, 5147; (*d*) T. K. Maji, P. S. Mukherjee, G. Mostafa, T. Mallah, J. Cano-Boquera and N. Ray Chaudhuri, *Chem. Commun.*, 2001, 1012; (*e*) S. Triki, C.J. Gomez-Garcia, E. ruiz and J. Sala-Pala, *Inorg. Chem*., 2005, **44**, 5501.

5. (*a*) H. Wen, J. Zuo, W. Liu, Y. Song and X. You, *Inorg. Chim. Acta*, 2005, 2565; (*b*) M. Liang, W. Wang, Z. Liu, D. Liao, Z. Jiang, S. Yan and P. Cheng, *J. Coord. Chem*., 2003. **56**, 1473; (*c*) M. Monfort, L. Resino, J. Ribas and H. Stoeckli-Evans, *Angew. Chem. Int. Ed.*, 2000, **39**, 191; (*d*) E.-Q. Gao, Y.-F. Yue, S.-Q. Bai, Z. He and C.-H. Yan, *J. Am. Chem. Soc.*, 2004, **126**, 14.
6. (*a*) A. M. Abu-Youssef, A. Escuer, F. A. Mautner and Lars Öhrström, *Dalton Trans.*, 2008, 3553; (*b*) F.-C. Liu, Y.-F. Zeng, J. R. Li, X.-H. Bu, H. J. Zhang and J. Ribas, *Inorg. Chem.*, 2005, **44**, 7298; (*c*) F.-C. Liu, Y.-F. Zeng, J. Jiao, J. R. Li, X.-H. Bu, J. Ribas and S. R. Batten, *Inorg. Chem.*, 2006, **45**, 6129; (*d*) F.-C. Liu, Y.-F. Zeng, J. Jiao, J. R. Li, X.-H. Bu, J. Ribas and S. R. Batten, *Inorg. Chem.*, 2006, **45**, 2776; (*e*) S. Naiya, C. Biswas, M. G. B. Drew, C. J. Gomez-Garcıa, J. M. Clemente-Juan, and A. Ghosh, *Inorg. Chem*., 2010, **49**, 6616.
7. (*a*) K. C. Mondal and P. S. Mukherjee, *Inorg. Chem.*, 2008, **47**, 4215; (*b*) S. Mukherjee, B. Gole, R. Chakrabarty and P. S. Mukherjee, *Inorg. Chem.*, 2009, **48**, 11325; (*c*) S. Mukherjee, B. Gole, Y. Song, and P. S. Mukherjee, *Inorg. Chem.*, 2011, **50**, 3621.
8. (*a*) T.C. Stamatatos, S. P. Perlepes, C. P. Raptopoulou, A. Terzis, C.S. Patrickios, A. J. Tasiopoulos and A. K. Boudalis, *Dalton Trans.*, 2009, 3354; (*b*) S. Mukherjee, T. Weyhermüller, E. Bill and P. Chaudhuri, *Eur. J. Inorg. Chem.*, 2004, 4209; (*c*) E. Colacio, J.M. Domínguez-Vera, M. Ghazi, R. Kivekas, M. Klinga and J.M. Moreno, *Inorg. Chem*., 1998, **37**, 3040; (*d*) K. Sakai, T. Akutagawa and T. Nakamura, *Eur. J. Inorg. Chem*., 2011, 116; (*e*) B-d. Wu, S-w. Wang, L. Yang, T.-l. Zhang, J.-g. Zhang, Z.-n. Zhou and K.-b. Yu, *Eur. J. Inorg. Chem.*, 2011, 2616.
9. (*a*) SMART (V 5.628), SAINT (V 6.45a), XPREP, SHELXTL; Bruker AXS Inc. Madison, Wisconsin, USA, 2004; (*b*) G. M. Sheldrick, Siemens Area Detector Absorption Correction Program, University of Göttingen, Göttingen, Germany, 1994; (*c*) A. Altomare, G. Cascarano, C. Giacovazzo, A. Gualaradi, *J. Appl. Cryst.*, 1993, **26**, 343; (*d*) G. M. Sheldrick, SHELXL-97, Program for Crystal Structure Solution and Refinement; University of Göttingen, Göttingen, Germany, 1997; (*e*)

A. L. Spek, *J. Appl. Cryst.*, 2003, **36**, 7; (*f*) L. J. Farrugia, WinGX - A Windows Program for Crystal Structure Analysis. *J. Appl. Crystallogr.*, 1999, **32**, 837.

10. Gaussian 03, Revision C.02, M. J. Frisch *et al*. Wallingford CT, 2004.
11. (*a*) C. Lee, W. Yang and R. G. Parr, *Phys. Rev. B*, 1988, **37**, 785; (b) B. Miehlich, A. Savin, H. Stoll and H. Preuss, *Chem. Phys. Lett*., 1989, **157**, 200; (*c*) A. D. Becke, *J. Chem. Phys.*, 1993, **98**, 5648.
12. (*a*) P. J. Hay and W. R. Wadt, *J. Chem. Phys.*, 1985, **82**, 270; (*b*) W. R. Wadt and P. J. Hay, *J. Chem. Phys.* 1985, **82**, 284; (*c*) P. J. Hay and W. R. Wadt, *J. Chem. Phys.*, 1985, **82**, 299.
13. (*a*) D. Maity, A. K. Manna, D. Karthigeyan, T. K. Kundu, Swapan K. Pati, and T. Govindaraju, *Chem. Eur. J.*, 2011, **17**, 11152; (*b*) K. L. Gurunatha, S. Dutta, G. Mostafa, S. K. Pati, and T. K. Maji, *Inorg. Chim. Acta*, 362, **3745**, 2009.
14. (*a*) W. J. Caspers, Spin Systems, World Scientific, Singapore, 1989; (*b*) J. M. Ricart, R. Dovesi, C. Roetti and V. R. Saunders, *Phys. Rev. B.*, 1995, **52**, 2381. [Erratum: J. M. Ricart, R. Dovesi, C. Roetti and V. R. Saunders, *Phys. Rev. B.*, 1997, **55**, 15942.
15. (*a*) L. Noodleman, *J. Chem. Phys*., 1981, **74**, 5737; (*b*) L. Noodleman, E. R. Davidson, *Chem. Phys*., 1986, **109**, 131; (*c*) L. Noodleman, C. Y. Peng, D. A. Case and J. M. Mouesda, *Coord. Chem. Rev*., 1995, **144**, 199.
16. A. W. Addison, T. N. Rao, J. Reedijk, J. van Rijn and G. C. Verschoor, ***J. Chem. Soc***., *Dalton Trans*., 1984, 1349.
17. Magpack (Magnetic Properties Analysis Package for Spin Clusters) [(a)] employed with a nonlinear least-squares curve-fitting program, DSTEPIT [(b)]. (*a*) J.J. Borrás-Almenar, J.M. Clemente-Juan, E. Coronado and B.S. Tsukerblat, *J. Comput. Chem.* 2001, **22**, 985 and *Inorg. Chem.*, 1999, **38**, 6081; (*b*) Program 66, Quantum Chemistry Program Exchange, Indiana University, Bloomington, IN, 1965.
18. J.J. Borras-Almenar, E. Coronado, J. Curely, R. Georges and J. C. Gianduzzo, *Inorg. Chem.*, 1994, **33**, 5171.
19. N. Koyama, R. Watanabe, T. Ishida, T. Nogami and T. Kogane, *Polyhedron*, 2009, **28,** 2001 and references there.

Chapter 4A

2D $[M^{II}(N_3)_2(pyz)]_n$ (M = Co/Ni) Metamagnetic Coordination Polymers: Synthesis, Structure and Magnetic Properties

Abstract

This chapter reports synthesis, structure, characterization and metamagnetic behaviour of two new iso-structural two-dimensional (2D) metal-organic coordination compounds, $[Co^{II}(N_3)_2(pyz)]_n$ (**1**) and $[Ni^{II}(N_3)_2(pyz)]_n$ (**2**) (pyz = pyrazine). Compound **1** has been characterized by single-crystal X-ray diffraction while the isostructural Ni(II) compound has been synthesized in phase-pure form as evident from the PXRD pattern. In case of **1**, Co(II) ions are doubly bridged by $\mu_{1,1}$-N_3 ligand in an end-on fashion to afford 1D linear chain and such 1D chains are further extended through the pyz linkers resulting in a 2D rectangular net. The end-on azide bridge mediates ferromagnetic interaction within the 1D chain while interchain antiferromagnetic interaction operates through pyz linker. Various temperature and field dependent magnetic study reveals that **1** exhibits metamagnetic behaviour. The anisotropic magnetic properties of **1** have been studied by applying magnetic field on a single-crystal which shows easy magnetization of the system along the long axis of the crystal. The Ni(II) analogue (**2**) shows similar metamagnetic behaviour.

Paper based on this study:

A. Chakraborty, S. R. Lingampalli, M. Kurmoo, T. K. Maji, *manuscript to be submitted*.

4A.1 INTRODUCTION

Metamagnets are a class of magnetically ordered materials which undergo field-induced magnetic phase transition from an antiferromagnetic ground state to a ferromagnetic-like excited state.[1] Synthesis and investigation of the metamagnets has been an active area of research owing to their fascinating magnetic properties,[2] which are still at an early stage of understanding. Recently, Shivaram and co-workers have shown many electronic materials that undergo metamagnetic transition exhibit "universal features" in their non-linear susceptibility and such universal properties of metamagnets would be highly promising in magnetic refrigeration.[3,4] However, magnetic refrigerators are in the experimental stage and hence extensive research is required to synthesize new metamagnets and investigating their properties properly before they could be used for practical applications.

Metal-organic coordination polymers have emerged as new hybrid materials with several promises including novel magnetic properties.[5-7] In this chapter, the goal was design and synthesis of new metal-organic coordination polymers with metamagnetic behaviour. Metamagnetic behaviour can arise from competitive ferromagnetic (F)/ antiferromagnetic (AF) interactions present in an appropriate anisotropic system.[1,8] The choice of the paramagnetic metal ions and the bridging ligands play pivotal role in determining the type and magnitude of the magnetic interaction.[9] Azide is one of the well-known bridging ligands that can result in versatile magnetic interactions depending on its binding modes and has been exploited widely to synthesize new magnetic materials.[10, 7c-d] The end-on $\mu_{1,1}$-N_3 bridge is typically known to propagate ferromagnetic interaction between the metal (M) centres (the magnitude and type of the interaction vary with the $\angle$M-N_3-M angle (θ) and theoretical calculation predicted that the J value decreases from a maximum ($J \sim +300$ cm^{-1}) at about $\theta = 90^{o}$ with increasing θ).[11] If such a ferromagnetically coupled metal-azido system is furnished and further weak AF interaction through another suitable coligand can be employed, the weak AF interaction can be switched to F interaction under a strong external field. Adopting such strategy, metamagnetic behaviour can be observed. In this regard, selection of the coligands like exobidentate bridging π-conjugated linkers or blocking bridging ligand with well-defined coordination compartments that will propagate weak AF interaction is also crucial. The ditopic spacer pyrazine (pyz) is known to mediate AF superexchange interaction through the aromatic bridge.[12] Interesting metamagnetic systems can be synthesized by bridging

aniosotropic metal ions like Co(II) ions by these two different ligands (azide and pyz). Indeed, such synthetic design strategy has been adopted previously, but the metamagnetic behaviour has not studied elaborately and appropriately. Zhang and co-workers have reported a 2D layered Fe(II) compound with the formula $[Fe^{II}(N_3)_2(pyz)]_n$[13] which showed metamagnetic behaviour. However, the magneto-structural correlation of this compound has not been studied in detail. On the other hand, isomorphous Mn(II) and Cu(II) compounds have not shown any metamagnetic behaviour due to the lack of local anisotropic metal centres in the systems.[14] To have proper understanding of the magnetic properties of similar systems, anisotropic Co(II) and Ni(II) analogue were synthesized and studied. The Co(II) compound, $[Co^{II}(N_3)_2(pyz)]_n$ (**1**) is a 2D coordination polymer consisting of 1D end-on $\mu_{1,1}$-N_3 Co(II) chains which are further bridged through pyz linkers to afford a 2D net. Detail magnetic studies of **1** were carried out which reveal its metamagentic behaviour arising from the competitive ferromagnetic interaction through $\mu_{1,1}$-N_3 bridge and antiferromagnetic interaction through pyz linkers. **1** shows Neel temperature at 11 K and metamagnetic transition occur at the critical field, where the appropriate field can overcome the AF interaction forcing the spins to align parallel to the field. The magnetic study carried out with a single-crystal of **1**, which clearly demonstrates the magneto-crystalline anisotropy and presence of easy axis in the system. The isostructural Ni(II) was also synthesized in phase-pure crystalline form which showed similar metamagnetic behaviour.

4A.2 EXPERIMENTAL SECTION

4A.2.1 Materials

All the reagents and solvents employed are commercially available and used as supplied without further purification. $Co(NO_3)_2.6H_2O$, $Ni(NO_3)_2.6H_2O$, sodium azide (NaN_3) and pyrazine (pyz) were obtained from the Aldrich Chemical Co.

4A.2.2 Synthesis

$[Co^{II}(N_3)_2(pyz)]_n$ (**1**): A methanolic solution (25 mL) of NaN_3 (0.065 g, 1 mmol) was mixed with a methanolic solution (25 mL) of pyz (0.040 g, 0.5 mmol) and the resulting solution was stirred for 30 min. $Co(NO_3)_2.6H_2O$ (0.146 g, 0.5 mmol) was dissolved in 50 mL of water and 2 mL of this Co(II) solution was slowly and carefully layered with the above mixed ligand solution employing 1 mL of water/MeOH (1:1) buffer solution. Pink colored block-shaped crystals were obtained after 3 weeks. The crystals were separated

and washed with a methanol-water mixture (1:1) and dried. The bulk amount of the compound was obtained by direct mixing of the ligand solution (mixture of pyz and NaN_3) to an aqueous solution of Co(II) with appropriate ratios, and the phase purity of the sample was checked by elemental and PXRD analysis (Figure 1). Yield, 77%, relative to Co(II). Anal. calcd. for $C_4H_4CoN_8$: C, 21.54; H, 1.80; N, 50.23. Found: C, 21.63; H, 1.61; N, 50.45 %. Selected IR data (KBr, cm^{-1}); ν_{as} (azido) 2100 s, 2062 s; ν_s (azido) 1330 m.

$[Ni^{II}(N_3)_2(pyz)]_n$ (**2**): Efforts to synthesize suitable single-crystals of compound **2** were unsuccessful. The phase-pure powder of compound **2** was obtained by direct mixing of ligand solution (mixture of pyz and NaN_3) to an aqueous solution of $Ni(NO_3)_2.6H_2O$ using the similar stoichiometry as of **1**. The PXRD pattern of **2** exactly matches with **1** suggesting that the two compounds are isomorphous. Anal. calcd. for $C_4H_4NiN_8$: C, 21.56; H, 1.80; N, 50.29. Found: C, 21.62; H, 1.67; N, 50.48 %. Selected IR absorbtions (KBr, cm^{-1}); ν_{as} (azido) 2098 s, 2065 s; ν_s (azido) 1328 m.

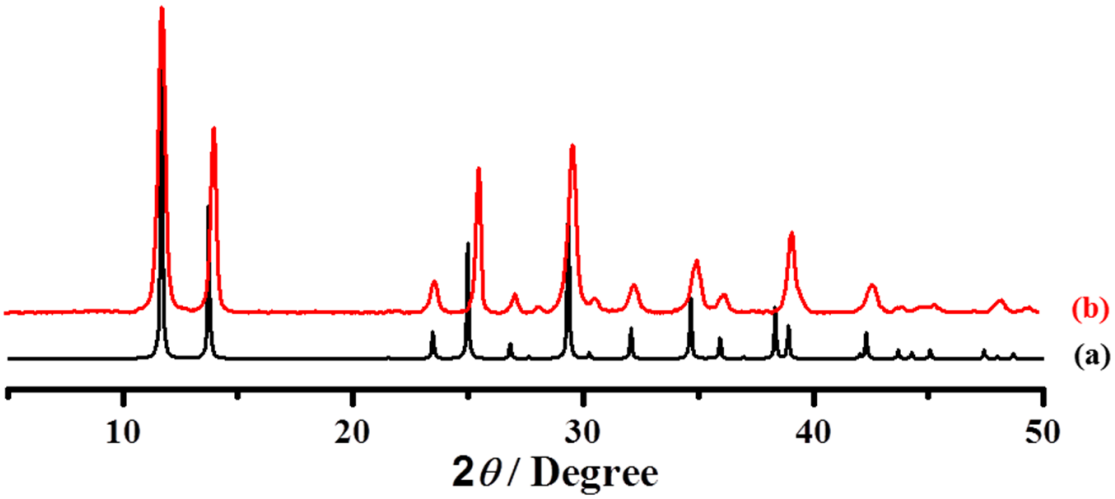

Figure 1. PXRD patterns of compound **1**: (a) simulated; (b) bulk as-synthesized. Similarity in simulated and as-synthesized pattern indicates high purity of the compound.

4A.2.3 Single-crystal X-ray Diffraction

X-ray single-crystal structural data of **1** was collected on a Bruker Smart-CCD diffractometer equipped with a normal focus, 2.4 kW sealed tube X-ray source with graphite monochromated Mo–Kα radiation (λ = 0.71073 Å) operating at 50 kV and 30 mA. The program SAINT[15a] was used for integration of diffraction profiles and absorption correction was made with SADABS[15b] program. All the structures were solved by SIR 92[15c] and refined by full matrix least square method using SHELXL-97.[15d] All the non-hydrogen atoms were refined anisotropically and the hydrogen atoms were fixed by

HFIX and placed in ideal positions. All calculations were carried out using SHELXL 97, PLATON[16e] and WinGX system, Ver 1.70.01.[15f] All crystallographic and structure refinement data of **1** are summarized in Table 1. Selected bond lengths and angles are displayed in Tables 2.

4A.2.4 Physical Measurements

Elemental analyses were carried out on a Thermo Fischer Flash 2000 Elemental Analyzer. IR spectra were recorded in KBr pellets on a Bruker IFS 66v/S spectrophotometer in the region of 4000 – 400 cm^{-1}. Powder X-ray diffraction (PXRD) patterns were recorded on a Bruker D8 Discover instrument using Cu–Kα radiation. The magnetic measurements for polycrystalline powder sample of **1** and **2** were carried out using Vibrating Sample Magnetometer (VSM) in physical property measurement system (PPMS, Quantum Design, USA). Variable temperature field-cooled (FC) magnetization studies at different fields were performed to investigate the filed-dependence of the magnetic state transition. Anisotropic magnetic measurements were performed by aligning a single-crystal of dimension 300 µm x 168 µm x 25 µm.

4A.3 RESULTS AND DISCUSSION

4A.3.1 Crystal Structure Description

Single–crystal X–ray diffraction study reveals that $[Co^{II}(N_3)_2(pyz)]_n$ (**1**) crystalize in the orthorhombic *Cmcm* space group. The asymmetric unit contains one crystallographic independent Co(II) centre, which is present in a slightly distorted octahedral geometry and coordinated to four nitrogen atoms (N2, N2a, N2b and N2c; symmetry codes: a = -x, y, ½-z, b = x, -y, 1-z, c = -x, -y, 1/2+z) from the symmetry-related $\mu_{1,1}$-azide groups. The other two coordination sites are furnished by N5 and N5a (symmetry codes: a = x, -y, 1-z) atoms from pyz pillar (Figure 2). The Co1-N($\mu_{1,1}$-azide) and Co1-N(pyz) bond distances are 2.147 (4)Å and 2.151(7) Å respectively. Deviation from ideal octahedral geometry can be realized from the cisoid and transoid angles (Table 1). The inversion centres reside at the Co(II) atoms and at the centroid of pyz linker. Two adjacent Co(II) centres are doubly bridged by $\mu_{1,1}$-N_3 ligand in an end-on fashion along the *c* axis to form the 1D linear chain (Figure 2). Each unit cell can be depicted as an unit consisting of two consecutive $[Co^{II}(\mu_{1,1}\text{-}N_3)_2]$ units and the shortest Co(II)-Co(II) distance along $[Co^{II}(\mu_{1,1}\text{-}N_3)_2]$ units is exactly the half (3.302 Å) of the crystallographic *c* axis (Figure 2). The 1D $[Co^{II}(\mu_{1,1}\text{-}N_3)_2]$ chains are further connected through the pyz linker along the

crystallographic *b* axis resulting in the 2D layers along the crystallographic *bc* plane. The pyz linkers are along the *b* axis and the shortest Co(II)-Co(II) distance through pyz is equal to length of the crystallographic *b* axis (7.09 Å). Along the crystallographic *a* axis, two adjacent 2D layers are displaced by half a repeat unit along the crystallographic *b* axis (Figure 3). Such packing originates to avoid the steric hindrance between the interlayer azido ligands and favours the closer packing. The shortest interlayer Co(II)-Co(II) distance is 8.347 Å.

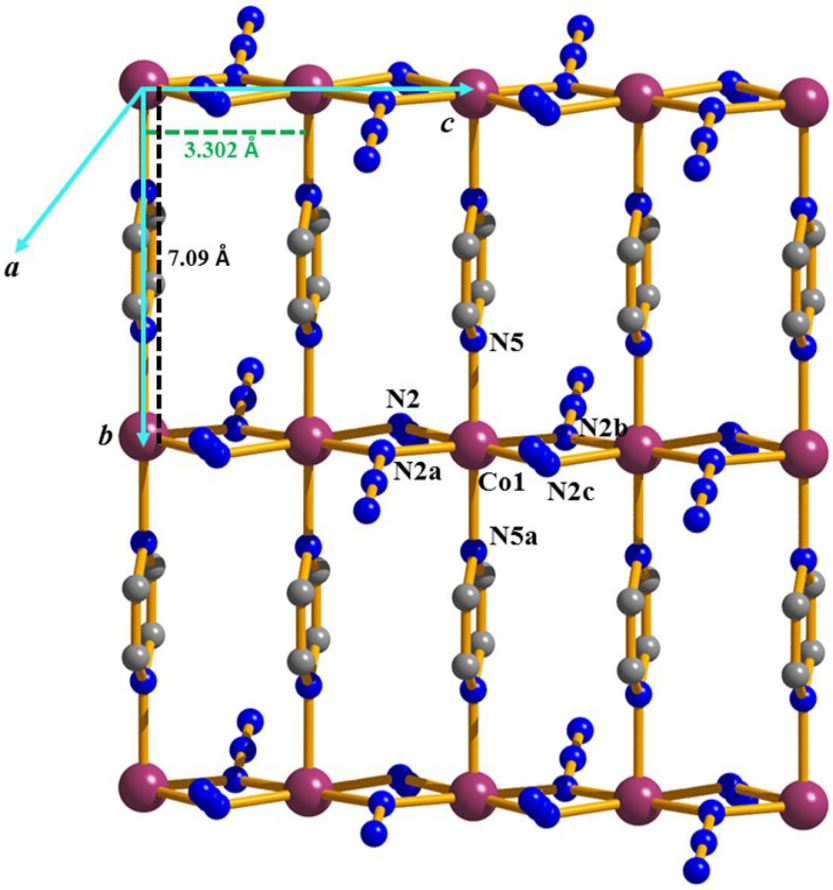

Figure 2. The 2D layer structure of **1** consisting of the 1D $[Co^{II}(N_3)_2]$ linear chain along the crystallographic *bc* plane. The Oh coordination of the Co(II) centre is also shown. The unit cell edges are shown in sky blue colour. Colour code: Co: purple; N: blue; C: grey.

The iso-structural Ni(II) compound (**2**) was synthesized in phase-pure form as evident from the PXRD pattern. Lebail fitting was carried out using Fullprof software in order to obtain the cell parameters of **2**, which suggests that **2** also has an orthorhombic structure with a = 15.1415(3) Å, b = 7.0040 (2) Å, c = 6.6023(4) Å, V = 700.18 $Å^3$ [R_{wp} = 2.00%, R_p = 1.21%] (Figure 4). The cell parameters of **2** are very close to that of **1** [a = 15.110(4) Å, b = 7.0972 (19) Å, c = 6.6048(18) Å] and hence the structural parameters of **2** are expected to be very close to that of **1**.

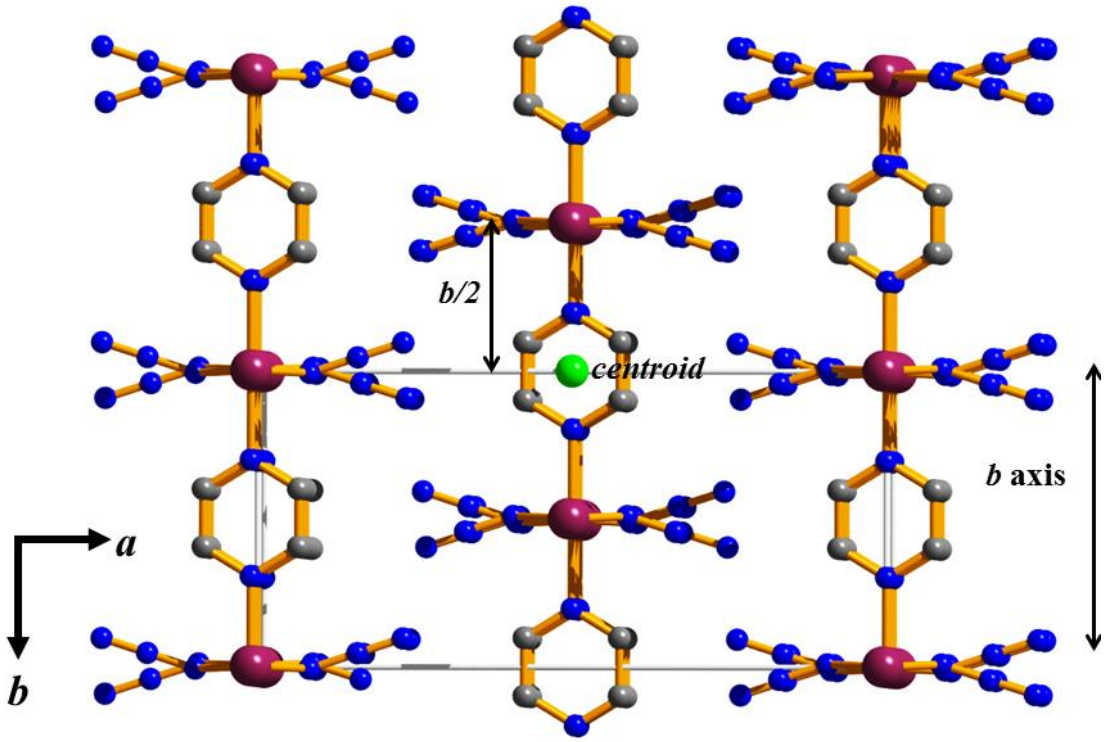

Figure 3. The packing diagram of **1** showing the displacement of adjacent 2D by half a repeat unit along the crystallographic *b* axis.

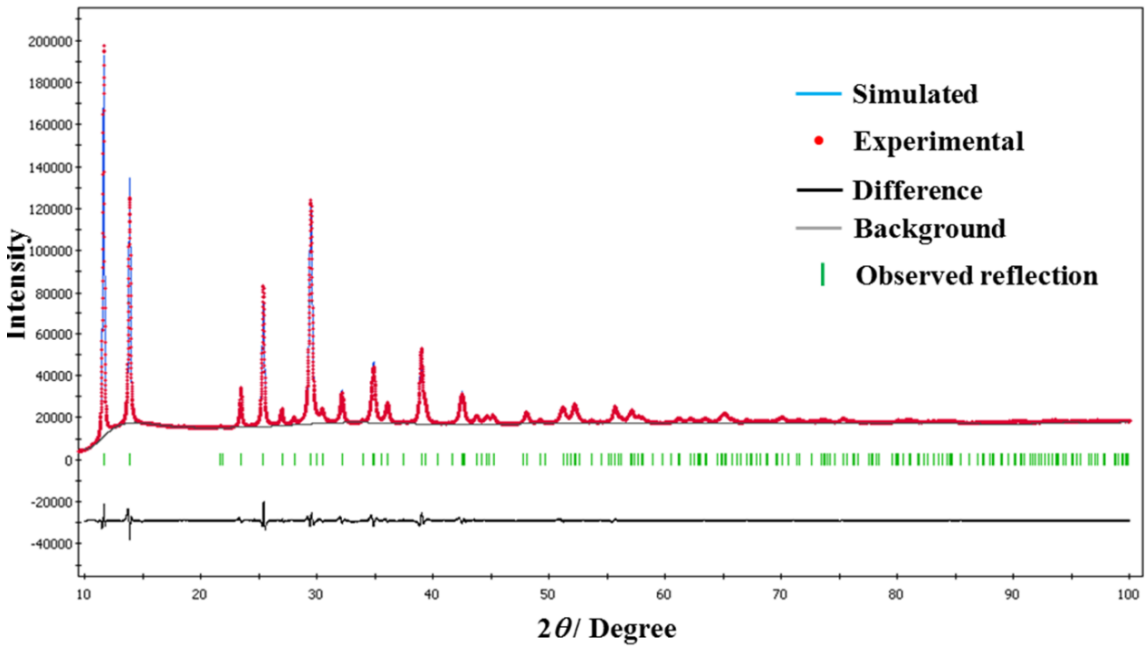

Figure 4. The profile matching pattern for compound **2**. R_{wp} = 2.00%

Table 1. Crystal data and structure refinement parameters of Compound **1.**

parameters	**1**
empirical formula	$C_4H_4CoN_8$
formula weight	223.08
crystal system	Orthorhombic
space group	*Cmcm*
a, Å	15.110(4)
b, Å	7.0972(19)
c, Å	6.6048(18)
V, Å^3	708.3(3)
Z	2
T, K	100
D_{calcd}, g/cm^3	2.092
F (000)	444
reflections [$I>2\sigma(I)$]	450
R_{int}	0.020
GOF on F^2	1.22
$R_1{}^a$	0.0174
$R_w{}^b$	0.0558

$^a R = \sum||F_o|-|F_c||/\sum|F_o|$. $^b R_w = [\sum\{w(F_o^2-F_c^2)^2\}/\sum\{w(F_o^2)^2\}]^{1/2}$

Table 2. Selected bond lengths (Å) and angles (º) for Compound **1**.

Co1-N2	2.1473(12)	Co1-N5	2.1512(15)
N2-Co1-N5 a	91.86(4)	N2-Co1-N2c	180.00
N2-Co1-N5	88.14(4)	N2-Co1-N2b	100.64(5)
N2-Co1-N5	88.14(4)	Co1-N2-Co1a	100.53(7)
N2-Co1-N2a	79.36(5)	N5-Co1-N5a	180.00

Symmetry Codes: a = -x, y, ½-z, b = x, -y, 1-z, c = -x, -y, 1/2+z

4A.3.2 Magnetic properties

Figure 5 shows the $\chi_M T$ *vs*. T plot of **1** measured at 100 Oe in field-cooled (FC) condition. At 300 K, the $\chi_M T$ value is 4.16 cm^3 K mol^{-1}, which is significantly higher than the spin-only value of 1.87 cm^3 K mol^{-1}, typical for one S = 3/2 Co(II) ion, due to the orbital contribution of high spin Co(II) centres in octahedral (Oh) geometry. The $\chi_M T$ product increases gradually from room temperature up to 50 K and then increases rapidly and finally decreases beyond 11 K. The spontaneous increase in $\chi_M T$ at low temperature indicates a possibility of long range FM ordering, while the decrease below 11 K can be the result of spin-orbit coupling of Co(II) ions in Oh geometry or the AF coupling between Co(II) ions through the pyz linkers.[12] The χ_M *vs*. T plot of **1** (Figure 5b) exhibits a maximum at 9.7 K and thus suggests an AF transition at this temperature. On the other hand, the temperature dependence of the reciprocal susceptibility above 150 K (Figure 5c) follows the Curie–Weiss law with a Weiss constant θ of 25.4 K with C = 3.8 cm^3

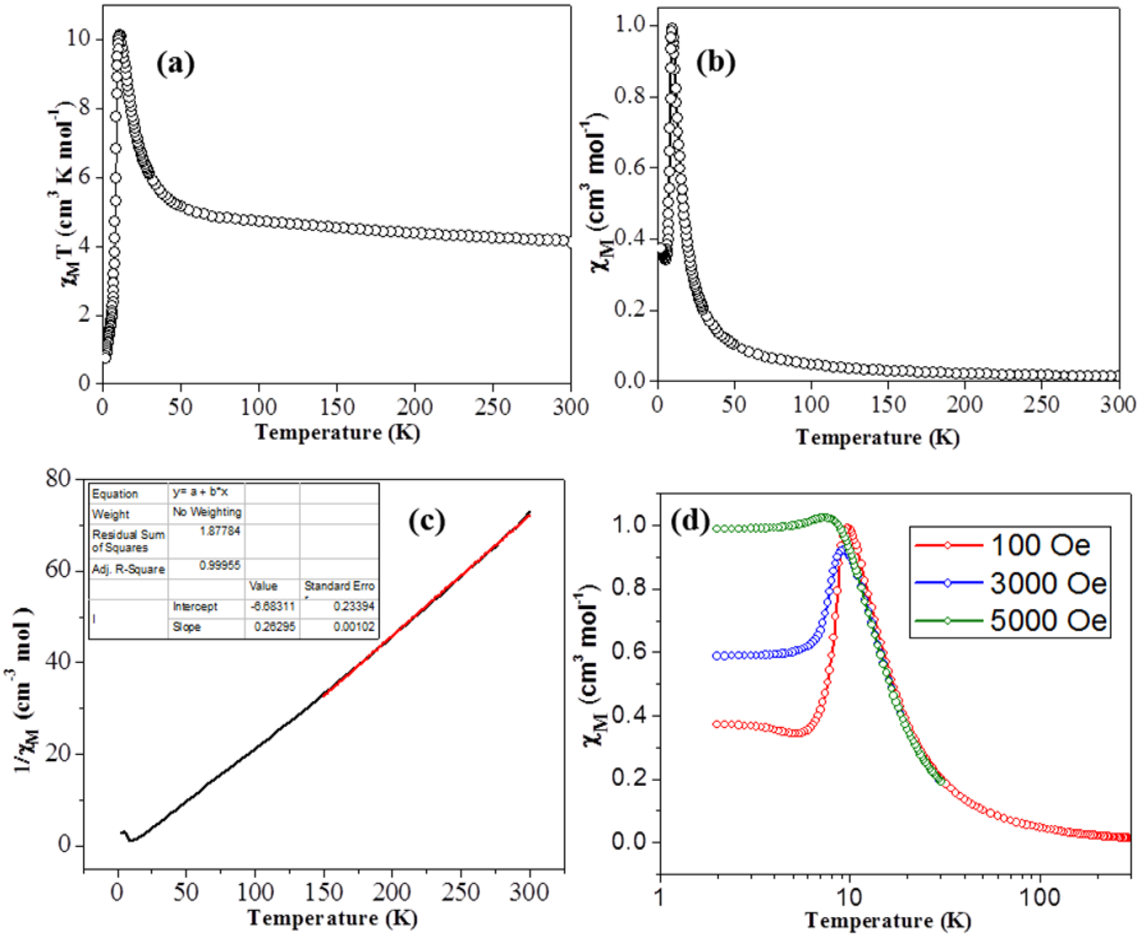

Figure 5. (a) The plots of $\chi_M T$ vs. T for **1**. (b) The temperature dependence of the magnetic susceptibility of **1** at 100 Oe K under field-cooled (FC) conditions. (c) Curie–Weiss fitting for **1** above 150 K. The red line indicates the best fit obtained. Weiss constant (θ) is 25.4 K. (d) Temperature dependence of the magnetic susceptibility of **1** at 100, 3000, and 5000 Oe under field-cooled (FC) condition.

K mol^{-1}, which suggests FM coupling between Co(II) ions, which is mediated by the azide bridge.[11]

The dM/dT *vs.* T plot (Figure 6) exhibits a minimum at 11.5 K and suggests occurrence of a magnetized state. In order to understand the above observation and to investigate the magnetic properties of **1**, variable temperature FC magnetization studies were carried out at different fields (Figure 5d). A strong field dependence of the magnetic susceptibility is observed below T_N. At 100 Oe and 3000 Oe, the magnetic susceptibility shows a maximum demonstrating the AF state. On application of a field of 5000 Oe, the cusp disappears and the susceptibility value tends to saturate. This suggests that the AF transition can be suppressed by applying higher field value (5000 Oe) which overcomes the AF interaction and induce a ferromagnetic-like state having relatively large magnetic

moment. Thus **1** demonstrates field induced phase-transition from antiferromagnetic to ferromagnetic-like state, characteristic for a metamagnet. Such behaviour probably arises from the two competitive interactions; the ferromagnetic exchange prevailing in 1D $[Co^{II}(N_3)Co^{II}]_n$ chains and the antiferromagnetic exchange through pyz linker present in the 2D layer compound (**1**). The end-on azide bridge is well-known to propagate ferromagnetic exchange when the ∠M-N_3-M angle is less than 103-104°[11], and for the present case, the ∠Co-N_3-Co angle is 100.5°which ensue ferromagnetic exchange interaction. On the other hand, antiferromagnetic interaction prevails through pyz linkers, as it has been reported earlier.[12] The magnetic field required to switch an AF to an F interaction is termed as the "critical field (Hc)". To further investigate the metamagnetic behaviour and to check the presence of the critical field, the isothermal magnetization (M) *vs*. field (H) studies were carried out. Figure 7 shows the magnetization ($N\mu_\beta$) vs applied field (H, kOe) plot at 2 K, which shows typical sigmoidal nature expected for a metamagnet. The variation of magnetization in low field is shown in the inset, which shows magnetization increases slightly with increasing field strength because of weak antiferromagnetic interactions (operating through pyz linkers) and subsequently increases sharply for a phase transition to a ferromagnetic-like state. To realize the effect of temperature on the phase transition, experiments are performed at various temperatures (2 K-12 K) and the results are plotted in Figure 8.

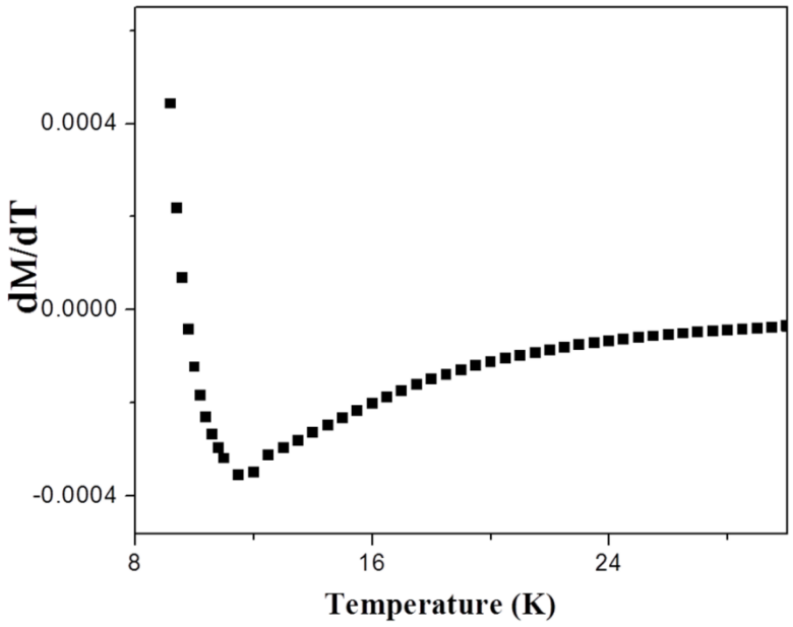

Figure 6. The derivative of magnetization (M) measured at FC condition (100 Oe) *vs*. temperature (T) plot for compound **1**.

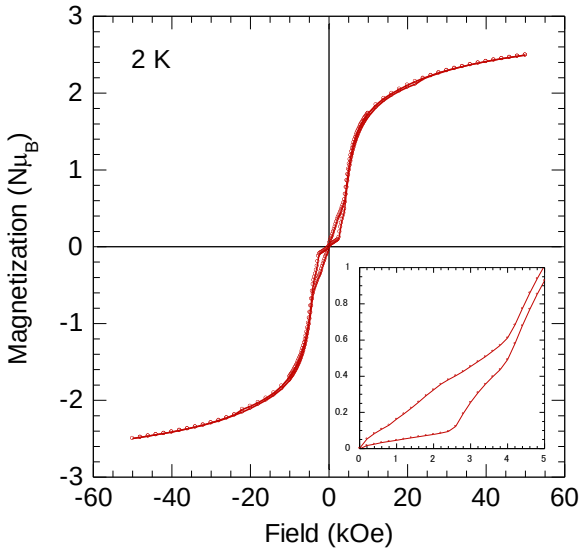

Figure 7. Isothermal magnetization of **1** measured by cycling the field between 50 and -50 kOe at 2 K (inset shows the variation of magnetization in low field).

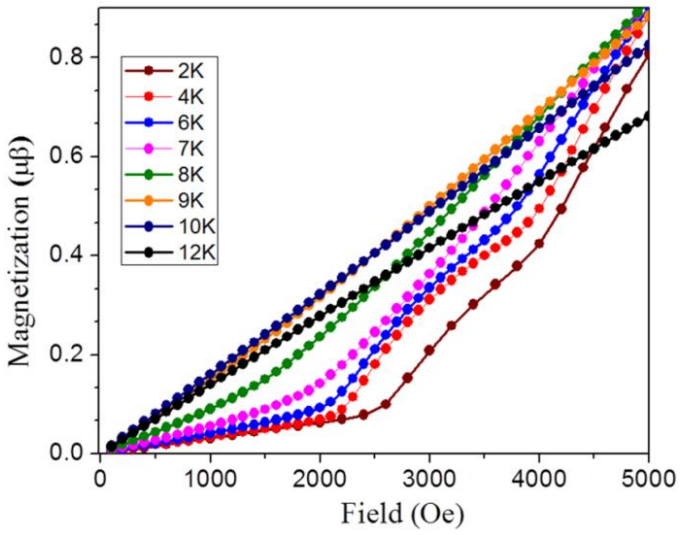

Figure 8. The field dependence of the isothermal magnetization of **1** at the indicated temperatures.

It is observed that for different temperature, the steps in magnetization curve occur at different field values, demonstrating the field-dependent magnetic transition. Above 8 K, the magnetization increases nearly linearly, thus no phase transitions occur at high temperatures. The calculated derivatives dM/dH also show field-induced spin reorientation transitions at critical fields (Figure 9). At the temperature range 2 K-7 K. two steps are observed in dM/dH vs. H plots and the critical fields as a function of temperature are shown in Figure 9b. The metamagnetic transitions at lower temperature

involve higher critical field values, thus suggesting that the antiferromagnetic interaction is stronger at low temperatures. The double sigmoidal shape of magnetization and two peaks in dM/dH *vs*. H plots suggest either occurrence of two step magnetic phase transitions or these transitions are originated from applying fields on the different eigen directions (easy, intermediate, or hard axis) for the polycrystalline sample. At 8 K, only a broad peak is observed in dM/dH vs. H plot and beyond this temperature, the step is suppressed since no transition occurs.

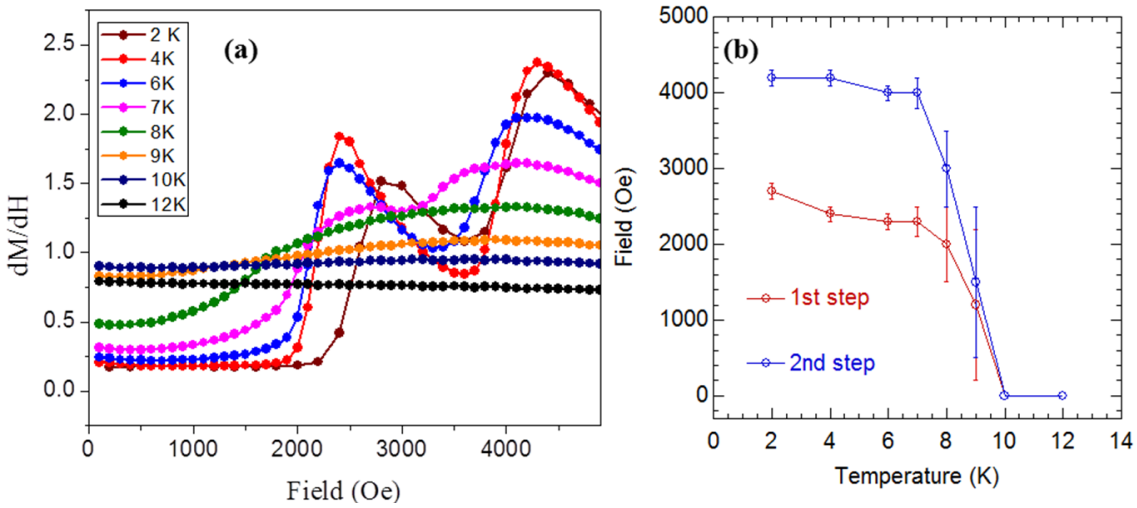

Figure 9. (a) The derivatives of M against field H of at **1** the indicated temperatures. (b) The two critical fields at which steps occur at the indicated temperatures.

It is important to note that in addition to the competitive F/AF exchange interaction through azide or pyz linkers respectively, the high single-ion anisotropy of Co(II) ions also play crucial role to result in the metamagentic behaviour. Similar systems with lack of anisotropic metal ion such as Mn(II) and Cu(II), have shown only weak antiferromagnetic transition.[14] To investigate the magnetic anisotropy in **1**, a single-crystal (dimension 300 x 168 x 25 µm) of **1** was taken and the magnetization was measured by applying magnetic field in three different directions (parallel to the long axis of the crystal, parallel to the short axis of the crystal and perpendicular to the plate), as shown in Figure 10. Clearly, the long axis of the crystal represents an easy axis since the magnetization saturates at lower field value (~6 kOe) in this direction compared to the other directions. Around 3 K, the magnetization plot shows a small step and then again rises steeply, which is attributed to the field-induced metamagnetic transition. On the other hand, the hard plane would be present along the short axis of the crystal as evident from Figure 10, where the magnetization tends to saturates only after 33 kOe. When

magnetic field was applied perpendicular to the plate, the magnetization initially increases slowly and then more steeply beyond 10 kOe and finally tends to saturate slowly. Thus this direction represents an intermediate axis. The above observations clearly advocates the magnetic anisotropy of the system which probably originates from the Co(II) ions having high single-ion anisotropy.

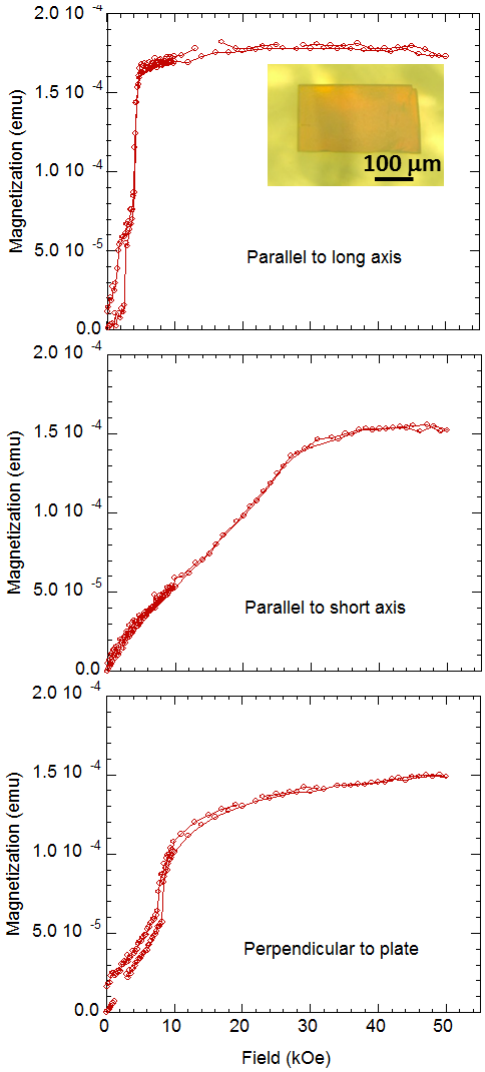

Figure 10. The magnetization *vs.* field plots for a single crystal of **1** by applying magnetic field along three different directions. The photograph of the single-crystal (dimension 300 x 168 x 25 µm) is shown in inset of the top figure.

Compound **2** exhibits similar magnetic properties as **1**, because of their structural similarity. The room temperature $\chi_M T$ value is 1.69 cm^3 K mol^{-1}, typical value for one Ni(II) centre with orbital contribution (Figure 11). The $\chi_M T$ *vs.* T plot of **2** was measured at 100 Oe in field-cooled (FC) condition, which shows continuous increase from room

temperature due to the ferromagnetic interaction through the end-on azide bridge. The $\chi_M T$ profile shows spontaneous increase below 30 K and exhibits a maximum at 23 K below which it decreases. The χ_M *vs*. T plots (Figure 12) shows that the magnetization value starts increasing rapidly below 50 K and the zero field-cooled (ZFC) and FC plots diverges below 25 K, suggesting presence of a long-range magnetically ordered state. Below 25 K, a maximum is observed in The FC magnetization shows a maximum at 16 K, which originates from the antiferromagnetic interaction through pyz bridge (Figure 12). The Curie–Weiss fitting of the temperature dependence of the reciprocal susceptibility above 100 K (Figure 13) yields a Weiss constant θ of 54.7 K with C = 1.4 cm^3 K mol^{-1}, which suggests ferromagnetic coupling between Ni(II) ions, which is mediated by the azide bridge. The dM/dT *vs*. T plot (Figure 14) shows a minimum at 28 K, which further indicates that beyond this temperature a magnetized state exists.

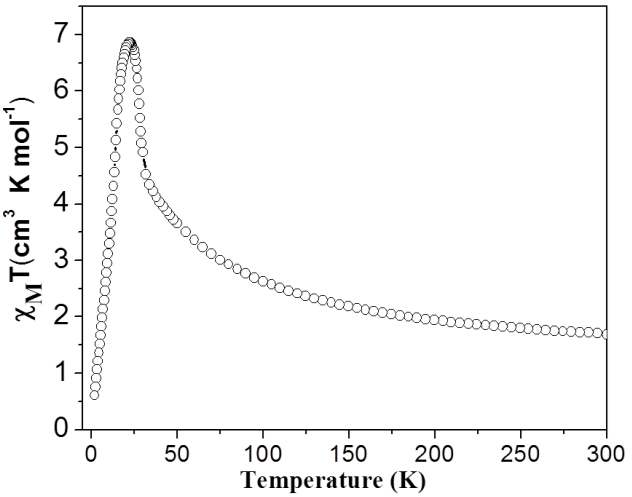

Figure 11. The plots of $\chi_M T$ vs. T for **2**.

To clarify the above observation and to further investigate the occurrence of a field-dependent magnetic transition, magnetization was measured by applying different field (Figure 12b). The temperature dependent field-cooled (FC) and zero field-cooled (ZFC) susceptibility were measured at 100 Oe, which show clear divergence below 28 K, thus further suggesting the presence of a magnetized state below this temperature. Strong field dependence is also observed in the magnetic susceptibility measured at 10 Oe, 100 Oe, 500 Oe, 5000 Oe, 20 kOe and 30 kOe under FC condition (Figure 12b). It is observed that the value of the spontaneous magnetization is highest at 10 Oe and gradually decreases with increasing magnetic field value. When the applied field value is 30 kOe, no maxima is found in the variable temperature susceptibility plot and the magnetization value

saturates at low temperature, suggesting that a field of 30 kOe is sufficient to supress the magnetic transition. These observations confirm a field-induced antiferromagnetic to ferromagnetic transition in **2**. The magnetization ($N\mu_\beta$) vs applied field (H, kOe) plot at 2 K (Figure 15) shows typical sigmoidal nature expected for a metamagnet with $M_{saturation}$ and $M_{remanance}$ values of 2 μβ and 0.0094 μβ respectively. The dM/dH *vs*. H plot (Figure 16) shows peak at 24 kOe, suggesting that the metamagnetic transition occurs at this field (Hc =24 kOe).

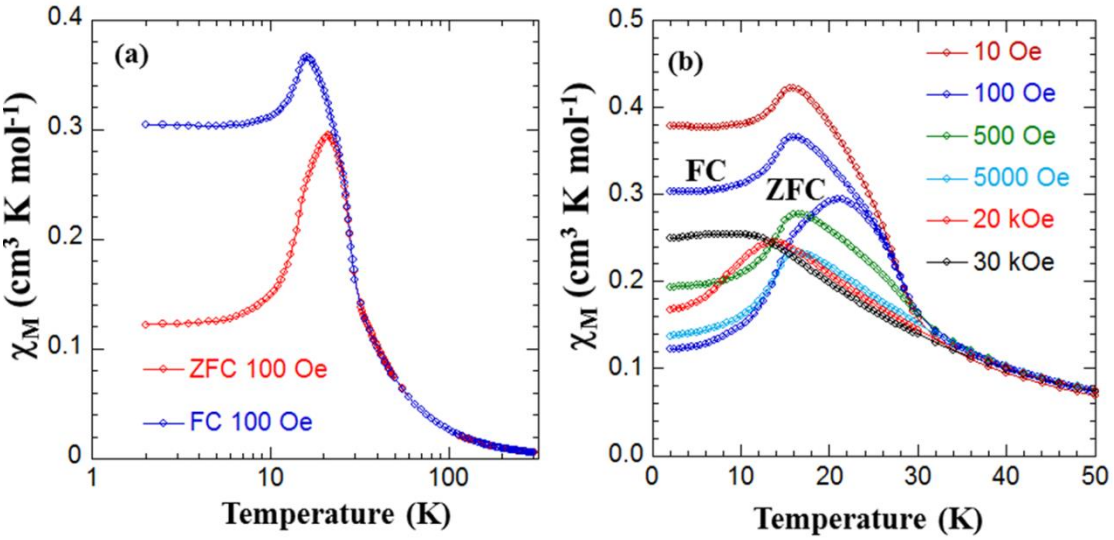

Figure 12. (a) The temperature dependence of the magnetic susceptibility of **2** at 100 Oe under field-cooled (FC) and zero field-cooled (ZFC) conditions. (b) The temperature dependence of the magnetic susceptibility of **2** at 10 Oe, 100 Oe, 500 Oe, 5000 Oe, 20 kOe and 30 kOe under FC condition. The temperature dependence of the magnetic susceptibility at 100 Oe under ZFC condition is also shown.

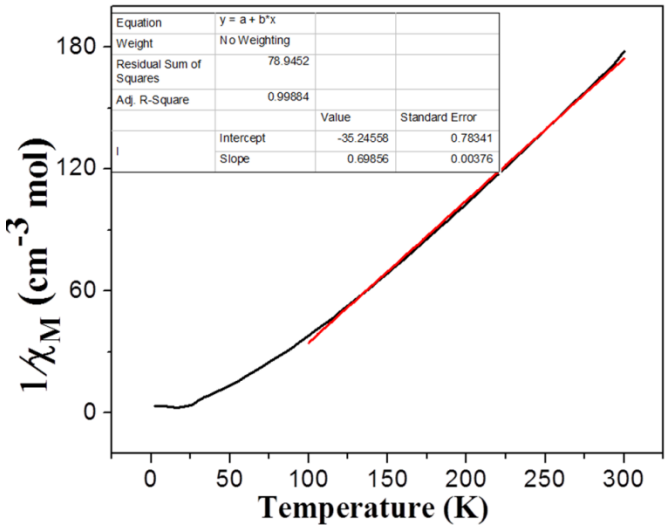

Figure 13. Reciprocal molar susceptibility as function of temperature for **2**; solid red line indicates Curie-Weiss fitting in the range 100-300 K.

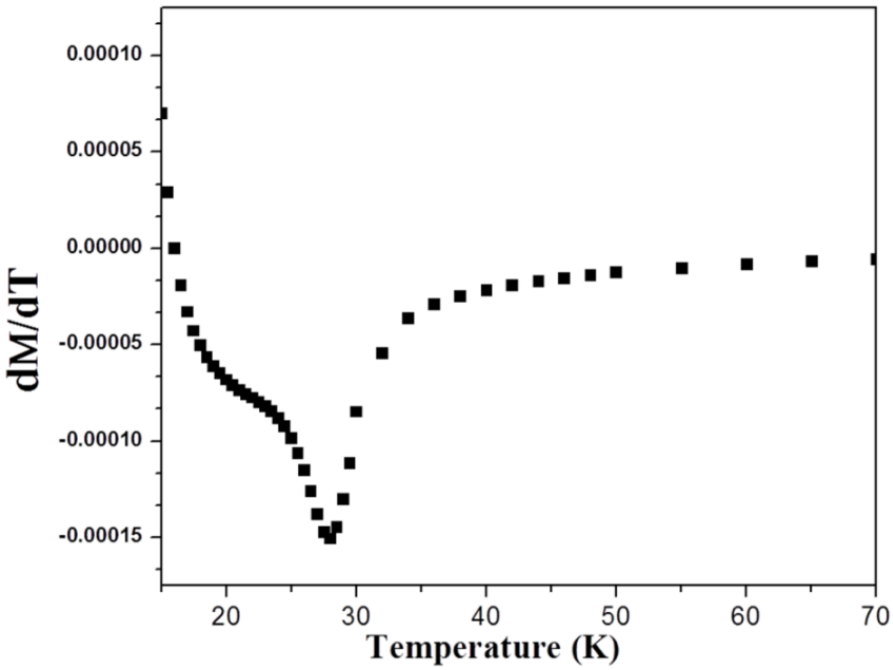

Figure 14. The derivative of magnetization (M) measured at FC condition (100 Oe) *vs*. temperature (T) plot for compound **2**.

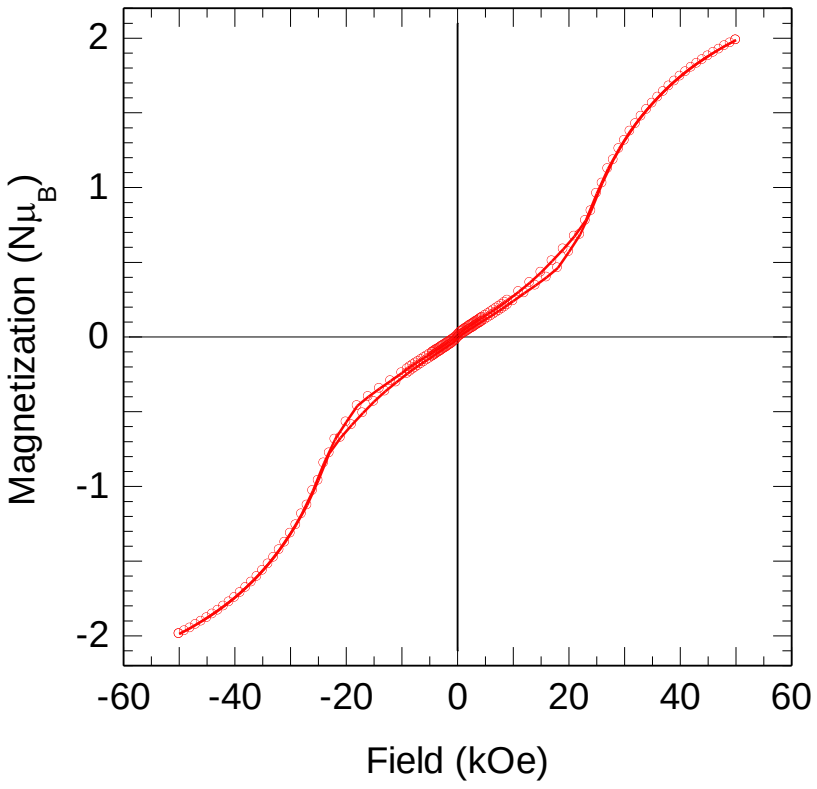

Figure 15. Isothermal magnetization of compound **2** at 2 K.

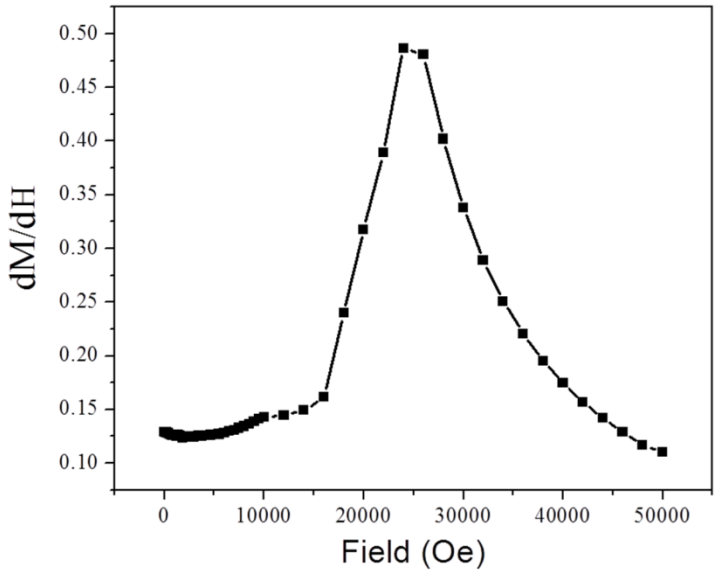

Figure 16. The derivative of magnetization (M) against H (Oe) at 2 K for compound **2**.

4A.4 SUMMARY

In this chapter, synthesis and detail magnetic studies of two new 2D metamagnetic compounds are presented. The compounds have been synthesized by adopting judicious self-assembly approach using anisotropic metal ions, proper coligand (pyz) and azide ligand. Unlike previous reports, detail magnetic studies including various temperature and field-dependent measurements were performed to understand the fundamental magnetic properties of the two compounds. Competition of the ferromagnetic interaction between the metal ions through end-on bridged azido ligands and antiferromagnetic interaction operating through the pyz linker result in metamagnetic transitions in the compounds. Presence of magneto-crystalline anisotropy was also demonstrated in one of the compounds, by aligning a single-crystal in different eigen directions and such studies have been performed for the first time in similar 2D systems. Synthesis, structure and magneto-structural correlations of such anisotropic metal-organic coordination compounds is highly motivating to understand their magnetic properties in depth and further make use of the compounds in suitable applications, like magnetic refrigeration which needs significant research. Adopting proper synthetic strategies, design of new metamagnetic compounds with novel structural topologies would facilitate the fabrication of desired magnetic device and would also shed light on the fundamental magnetic properties of these systems.

4A.5 REFERENCES

1. J. S. Miller, *Chem. Soc. Rev*., 2011, **40**, 3266.
2. (*a*) M. L. Taliaferro, F. Palacio and J. S. Miller, *J. Mater. Chem*., 2006, **16**, 2677; (*b*) S. J. Blundell, T. Lancaster, M. L. Brooks, F. L. Pratt, M. L. Taliaferro and J. S. Miller, *Phys. B: Condens. Matter*, 2006, **374–375**, 114; (*c*) H. Miyasaka, T. Izawa, M. Yamashita and K. R. Dunbar, *J. Am. Chem. Soc*., 2006, **128**, 11358; (*d*) R. S. Fishman, S. Okamoto, W. W. Shum and J. S. Miller, *Phys. Rev. B: Condens. Matter*, 2009, **80**, 064401; (*e*) L. M. Toma, C. Ruiz-Pérez, J.Pasán, W. Wernsdorfer, F. Lloret and M. Julve, *J. Am. Chem. Soc.*, 2012, **134**, 15265.
3. B.S. Shivaram, D.G. Hinks, M.B. Maple and P. Kumar, *Phys. Rev., B*, 2014, **89**, 241107.
4. B.S. Shivaram, Brian Dorsey, D.G. Hinks and Pradeep Kumar, *Phys. Rev. B*, 2014, **89**, 161108.
5. (*a*) G. J. Halder, C. J. Kepert, B. Moubaraki, K. S. Murray and J. D. Cashion, *Science*, 2002, **298**, 1762; (*b*) M. Kurmoo, *Chem. Soc. Rev.*, 2009, **38**, 1353; (*c*) H. Kumagai, H. Sobukawa and M. Kurmoo, *J. Mater. Sci.*, 2008, **43**, 2123.
6. (*a*) P. Dechambenoit and J. R. Long, *Chem. Soc. Rev.*, 2011, **40**, 3249; (*b*) N. Guillou, S. Pastre, C. Livage and G. Férey, *Chem. Commun*., 2002, 2358; (*c*) C. N. R. Rao, A. K. Cheetham and A. Thirumurugan, *J. Phys.: Condens. Matter*, 2008, **20**, 083202.
7. (*a*) A. Hazra, P. Kanoo and T. K. Maji, C*hem. Commun.*, 2011, **47**, 538; (*b*) A. Chakraborty, K. L. Gurunatha, A. Muthulakshmi, S. Dutta, S. K. Pati and T. K. Maji, *Dalton Trans*. 2012, **41**, 5879; (*c*) A. Chakraborty, B. K. Ghosh, J. R. Arino, J. Ribas and T. K. Maji, *Inorg. Chem*. 2012, **51**, 6440; (*d*) A. Chakraborty, L. S. Rao, A. K. Manna, S. K. Pati, J. Ribas and T. K. Maji, *Dalton Trans*. 2013, **42**, 10707; (*e*) A. Chakraborty, L. S. Rao, A. Kumari, J. Ribas and T. K. Maji, *Inorg. Chem*, 2014, **53**, 11991.
8. M. Monfort, I. Resino, J. Ribas, and H. Stoeckli-Evans, *Angew. Chem. Int. Ed*. 2000, **39**,191.
9. (*a*) O. Kahn, M. F. Charlot, *Nouv. J. Chim.*, 1980, **4**, 567; *(b)* P. J. Hay, J. C. Thibeault and R. J. Hoffmann, *J. Am. Chem. Soc.*, 1975, **97**, 4884; (*c*) V. M. Crawford, H. W. Richardson, J. R. Wasson, D. J. Hcdgson and W. E. Hatfield, *Inorg. Chem.*, 1976, **15**, 2107; (*d*) D. J. Hodgson, *Inorg. Chem.*, 1976, **15**, 3174; (*e*) L. K. Thompson and S. K. Tandon, *Comments Inorg. Chem*., 1996, **18**, 125; (*f*) R.

D. Willett, D. Gatteschi and O. Kahn, *Magneto-Structural Correlations in Exchange Coupled Systems*, Dordrecht, The Netherlands, 1985.

10. (*a*) Y.-F. Zeng, X.Hu, F.-C. Liu and X.-H. Bu, *Chem. Soc. Rev*., 2009, **38**, 469; (*b*) C. Adhikary and S. Koner, *Coord. Chem. Rev*., 2010, **254**, 2933; (*c*) S. Naiya, C. Biswas, M. G. B. Drew, C. J. Gomez-Garcıa, J. M. Clemente-Juan, and A. Ghosh, *Inorg. Chem*., 2010, **49**, 6616; (*d*) S. Mukherjee, B. Gole, Y. Song, and P. S. Mukherjee, *Inorg. Chem.*, 2011, **50**, 3621.
11. E. Ruiz, J. Cano, S. Alvarez and P. Alemany, *J. Am. Chem. Soc*., 1998, **120**, 11122.
12. (*a*) H. W. Richardson and W. E Hatfield, *J. Am. Chem. Soc.*, 1976, **98**, 835; (*b*) A. Chakraborty, R. Haldar and T. K. Maji, *Cryst. Growth Des*. 2013, **13**, 4968.
13. X. Hao, Y.Wei and S. Zhang, *Chem. Commun.*, 2000, 2271.
14. (*a*) J. L. Manson, A. M. Arif and J. S. Miller, *Chem. Commun.*, 1999, 1479; (*b*) W.Dong, Y. Ouyang, D.-Z. Liao, S.-P. Yan, P. Cheng and Zong-Hui Jiang, *Inorg. Chim. Acta*, 2006, **359**, 3363.
15. (*a*) SMART (V 5.628), SAINT (V 6.45a), XPREP, SHELXTL; Bruker AXS Inc. Madison, Wisconsin, USA, 2004; (*b*) G. M. Sheldrick, Siemens Area Detector Absorption Correction Program, University of Göttingen, Göttingen, Germany, 1994; (*c*) A. Altomare, G. Cascarano, C. Giacovazzo, A. Gualaradi, *J. Appl. Cryst.*, 1993, **26**, 343; (*d*) G. M. Sheldrick, SHELXL-97, Program for Crystal Structure Solution and Refinement; University of Göttingen, Göttingen, Germany, 1997; (*e*) A. L. Spek, *J. Appl. Cryst.*, 2003, **36**, 7; (*f*) L. J. Farrugia, WinGX - A Windows Program for Crystal Structure Analysis. *J. Appl. Crystallogr.*, 1999, **32**, 837.

Chapter 4B

Bifunctional Co(II)-Ag(I) and Ni(II)-Ag(I) Frameworks: Modulation of Magnetic Property and CO_2 Uptake Based on Organic Pillars

Abstract

This chapter articulates synthesis, characterization, adsorption and magnetic properties of four isomorphous bimetallic Co(II)/Ni(II)-Ag(I) 3D porous frameworks synthesized based on a mixed-ligand system. The cyanide-bridged M(II)-Ag(I) bimetallic compounds, $[M^{II}(L)\{Ag(CN)_2\}_2 \cdot 5H_2O]$ [**1**: L= piperazine, M(II) = Co; **2**: L= piperazine, M(II) = Ni; **3**: L = 1,4-diazabicyclo[2.2.2]octane (dabco), M(II) = Co; **4**: L = pyrazine, M(II) = Co)] have been synthesized by liquid phase diffusion method at room temperature. Structure determination revealed that all the compounds have α-polonium type topology where $Ag(CN)_2^-$ metallo-ligand has been used to generate 2D -M(II)-CN-Ag(I)-CN-M(II)- layers which are further linked by different organic pillars to construct 3D porous pillared-layered structure. The magnetic and adsorption properties of these compounds have been tuned by systematic variation of the pillars (piperazine, pyrazine and dabco). Temperature dependent magnetic study reveals that at low temperature magnetized states exist for compound **1**, **2** and **3** and spin canting behaviour is evident; while **4** exhibits dominant antiferromagnetic behaviour. Compounds **1**, **2** and **4** also exhibit permanent porosity as established by gas adsorption studies whereas **3** does not adsorb any gas. Compound **1** exhibits selective CO_2 uptake properties over other gases, such as N_2, H_2, O_2 and Ar at 195 K, suggesting that quadrupolar CO_2 molecules interact effectively with the pore surfaces decorated with polar –CN group.

Paper based on this study:

A. Chakraborty, R. Haldar, T. K. Maji, *Cryst. Growth Des*. 2013, **13**, 4968.

4B.1 INTRODUCTION

Metal-organic frameworks (MOFs) or porous coordination polymers (PCPs)[1-3] have been well-explored over the last two decades to achieve applications in diverse fields like gas storage[4-6], catalysis[7-9], separation[10,11], drug delivery[12,13] and magnetism.[14-19] Recently, there is an upsurge in research to design multifunctional MOFs that combine a set of well-defined properties e.g. porosity and optical property, porosity and magnetism.[20-23] Combining magnetism and porosity in a single material[22-24] is not straightforward because of the incompatibility in the properties; the strength of magnetic coupling decreases with distance while porosity is usually enhanced with the large separation between the metal nodes. However, there are certain MOFs where the structural foundation is built by the infinite inorganic array (like -M-O(H)-M-, -M-CN-M-) which are extended by the organic/inorganic linkers to higher dimension.[11, 24a] These MOFs serve as ideal platforms to study both magnetic and porous properties. There are few compounds so far reported showing both long-range magnetic ordering and porous properties; especially weak ferromagnetism or spin canting[25-27] have been rarely achieved for truly microporous solids.[28-30] Hence it is highly motivating to construct porous frameworks exhibiting both spin canting and guest selectivity, such as selective CO_2 adsorption properties which is quite relevant in the context of CO_2 separation from post-combustion flue gas or pre-combustion natural gas.[31-36]

Construction of a spin-canted system requires sufficient anisotropy and an appropriate ligand system is necessary to incorporate structural anisotropy as well as the magnetic interaction between the metal centres. In 3D MOFs, an extended anisotropic 3D system based on the anisotropic metal ions like Co(II), Ni(II) or Mn(II) can direct spin canting, while the suitable microporous nature may ensue guest selectivity. Moreover, a fine tuning in the organic linkers would allow in subtle changes in magnetic and porous properties. In this chapter, we envisage fabrication of a series of bifunctional porous magnetic frameworks and the systematic study of variation of the properties with structural modification. We have chosen assembly of different small exobidentate organic linkers and dicyanoargentate(I), $[Ag(CN)_2]^-$ with Co(II)/Ni(II) metal ions. $[Ag(CN)_2]^-$ can act as a metallo-ligand[37] which is yet to be properly explored in construction of functional MOF system and a recent report shows this ligand can render long range magnetic ordering through the five atom NC–Ag–CN bridge.[38] We envisioned that employment of $[Ag(CN)_2]^-$ along with anisotropic Co(II)/Ni(II) ions would generate a

square grid 2D magnetic net and further incorporation of a second spacer like piperazine, pyrazine and 1,4-diazabicyclo[2.2.2]octane into this 2D layer would ensue 3D magnetic porous structures. Introduction of these different spacers having different shape, size and backbone would also modulate the magnetic and porous properties of these 3D frameworks (Scheme 1). Moreover, preparation of isostructural frameworks incorporating different paramagnetic metal ions would also render versatile magnetic systems. Herein we report synthesis and structural characterization of four isomorphous 3D porous frameworks $[M^{II}(L)\{Ag(CN)_2\}_2 \cdot xH_2O]_n$ [**1**: L = piperazine (pip), M = Co; **2**: L = piperazine, M = Ni; **3**: L = 1,4-diazabicyclo[2.2.2]octane (dabco), M = Co; **4**: L= pyrazine (pz), M=Co] obatined by the self-assembly of $[Ag(CN)_2]^-$ and different organic pillars with Co(II)/Ni(II) ions. Compound **1, 2** and **3** show canted antiferromagnetism, while **4** exhibits dominant antiferromagnetic behaviour exerted by the pyrazine linker. Gas adsorption properties suggest permanent porosity in **1, 2** and **4,** whereas **3** is nonporous in nature. Furthermore, gas adsorption measurements at 195 K with several gases unveil CO_2 selectivity for **1**.

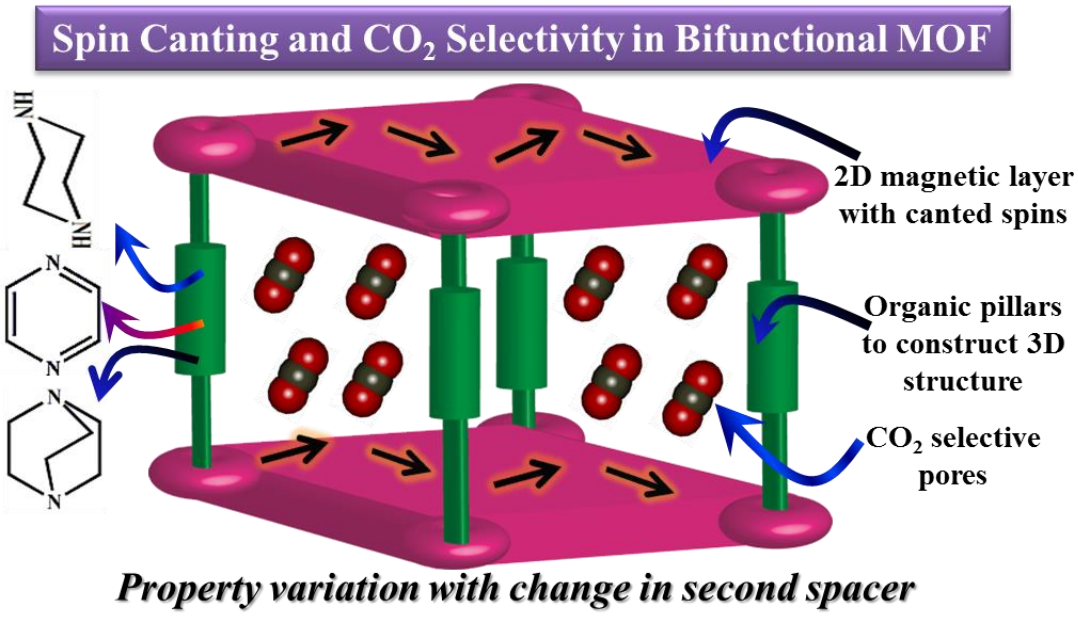

Scheme 1. Construction of 3D bifunctional framework where 2D magnetic layer are pillared by different organic linkers. The structural topology results spin canting and CO_2 selectivity and the properties are tuned by variation of the second spacer.

4B.2 EXPERIMENTAL SECTION

4B.2.1 Materials

All the reagents and solvents employed were commercially available and used as supplied without further purification. $Co(OAc)_2 \cdot 4H_2O$, $Ni(OAc)_2 \cdot 4H_2O$, piperazine and $K[Ag(CN)_2]_2$ were obtained from the Aldrich Chemical Co.

4B.2.2 Synthesis

$[Co(pip)\{Ag(CN)_2\}_2 \cdot xH_2O]_n$ (1): An aqueous solution (10 mL) of $K[Ag(CN)_2]$ (1 mmol, 0.199 g) was mixed with an aqueous solution (10 mL) of piperazine (0.5 mmol, 0.043 g) and the resulting solution was stirred for 20 min. to mix well. $Co(OAc)_2 \cdot 4H_2O$ (0.5 mmol, 0.124 g) was dissolved in 10 mL methanol and 2.5 mL of this metal solution was slowly and carefully layered with the above mixed ligand solution using 1 mL buffer (1:1 of water and MeOH) solution in a crystal tube, which was sealed and left undisturbed at room temperature. Slow diffusion yielded transparent orange block crystals of **1** after 15 days. Bulk amount of the compound was synthesized by direct mixing of the corresponding ligand solution with methanolic solution of Co(II). Yield 82%, relative to Co(II). Selected IR data (KBr, cm^{-1}); 3495 br, 3260 m, 2979 m, 2936 m, 2167 s, 1448 m, 1417 m, 1068 m, 1007 m, 877 s, (Figure 1). Compound purity was verified by PXRD (Figure 2). The IR spectra (Figure 1) show presence of water molecules. Elemental analysis shows the following result: C, 19.68; H, 2.49; N, 17.13. These values are close for $[Co(pip)\{Ag(CN)_2\}_2 \cdot H_2O]_n$ ($C_8H_{12}CoAg_2N_6O$: C, 19.89; H, 2.50; N, 17.40). This result is in accordance with the thermogravimetric analysis (Figure 3), which shows a loss corresponding to one water molecule.

$[Ni(pip)\{Ag(CN)_2\}_2 \cdot xH_2O]_n$ (2): Similar methodology was adopted to synthesize compound **2** except that $Co(OAc)_2 \cdot 4H_2O$ was replaced by $Ni(OAc)_2 \cdot 4H_2O$ (0.5 mmol, 0.124 g). Blue colour block shaped crystals of **2** were isolated after 15 days. Yield 79%, relative to Ni(II). Selected IR data (KBr, cm^{-1}); 3510 br, 3270 m, 2981 m, 2938 m, 2176 s, 1462 m, 1407 m, 1075 m, 1007 m, 883 s, (Figure 1). Compound purity was verified by PXRD (Figure 4). Elemental analysis shows the following result for **2**: C, 19.54; H, 2.26; N, 17.81, which resembles $[Ni(pip)\{Ag(CN)_2\}_2 \cdot H_2O]_n$ ($C_8H_{12}NiAg_2N_6O$: C, 19.91; H, 2.50; N, 17.41).

$[Co(dabco)\{Ag(CN)_2\}_2 \cdot xH_2O]_n$ (3) and $[Co(pz)\{Ag(CN)_2\}_2 \cdot xH_2O]_n$ (4) Synthetic procedure similar to **1** was adopted to synthesize compound **3** and **4** where piperazine was

replaced by dabco (0.5 mmol, 0.056 g) and pyrazine (0.5 mmol, 0.040 g) respectively. For **3**, yield 81%, relative to Co(II). Selected IR data (KBr, cm^{-1}); 3440 br, 2980 m, 2960 m, 2170 s, 1460 s, 1318 s, 1051 m, 997 m, 923 m, 790 m (Figure 1). Compound purity was verified by PXRD (Figure 5). Elemental analysis shows the following result for **3**: C, 23.78; H, 2.82; N, 16.34, which resembles $[Co(dabco)\{Ag(CN)_2\}_2 \cdot H_2O]_n$ ($C_{10}H_{14}CoAg_2N_6O$: C, 23.6; H, 2.77; N,16.51). For **4**, yield 75%, relative to Co(II). Selected IR data (KBr, cm^{-1}); 3440 br, 3120 m, 2170 s, 1572 m, 1420 s, 1165s m, 1130 m, 1090 s, 1060 s, 806 s, (Figure 1). Compound purity was verified by PXRD (Figure 6) and elemental analysis. Elemental analysis shows the following result for **4**: C, 20.48; H, 1.44; N, 17.56, which resembles $[Co(pz)\{Ag(CN)_2\}_2 \cdot H_2O]_n$ ($C_8H_6CoAg_2N_6O$: C, 20.15; H, 1.27; N,17.62).

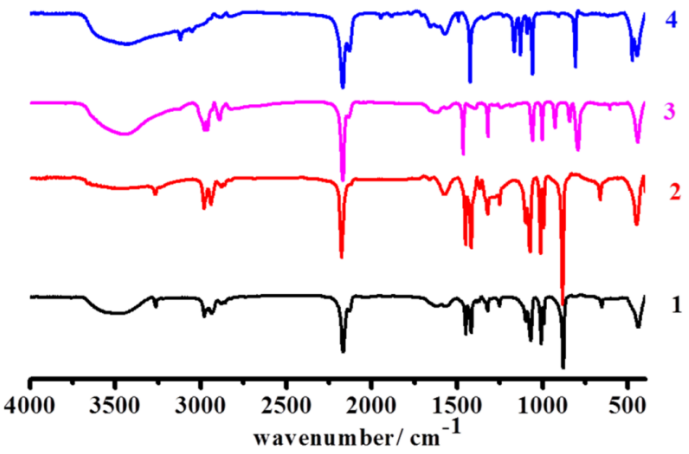

Figure 1. FT-IR spectra for compounds **1, 2, 3** and **4**.

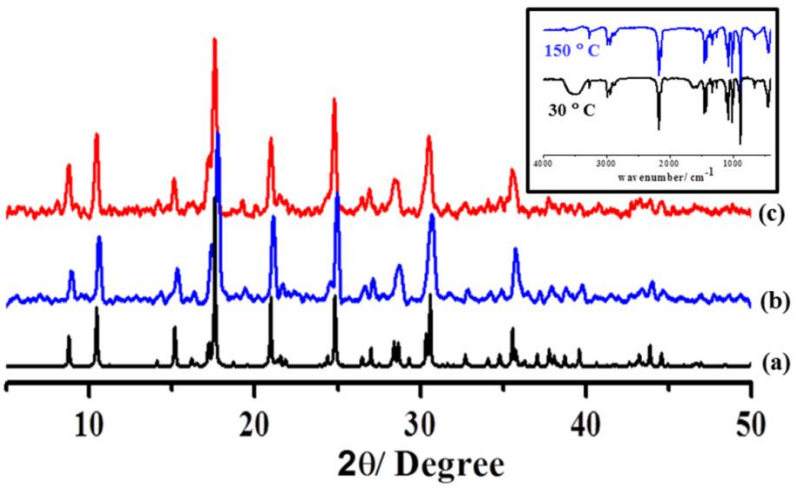

Figure 2. PXRD patterns of **1** in different state: (a) simulated; (b) as-synthesized; (c) desolvated at 160 ºC for 12 h. The inset shows IR spectra for **1** at 30 ºC and 150 ºC.

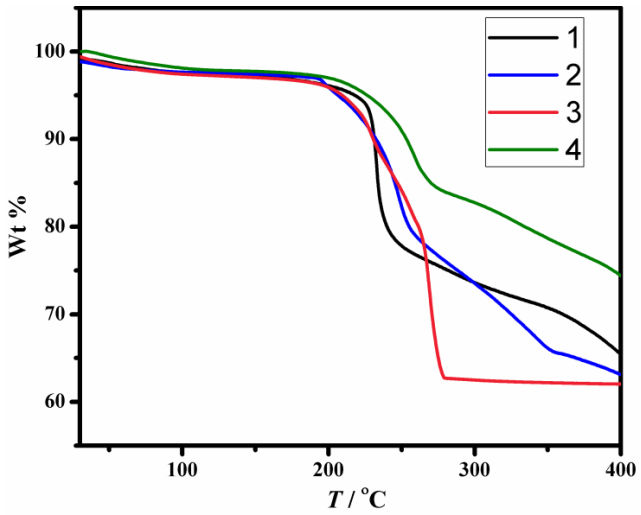

Figure 3. TGA curve for compounds **1, 2**, **3** and **4** in the temperature range 25−400 ºC (heating rate 5 °C min^{-1} under nitrogen).

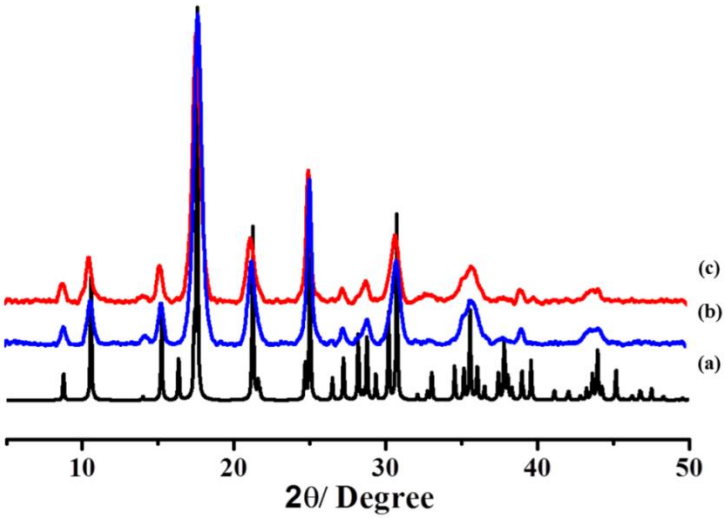

Figure 4. PXRD patterns of **2** in different state: (a) simulated; (b) as-synthesized; (c) desolvated at 160 ºC for 12 h.

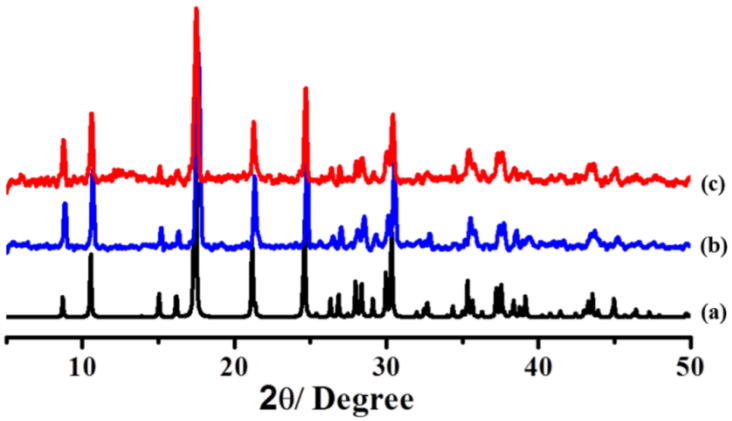

Figure 5. PXRD patterns of **3** in different state: (a) simulated; (b) as-synthesized; (c) desolvated at 160 ºC for 12 h.

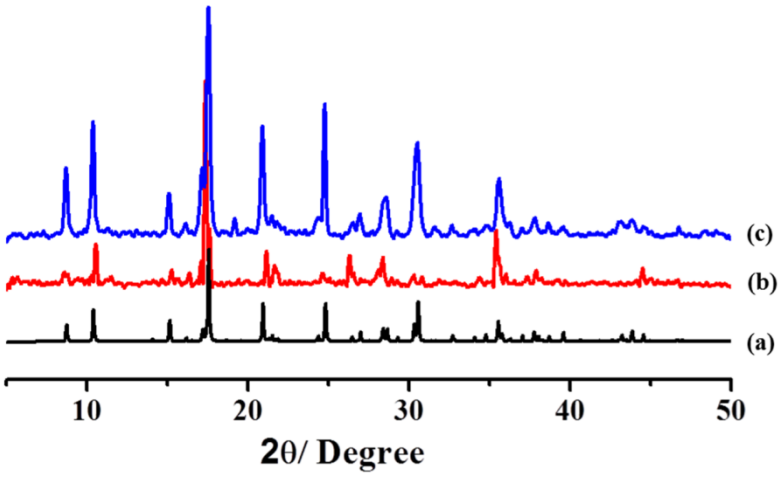

Figure 6. PXRD patterns of **4** in different state: (a) simulated; (b) as-synthesized; (c) desolvated at 160 ºC for 12 h.

4B.2.3 Single-crystal X-ray Diffraction

X-ray single-crystal structural data of **1**- **4** were collected on a Bruker Smart–CCD diffractometer equipped with a normal focus, 2.4 kW sealed tube X-ray source with graphite monochromated Mo–Kα radiation (λ = 0.71073 Å) operating at 50 kV and 30 mA. The SAINT program[39a] was used for integration of diffraction profiles and absorption correction was made with SADABS[39b] program. All the structures were solved by SIR 92[39c] and refined by full matrix least square method using SHELXL 97.[39d] All the non-hydrogen atoms were refined anisotropically and all the hydrogen atoms were fixed by HFIX and placed in ideal positions, except compound **4**. In **4**, the C3 atom of pyrazine pillar is in positional disorder and has been resolved in terms of occupancy. No hydrogen atom could be added due to such disorder. The solvent water molecules were highly disordered and hence could not be located. We have employed PLATON/SQUEEZE[39e] to produce a set of solvent-free diffraction intensities; the structures were then refined again using the data generated. All calculations were carried out using SHELXL 97, PLATON[39e] and WinGX system, Ver 1.70.01.[39f] All crystallographic and structure refinement data of **1-4** are summarized in Table 1. Selected bond lengths and angles are displayed in Table 2.

4B.2.4 Physical Measurements

Elemental analyses were carried out using a Perkin Elmer 2400 CHN analyzer. IR spectra were recorded on a Bruker IFS 66v/S spectrophotometer using KBr pellets in the region 4000–400 cm^{-1}. Thermogravimetric analyses (TGA) were carried out on METTLER

TOLEDO TGA850 instrument in the temperature range of 25–400 °C under nitrogen atmosphere (flow rate of 50 mL min^{-1}) at a heating rate of 5 °C min^{-1}. Powder X-ray diffraction (PXRD) patterns were recorded on a Bruker D8 Discover instrument using Cu–Kα radiation. DC magnetic susceptibility data of polycrystalline powder samples of **1-4** were collected on a Vibrating Sample Magnetometer, PPMS (Physical Property Measurement System, Quantum Design, USA) in the temperature range of 2 K to 300 K with different applied field (50, 100 and 500 Oe). Field variation (−5 kOe to 5 kOe) magnetization measurement was carried out at 2 K. The ac magnetic susceptibility measurements at different frequencies were carried out at H_{ac} = 5 Oe. Elemental analyses and TGA suggest presence of one guest water molecule in **1-4** and all the calculations for the magnetic data were carried out considering the molecular weight having the formula $[M^{II}(L)\{Ag(CN)_2\}_2 \cdot H_2O]_n$ [**1**: L= piperazine, M = Co; **2**: L= piperazine, M = Ni; **3**: L = 1,4-diazabicyclo[2.2.2]octane (dabco), M = Co; **4**: L = pyrazine, M = Co].

4B.2.5 Adsorption Measurements

Adsorption isotherms of CO_2, N_2, H_2, Ar, O_2 at 195 K and N_2 at 77 K and 195 K were recorded with the dehydrated samples using QUANTACHROME QUADRASORB-SI analyser. To prepare the dehydrated samples of **1**, **2** , **3** and **4** (**1′, 2′, 3′** and **4′** respectively) approximately 100 mg of sample was degassed at 160 ºC under 10^{-1} pa vacuum for about 12 hours prior to the measurements. CO_2 adsorptions isotherms at 195 K were measured for all the samples. To check CO_2 selectivity of the frameworks, adsorption isotherms of CO_2, N_2, H_2, Ar, O_2 at 195 K were measured only for **1′**, since the frameworks are isostructural**.** Dead volume of the sample cell was measured using helium gas of 99.999% purity. The amount of gas adsorbed was calculated from the pressure difference ($P_{cal} - P_e$), where P_{cal} is the calculated pressure with no gas adsorption and P_e is the observed equilibrium pressure. All the operations were computer-controlled and automatic.

4B.3 RESULTS AND DISCUSSION

4B.3.1 Crystal Structure Description

Single–crystal X–ray diffraction reveals compounds **1-4** crystalize in the orthorhombic *Cmcm* space group. The asymmetric unit of **1** contains one Co(II) centre, two $Ag(CN)_2^-$ ligands, one pip linker and four guest water molecules. Co(II) centre is present in a

distorted octahedral geometry and coordinated to four nitrogen atoms (N1, N1_a, N2 and N2_a) from –CN groups. The other two coordination sites are furnished by N3 and N3_a atoms from pip pillars (Figure 7). Deviation from ideal octahedral geometry can be realized from the cisoid and transoid angle (Table 2). The Co(II)–N bond lengths are in the range of 2.108(11)–2.151(10) Å (Table 2).

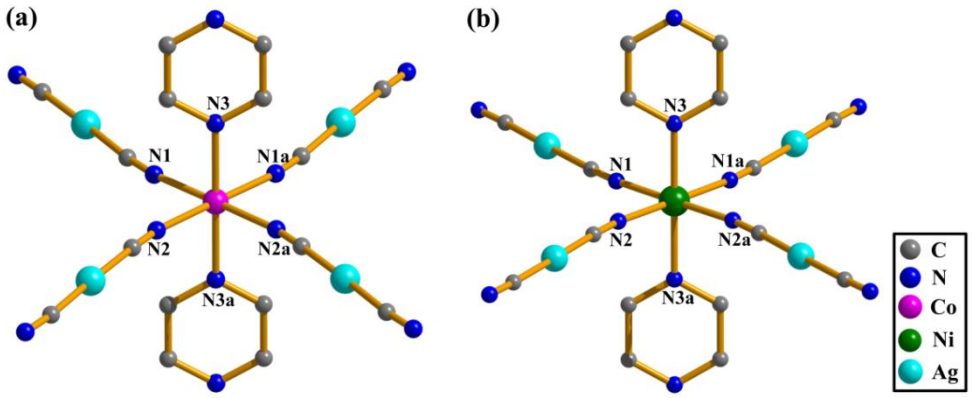

Figure 7. View of the coordination environment around Co(II)/ Ni(II): (a) for compound **1** and (b) for compound **2**. Symmetry code: a = 1−x, y, ½−z.

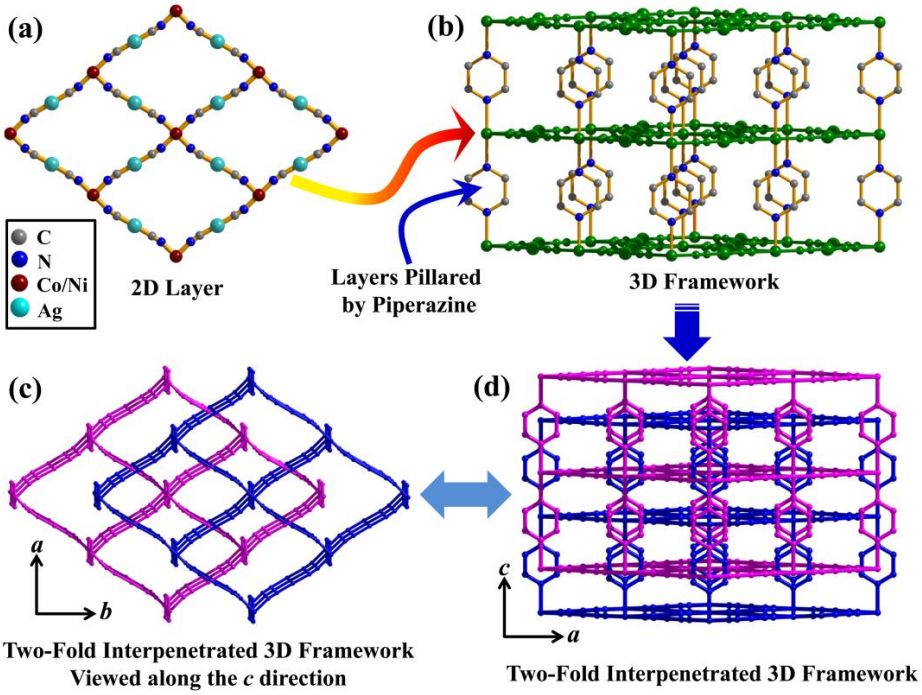

Figure 8. (a) View of the 2D sheet of -Co(II)-CN-Ag(I)-CN-Co(II)- of **1** in the crystallographic *ab* plane. (b) View of the pillared-layer 3D structure along the crystallographic *a*-axis. (c) View of the 2-fold interpenetrated structure along the crystallographic *c*-axis. (d) View of the 2-fold interpenetrated 3D framework along the crystallographic *b*-axis (hydrogen molecules have been omitted for clarity).

The Co(II) centres are connected by $Ag(CN)_2^-$ linkers along the *ab* plane to form 2D corrugated sheets which are further pillared by pip pillars forming a 3D framework with α-polonium topology (Figure 8). Topological analysis of these 3D frameworks using TOPOS 4.0[39e] suggests a 6-connected uninodal net (Figure 9) with Schläfli symbol $\{4^{12}.6^3\}$. The Co(II)-Co(II) separation along the *ab* plane and along the *c* axis are 10.546 Å and 7.177 Å, respectively. Two 3D frameworks interpenetrate each other resulting in a 2-fold interpenetrated 3D framework (Figure 8d). The single nets of the 3D framework contain 1D channel with the pore dimensions 12 × 6.2 $Å^2$; upon interpenetration which gives two different types of pore along the *c* direction; a hexagonal shaped large pore and a smaller diamond shaped pore (Figure 10). The dimensions of the pores are 4.9 × 3.1 $Å^2$ and 3.3 × 2.6 $Å^2$. Origin of two different shaped pore windows is due to the interpenetration of the nets which reduces the void space. The void space, 352 $Å^3$ (23% total of cell volume), has been calculated using PLATON[39e] after removal of all the guest water molecules.

Compound **2** is isomorphous to compound **1** and it bears similar metal coordination topology as **1** (Figure 7) with slight differences in bond distances and angles (Table 2). The Ni(II)–N bond lengths are in the range of 2.078(15)–2.106(14) Å (Table 2). **2** exhibits similar pore size and void space as that of **1**. The pore window dimension for **2** are 4.8 × 3.2 $Å^2$ and 3.2 × 2.5 $Å^2$. Calculated void space using PLATON for compound **2** was found to be 342.5 $Å^3$ (22.7% total of cell volume) which is close to that of compound **1**. Compound **3** and **4** are obtained by replacing the pillar module pip by dabco and pz respectively. The coordination environment of **3** and **4** are presented in Figure 11. The overall 3D structure is similar to **1** and 2-fold interpenetrated 3D frameworks are observed. The Co(II)–N bond lengths are in the range of 2.106(10)–2.298(10) Å and 2.086(11)–2.163(7) Å for **3** and **4** respectively (Table 2). For **3**, the Co(II)-Co(II) separation along the *ab* plane and along the c axis are 10.539 Å and 7.229 Å respectively, while that for **4** are 10.505 Å and 7.095 Å respectively. In **3**, the larger linker dabco reduces pore size and decreases the void space significantly, (Figure 12) compared to compound **1**. Only one small pore having dimension 3.4 × 2.1 $Å^2$ is observed in **3**, while the other pore is blocked. The void space is 168 $Å^3$ (10.9% total of cell volume) for **3**. For **4**, the pore window dimensions are 5 × 3.2 $Å^2$ and 2.9 × 2.1 $Å^2$ and void space is 361 $Å^3$ (24% total of cell volume) (Figure 12c,d). Based on the modulation of the organic pillars, it is possible to tune the pore size and void space in the frameworks.

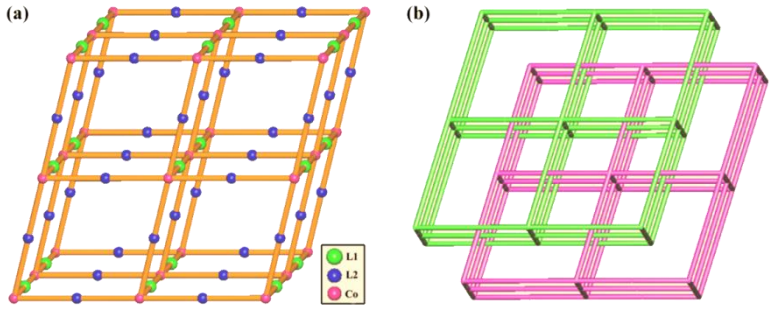

Figure 9. (a) View of the 6-connected uninodal node. In the legend L1 = piperazine; L2 = $Ag(CN)_2$. (b) The 2-fold interpenetrated nets in compound **1**.

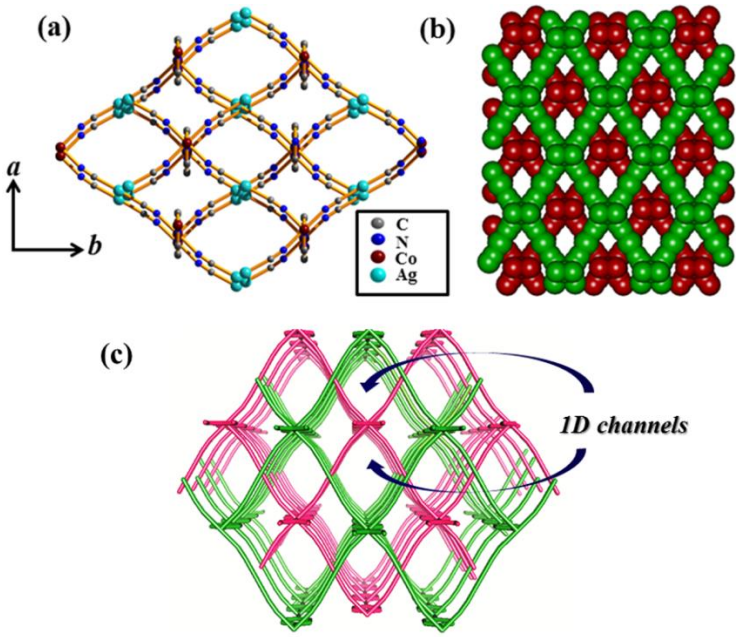

Figure 10. (a) Pore view of compound **1** along the crystallographic *c*-axis showing two different types of channels; one hexagonal and the other diamond shaped channel. (b) Space filling diagram of the two-fold interpenetrated 3D framework with 1D hexagonal and diamond shaped channels along the crystallographic *c*-axis. (c) View of the 1D channels along the crystallographic *c*-axis.

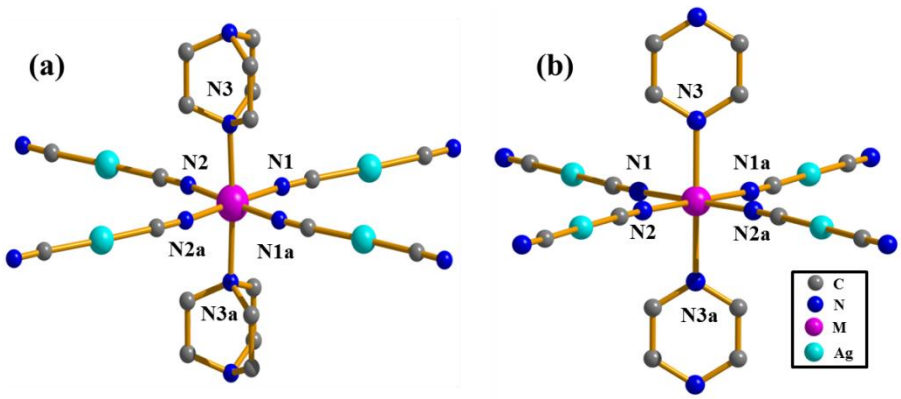

Figure 11. View of the coordination environment around Co(II): (a) for compound **3** and (b) for compound **4**. Symmetry code: a = 1−x, y, ½−z.

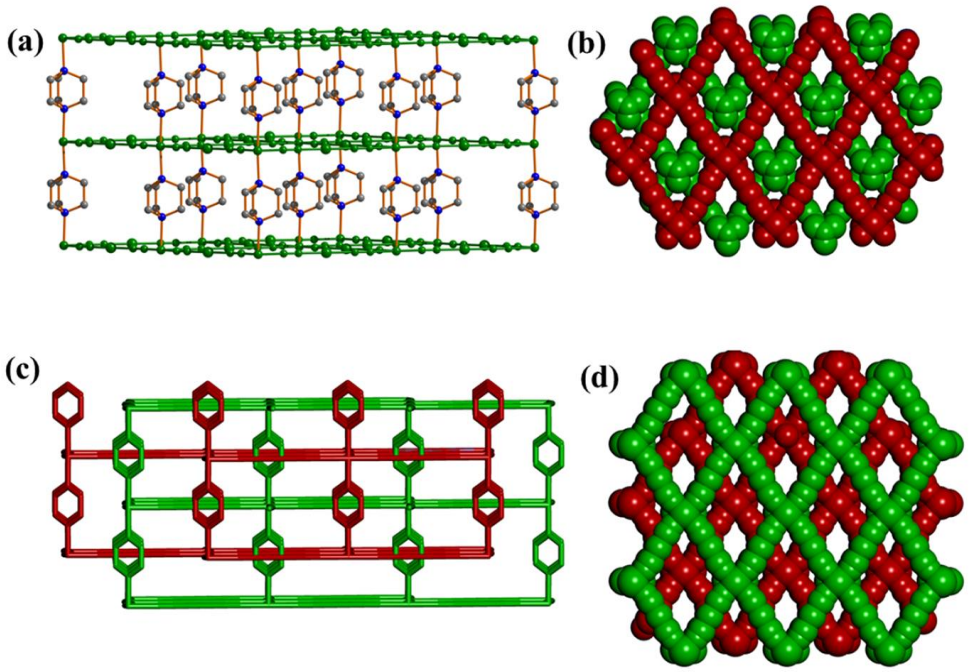

Figure 12. (a) View of the pillared-layer 3D structure of **3** along the crystallographic *a*-axis. (b) Space filling diagram the two-fold interpenetrated 3D framework of **3** with the 1D channels along the crystallographic *c*-axis. (c) The pillared-layer 2-fold interpenetrated structure of **4** along the crystallographic *a*-axis. (d) Space filling diagram the two-fold interpenetrated 3D framework of **4** with the 1D channels along the crystallographic *c*-axis s(hydrogen and non-coordinated water molecules have been omitted for clarity).

Table 1. Crystal data and structure refinement parameters of compounds **1-4**.

Parameters	**1**	**2**	**3**	**4**
Crystal System	Orthorhombic	Orthorhombic	Orthorhombic	Orthorhombic
Space Group	*Cmcm* (No. 63)	*Cmcm* (No. 63)	*Cmcm* (No. 63)	*Cmcm* (No. 63)
a (Å)	12.5528(2)	12.6541(14)	12.756(5)	12.6038(10)
b (Å)	16.9488(3)	16.7209(17)	16.781(5)	16.8086(15)
c (Å)	7.1769(1)	7.1163(7)	7.229(5)	7.0952(6)
V (Å^3)	1526.92(4)	1505.7(3)	1547.4(13)	1503.1(2)
Z	4	4	4	4
T (K)	298	298	298	298
μ (mm^{-1})	3.635	3.835	3.593	3.691
D_{calcd} (g cm^{-3})	2.292	2.323	2.382	2.293
F (000)	1004	1008	1068	972
Measured reflections	11319	8874	6043	4552
Unique reflections	763	682	1053	1078
Reflections [$I>2\sigma(I)$]	607	527	910	831
R_{int}	0.036	0.092	0.036	0.029
GOF on F^2	1.23	1.11	1.25	1.24
$R_1[I>2\sigma(I)]$[a]	0.0513	0.0875	0.0559	0.0576
$R_w[I>2\sigma(I)]$[b]	0.2151	0.2683	0.1898	0.3034

[a] $R = \sum||F_o|-|F_c||/\sum|F_o|$. [b] $R_w = [\sum\{w(F_o^2-F_c^2)^2\}/\sum\{w(F_o^2)^2\}]^{1/2}$

Table 2. Selected bond lengths (Å) and angles (º) for compounds **1**-**4**.

Compound 1			
Co1-N1	2.143(10)	Co1-N2	2.108(11)
Co1-N3	2.151(10)		
N1-Co1-N3	89.3(3)	N1-Co1-N1a	89.5(4)
N1-Co1-N2a	179.6(4)	N1-Co1-N2	90.9(4)
N3-Co1-N3a	178.0(5)	N2 -Co1-N3a	90.7(3)
N2 -Co1-N2a	88.7(4)		
Compound 2			
Ni1-N1	2.093(13)	Ni1-N2	2.078(15)
Ni1-N3	2.106(14)		
N1-Ni1-N2a	178.8(6)	N1-Ni1-N3	89.9(4)
N1-Ni1-N1a	91.4(5)	N1-Ni1-N2	89.8(5)
N2-Ni1-N3	90.1(4)	N2-Ni1-N2_a	88.9(6)
N3-Ni1-N3a	179.8(8)		
Compound 3			
Co1-N1	2.118(10)	Co1-N2	2.106(10)
Co1-N3	2.298(10)		
N1-Co1-N3	91.15(16)	N1-Co1-N1a	86.5(4)
N1-Co1-N2a	177.1(4)	N1-Co1-N2	90.6(4)
N3-Co1-N3a	176.8(3)	N2 -Co1-N3a	88.91(15)
N2 -Co1-N2a	92.3(4)		
Compound 4			
Co1-N1	2.109(10)	Co1-N2	2.086 (11)
Co1-N3	2.163(7)		
N1-Co1-N3	89.61 (13)	N1-Co1-N1a	88.0(4)
N1-Co1-N2a	179.7 (4)	N1-Co1-N2	91.1(4)
N3-Co1-N3a	178.9 (3)	N2 -Co1-N3a	90.38(13)
N2 -Co1-N2a	90.0(4)		

Symmetry Codes: a = 1−x, y, 1/2−z.

4B.3.2 Framework Stability: TGA, IR and PXRD Analysis

TGA, temperature dependent IR and PXRD analyses were carried out to study the thermal stability of the frameworks. Compound **1** is stable up to 205 °C after initial weight loss of 3.2% which corresponds to the loss of one non-coordinated water molecule (Figure 3). Beyond 205 °C, subsequent ligand loss results into decomposition of the structure. Compound **2** is stable up to 190 °C after initial weight loss of 3% while **3** and **4** are stable up to 195 °C and 200 °C respectively, after initial weight loss of 3.3% and 2.9% respectively. Temperature dependent IR (30ºC – 200ºC) spectra have been recorded for **1**, which shows no significant change in the stretching frequencies with increase in temperature, except that for the *ν*(O–H) frequency (Figure 13). The *ν*(O–H) frequency arises from the coordinated guest water molecule and its intensity decreases with the gradual increase in temperature. At 150 ºC, the peak corresponding to this *ν*(O–H)

frequency disappear with the removal of the guest molecules. PXRD pattern of the dehydrated solids (**1′ - 4′**) do not show any significant change in the peak positions compared to as-synthesized pattern, suggesting the rigidity of the frameworks (Figure 2, 4-6).

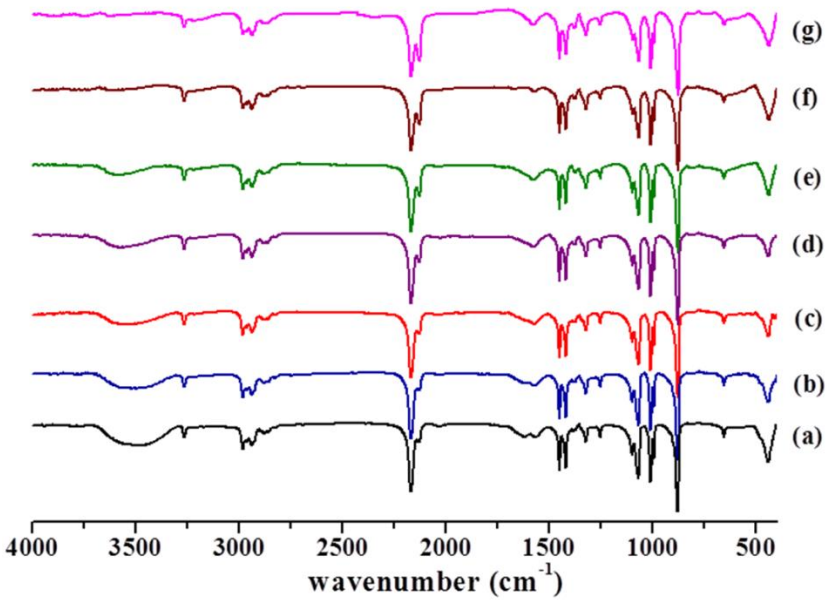

Figure 13. IR spectra for **1** at different temperature; (a) 30 ºC, (b) 60 ºC, (c) 80 ºC, (d) 100 ºC, (e) 120 ºC, (f) 150 ºC, and (g) 200 ºC.

4B.3.3 Magnetic properties

Figure 14a shows the variable-temperature magnetic susceptibility of **1** measured at 500 Oe. At 300 K, the $\chi_M T$ value is 2.99 cm^3 mol^{-1} K, typical for one high spin Co(II) ions, with orbital contribution of the Co(II) centres. The temperature dependence of the reciprocal susceptibility above 104 K (Figure 15) follows the Curie–Weiss law with a Weiss constant θ of −7.09 K, which can be a result of spin-orbit coupling effect of Co(II) ions in octahedral field or due to antiferromagnetic coupling between Co(II) ions. The product $\chi_M T$ first decreases up to 31 K and then increases rapidly and finally decreases on further cooling (Figure 14a). The spontaneous increase in $\chi_M T$ at low temperature indicates a possibility of long range ordering. The field-cooled (FC) and zero field-cooled (ZFC) magnetization measured at 500 Oe show a bifurcation at 5 K, suggesting a phase transition (Figure 14a inset). In the ac susceptibility data (Figure 14b), the maximum of χ_M' observed at T_c = 6 K, in agreement with the above results, confirms the occurrence of a phase transition and magnetic long range ordering. The imaginary χ_M'' component shows a peak at 5 K, indicating that a magnetized state exists below this temperature. No

frequency dependence of these transitions is observed, thus excluding the possibility of relaxation behaviour. A plot of FC susceptibility *vs. T* at different dc field strengths shows a field-dependent behaviour below 6 K (Figure 14c) and the spontaneous increase of $\chi_M T$ product is more pronounced at lower field strength, suggesting spin-canting in this system. The plot of the reduced magnetization(M) *vs. H* at 2 K (Figure 14d) is clearly indicative of a hysteresis loop corresponding to a very soft ferromagnet (small coercive field) with a remnant magnetization (M_r) of 0.076 Nβ and a coercive field (H_c) of 314 Oe. Assuming the saturation magnetization value of 3 Nβ (expected value for a spin only Co(II) ion), the estimated canting angle [$\sin^{-1}(0.076/3)$] for **1** is 1.5°.

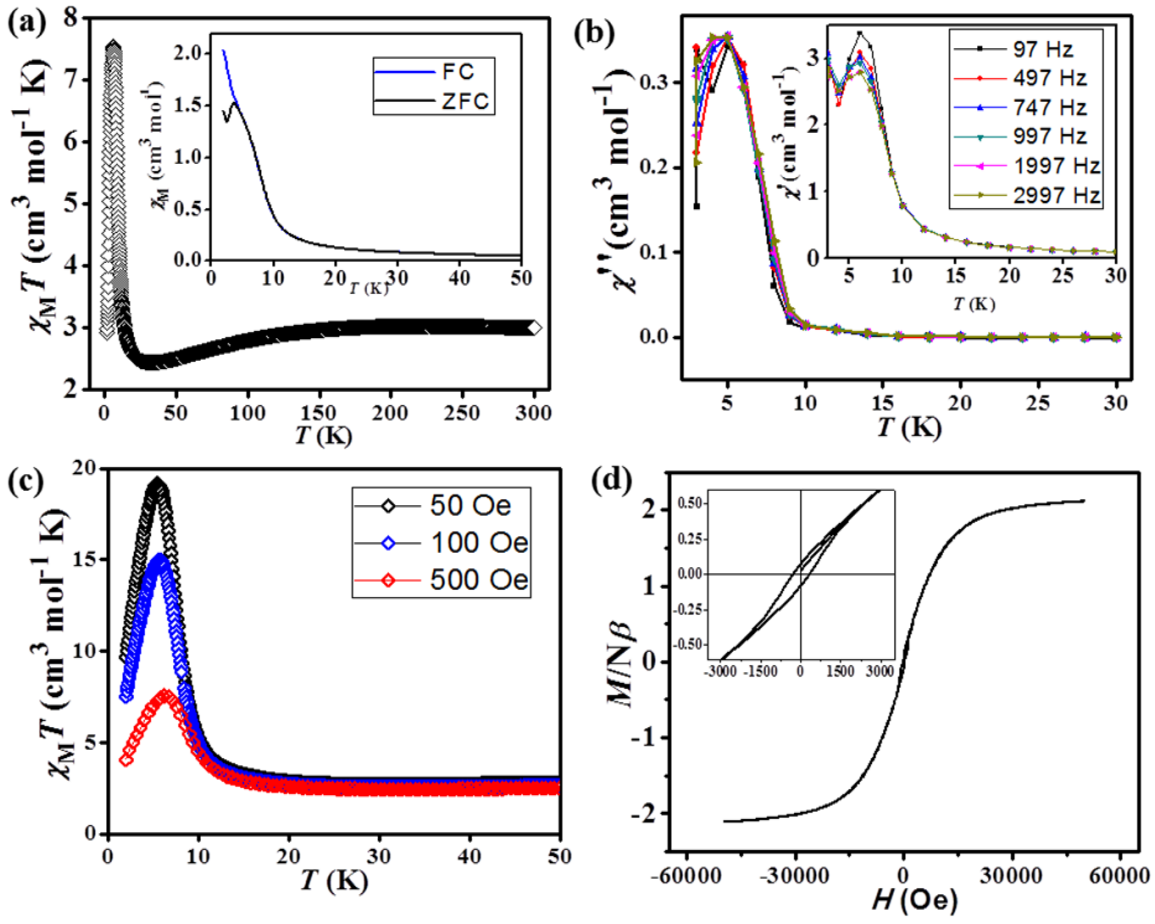

Figure 14. (a) The plots of $\chi_M T$ *vs. T* for **1**. The inset shows temperature dependence of the magnetic susceptibility of **1** at 500 Oe in temperature range 2-50 K under field-cooled (FC) and zero-field-cooled (ZFC) conditions. (b) The ac susceptibility out-of-phase, χ_M" of **1** at applied field of 5 Oe (inset shows in-phase, χ_M' data). (c) Temperature dependence of the magnetic susceptibility of **1** at 50, 100, and 500 Oe under field-cooled (FC) condition. (d) Isothermal magnetization of **1** measured by cycling the field between 50 and -50 KOe at 2 K (inset shows the hysteresis loop).

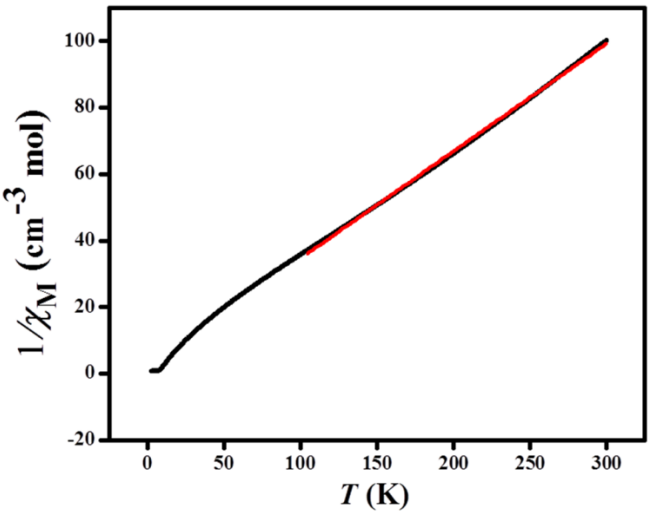

Figure 15. Curie–Weiss fitting for **1** above 104 K. The red line indicates the best fit obtained. Weiss constant θ is −7.09 K.

Compound **2** exhibits similar magnetic behaviour (Figure 16) as of **1**, owing to the structural similarity. Figure 16a shows $\chi_M T$ *vs.* T plot where an abrupt increase is observed at a temperature 14 K. The Curie–Weiss fitting of the reciprocal susceptibility above 75 K gives a Weiss constant θ of −6.2 K (Figure 17). The maxima of χ_M' and χ_M'' are observed at 16 and 14 K, respectively (Figure 16b) and hence a canted antiferromagnetic structure exists below 14 K. The field dependence of $\chi_M T$ product is shown in Figure 16c. The hysteresis loop (Figure 16d) reveals that **2** has a smaller coercive field (235 Oe) than **1** with a remnant magnetization (M_r) of 0.024 Nβ; and the estimated the canting angle is 0.65° [$\sin^{-1}(0.024/2.1)$]. Now for two isomorphous systems, the antisymmetric exchange should be of the same order; however the local anisotropy of the Co(II) ions is much greater than that for Ni(II). For Co(II) the anisotropy results from unquenched orbital momentum and first-order spin–orbit coupling, while for Ni(II) it is only due to the second order spin–orbit coupling. Probably this enhanced anisotropy for **1** gives rise to a greater coercivity than in **2**. The magnetic behaviour (Figure 18) of compound **3** closely resembles to that of **1**. For **3**, the FC and ZFC magnetization measured at 500 Oe show a bifurcation at 8 K and the Curie–Weiss fitting of the $1/\chi_M$ *vs.* T plot (300-157 K) gives $\theta = -13.45$ K (Figure 18b). The M_r and H_c are 0.12 Nβ and 315 Oe respectively, which are very close to that of compound **1**. Significant difference is observed in case of **4**, where antiferromagnetism is dominant than weak ferromagnetism. The product $\chi_M T$ decreases from room temperature monotonically to 12 K and then there is a small increase of $\chi_M T$ value followed by a

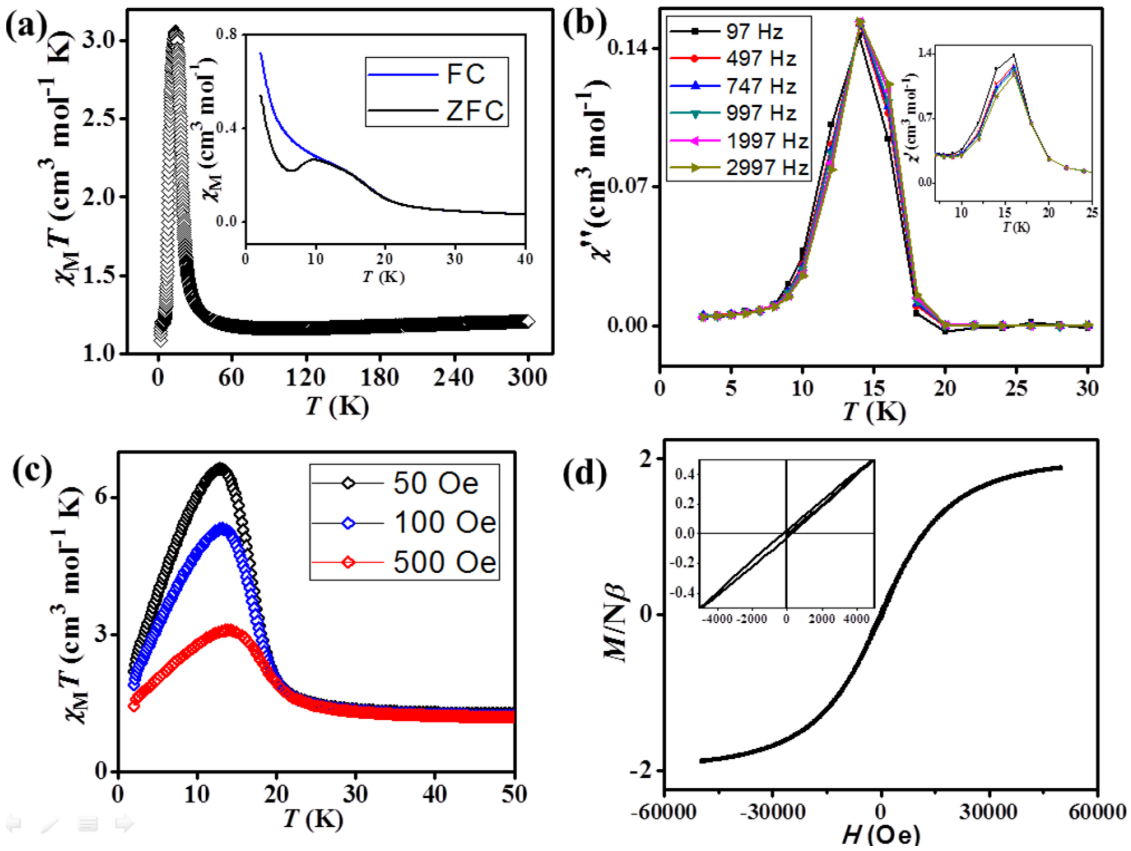

Figure 16. (a) The plots of $\chi_M T$ *vs.* T for **2**. The inset shows temperature dependence of the magnetic susceptibility of **2** at 500 Oe in temperature range 2-50 K under field-cooled (FC) and zero-field-cooled (ZFC) conditions. (b) The ac susceptibility out-of-phase, χ_M" of **2** at applied field of 5 Oe (inset shows in-phase, χ_M' data). (c) Temperature dependence of the magnetic susceptibility of **2** at 50, 100, and 500 Oe under field-cooled (FC) condition. (d) Isothermal magnetization of **2** measured by cycling the field between 50 and -50 KOe at 2 K (inset shows the hysteresis loop).

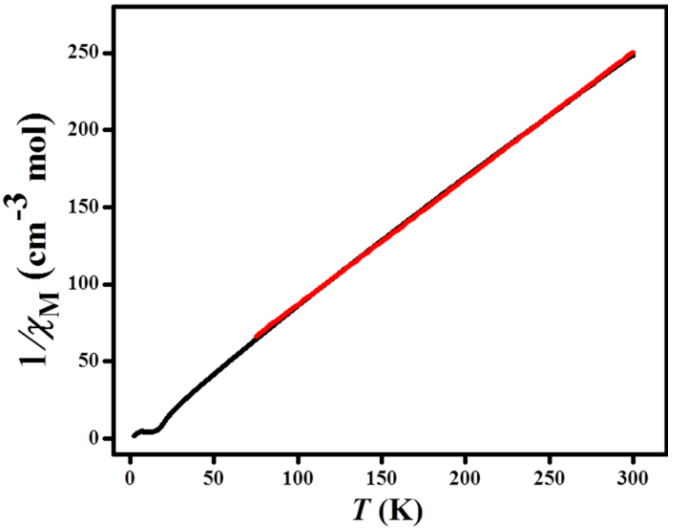

Figure 17. Curie–Weiss fitting for **2** above 75 K. The red line indicates the best fit obtained. Weiss constant θ is −6.2 K.

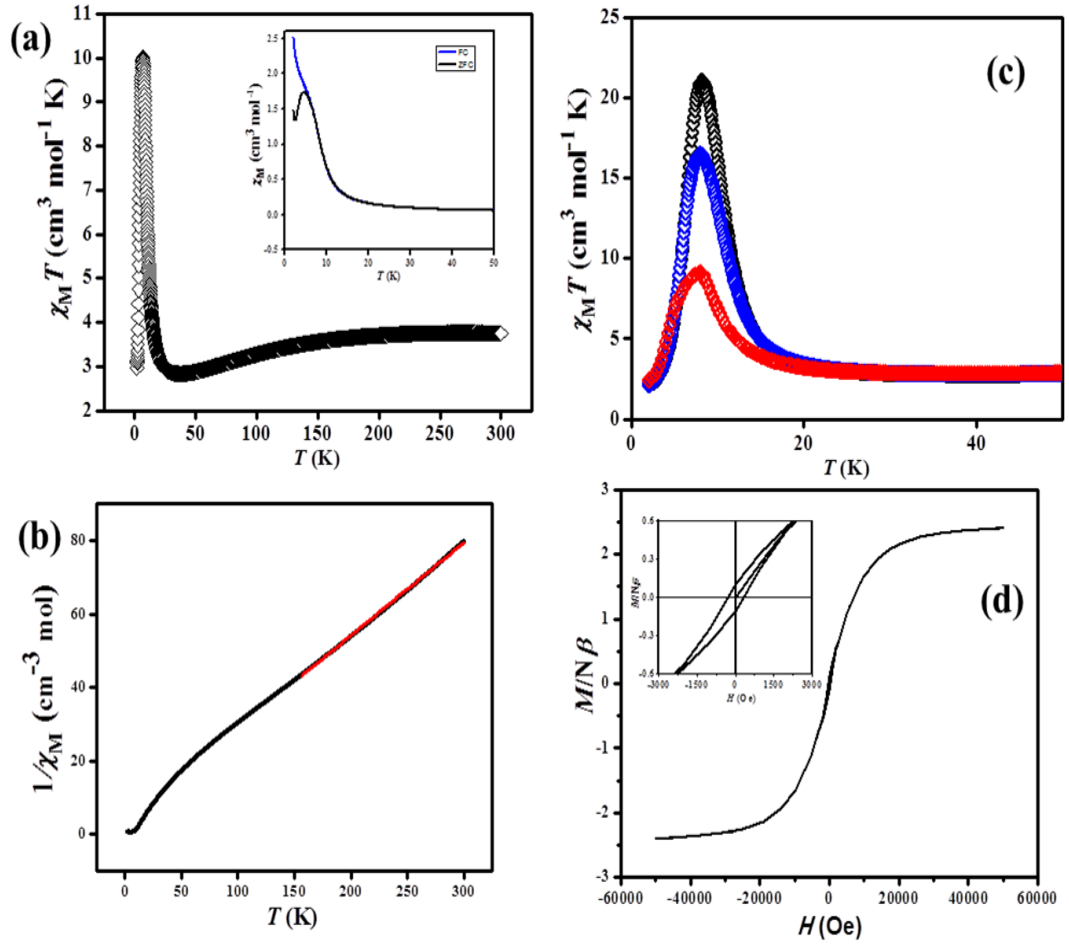

Figure 18. (a) The plots of $\chi_M T$ *vs.* T for **3**. The inset shows temperature dependence of the magnetic susceptibility of **3** at 500 Oe under field-cooled (FC) and zero-field-cooled (ZFC) conditions. (b) Curie–Weiss fitting of **3** in the temperature range 300-155 K. The red line indicates the best fit obtained. Weiss constant θ is −13.45 K. (c) Temperature dependence of the magnetic susceptibility of **3** at 50 (black), 100 (blue), and 500 (red) Oe under field-cooled (FC) condition. (d) Isothermal magnetization of **3** measured by cycling the field between 50 and -50 KOe at 2 K. The inset shows the hysteresis loop.

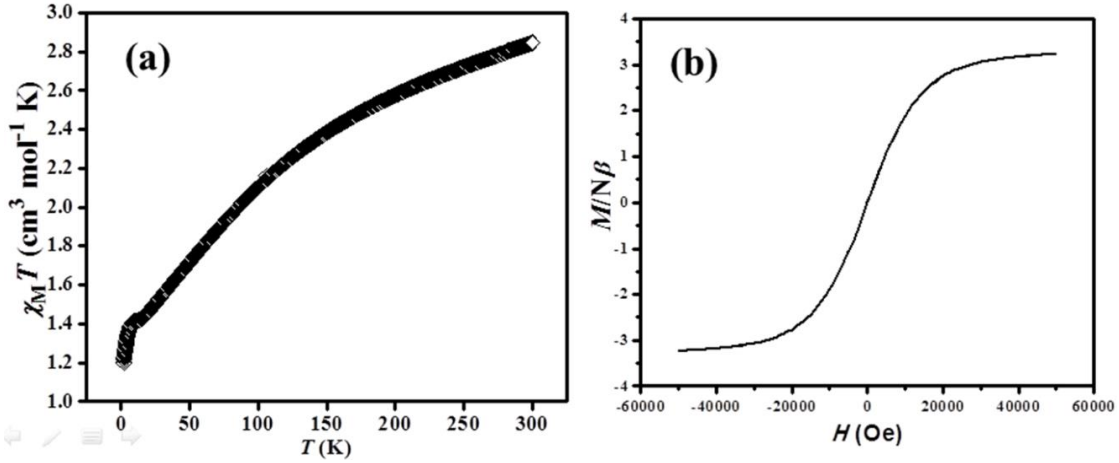

Figure 19. (a) The plots of $\chi_M T$ *vs.* T for **4**. (b) Isothermal magnetization of **4** measured by cycling the field between 50 and -50 KOe at 2 K.

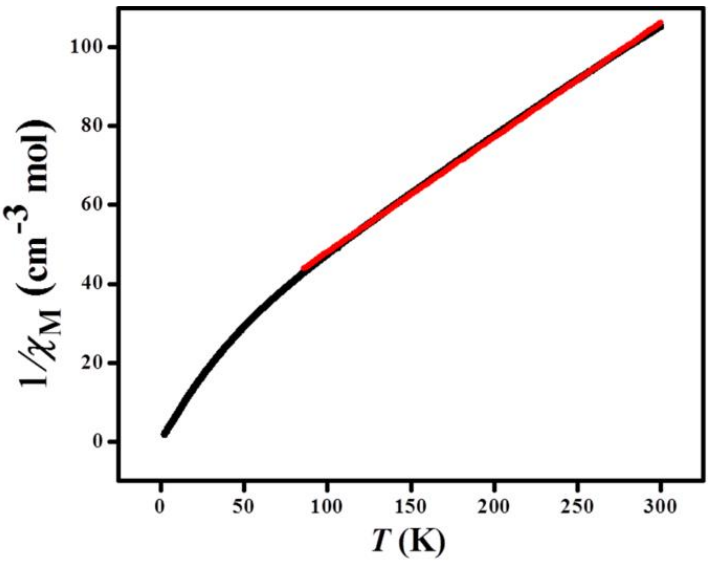

Figure 20. Curie–Weiss fitting for **4** above 85 K. The red line indicates the best fit obtained. Weiss constant θ is −64.9 K.

decrease beyond 7 K (Figure 19a). The spontaneous increase in $\chi_M T$ value is quite insignificant compared to that of **1**. Temperature dependence of the reciprocal susceptibility above 85 K (Figure 20) follows the Curie–Weiss law with a Weiss constant θ of −64.9 K, thus indicating a moderately stronger antiferromagnetic interaction. The plot of the *M vs. H* (Figure 19b) shows negligible coercive field suggesting that weak ferromagnetism is suppressed here.

The origin of spin canting in these 3D compounds can be correlated from their structures. The magnetic ions in the unit cell of **1**-**4** are not related by a centre of symmetry. As well established, two factors can then result into spin canting, (i) single-ion anisotropy, which originates if the anisotropy axes on neighbouring interacting sites are different and (ii) the antisymmetric Dzyaloshinsky–Moriya (DM)[40] interaction. Now both mechanisms favour the spin canting in these frameworks as the metal ions have single-ion anisotropy and the dicyanoargentate bridging in the 2D corrugated sheet afford a low symmetry exchange pathway. The similarity of magnetic signature of **1** and **3** is because of the fact that magnetic pathway remain almost unaltered in both the compounds. However, for **4**, significant antiferromagnetism is observed compared to the other compounds containing aliphatic linkers like pip or dabco. The strong antiferromagnetism in **4** arises through aromatic conjugation by pyrazine.[41] Here antiferromagnetic exchange can prevail between the layers, operating through the aromatic pyrazine ring thus exhibiting dominating antiferromagnetic character for **4**.

4B.3.4 Adsorption study

Apart from the interesting magnetic behaviour, the structure also contains void space which motivated us to study the porous properties. Measurements were carried out with the dehydrated samples **1′, 2′, 3′** and **4′**. Despite having sufficient window dimension considering the kinetic diameter of N_2 (3.64 Å), a type-II isotherm was obtained for N_2 at 77 K (Figure 21) for **1′**. Such behaviour can be attributed to the higher diffusion barrier for N_2.

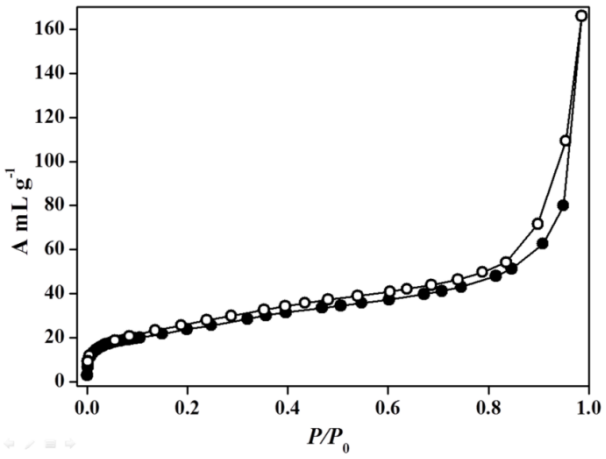

Figure 21. N_2 gas adsorption isotherms for **1′** at 77 K showing only surface adsorption. (Closed symbols indicate adsorption and open symbols indicate desorption).

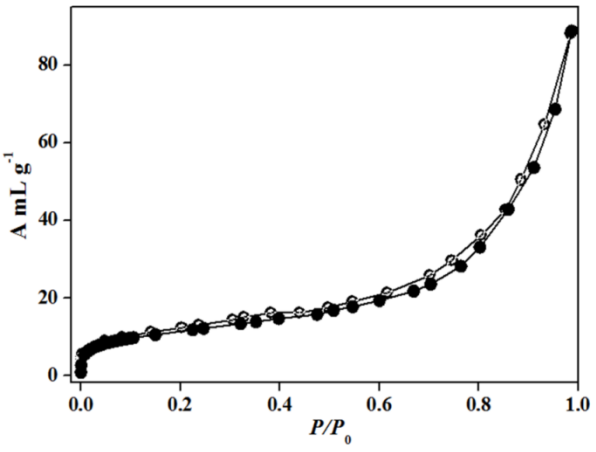

Figure 22. N_2 gas adsorption isotherms for **2′** at 77 K showing only surface adsorption. (Closed symbols indicate adsorption and open symbols indicate desorption)

Compound **2′**, the Ni(II) analogous of **1′**, shows similar N_2 adsorption behaviour (Figure 22) and similar explanation that of **1′** can be validated. Adsorption measurement with CO_2 (3.3 Å) at 195 K shows a type-I uptake profile for **1′** (Figure 23) and **2′** (Figure 24). The CO_2 uptake capacities at 1 atm are ~ 40 and ~ 45 mL g^{-1}, for **1′** and **2′** respectively.

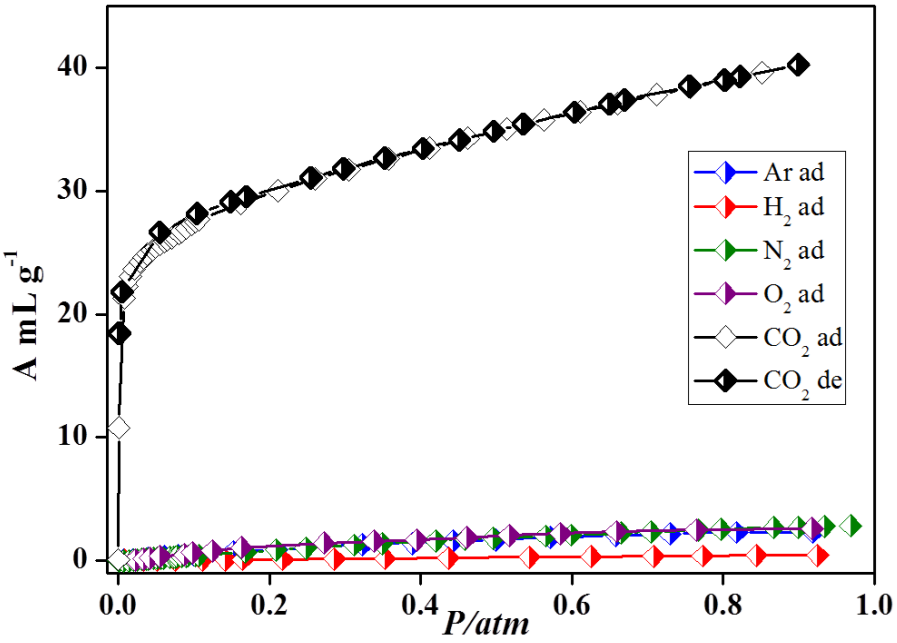

Figure 23. Gas adsorption isotherms for **1′** showing selectivity for CO_2: CO_2 (black), Ar (blue), H_2 (red), N_2 (green) and O_2 (red) at 195 K. (half-closed symbols indicate adsorption and open symbols indicate desorption).

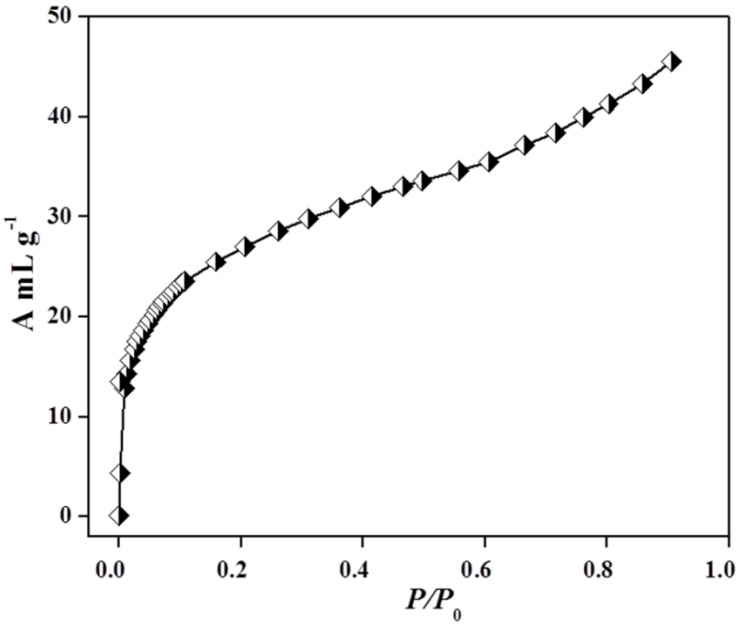

Figure 24. CO_2 gas adsorption isotherm for **2′** at 195 K.

To check CO_2 selectivity, we have performed measurement with other gases like N_2, Ar, H_2 and O_2 only for **1′** at 195 K**,** since the frameworks are isostructural. For all these gases, we observed negligible uptake suggesting compounds **1′** as a potential selective CO_2 adsorbent (Figure 23). Surface area calculated using Langmuir equation from the CO_2 profiles turns out to be ~ 195 and ~ 205 $m^2\ g^{-1}$ for **1′** and **2′**, respectively. The profiles

were further analyzed by the Dubinin-Radushkevich equation[42] to realize the adsorbate-adsorbent interaction and the $q_{st,\phi}$ value for **1′** and **2′** are found to be ~ 35.7 and ~ 32.5 kJ mol^{-1} respectively, suggesting strong interaction of CO_2 with the frameworks. The strong and preferential interaction of CO_2 with framework could be attributed to the–CN groups at the pore surfaces.

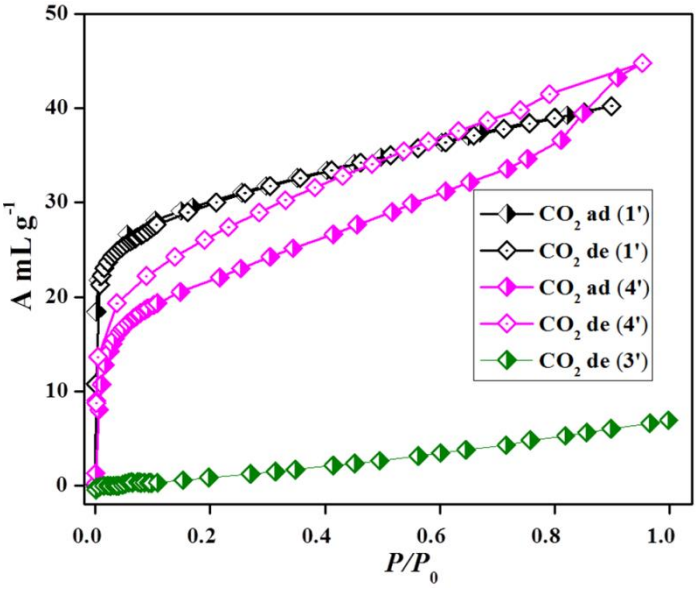

Figure 25. CO_2 gas adsorption isotherms for **1′**, **3′** and **4′** at 195 K. (half-closed symbols indicate adsorption and open symbols indicate desorption).

Compound **3′** contains dabco as pillar which is distinctly larger in size compared to pip in compound **1′** and **2′**. Larger size of the second spacer (dabco) diminishes the porosity in compound **3′** and eventually CO_2 molecule cannot diffuses (Figure 25) into the pores of compound **3′**. Changing the pillar from pip to pz, we observed an interesting change in the CO_2 adsorption profile for **4′** (Figure 25). The desorption path does not follow the adsorption path making a clear hysteresis. The uptake at low pressure is smaller than that **1′**. The smaller uptake at low pressure and the hysteric profile suggest that there is a higher diffusion barrier in adsorption and desorption path for CO_2 molecules compared to **1′**. This can be attributed to higher rotational degrees of freedom for pz molecules compared to the aliphatic pip molecule.[33] There can be a local flexibility originating from the rotation of pz molecules which results in inhibition of easy desorption of gas molecules. The $q_{st,\phi}$ value for **4′** is found to be ~ 31.2 kJ mol^{-1}. Compound **4′** exhibits type-II N_2 adsorption isotherm at 77 K (Figure 26).

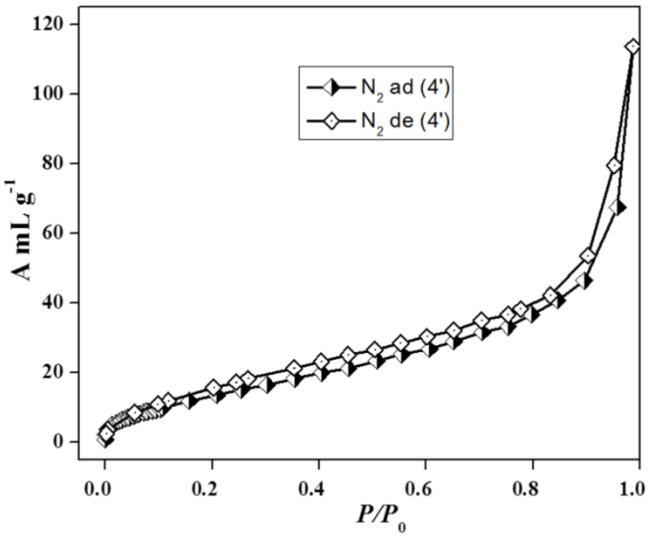

Figure 26. N_2 gas adsorption isotherms for **4′** at 77 K showing only surface adsorption. (Closed symbols indicate adsorption and open symbols indicate desorption).

4B.4 SUMMARY

In summary, four 3D porous frameworks were synthesized by employing mixed-ligand system and their adsorption and magnetic properties are presented. The properties were modulated by changing the organic pillar modules. The observed spin canting behaviour is attributed to the single-ion anisotropy of metal ions, no inversion centre between the adjacent metal centres and the low symmetry exchange pathway provided by the $[Ag(CN)_2]^-$ bridging. Use of an aromatic pillar module (pyrazine) results antiferromagnetic exchange between the layers and eventually weak ferromagnetism is suppressed by dominant antiferromagnetic interaction. In the pillared-layer structure of **1**, **2** and **4**, the pore surfaces are decorated with polar –CN groups, which results selective adsorption of CO_2 over other gases by the dehydrated frameworks. This work presents a systematic study of modulation of magnetic and porous properties in a series of 3D frameworks by changing the second spacer.

4B.5 REFERENCES

1. Cheetham, A. K.; Rao, C. N. R. *Science* **2007**, *318*, 58.
2. J. R. Long and O. M. Yaghi, *Chem. Soc. Rev*., 2009, **38**, 1213.
3. O. M. Yaghi, M. O'Keeffe, N. W. Ockwig, H. K. Chae, M. Eddaoudi and J. Kim, *Nature*, 2003, **423**, 705.

4. M. Eddaoudi, J. Kim, N. Rosi, D. Vodak, J. Wachter, M. O'Keeffe and O. M. Yaghi, *Science*, 2002, **295**, 469.
5. T. K. Maji, R. Matsuda and S. Kitagawa, *Nat. Mater*., 2007, **6**, 142.
6. S. Kitagawa, R. Kitaura and S. Noro, *Angew. Chem. Int. Ed*., 2004, **43**, 2334.
7. J. Y. Lee, O. K. Farha, J. Roberts, K. A. Sheidt, S. B. T. Nguyen and J. T. Hupp, *Chem. Soc. Rev*., 2009, **38**, 1450.
8. S. Horike, M. Dinca, K. Tamaki and J. R. Long, *J. Am. Chem. Soc*., 2008, **130**, 5854.
9. S. Hasegawa, S. Horike, R. Matsuda, S. Furukawa, K. Mochizuki, Y. Kinoshita and S. Kitagawa, *J. Am. Chem. Soc.*, 2007, **129**, 2607.
10. H. K. Chae, M. Eddaoudi, J. Kim, S. I. Hauck, J. F. Hartwig, M. O'Keeffe and O. M. Yaghi, *J. Am. Chem. Soc.*, 2001, **123**, 11482.
11. P. Kanoo, K. L. Gurunatha and T. K. Maji, *J. Mater. Chem.*, 2010, **20**, 1322.
12. P. Horcajada, C. Serre, M. Vallet-Regi, M. Sebban, F. Taulelle and G. Férey, *Angew Chem., Int. Ed.*, 2006, **45**, 5974.
13. P. Horcajada, C. Serre, G. Maurin, N. A. Ramsahye, F. Balas, M. Vallet-Regi, M. Sebban, F. Taulelle and G. Férey, *J. Am. Chem. Soc.*, 2008, **130**, 6774.
14. G. J. Halder, C. J. Kepert, B. Moubaraki, K. S. Murray and J. D. Cashion, *Science*, 2002, **298**, 1762.
15. M. Kurmoo, *Chem. Soc. Rev.*, 2009, **38**, 1353.
16. H. Kumagai, H. Sobukawa and M. Kurmoo, *J. Mater. Sci.*, 2008, **43**, 2123.
17. P. Dechambenoit and J. R. Long, *Chem. Soc. Rev.*, 2011, **40**, 3249.
18. N. Guillou, S. Pastre, C. Livage and G. Férey, *Chem. Commun*., 2002, 2358.
19. C. N. R. Rao, A. K. Cheetham and A. Thirumurugan, *J. Phys.: Condens. Matter*, 2008, **20**, 083202.
20. D. Maspoch, D. Ruiz-Molina and J. Veciana, *Chem. Soc. Rev.*, 2007, **36**, 770.
21. D. Maspoch, D. Ruiz-Molina and J. Veciana, *J. Mater. Chem*., 2004, **14**, 2713.
22. E. Coronado, F. Palacio and J. Veciana, *Angew. Chem. Int. Ed*., 2003, **42**, 2570.
23. (*a*) L. Wang, J. Morales, T. Wu, X. Zhao, W. P. Beyermann, X. Bu and P. Feng, *Chem. Commun.*, 2012, **48**, 7498; (*b*) Y. Ning, C. Wang, T. Ngai and Z. Tong, *Langmuir*, 2013, **29**, 5138; (*c*) P. Kar, R. Haldar, C. J. Gómez-Garcia and A. Ghosh, *Inorg. Chem.*, 2012, **51**, 4265.
24. (*a*) A. Hazra, P. Kanoo and T. K. Maji, *Chem. Commun*., 2011, **47**, 538; (*b*) M. Kurmoo, H. Kumagai, S. M. Hughes and C. J. Kepert, *Inorg. Chem.*, 2003, **42**,

6709; (*c*) S. Mohatapatra, B. Rajeswaran, A. Chakraborty, S. Sundaresan and T. K. Maji, *Chem. Mater*., 2013, **25**, 1673.

25. D.-F. Weng, Z.-M. Wang and S. Gao, *Chem. Soc. Rev.*, 2011, **40**, 3157.
26. S. C. Xiang, X. T. Wu, J. J. Zhang, R. B. Fu, S. M. Hu and X. D. Zhang, *J. Am. Chem. Soc.*, 2005, **127**, 16352.
27. J. A. R. Navarro, E. Barea, A. Rodriguez-Dieguez, J. M. Salas, C. O. Ania, J. B. Parra, N. Masciocchi, S. Galli and A. Sironi, *J. Am. Chem. Soc*., 2008, **130**, 3978.
28. N. Guillou, Q. Gao, P. M. Forster, J.-S. Chang, M. Nogués, S.-E. Park, G. Férey and A. K. Cheetham, *Angew. Chem. Int. Ed.*, 2001, **40**, 2831.
29. M. Cavellec, D. Riou, C. Ninclaus, J.-M. Grenéche and G. Férey, *Zeolites*, 1996, **17**, 250.
30. Q. Chen, W. Xue, J.-B. Lin, R.-B. Lin, M.-H. Zeng and X.-M. Chen, *Dalton Trans.*, 2012, **41**, 4199.
31. K. L. Mulfort, O. K. Farha, C. D. Malliakas, M. G. Kanatzidis and J. T. Hupp, *Chem. Eur. J*., 2010, **16**, 276.
32. B. Wang, A. P. Cote, H. Furukawa, M. O'Keeffe and O. M. Yaghi, *Nature*, 2008, **453**, 207.
33. P. Kanoo, S. K. Reddy, G. Kumari, R. Haldar, C. Narayana, S. Balasubramanian and T. K. Maji, *Chem. Commun*., 2012, **48**, 8487.
34. P. Kanoo, G. Mostafa, R. Matsuda, S. Kitagawa and T. K. Maji, *Chem. Commun*., 2011, **47**, 8106.
35. C. M. Nagaraja, R. Haldar, T. K. Maji, and C. N. R. Rao, *Cryst. Growth Des*., 2012, **12**, 975.
36. R. Vaidhyanathan, S. S. Iremonger, G. K. H. Shimizu, P. G. Boyd, S. Alavi and T. K. Woo, *Science*, 2010, **330**, 650.
37. (*a*) V. Niel, M.C. Munoz, A.B. Gaspar, A. Galet, G. Levchenko and J.S. Real, *Chem. Eur. J*,. 2002, **8**, 2446; (*b*) V. Niel, A. L. Thompson, M.C. Munoz, A. Galet, A. E. Goeta and J.S. Real, *Angew. Chem. Int. Ed*., 2003, **42**, 3760.
38. J.-P. Costes, C. Duhayon, L. Vendier, E. Colacio, A. J. Mota and J. S. Varela, *Inorg. Chem.*, 2012, **51**, 1011.
39. (*a*) SMART (V 5.628), SAINT (V 6.45a), XPREP, SHELXTL; Bruker AXS Inc. Madison, Wisconsin, USA, 2004; (*b*) G. M. Sheldrick, Siemens Area Detector Absorption Correction Program, University of Göttingen, Göttingen, Germany, 1994; (*c*) A. Altomare, G. Cascarano, C. Giacovazzo, A. Gualaradi, *J. Appl. Cryst.*,

1993, **26**, 343; (*d*) G. M. Sheldrick, SHELXL-97, Program for Crystal Structure Solution and Refinement; University of Göttingen, Göttingen, Germany, 1997; (*e*) A. L. Spek, *J. Appl. Cryst.*, 2003, **36**, 7; (*f*) L. J. Farrugia, WinGX - A Windows Program for Crystal Structure Analysis. *J. Appl. Crystallogr.*, 1999, **32**, 837.

40. (*a*) I. Dzyaloshinsky, *J. Phys. Chem. Solids*, 1958, **4**, 241; (*b*) T. Moriya, *Phys. Rev.*, 1960, **120**, 91; (*c*) T. Moriya, *Phys. Rev.*, 1960, **117**, 635.
41. H. W. Richardson and W. E Hatfield, *J. Am. Chem. Soc.*, 1976, **98**, 835.
42. A. Kapoor, J. A. Ritter and R. T. Yang, *Langmuir*, 1989, **5**, 1118.

Chapter 5A

CuBTC-Aminoclay Nanocomposites for CO_2 Capture, Separation and Enhanced Catalytic Activity in Chemical Fixation of CO_2

Abstract

Integration of different active species towards novel metal-organic framework (MOF) composites has recently attracted significant research interests. In this chapter, the growth and stabilization of ultra-small (2-3 nm) $\{Cu_3(BTC)_2(H_2O)_2.xH_2O\}$ MOF nanoparticles (NPs) on 2D layered aminoclay template is reported for the first time. The composite shows 10% increase in surface area and 46% increase in CO_2 uptake capacity (5.35 mmol g^{-1} at 298 K, 1 bar) compared to the pristine bulk MOF. The composite also exhibits superior CO_2 separation efficiency from CO_2/N_2 and CO_2/CH_4 mixtures as realized from the breakthrough column experiments and shows higher catalytic proficiency for chemical fixation of CO_2 into cyclic carbonates. The enhanced carbon capture and sequestration by the composite is attributed to the synergistic combination of ultra-small MOF NPs and functional aminoclay template.

Paper based on this study:

A.Chakraborty, A. Achari, M. Eswaramoorthy, T. K. Maji, *Chem. Commun.*, 2016, DOI: 10.1039/C6CC05289D.

5A.1 INTRODUCTION

Recent upsurge in the synthesis of nanoscale metal-organic frameworks (NMOFs) is stemming from their superior applications compared to the bulk counterpart.[1] The pore accessibility of well-dispersed MOF nanoparticles is higher compared to the bulk MOF, resulting in enhanced gas uptake and catalytic efficiency.[2-4] However, downsizing of metal-organic frameworks (MOF) crystals to a very small scale[5] is one of the highly challenging and demanding assignments. Template assisted synthesis of MOF nanostructures using different templates like silica, organic polymers, graphene oxide (GO), reduced graphene oxide (RGO) and carbon nanotube have been recently reported.[6-9] However, stabilization of 2-3 nm MOF nanoparticles (NPs) using these scaffolds is yet to be realized. Moreover, some of these scaffolds are poorly dispersed in water which limit their applications in water based medium. Integration of ultra-small MOF nanocrystals with a smart functional scaffold which could disperse well at nanoscopic level would enlarge the scope of the composites in several applications. Research on MOF composites has shown that a judicious integration of two components would mitigate the drawbacks of the individual components and provide synergistic effects to accomplish enhanced and novel properties.[6,10] In this chapter, highly water dispersible 2D sheets of aminoclay (AC) is used as a functional template to assist the growth of ultra-small MOF NPs. The AC used here is aminopropyl functionalized magnesium phyllosilicate with approximate unit cell composition of $[H_2N(CH_2)_3]_8Si_8Mg_6O_{16}(OH)_4$ (Scheme 1). AC has been used as a support to stabilize metal NPs and different organic chromophores for catalytic and light harvesting applications.[11-14] It was anticipated that amine groups in AC can act as metal binding sites to facilitate the growth of small MOF NPs. Furthermore, the resulting composites could show enhanced CO_2 uptake based on specific interaction of quadrupolar CO_2 with the active sites at the MOF NPs-AC interface, as the role of alkylamine group in carbon capture and sequestration (CCS) technology is well established.[15] In this study, the well-studied $\{Cu_3(BTC)_2(H_2O)_2.xH_2O\}$[16] MOF (abbreviated as CuBTC) [BTC = benzene-1,3,5-tricarboxylate] was chosen which has shown applications in gas storage (H_2, CO_2, CH_4), separation[16b] and catalysis.[16c,d] In this chapter, the growth and stabilization of ultra-small (2-3 nm) CuBTC NPs are reported on AC. The composite exhibits

higher surface area, higher CO_2 uptake and a superior separation efficiency of CO_2 from CO_2/N_2 and CO_2/CH_4 mixtures compared to that of pristine bulk CuBTC. The composite also exhibits significant catalytic activity in the chemical fixation of CO_2 into cyclic carbonates.

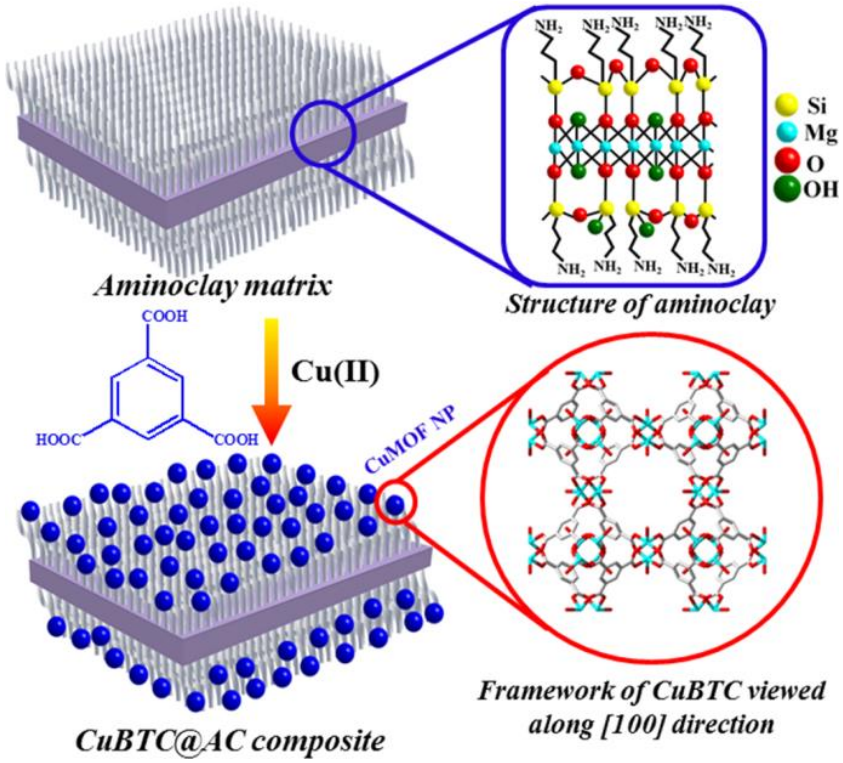

Scheme 1. Schematic representation of the synthesis of CuBTC@AC composite. The scheme and structure of aminoclay (top) and the 3D framework of CuBTC (bottom right) viewed along [100] direction are shown. The blue sphere represents the CuBTC NPs in the composite.

5A.2 EXPERIMENTAL SECTION

5A.2.1 Synthesis

Synthesis of aminoclay:

Aminoclay was prepared following typical reaction conditions reported by Mann and co-workers.[11d] 3-aminopropyltriethoxysilane (1.3 mL, 5.85 mmol) was added dropwise to an ethanolic solution of $MgCl_2$ (0.84 g, 3.62 mmol) in ethanol (20 g). The white slurry obtained was stirred overnight and the precipitate was isolated by centrifugation and then was washed with ethanol (50 mL) and dried at 40 °C. PXRD pattern (Figure 1) of the dried compound shows typical reflections corresponding to the interlayer spacing originating from the bilayer arrangement of propylamine groups.

Synthesis of {$Cu_3(BTC)_2(H_2O)_2.xH_2O$} (CuBTC) and CuBTC@AC composites:

{$Cu_3(BTC)_2(H_2O)_2.xH_2O$} (abbreviated as CuBTC) was prepared by following typical solvothermal reaction conditions. Copper nitrate trihydrate (1 mmol) and 1,3,5 benzenetricarboxylic acid (0.67 mmol) were taken in a mixture of 12 mL DMF, 12 mL ethanol and 8 mL deionized water in a 23 mL teflon-lined stainless steel autoclave and the mixture was stirred for 10 minutes. The autoclave was sealed and was kept in an oven at 80 °C for 24 h. After completion of the reaction, the reactor was cooled at RT for 12 h. The resulting blue product was collected by filtration, washed with DMF and ethanol repeatedly and finally dried. Selected IR data (KBr): $\tilde{\nu}$ (cm^{-1}) = 3421 (br), 2920 (m), 1646 (s), 1590 (m), 1449(s), 1377 (s), 1112 (m), 760 (s), 731 (s), 488 (m). The PXRD pattern of the dried compound shows formation of pure phase of CuBTC (Figure 1). However, the characteristic peaks for AC are not observed in the composites due to the fact that AC shows low intensity broad peaks compared to high intensity sharp peaks of CuBTC.

Three different composites denoted as **CuBTC@AC-1**, **CuBTC@AC-2** and **CuBTC@AC-3** were synthesized. To prepare the **CuBTC@AC-1** composite, first 5 mg of aminoclay (AC) was dispersed in 5 mL of water/ethanol (60: 40) mixture (pH= 7). In aqueous solution, the amine groups of AC are protonated and thus the layers of AC are exfoliated. They can be reverted to their stacked form by the addition of less polar solvents like ethanol. AC was taken in water/ethanol mixture so that there are sufficient numbers of NH_2 groups (which can bind metal ions) rather than NH_3^+ ions. Indeed, the dispersed solution of AC in water/ethanol mixture showed smaller positive zeta potential value (12 mV) suggesting the presence of sufficient number of NH_2 groups. To the dispersed solution of AC in water/ethanol mixture, the precursor solutions of CuBTC are added as described above for the synthesis of CuBTC and similar solvothermal reaction was carried out. The resulting solid was dried after repeatedly washing with ethanol, and is referred to as **CuBTC@AC-1.** Similar procedure was repeated for the synthesis of **CuBTC@AC-2** and **CuBTC@AC-3** where 10 mg and 20 mg of aminoclay were taken, respectively. The weight % of CuBTC in the composites were calculated through Inductively Coupled Plasma-Atomic Spectroscopy (ICP-AES) study based on the relative ratio of Cu(II) in the pristine CuBTC and the composites. Selected IR data for **CuBTC@AC-2:** (KBr): $\tilde{\nu}$ (cm^{-1}) = 3389 (br), 2499 (m), 1647 (s), 1576 (br, s), 1448 (s), 1370 (s), 1114 (s), 1017 (m), 766 (s), 734 (s), 637 (s), 475 (s). The well-correspondence

of the PXRD patterns of CuBTC and the composites suggests existence of pure crystalline phase of CuBTC in the composites (Figure 1). To check the water dispersibility, same amount (5 mg in 1 mL of water) of both CuBTC and **CuBTC@AC-2** samples were dispersed in water. The dispersion remains stable even after 6 hours for the **CuBTC@AC-2** sample, while the bulk CuBTC precipitates within 15 minutes (Figure 2).

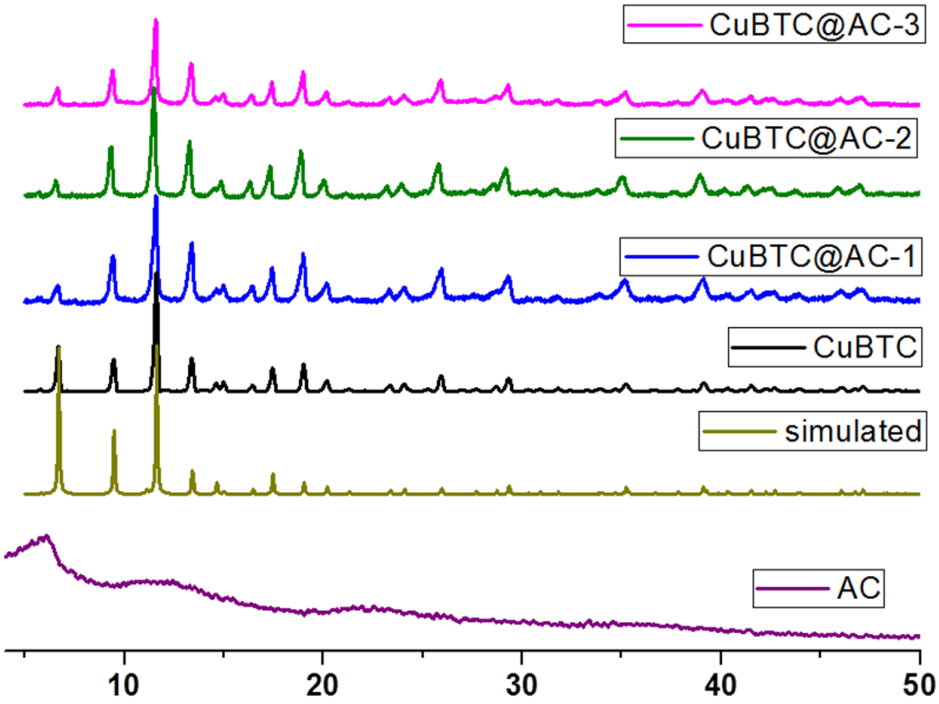

Figure 1. PXRD patterns of AC, simulated CuBTC, as-synthesized bulk CuBTC and different composites.

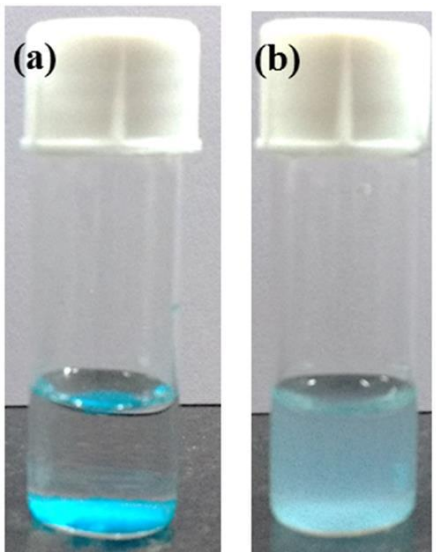

Figure 2. Images of the solutions of (a) CuBTC after 15 minutes of preparation of dispersion and (b) **CuBTC@AC-2** after 6 hours of preparation of dispersion.

Control experiments to study the growth and stabilization of CuBTC NPs on the aminoclay:

10 mg of aminoclay (AC) was dispersed in 5 mL of water/ethanol mixture (pH= 7). Copper nitrate trihydrate (1 mmol) was added to the above solution and the mixture was stirred for 10 minutes at room temperature. The green solid product (obtained after precipitation by adding ethanol to the reaction mixture) was washed several times with ethanol and dried. Elemental mapping and EDX analysis of the solid (referred as Cu@AC) show the presence of Cu distributed uniformly throughout the clay (Figure 3). This suggests that the Cu(II) ions are strongly bound to the free amine groups of AC. Then Cu@AC solid and BTC linker (0.67 mmol) were mixed in a 23 mL teflon-lined stainless steel autoclave containing 12 mL DMF, 12 mL ethanol and 8 mL deionized water and the mixture was stirred for 10 minutes. The autoclave was sealed and was kept in an oven at 80 °C for 24 h. After completion of the reaction, the reactor was cooled at RT for 12 h. The resulting blue product was collected by filtration, was washed with DMF and ethanol repeatedly and finally was dried. The PXRD pattern of the resulting composite reveals formation of the pure phase of CuBTC (Figure 4).

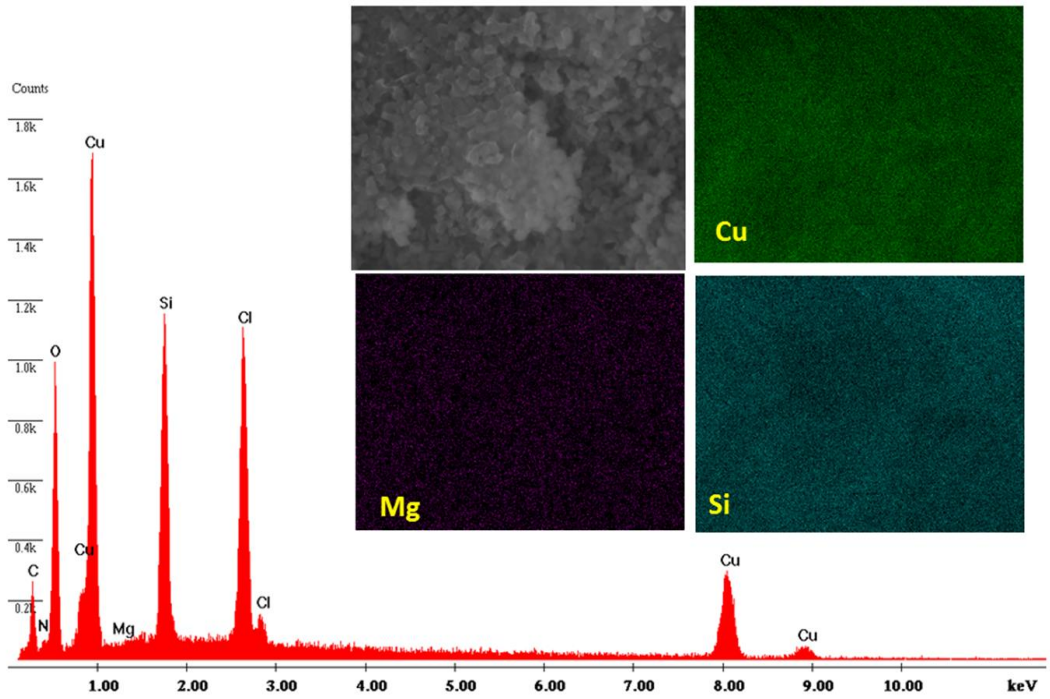

Figure 3. EDX spectrum of the Cu@AC solid showing the presence of Cu. Inset shows elemental mapping showing the homogeneously distribution of the elements (Si, Mg and Cu) throughout the sample.

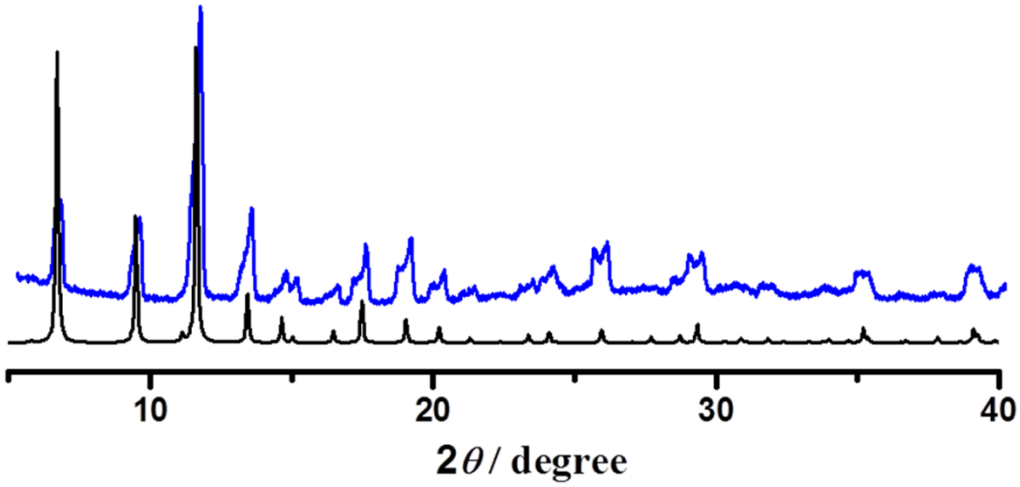

Figure 4. PXRD patterns of simulated (black) and the solid (blue) obtained from the solvothermal reaction of Cu@AC and BTC linker.

5A.2.2 Physical Measurements

^{1}H NMR data were measured on a Bruker AV-400 spectrometer with chemical shifts reported as ppm (TMS as internal standard). Powder X-ray diffraction (PXRD) patterns were recorded on a Bruker D8 Discover instrument using Cu-Kα radiation. Inductively Coupled Plasma-Atomic Emission Spectroscopy (ICP-AES) measurements were recorded on Perkin Elmer Optima 7000dv ICP-AES instrument. Energy dispersive analysis of X-rays (EDX) was carried out using field emission scanning electron microscope. The scanning electron microscopy images were obtained using a Nova Nanosem 600 FEI field emission scanning electron microscope (FESEM). The samples were prepared by dispersing the sample in MeOH and then dropping 5 μL of the solution onto a small piece of silicon wafer and drying into air. Transmission electron microscopy (TEM) images were taken with a JEOL JEM-3010 transmission electron microscope operating at 200 kV. The samples were prepared in the same way as described above, but the drop cast was made onto a carbon-coated TEM grid.

5A.2.3 Adsorption Measurements

Adsorption isotherms of N_2 (at 77 K, 298 K), CO_2 (at 273 K and 298 K) and CH_4 (at 298 K) were recorded with the desolvated samples using QUANTACHROME QUADRASORB-SI analyser and AUTOSORB IQ2 instrument. To prepare the desolvated samples of CuBTC and the composites, approximately 70 mg of sample was degassed at 160 ºC under 10^{-1} pa vacuum for about 8 hours prior to the measurements.

Dead volume of the sample cell was measured with helium gas of 99.999% purity. The MeOH adsorption isotherms were measured at 298 K in the gaseous state by using BELSORP-aqua-3 analyzer. All operations were computer controlled and automatic. The kinetic data were fitted into the linear driving force mass transfer (LDF) model which can be described by the equation: $M_t/M_e = 1-\exp(-kt)$, where M_t and M_e are the mass uptake at time t and at equilibrium respectively, and k is the kinetic rate constant. To ensure equilibrium, the adsorption kinetics measurements were performed with sufficient equilibrium time (1500 seconds). The adsorption rate graph and the kinetic data were analysed using BELDyna software.

5A.2.4 Breakthrough Column Experiments

Breakthrough experiments were performed using a column (packed with about 150 mg of desolvated samples) of 1 cm long length and 0.3 cm diameter. The sample was first activated (at 160 ºC under 10^{-1} pa vacuum for about 8 hours) prior to loading in column. For both CuBTC and **CuBTC@AC-2**, the same amount of samples (150 mg, column length is 1 cm) was used. After loading the sample was again activated with the He flow for 30 minutes. CO_2/N_2 (V/V: 15/85) and CO_2/CH_4 (V/V: 50:50) streams were passed from the corresponding gas cylinders containing the gas mixtures through the column with He. The flow was continuous and the flow rate was regulated by mass flow controller (MFC). The rate of the flow (He: binary gas mixture = 90: 10) was fixed at 1 ml/min. The gas stream at the outlet of the column was analyzed on-line with a GC.

5A.2.4 Catalysis Study

The catalyst was activated (at 160 ºC under 10^{-1} pa vacuum for about 8 hours) prior to the catalysis reaction. The catalytic reaction was conducted in a Schlenk tube using propylene oxide (25 mmol) with CO_2 purged at 1 atm under solvent free environment at room temperature catalyzed by the activated catalyst (0.125 mol% calculated based on copper paddlewheel units; 0.03125 mmol for CuBTC) and co-catalyst of tetra-*n*-tertbutylammonium bromide (TBAB, 0.58g) for 48 hours. Catalytic reaction of 1,2-epoxybutane with CO_2 was performed using similar synthetic condition. After the reaction, the product was collected by adding $CHCl_3$ and the solid catalyst was removed by centrifuge. The yield was calculated based on ^{1}H NMR analysis (Figures 18-22). To perform the recyclability tests, the recovered catalyst was washed with fresh $CHCl_3$

thoroughly and was dried in air first and then activated at 160 ºC under 10^{-1} pa vacuum for 8 hours to perform further reactions under identical conditions.

5A.3 RESULTS AND DISCUSSION

The AC content in **CuBTC@AC-1**, **CuBTC@AC-2** and **CuBTC@AC-3** were were found to be 4.6, 9.6 and 15.3 weight%, respectively, as obtained from the inductively coupled plasma atomic emission spectrometry. The as-synthesized bulk CuBTC and the composites show similar PXRD patterns suggesting formation of pure phase of CuBTC in the composites (Figure 1). TEM images (Figure 5) show well-defined CuBTC NPs stabilized on the AC layers as observed for both **CuBTC@AC-1** and **CuBTC@AC-2**.The sizes of the NPs are 7-8 nm (Figure 5a) and 2-3 nm (Figure 5b) for **CuBTC@AC-1** and **CuBTC@AC-2** respectively.

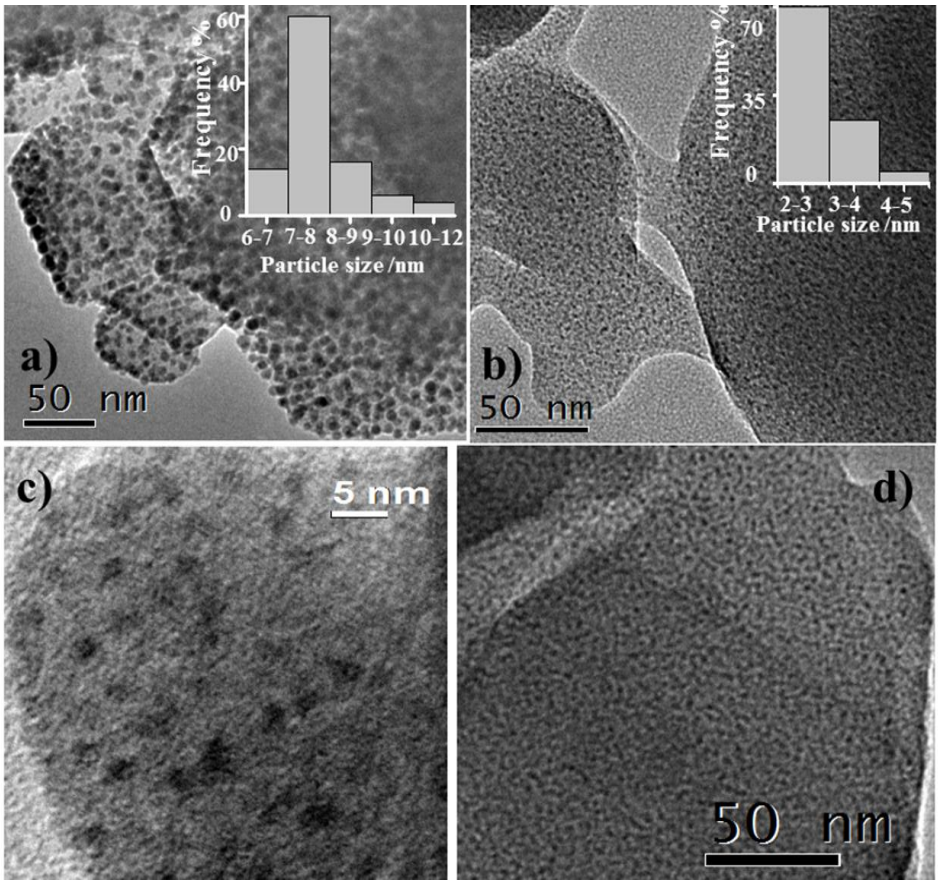

Figure 5. TEM images of (a) **CuBTC@AC-1** and (b) **CuBTC@AC-2**. The inset shows the size distribution histogram plots (c) HRTEM of **CuBTC@AC-2**. (d) Sample obtained after solvothermal reaction of Cu@AC and BTC.

HRTEM image of **CuBTC@AC-2** reveals that ultra-small NPs with average size of 2-3 nm (Figure 5c) are distributed uniformly on the AC surface. Importantly, **CuBTC@AC-2** produces more stable dispersion in water (stable more than 6 hours) compared to the bulk CuBTC which precipitates within 15 minutes (Figure 2). In case of **CuBTC@AC-3** where the clay content is higher, the particle size of CuBTC becomes larger and unevenly distributed (Figure 6) due to incomplete dispersion of AC. The formation of microsized particles for bulk CuBTC (revealed by the FESEM image; Figure 7) in the absence of AC reveals the role of AC in nucleation and stabilization of MOF NPs.

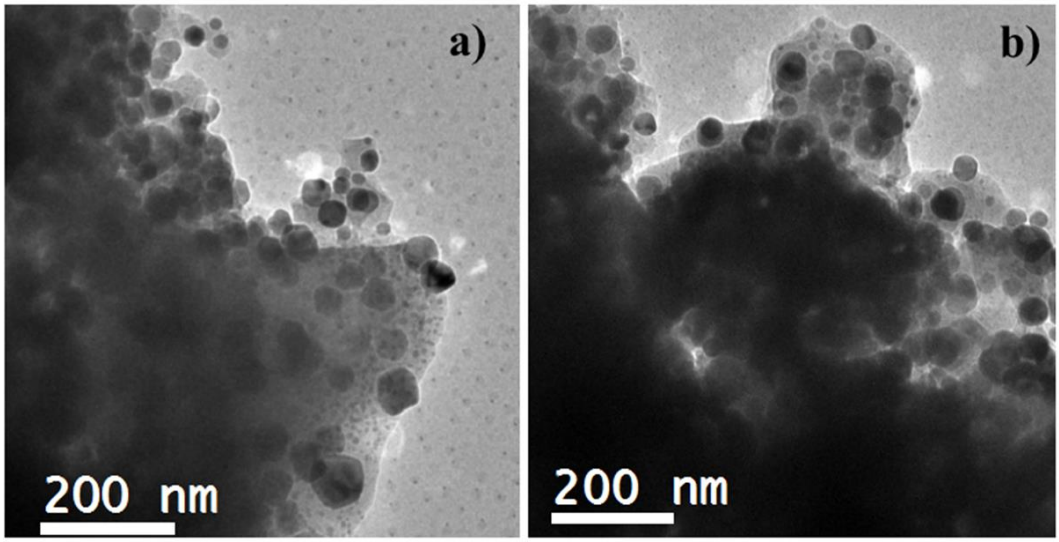

Figure 6. (a), (b) TEM images of **CuBTC@AC-3**

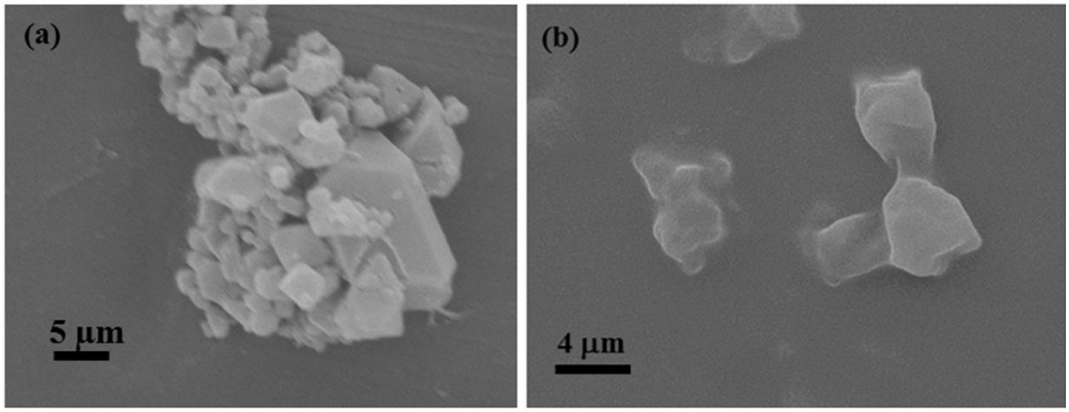

Figure 7. FESEM images of (a) as-synthesized bulk CuBTC and (b) AC.

To further understand the growth of the CuBTC NPs, control experiments were performed. The Cu@AC solid obtained after the addition of Cu(II) salt to the AC solution in water/ethanol mixture followed by precipitation and washing shows presence of Cu distributed uniformly throughout the clay, as seen in the EDX mapping (Figure 3). Thus the Cu(II) ions are strongly bound to the free amine groups of AC. Further solvothermal reaction was carried out with the Cu@AC solid and BTC linker. The PXRD pattern of the resulting composite reveals the formation of pure phase of CuBTC (Figure 4), while TEM analysis shows small NPs (2-3 nm) stabilized on AC similar to **CuBTC@AC-2** (Figure 5d). The above experiments suggest that the amine groups of AC first stabilize Cu(II) ions on its surface and further nucleation of CuBTC nanocrystals starts when the BTC linker is added. Thus AC assists growth of MOF nanocrystals by acting as a seed and preventing the aggregation between the crystallites.

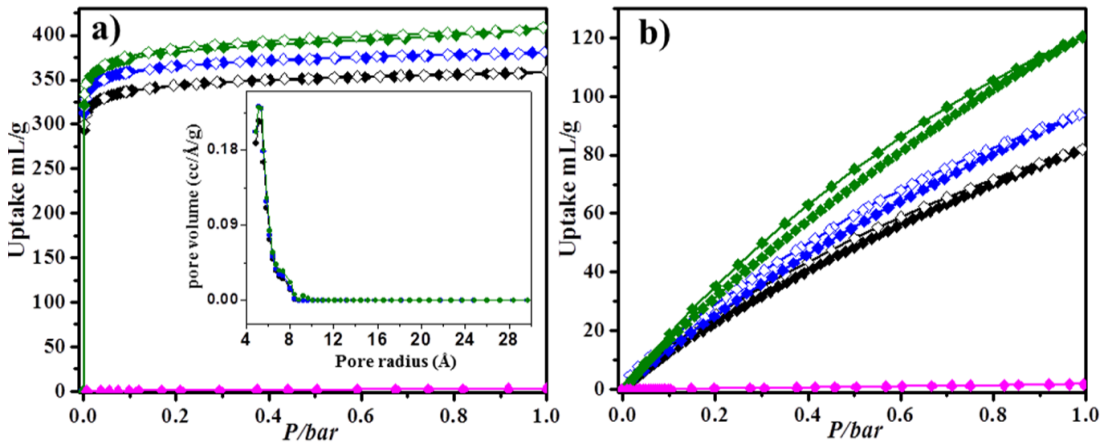

Figure 8. Adsorption isotherms of the activated bulk CuBTC and the composites: (a) N_2 adsorption isotherms at 77 K; the inset show the pore size distribution (b) CO_2 adsorption isotherms at 298 K. Colour code: black: CuBTC, blue: **CuBTC@AC-1**, green: **CuBTC@AC-2** and pink: AC. Open and closed symbol denotes adsorption and desorption respectively.

The bulk CuBTC shows a typical type-I N_2 isotherm at 77 K attributed to its microporous nature (Figure 8a). The BET surface area (1253 m^2/g) is close to the value reported for the bulk CuBTC samples prepared under similar condition.[9e,16a] The densely stacked layered of bulk AC do not have any significant surface area as revealed by its N_2 adsorption isotherm. N_2 adsorption isotherm of the physical mixture of CuBTC and AC reveals lesser uptake (Figure 9) and surface area (810

m^2/g) compared to bulk CuBTC, due to the presence of non-porous AC. In contrast, **CuBTC@AC-1** and **CuBTC@AC-2** show enhanced BET surface area of 1305 and 1381 m^2/g, respectively.

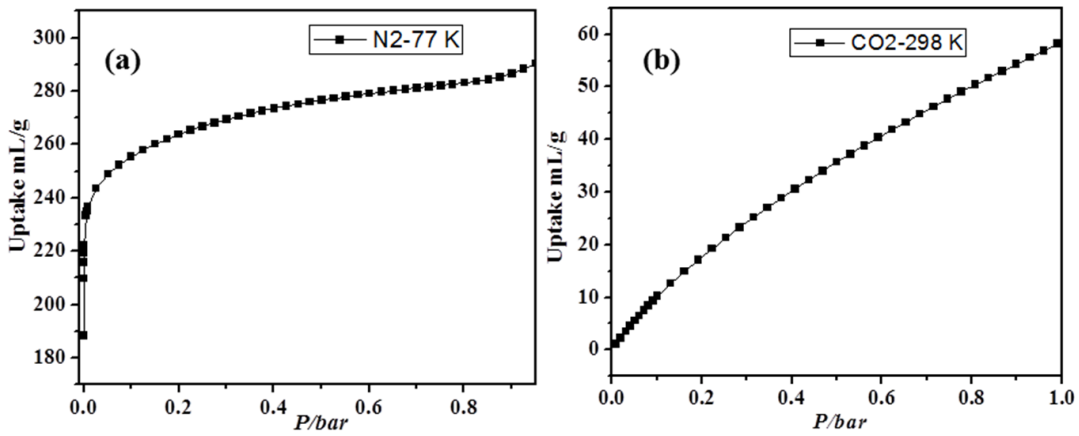

Figure 9. Adsorption isotherms of the physical mixture of CuBTC and AC (90.4: 9.6 wt%; similar to **CuBTC@AC-2**): (a) N_2 adsorption isotherm at 77 K; (b) CO_2 adsorption isotherm at 298 K. The lesser adsorption uptake compared to CuBTC is attributed to the presence of non-porous AC component. The lesser uptake of the physical mixture suggests that the effect of composite is not realized.

The wt% of non-porous AC in the two composites are less (<10 wt%). AC template prevents aggregation between the crystallites and favours well dispersion of nanocrsytals throughout AC. This increases accessibility of MOF for N_2 molecules, thus increasing the surface area. Furthermore, there could be formation of some voids at the interface of MOF NPs and AC layers, which can also contribute to enhance the surface area of the composites. The pore size distribution plots calculated using non-local density functional theory (NLDFT) method show that the pore diameter of both **CuBTC@AC-1** and **CuBTC@AC-2** are about ~10 Å, which corresponds the typical micropore of CuBTC (Figure 8a inset). While the pore volume of non-porous AC is negligible, pore volumes for CuBTC, **CuBTC@AC-1** and **CuBTC@AC-2** are 0.49, 0.52 and 0.56 cc/g respectively. Similar to the surface area, non-porous AC does not contribute to the pore volumes of the composites, but the composites shows enhanced pore volumes due to the formation of well-dispersed nanocrystals in the composites.

CO_2 is a major greenhouse gas which continues to accumulate in the atmosphere at an alarming pace and thus CO_2 capture and separation is of utmost importance.[18] The enhanced surface area of **CuBTC@AC-2** motivated us to investigate the

potential of this composite for CCS. We have measured the CO_2 adsorption isotherms at 273 K and 298 K up to 1 bar. AC does not adsorb any significant amount of CO_2 as revealed from the isotherm at 298 K (Figure 8b). The CO_2 uptake capacity of **CuBTC@AC-2** at 273 K is considerably high (182 ml/g or 8.1 mmol/g at 1 bar), which is increased by 39% compared to that of CuBTC (Figure 10). CO_2 uptake capacity of **CuBTC@AC-2** (Figure 8b) at 298 K, 1 bar is 120 ml/g or 5.35 mmol/g which is 46% higher than that of CuBTC (82 ml/g or 3.7 mmol/g). It is noteworthy that such enhancement in the CO_2 uptake of CuBTC at room temperature has rarely been achieved.[19]

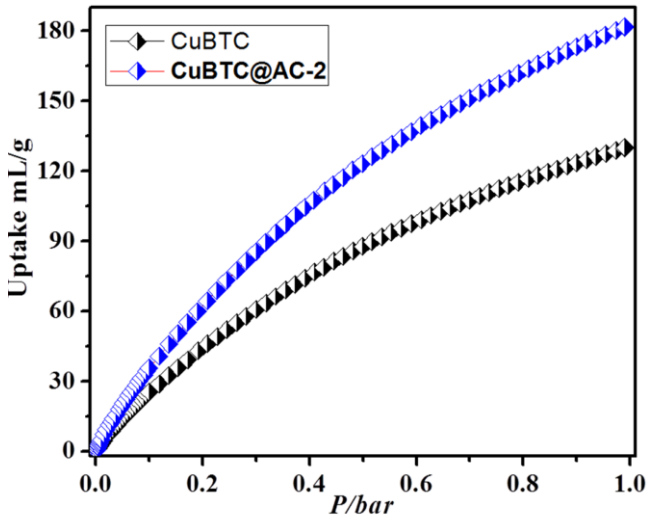

Figure 10. CO_2 adsorption isotherms of activated CuBTC and **CuBTC@AC-2** at 273 K. Open and closed symbol denotes adsorption and desorption respectively.

To extract the coverage-dependent isosteric heat of adsorption, we have fitted the CO_2 adsorption data at 273 K and 298 K with a virial-type expression[3a] (Figure 11, 12). At zero loading, the isosteric heat of adsorption (Q_{st}) for CuBTC and **CuBTC@AC-2** are 24 and 38 kJ mol^{-1} respectively. The Q_{st} value of **CuBTC@AC-2** is close to that of some amine functionalized MOFs.[15c] The stronger CO_2 affinity of **CuBTC@AC-2** can arise from the formation of active sites at MOF NPs-AC interface for facile interaction with quadrupolar CO_2. To compare the adsorption kinetics in CuBTC and **CuBTC@AC-2** composite, we have performed adsorption kinetic measurements with methanol vapour. The adsorption uptake is considerably higher in **CuBTC@AC-2** compared to bulk CuBTC (Figure 13). The kinetic data are fitted into the linear driving force mass

transfer (LDF) model which can be described by the equation: $M_t/M_e = 1-\exp(-kt)$, where M_t and M_e are the mass uptake at time t and at equilibrium respectively, and k is the kinetic rate constant. The plot of M_t/M_e vs. t shows distinct differences between the rates of mass diffusion (Figure 13) and **CuBTC@AC-2** shows a faster rate of adsorption with a rate constant value of 4.07×10^{-3} s^{-1} (P/P_0 at 0.0073978), while the rate constant for CuBTC is 2.46×10^{-3} s^{-1} (P/P_0 at 0.0073975). These results suggest smaller diffusion barrier and accelerated adsorption kinetics in the composite.

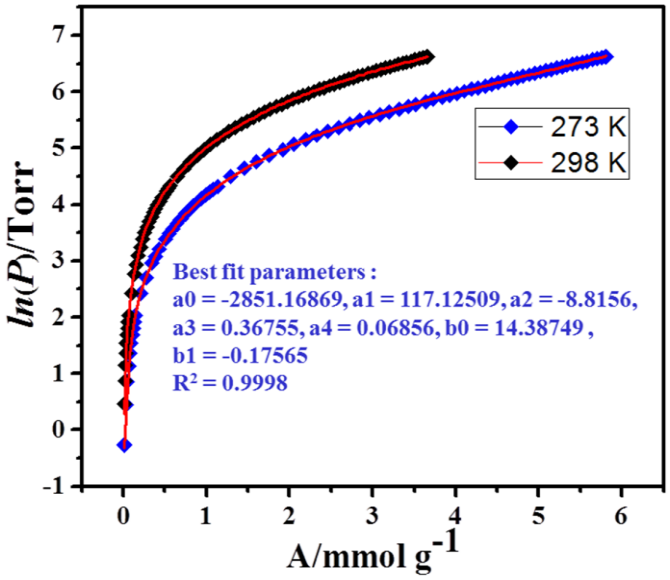

Figure 11. Pure component CO_2 isotherms of CuBTC at 273 K and 298 K fitted into virial-type expression. The solid red line indicates the best fitting using virial equation.

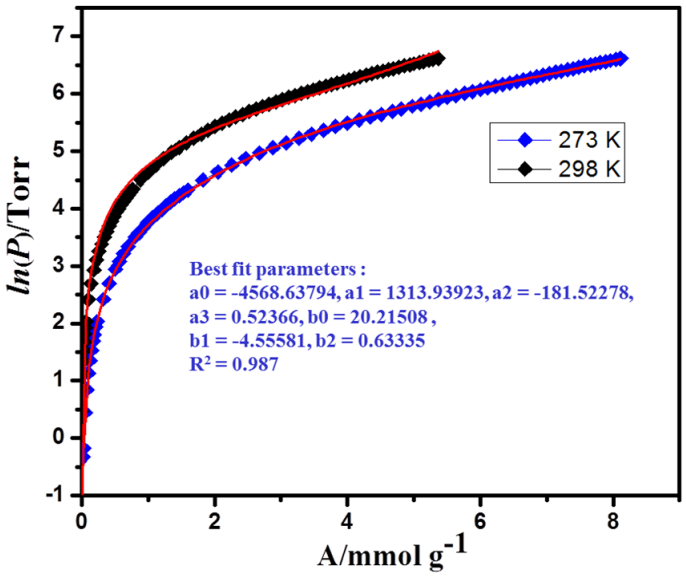

Figure 12. Pure component CO_2 isotherms of **CuBTC@AC-2** at 273 K and 298 K fitted into virial-type expression. The solid red line indicates the best fitting using virial equation.

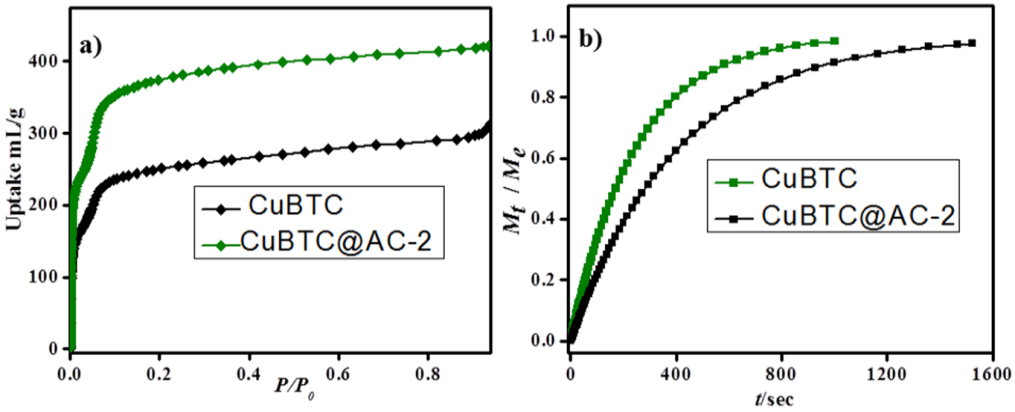

Figure 13. (a) MeOH vapor adsorption isotherms at 298 K. (b) Kinetics of adsorption of MeOH at 298 K (fitted into LDF model) showing higher mass diffusion in **CuBTC@AC-2** compared to bulk CuBTC.

Single-component CO_2, N_2 and CH_4 adsorption isotherms at 298 K, 1 bar clearly demonstrated high CO_2 selectivity of the **CuBTC@AC-2** composite (Figure 14). To test the gas separation capability of the composite, breakthrough column experiments were carried out using binary CO_2/N_2 (V/V: 15:85) and CO_2/CH_4 (V/V: 50:50) mixture at room temperature.

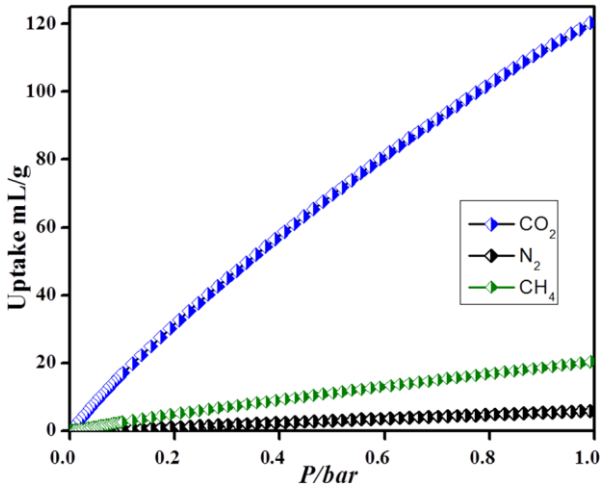

Figure 14. CO_2, N_2 and CH_4 adsorption isotherms at 298 K of activated **CuBTC@AC-2**.

The breakthrough curves of the binary mixtures of CO_2/N_2 and CO_2/CH_4 for **CuBTC@AC-2** exhibit significant retention time for CO_2 (410 seconds and 305 seconds respectively) (Figure 15). This suggests the efficiency of the composite to separate CO_2 gas from the gas mixtures. The retention time for CO_2 are enhanced in the composites compared to the bulk CuBTC (retention time of CO_2 are 337 seconds and 250 seconds for CO_2/N_2 and CO_2/CH_4 mixtures, respectively) (Figure 16).

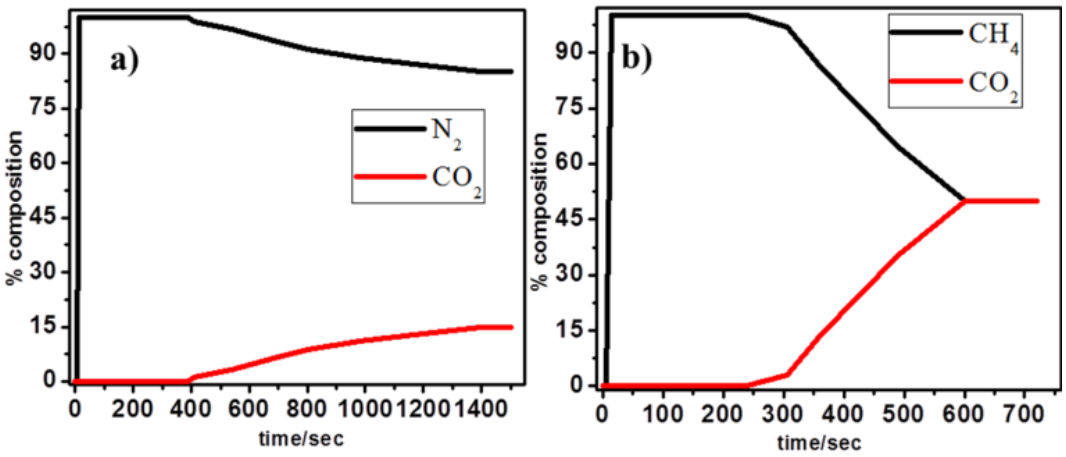

Figure 15. Breakthrough curves of **CuBTC@AC-2** for the binary mixture of (a) CO_2 (red)/ N_2 (black) (V/V: 15:85) and (b) CO_2/CH_4 (red)/ (black) (V/V: 50: 50).

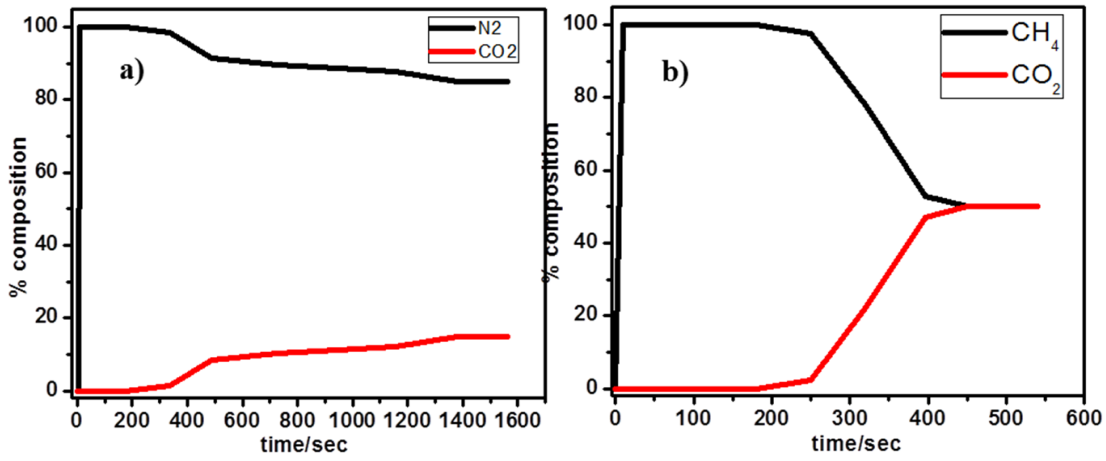

Figure 16. Breakthrough curves of bulk CuBTC for binary mixture of (a) CO_2 (red)/N_2 (black) (V:V: 15:85) and (b) CO_2 (red)/CH_4 (black) (V:V: 50:50).

An effective method of CCS process is chemical fixation of the adsorbed CO_2 into important value added products. One of such chemical fixation reactions is the Lewis acid catalyzed cycloaddition of CO_2 with different epoxides yielding cyclic carbonates.[16c,d] The cycloaddition reaction of propylene oxide (PO) with CO_2 into propylene carbonate was performed using **CuBTC@AC-2** as a catalyst at room temperature and under 1 atm of CO_2 pressure. The yield of the product is 79.6% over 48 h, while the yield is only 49% using bulk CuBTC catalyst under similar reaction conditions,[16c] which demonstrates that the catalytic activity is significantly enhanced in the composite. The improved catalytic performance of **CuBTC@AC-2** is attributed to the highly dispersed ultra-small NPs with exposed catalytic sites (open Cu^{II} sites) facilitating enhanced interaction between substrate and the

catalytic sites. The high CO_2 uptake of **CuBTC@AC-2** also helps to improve the catalytic efficiency. The yield of the product is reduced when a larger epoxide substrate (1,2-epoxybutane) is used, but the composite still shows better yield (61%) compared to that of CuBTC (37%) (Figure 17).

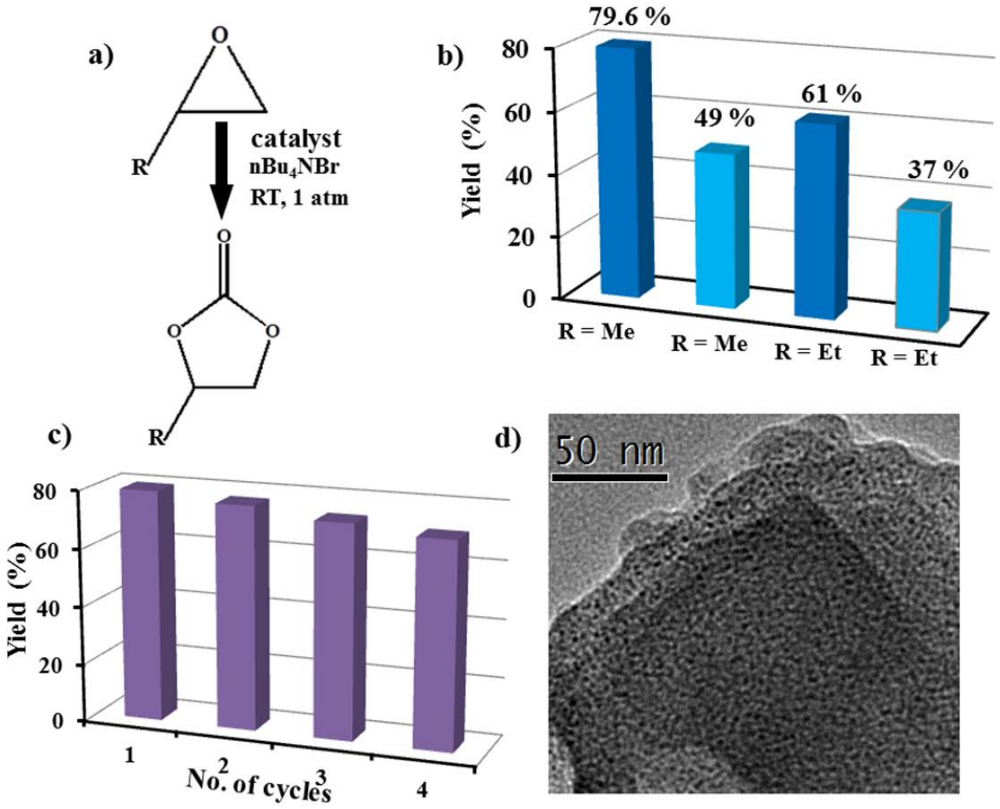

Figure 17. Scheme showing the catalytic cycloaddition of CO_2 with epoxides. (b) Yields of different products with related epoxides catalyzed by **CuBTC@AC-2** (blue) and CuBTC (light blue). (c) Recycling efficiency of **CuBTC@AC-2** (d) TEM images of the recycled **CuBTC@AC-2** catalyst collected after the 4th cycle.

Recyclability tests were carried out for the cycloaddition of PO by using the recycled **CuBTC@AC-2** catalyst. No significant decrease in the catalytic activity was observed even after 4th cycle (Figure 17c). PXRD data of the recycled compounds suggest that the framework integrity retains well after the catalytic reactions (Figure 18). Interestingly, TEM analysis carried out with the recycled catalyst after the 4th cycle shows uniformly distributed 2-3 nm NPs on AC template without agglomeration between the NPs (Figure 17d) and the texture is similar to that of pristine **CuBTC@AC-2**. Thus the nanostructure is retained even after the 4th catalytic cycle suggesting good stability of the MOF nanocrystals on AC template.

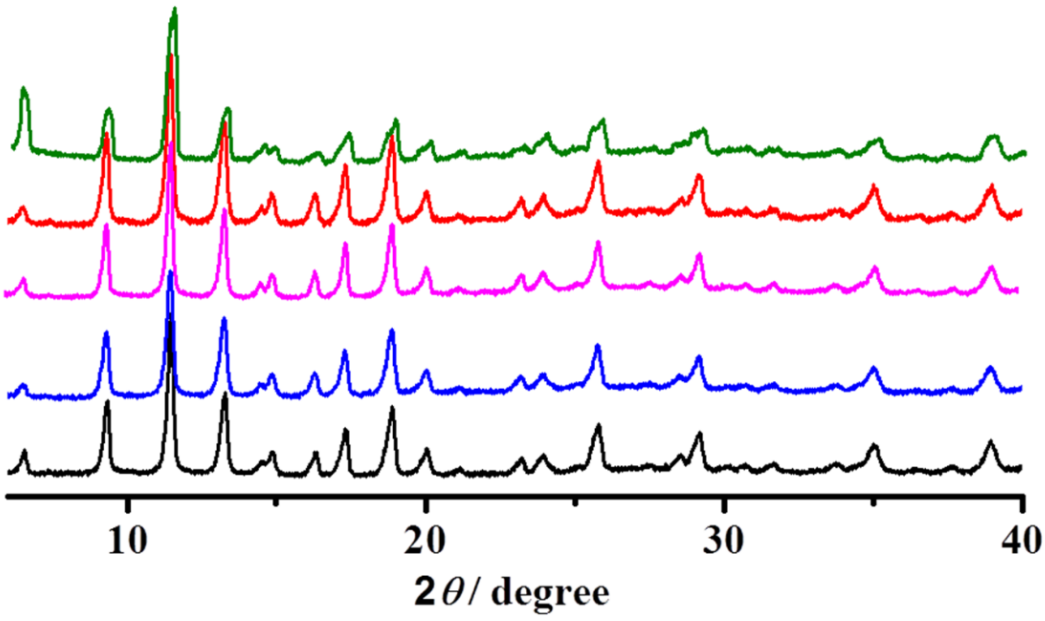

Figure 18. PXRD patterns of **CuBTC@AC-2** (black) and the recovered catalyst after 1st (blue), 2nd (pink), 3rd (red) and 4th cycle (green) of the catalytic reaction.

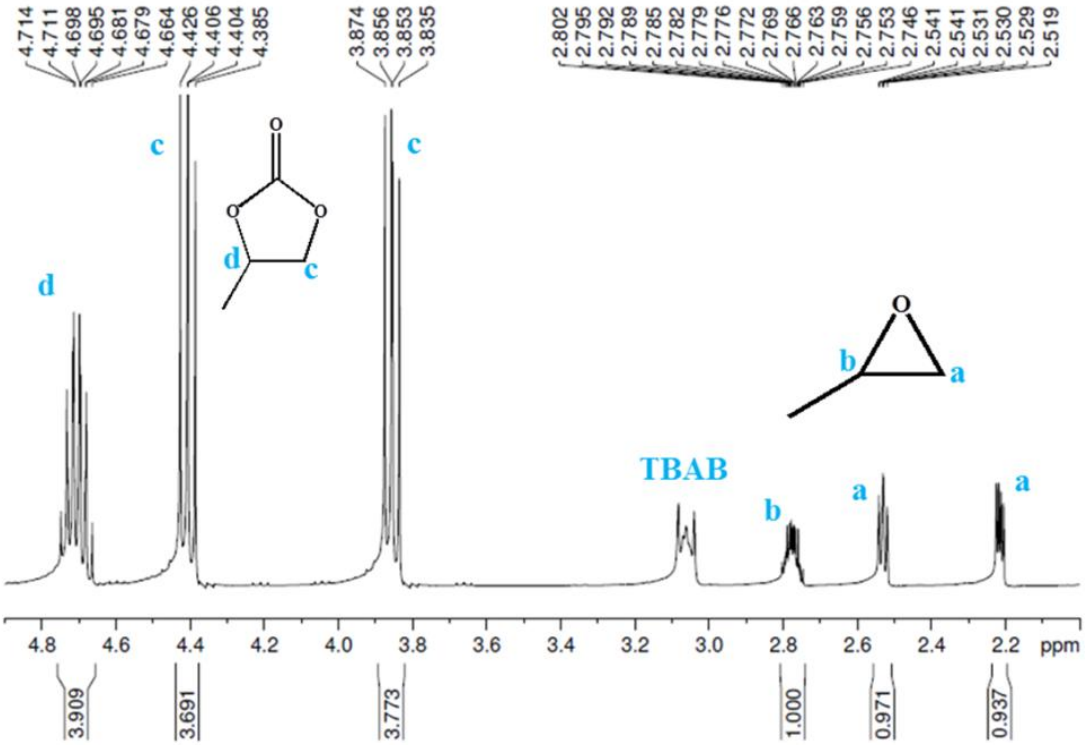

Figure 19. ^{1}H-NMR spectra (in $CDCl_3$) of the reaction mixture using **CuBTC@AC-2** as a catalyst for the cycloaddition reaction of propylene oxide. The peaks corresponding to propylene oxide, propylene carbonate and the co-catalyst tetrabutylammonium bromide (TBAB) are shown.

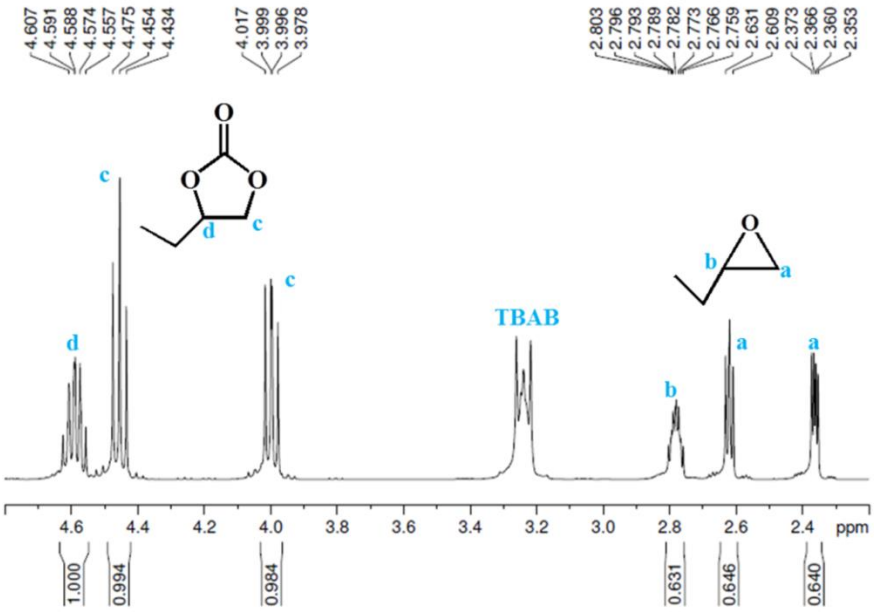

Figure 20. ^{1}H-NMR spectra (in $CDCl_3$) of the reaction mixture using **CuBTC@AC-2** as a catalyst for the cycloaddition reaction of 1,2-epoxybutane. The peaks corresponding to 1,2-epoxybutane, 1,2-butylene carbonate and the co-catalyst tetrabutylammonium bromide (TBAB) are shown.

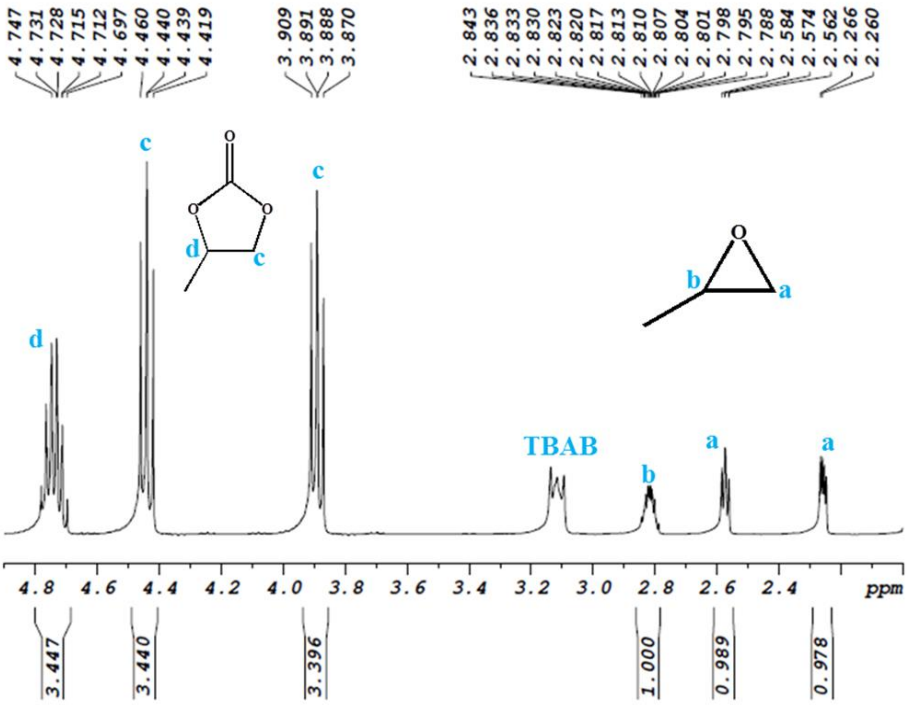

Figure 21. ^{1}H-NMR spectra (in $CDCl_3$) of the reaction mixture using **CuBTC@AC-2** catalyst in the 2nd cycle of recyclability test.

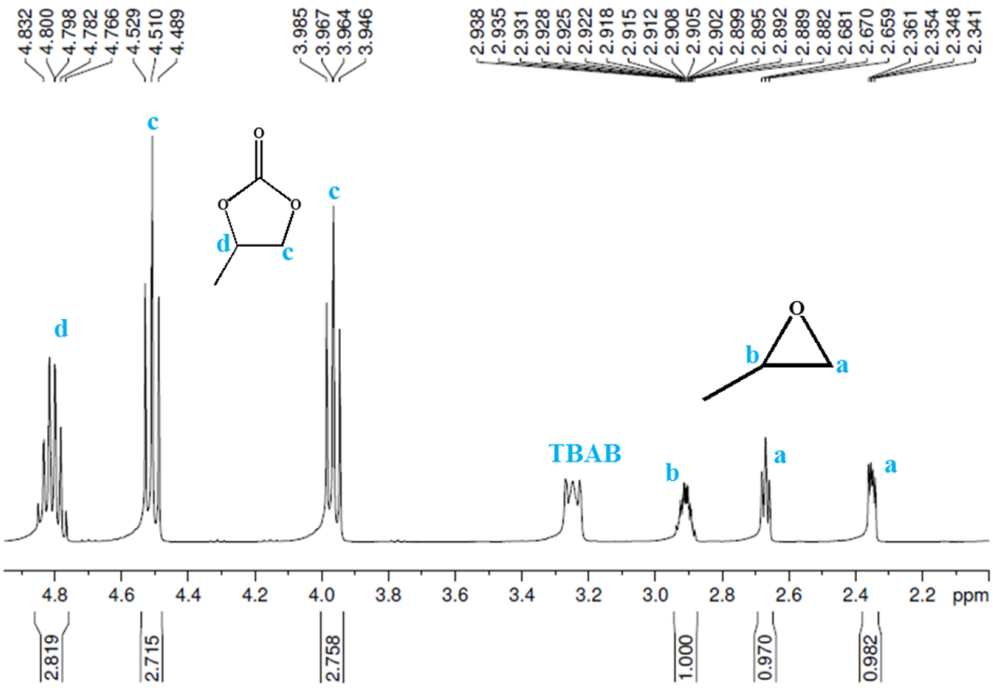

Figure 22. ^{1}H-NMR spectra (in $CDCl_3$) of the reaction mixture using **CuBTC@AC-2** catalyst in the 3rd cycle of recyclability test.

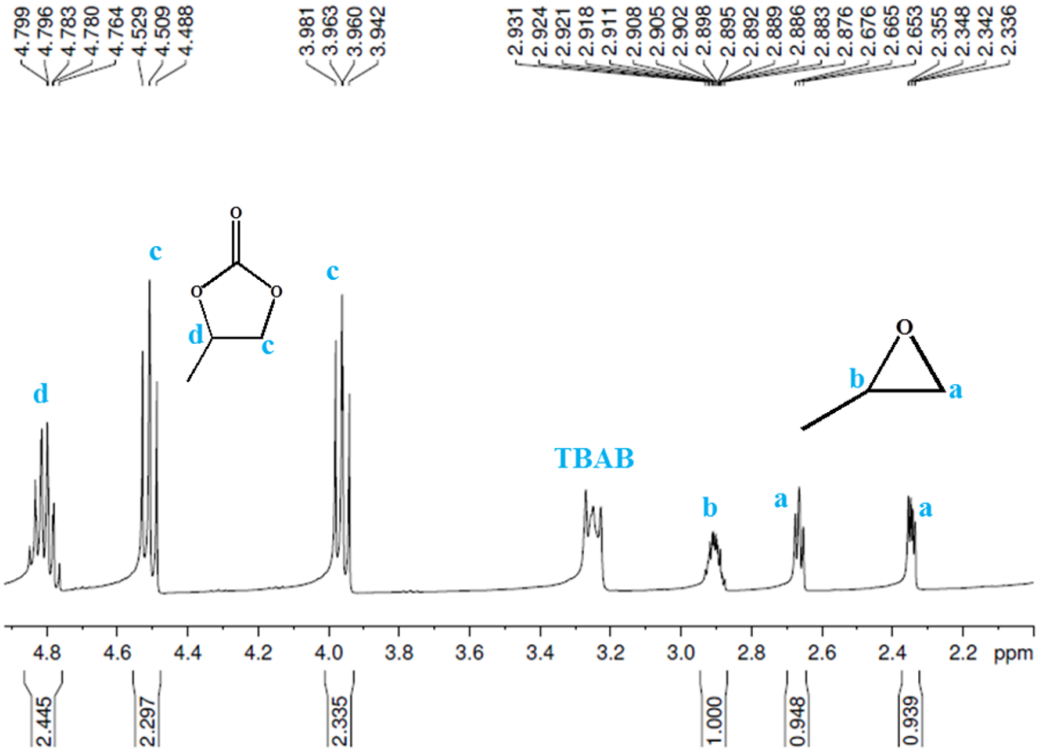

Figure 23. ^{1}H-NMR spectra (in $CDCl_3$) of the reaction mixture using **CuBTC@AC-2** catalyst in the 4th cycle of recyclability test.

5A.4 SUMMARY

The results demonstrate facile growth and stabilization of ultra-small (2-3 nm) and highly monodisperse CuBTC NPs on water dispersible AC template. For the first time, we have AC was employed as a template that can assist the growth of MOF nanoparticles, thus proposing a new route of crystal downsizing. Significant increase in CO_2 uptake and catalytic efficiency is realized in the composite, which is attributed to the synergistic combination of ultra-small MOF NPs and functional aminoclay template. The stable dispersion of the composite in water suggests solution processability of this composite which would ease fabrication of membrane, large area coating or device fabrication.

5A.5 REFERENCES

1. (*a*) E. Flügel, A. Ranft, F. Haase and B.V. Lotsch, *J. Mater. Chem*., 2012, **22**, 10119; (*b*) A. Carne, C. Carbonell, I. Imaz and D. Maspoch, *Chem. Soc. Rev*., 2011, **40**, 291; (*c*) S. Furukawa, J. Reboul, S. Diring, K. Sumida and S. Kitagawa, *Chem. Soc. Rev*., 2014, **43**, 5700; (*d*) Y. Sakata, S. Furukawa, M. Kondo, K. Hirai, N. Horike, Y. Takashima, H. Uehara, N. Louvain, M. Meilikhov, T. Tsuruoka, S. Isoda, W. Kosaka, O. Sakata and S. Kitagawa, *Science*, 2013, **339**, 193.
2. (*a*) D. Tanaka, A. Henke, K. Albrecht, M. Moeller, K. Nakagawa, S. Kitagawa and J. Groll, *Nat. Chem.*, 2010, **2**, 410; (*b*) S. Diring, S. Furukawa, Y. Takashima, T. Tsuruoka and S. Kitagawa, *Chem. Mater*., 2010, **22**, 4531.
3. (*a*) N. Sikdar, A. Hazra and T. K. Maji, *Inorg. Chem.*, 2014, **53**, 5993; (*b*) T. Tsuruoka, S. Furukawa, Y. Takashima, K. Yoshida, S. Isoda and S. Kitagawa, *Angew. Chem. Int. Ed*., 2009, **48**, 4739.
4. T. Kiyonaga, M. Higuchi, T. Kajiwara, Y. Takashima, J. Duan, K. Nagashima and S. Kitagawa**,** *Chem. Commun***.,** 2015, **51**, 2728.
5. A. Ranft, S. Betzler, F. Haase and B.V. Lotsch, *CrystEngComm*, **2013**, ***15***, 9296.
6. Q-L. Zhu, Q. Xu, *Chem. Soc. Rev*., 2014, **43**, 5468.
7. (*a*) F. Hoffmann, M. Cornelius, J. Morell and M. Froba, *Angew. Chem. Int. Ed*., 2006, **45**, 3216; (*b*) D. Liu, R. C. Huxford and W. Lin, *Angew. Chem. Int. Ed*., 2011, **50**, 3696.
8. (*a*) P. Horcajada, T. Chalati, C. Serre, B. Gillet, C. Sebrie, T. Baati, J. F. Eubank, D. Heurtaux, P. Clayette, C. Kreuz, J.-S. Chang, Y. K. Hwang, V. Marsaud, P.-N. Bories, L. Cynober, S. Gil, G. Fe´rey, P. Couvreur and R. Gref, *Nat. Mater*., 2010,

9, 172; (*b*) M. D. Rowe, C.-C. Chang, D. H. Thamm, S. L. Kraft, J. F. Harmon, A. P. Vogt, B. S. Sumerlin and S. G. Boyes, *Langmuir*, 2009, **25**, 9487; (*c*) M. G. Schwab, I. Senkovska, M. Rose, M. Koch, J. Pahnke, G. Jonschker and S. Kaskel, *Adv. Eng. Mater*., 2008, **10**, 1151.

9. (*a*) R. Kumar, K. Jayaramulu, T. K. Maji and C. N. R. Rao, *Chem. Commun*., 2013, **49**, 4947; (*b*) C. Petit and T. J. Bandosz, *Adv. Mater*., 2009, **21**, 4753–4757; (*c*) C. Petit, J. Burress and T. J. Bandosz, *Carbon*, 2011, **49**, 563; (d) C. Petit and T. J. Bandosz, *Adv. Funct. Mater*., 2011, **21**, 2108; (*e*) S. Liu, L. Sun, F. Xu, J. Zhang, C. Jiao, F. Li, Z. Li, S. Wang, Z. Wang, X. Jiang, H. Zhou, L. Yang and C. Schick, *Energy Environ. Sci*., 2013, **6**, 818.
10. (*a*) A. Ranft, F. Niekiel, I. Pavlichenko, N. Stock and B.V. Lotsch, *Chem. Mater.*, 2015, **27**, 1961; (*b*) L. Li, X. Jiao, D. Chen, B.V. Lotsch and C. Li, *Chem. Mater.*, **2015**, ***27***, 7601.
11. (*a*) S. Mann, S. L. Burkett, S. A. Davis, C. E. Fowler, N. H. Mendelson, S. D. Sims, D. Walsh and N. T. Whilton, *Chem. Mater*., 1997, **9**, 2300; (*b*) N. T. Whilton, S. L. Burkett and S. Mann, *J. Mater. Chem*., 1998, **8**, 1927; (*c*) J. E. Martin, A. J. Patil, M. F. Butler and S. Mann, *Adv. Funct. Mater*., 2011, **21**, 674; (*d*) J. Patil, E. Muthusamy and S. Mann, *Angew. Chem. Int. Ed*., 2004, **43**, 4928.
12. K. R. Datta, A. Achari and M. Eswaramoorthy, *J. Mater. Chem. A*, 2013, **1**, 6707.
13. K. K. R. Datta, C. Kulkarni and M. Eswaramoorthy, *Chem. Commun*., 2010, **46**, 616.
14. K. V. Rao, K. K. R. Datta, M. Eswaramoorthy and S. J. George, *Angew. Chem. Int. Ed*., 2011, **50**, 1179.
15. (*a*) G.T. Rochelle, *Science*, 2009, **325**, 1652; (*b*) A. Demessence, D. M. D-Alessandro, M. L. Foo and J. R. Long, *J. Am. Chem. Soc*., 2009, **131**, 8784; (*c*) S. Couck, J. F. M. Denayer, G. V. Baron, T. Remy, J. Gascon and F. Kapteijn, *J. Am. Chem. Soc*., 2009, **131**, 6326.
16. (*a*) S. S. Y. Chui, S. M. F. Lo, J. P. H. Charmant, A. G. Orpen and I. D. Williams, *Science*, 1999, **283**, 1148; (*b*) L. Hamon, E. Jolimaitre and G. D. Pirngruber, *Ind. Eng. Chem. Res.*, 2010, **49**, 7497; (*c*) W.-Y. Gao, Y. Chen, Y. Niu, K. Williams, L. Cash, P.J. Perez, L. Wojtas, J. Cai, Y.-S. Chen and S. Ma, *Angew. Chem. Int. Ed*., 2014, **53**, 2615.
17. W.-Y. Gao, L. Wojtas and S. Ma, *Chem. Commun*., 2014, **50**, 5316.

18. (*a*) P. Li, Y. He, Y. Zhao, L. Weng, H. Wang, R. Krishna, H. Wu, W. Zhou, M. O'Keeffe, Y. Han and B. Chen, *Angew. Chem. Int. Ed*., 2015, **54**, 574; (*b*) Z. Zhang, Z. Yao, S. Xiang and B. Chen, *Energy Environ. Sci*., 2014, **7**, 2868; (*c*) S. Xiong, Y. Gong, H. Wang, H. Wang, Q. Liu, M. Gu, X. Wang, B. Chen and Z. Wang, *Chem. Commun*., 2014, **50**, 12101; (*d*) W. Bloch, R. Babarao, M. Hill, C. Doonan and C. Sumby, *J. Am. Chem. Soc*., 2013, **135**, 10441; (*e*) R. Lyndon, K. Konstas, B.P. Ladewig, P.D. Southon, P.C.J. Kepert and M.R. Hill, *Angew. Chem. Int. Ed*., 2013, **52**, 3695; (*f*) R. Babarao, C. J. Coghlan, D. Rankine, W. M. Bloch, G. K. Gransbury, H. Sato, S. Kitagawa, C. J. Sumby, M. R. Hill and C. J. Doonan, *Chem. Commun*., 2014, **50**, 3238; (*g*) D. M. D'Alessandro, B. Smit and J. R. Long, *Angew. Chem. Int. Ed*., 2010, **49**, 6058.

19. A. Yazaydın, A. I. Benin, S.A. Faheem, P. Jakubczak, J. J. Low, R.R. Willis,R. Q. Snurr, *Chem. Mater*., 2009, **21**, 1425.

Chapter 5B

Flexible MOF-Aminoclay Nanocomposites with Enhanced and Tunable Stepwise/Gated adsorption

Abstract

Miniaturization of flexible metal-organic frameworks (F-MOFs) to nanoscale is expected to show interesting structural dynamics and serve numerous applications from separation, drug delivery to sensing. However, nanoscale F-MOFs or their composite materials have remained largely unexplored till date. This chapter reports a new and facile method to stabilize F-MOF nanocrystals on aminoclay (AC) template and their tunable, enhanced gas adsorption and separation properties. Miniaturization of two different 2D F-MOFs, $(\{[Cu(pyrdc)(bpp)](5H_2O)\}_n$ (**F-MOF1**) with pillared-bilayer structure and $\{[Cu(dhbc)_2(4,4'\text{-bpy})]\cdot 5H_2O\}$ (**F-MOF2**) with interdigitated network on AC are reported. AC acts as a functional template to grow and stabilize MOF nanocrystals. Several **F-MOF1@AC** composites were synthesized where the gate/step pressure for specific adsorbate molecule could be tuned by varying the AC content. Enhanced guest adsorption with new stepwise behaviour has been realized by certain composite. Breakthrough column experiments with the **F-MOF2@AC-1** composite show its capability to separate CO_2/N_2 and CO_2/CH_4 gas mixture under ambient condition.

Paper based on this study:

A. Chakraborty, S. Roy, M. Eswaramoorthy, T. K. Maji, *manuscript under preparation.*

5B.1 INTRODUCTION

Structural flexibility is an intriguing characteristic of metal-organic framework (MOF)[1] which gives it an edge over the conventional porous materials like zeolites or mesoporous silica.[2] Flexible MOFs (F-MOFs) show unusual stepwise and gated adsorption for a specific molecule, and are therefore exploited for gas separation, sensing and drug delivery.[3,4] Although significant research on bulk F-MOFs have been carried out, downsizing F-MOFs to the nanoscale regime is under-explored compared to the rigid nanoscale MOFs.[5] In addition to the enhanced solution processability and applications in drug delivery, F-MOFs can also show new structural dynamics in nanoscale, that would result in unprecedented properties.[6] For example, recently Kitagawa *et al*. have shown that metastable open phase could be obtained by downsizing a F-MOF and demonstrated the so called "molecular-scale shape-memory effect".[6b] Recently, a new class of MOF composite materials have emerged based on the combination of MOF and another active species like graphene oxide (GO), porous silica, organic polymers.[7-9] Such combination of different functional components not only mitigate the drawbacks of the individual components, but also provide synergistic effects to accomplish enhanced and novel properties.[7] Stabilization of MOF nanoparticles (NPs) using a 2D functional scaffolds like GO have been documented in recent past,[10] however, the poor water dispersibility of GO limits the application of the composites in water based medium. Researchers are therefore looking for new 2D templates which can assist facile growth of MOF NPs in aqueous medium towards processable nanocomposite materials. Aminopropyl functionalized magnesium phyllosilicate with approximate unit cell composition of $[H_2N(CH_2)_3]_8Si_8Mg_6O_{16}(OH)_4]$, popularly known as aminoclay (AC), is a 2D synthetic layered compound.[11] AC has traditionally been used for stabilization of metal NPs and organic chromophores for catalysis, light harvesting and electrocatalytic applications.[11-13]

In previous chapter highly water dispersible composite materials of MOF and AC were reported, where the amine groups of AC trigger growth and stabilization of MOF NPs. However, composite materials based on flexible MOFs are underexplored. It would be worth to study the effect of flexibility in the composite materials as some of the intermediate phase of the MOF may be stabilized on the 2D template during activation process. Therefore in such composite, the gate or step pressure is expected to change during sorption, thus changing corresponding uptake and release of the guest molecules which will have profound impact on gas adsorption/separation and drug-delivery

applications. In this chapter, AC templated synthesis of F-MOF nanocrystals is explored for the first time towards new composites having enhanced and tunable gas adsorption and separation properties. For the fabrication of the composites, two different types of 2D F-MOFs were chosen; $\{[Cu(pyrdc)(bpp)].5H_2O\}_n$ (**F-MOF1**)[14] (pyrdc = pyridine-2,3-dicarboxylate; bpp = 1,3-bis(4-pyridyl)-propane] and $\{[Cu(dhbc)_2(4,4'\text{-bpy})]\cdot 5H_2O\}$ (**F-MOF2**)[15] (Hdhbc = 2,5-dihydroxybenzoic acid, 4,4'-bpy = 4,4'-bipyridine). Both show structural transformation upon dehydration leading to a contracted structure while structural re-expansion occurs with the guest inclusion. Several composites of **F-MOF1** were synthesized by varying the AC content. Although the pristine MOF and AC are non-porous to N_2, one of the composites shows significant increase in surface area. Guest-responsiveness is altered significantly in different composites and the gate/step pressure of CO_2/C_2H_2 adsorption has been modulated by changing the AC contents. The composite with minimum AC content shows enhanced CO_2 adsorption uptake compared to **F-MOF1** and exhibits new stepwise adsorption instead of showing a gated behaviour. **F-MOF2** was also downsized using AC template to synthesize **F-MOF2@AC** composites, thus demonstrating that AC can act as a versatile downsizing material to furnish different F-MOF nanocomposites. Breakthrough column experiments with **F-MOF2@AC-1** composite show its capability to separate CO_2/N_2 and CO_2/CH_4 binary gas mixture under ambient condition, suggesting that the composite can be potential candidate to separate greenhouse CO_2 gas from flue gas mixture.

5B.2 EXPERIMENTAL SECTION

5B.2.1 Materials

All the reagents and solvents employed are commercially available and used as supplied without further purification. $Cu(NO_3)_2\cdot 2.5H_2O$, 2, 3-pyridine dicarboxylic acid, 1,3-bis(4-pyridyl)-propane, 2,5-dihydroxybenzoic acid and 4,4'-bipyridine were obtained from the Aldrich Chemical Co.

5B.2.2 Synthesis

Aminoclay: Aminoclay (AC) was prepared following typical reaction conditions reported by Mann and co-workers.[12d] 3-aminopropyltriethoxysilane (1.3 mL, 5.85 mmol) was added dropwise to an ethanolic solution of $MgCl_2$ (0.84 g, 3.62 mmol) in ethanol (20 g). The white slurry obtained was stirred overnight and the precipitate was isolated by centrifugation and then was washed with ethanol (50 mL) and dried at 40 °C. PXRD

pattern (Figure 1) of the dried compound shows typical reflection corresponding to the d_{001} interlayer spacing of 1.6 nm originating from the bilayer arrangement of propylamine groups.

Bulk F-MOF1: 0.25 mmol of 2, 3-pyridine dicarboxylic acid was taken in 10 mL H_2O and the pH of the solution was adjusted to pH = 9 by adding 0.1 (M) KOH solution. 0.25 mmol of 1,3-bis(4-pyridyl)-propane was dissolved in 10 mL MeOH and this solution was added to the above solution of 2, 3-pyridine dicarboxylic acid and was stirred for ten minutes to prepare the ligand solution. $Cu(NO_3)_2{\cdot}2.5H_2O$ (0.25 mmol) was dissolved in 15 mL water and the ligand solution was dropwise added to the Cu(II) solution. The resulting blue turbid solution was stirred for 6 h and then filtered. The blue solid residue was washed several times with 1:1 H_2O:MeOH solution and was dried to obtain phase pure **F-MOF1** (Figure 2). Yield, 56%, relative to Cu(II).

Bulk F-MOF2: 0.8 mmol of 4,4'-bipyridine was dissolved in 10 mL EtOH and a solution of 2,5-dihydroxybenzoic acid (3.2 mmol in 10 mL EtOH) was added to the above solution. The mixture was stirred for ten minutes to prepare the ligand solution. $Cu(NO_3)_2{\cdot}2.5H_2O$ (0.8 mmol) was dissolved in 5 mL water and the ligand solution was slowly added to the Cu(II) solution. The resulting green turbid solution was stirred for 12 h and then filtered. The green solid residue was washed several times with 1:1 H_2O:EtOH solution and was dried to obtain phase pure **F-MOF2**. Yield, 64%, relative to Cu(II).

F-MOF@AC Composites: To prepare the **F-MOF1@AC** composites, first 20 mg of AC was dispersed in 5 mL of water/ethanol (60: 40) mixture (pH= 7). Aqueous solution of $Cu(NO_3)_2{\cdot}2.5H_2O$ (0.25 mmol, dissolved in 15 mL of water) was added to the clay solution and stirred for 30 minutes. The ligand solution was prepared (as mentioned for the synthesis of bulk MOF) and was added to the metal solution dropwise. The resulting solution was stirred for 6 h, filtered and the blue residue was washed several times with 1:1 H_2O:MeOH solution to obtain the first batch of composites. To increase the AC content, similar procedure was repeated taking different amount of AC (30 mg, 50 mg and 60 mg). The composites are denoted as **F-MOF1@AC-1**, **F-MOF1@AC-2**, **F-MOF1@AC-3** and **F-MOF1@AC-4**. The well-correspondence of the PXRD patterns of different composites and **F-MOF1** suggests existence of pure crystalline phase of **F-MOF1** in the composites (Figure 2). Similarly, composites of **F-MOF2** with AC were synthesized by adding Cu(II) solution to the solution of AC followed by addition of the ligand solutions (as mentioned for the synthesis of bulk MOF). Two different composites

were synthesized by taking different amount of AC (20 mg, 30 mg). The PXRD patterns of different composites show existence of pure crystalline phase of **F-MOF1** in the composites (Figure 3).

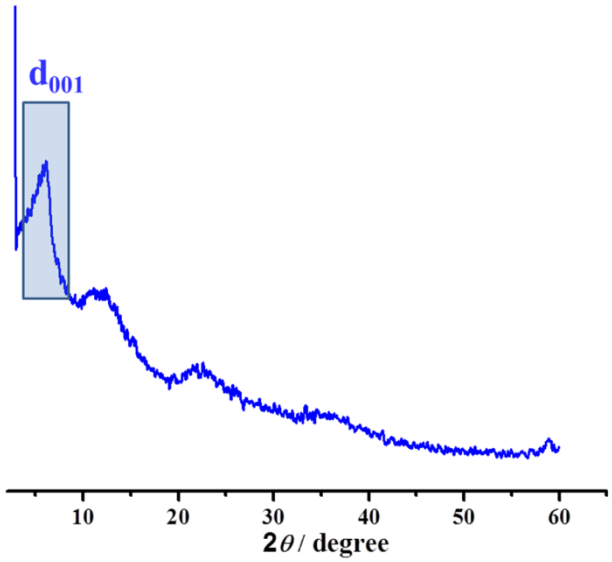

Figure 1. PXRD pattern of aminoclay. The d_{001} peak is highlighted.

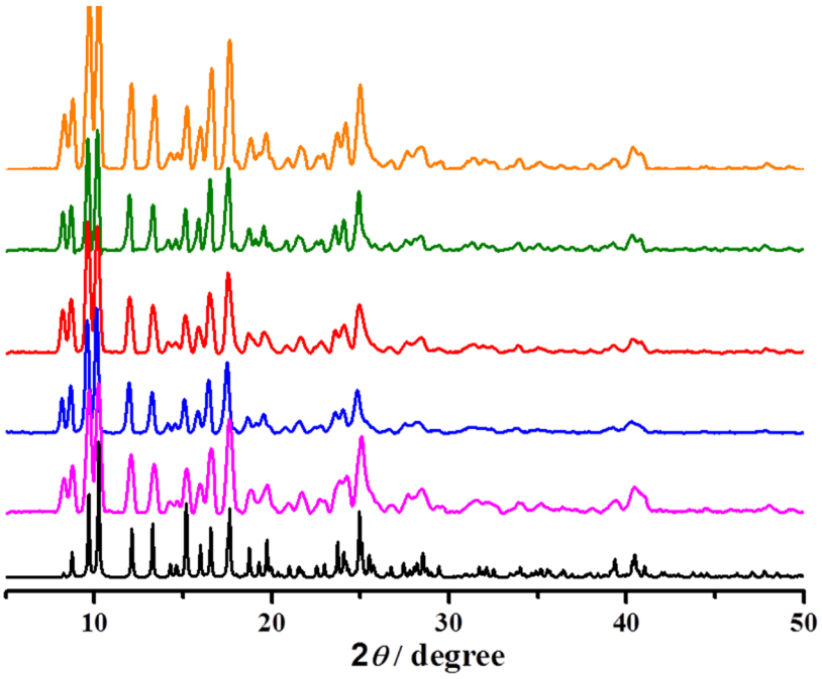

Figure 2. PXRD pattern of simulated (black) and experimental plots of **F-MOF1** (pink) and **F-MOF1@AC-1** (blue), **F-MOF1@AC-2** (red), **F-MOF1@AC-3** (green) and **F-MOF1@AC-4** (orange).

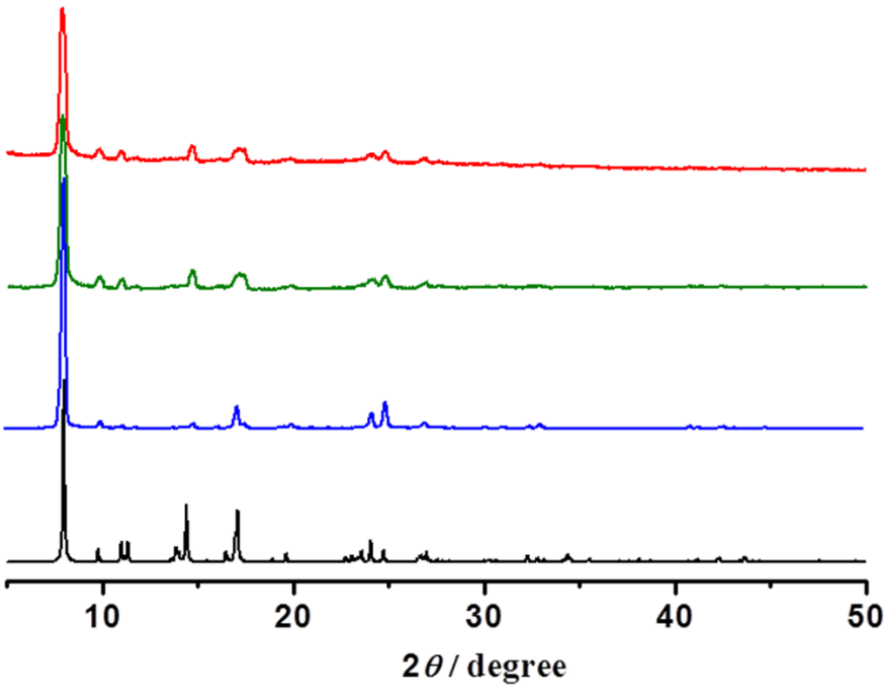

Figure 3. PXRD pattern of simulated (black) and experimental plots of **F-MOF2** (blue) and **F-MOF2@AC-1** (green) and **F-MOF2@AC-2** (red).

5B.2.3 Physical Measurements

Powder X-ray diffraction (PXRD) patterns were recorded on a Bruker D8 Discover instrument using Cu–Kα radiation. Energy dispersive analysis of X-rays (EDX) was carried out using field emission scanning electron microscope. Inductively Coupled Plasma-Atomic Emission Spectroscopy (ICP-AES) measurements were recorded on Perkin Elmer Optima 7000dv ICP-AES instrument. The scanning electron microscopy images were obtained using a Nova Nanosem 600 FEI field emission scanning electron microscope (FESEM). The samples were prepared by dispersing the sample in MeOH and then dropping 5 μL of the solution onto a small piece of silicon wafer and drying into air. Transmission electron microscopy (TEM) images were taken with a JEOL JEM-3010 transmission electron microscope operating at 200 kV. The samples were prepared in the same way as described above, but the drop cast was made onto a carbon-coated TEM grid. Adsorption isotherms were recorded with the desolvated samples using QUANTACHROME QUADRASORB-SI analyser and AUTOSORB IQ2 instrument. To prepare the desolvated samples, approximately 70 mg of sample was degassed under 10^{-1} pa vacuum for about 8 hours prior to the measurements. The **F-MOF1** and its composites were activated at 80 ºC while **F-MOF2** and its composites were activated at 100 ºC.

5B.3 RESULTS AND DISCUSSION

$\{[Cu(pyrdc)(bpp)].5H_2O\}_n$ (**F-MOF1**) is a 2D pillared-bilayer type of framework where 2D honeycomb layer is extended by the bpp linker.[14] The bpp linker shows conformational flexibility along -(CH_2)- chains and thus a pillared-bilayer framework with 2D water-filled channel is comprehended. **F-MOF1** shows structural contraction upon removal of the guest water molecules. Single-crystal structure determination shows that the dehydrated framework has the molecular formula $\{[Cu(pyrdc)(bpp)]_2\}_n$ and the cell volume decreases by 12.62% compared to the as-synthesized framework. The dehydrated framework contains two different 2D layers which are connected by one bpp linker. The other bpp linker is pendant because of the breaking of the Cu-N(bpp) bond and protrudes to the groove of the bilayer, thus reducing the effective open space and resulting in a non-porous dense framework (Scheme 1). The original structure is reversed back upon exposure to water with reformation of Cu-N(bpp) bond. The activated framework of **F-MOF1** shows gated adsorption profiles with MeOH, EtOH and CO_2, concomitant with structural transformation via with H-bonding interactions to the porous phase (**F-MOF1**). Crystal structure of the CO_2 included framework shows regeneration of the as-synthesized structure where several C-H---O interactions stabilizes CO_2 molecules inside the framework.

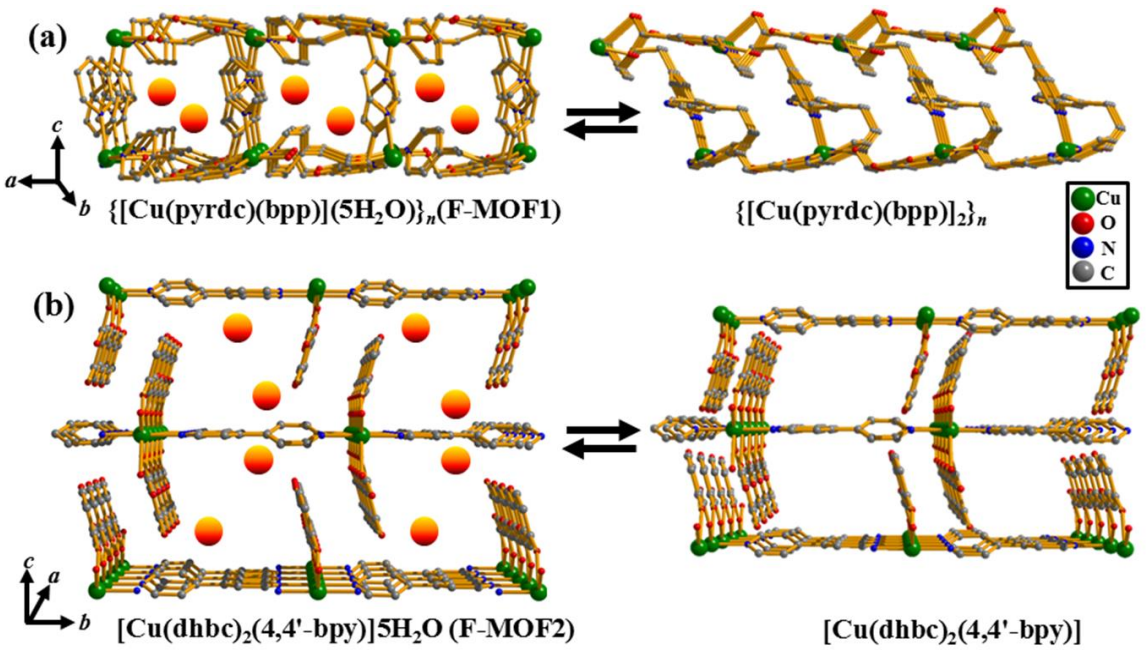

Scheme 1. Guest induced structural transformation in (a) **F-MOF1** and (b) **F-MOF2**

Such structural dynamism of this system motivated us to further explore the crystal downsizing of the F-MOF1 on 2D AC template and study the adsorption behaviour of resulting nanocomposites. The composites are synthesized at room temperature by dispersing AC in water/ethanol first and then adding the Cu(II) solution followed by the mixed linker solution. Four composites were prepared by varying AC amount as described in the synthesis section and the MOF/AC content in the composites were calculated from inductively coupled plasma atomic emission spectrometry (ICP-AES) based on the relative ratio of Cu(II) in the as-synthesized MOF and the composites. The composites are denoted as **F-MOF1@AC-1**, **F-MOF1@AC-2**, **F-MOF1@AC-3** and **F-MOF1@AC-4** and their AC contents are 9.7, 21.3, 32.7 and 32.8 weight% respectively (the AC loading in **F-MOF1@AC-3** and **F-MOF1@AC-4** are similar, indicating that it is the highest possible AC loading and **F-MOF1@AC-4** was not studied further). Energy dispersive X-ray spectroscopy (EDAX) analyses of **F-MOF1@AC-1** clearly show presence of Mg and Si element coming from AC and the element mapping suggests homogeneous distribution of the different elements throughout the sample (Figure 4). The SEM image of as-synthesized bulk **F-MOF1** shows micrometer sized particle, while that of AC shows typical layered structure (Figure 5). All the composites are characterized by

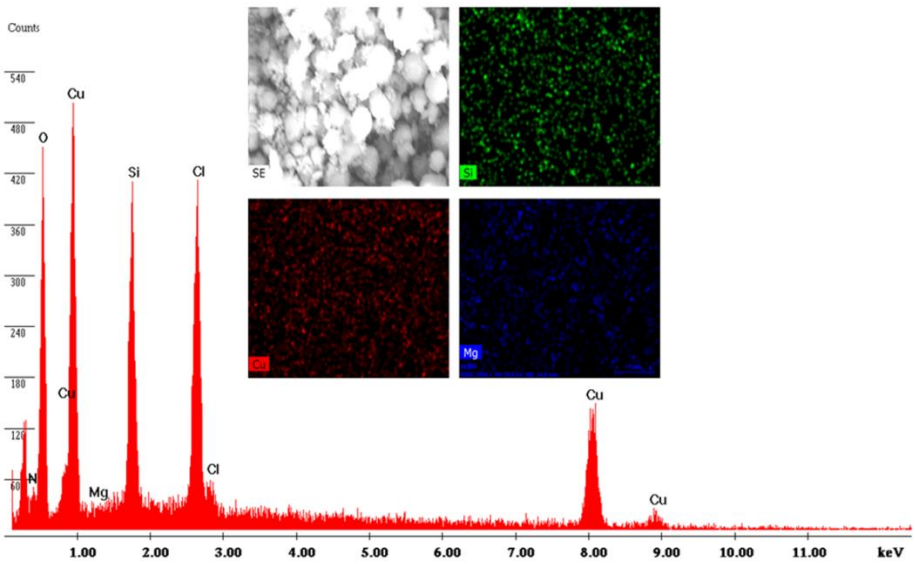

Figure 4. Element mapping of **F-MOF@AC-1** showing phase purity with homogeneous distribution of the elements (Si, Mg and Cu) throughout the sample. The EDX spectrum shows the presence of Cu (from **F-MOF1** component) and Si, Mg (from AC).

TEM analyses (Figure 6). TEM image of **F-MOF1@AC-1** shows growth and stabilization of **F-MOF1** nanocrystals throughout the layered AC template. The crystals

are mostly spherical in shape having diameter in the range of 10-15 nm (Figure 6a). **F-MOF1@AC-2** and **F-MOF1@AC-3** exhibit spherical NPs of average diameter 4-5 nm and 2-3 nm respectively (Figure 6b,c). The sizes of the NPs different composites do not vary significantly, but the number of AC layers increase with increasing AC loading, as evident from the TEM analysis. Thus the AC sheets appear to provide a platform for the nucleation and growth of **F-MOF1** nanocrystals.

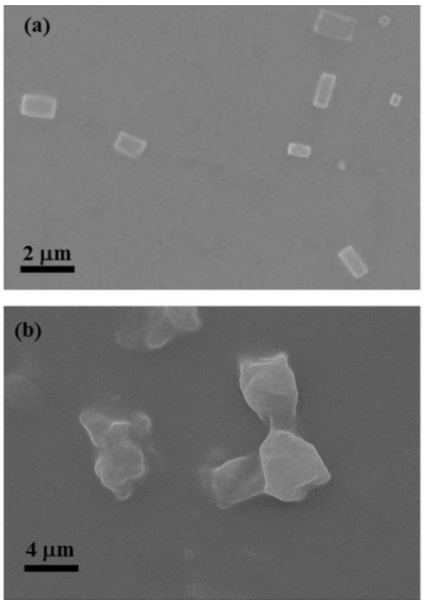

Figure 5. SEM images of (a) as-synthesized bulk **F-MOF1** and (b) AC.

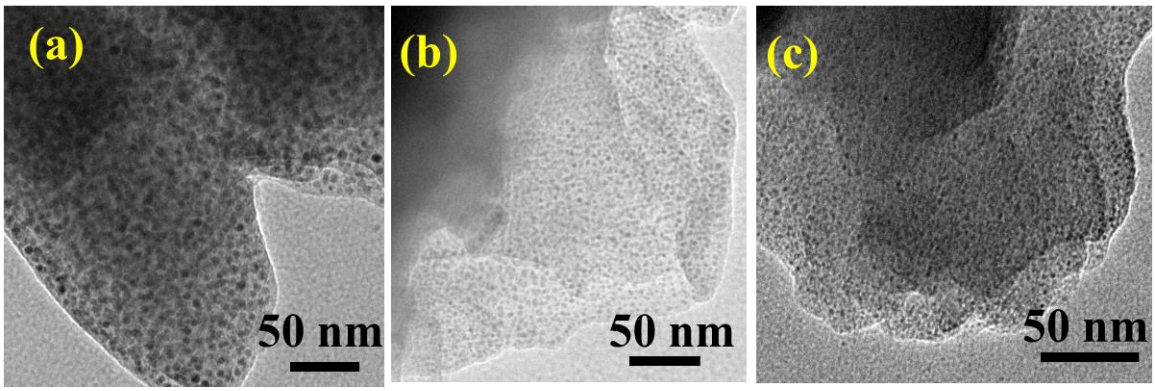

Figure 6. TEM images of (a) **F-MOF1@AC-1**, (b) **F-MOF1@AC-2**, and (c) **F-MOF1@AC-3** composites.

To understand the growth of the **F-MOF1** nanocrystals on AC template, further control experiments were performed similar to the work on CuBTC@AC composites in previous chapter. The Cu@AC solid obtained after the addition of Cu(II) salt to the AC solution followed by precipitation and washing with ethanol showed presence of Cu and AC, as seen by the EDX spectrum (Figure 7). This observation suggests binding of the Cu(II) ions to the free amine groups of AC. Further stirring of the ligand solution with the

Cu@AC solid resulted in the formation of **F-MOF1@AC** composite which was characterized by PXRD and TEM analysis (Figure 8). Thus AC acts as a seed to grow MOF nanocrystals by stabilizing Cu(II) sites first on its surface. Subsequently, crystallization of the nanocrystals start when ligand solution is added to the Cu@AC compound and then when ligand solution (Scheme 2).

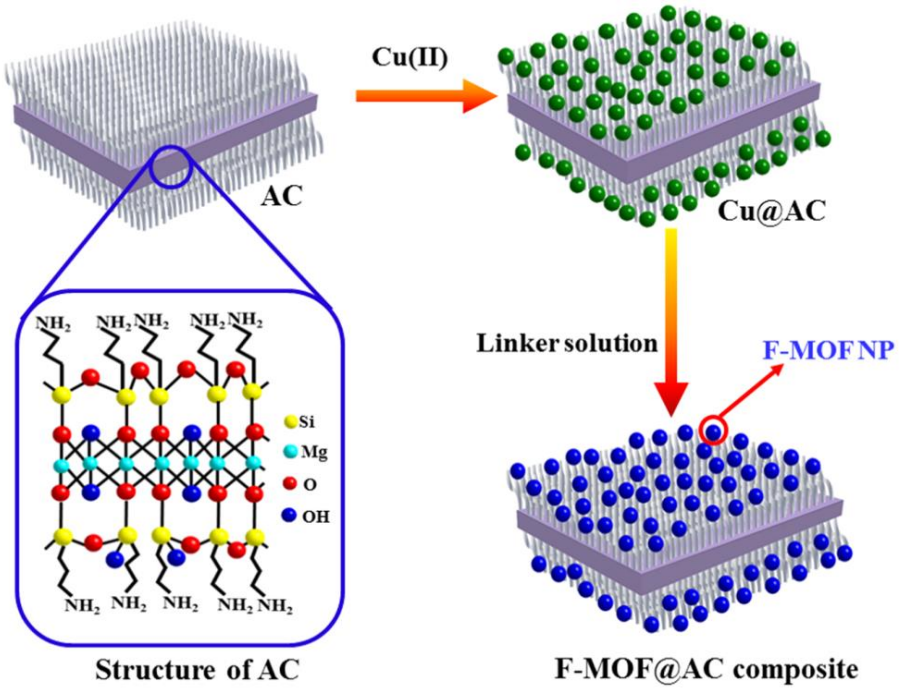

Scheme 2. The structure of AC and the schematic of stepwise formation of **F-MOF@AC** composites.

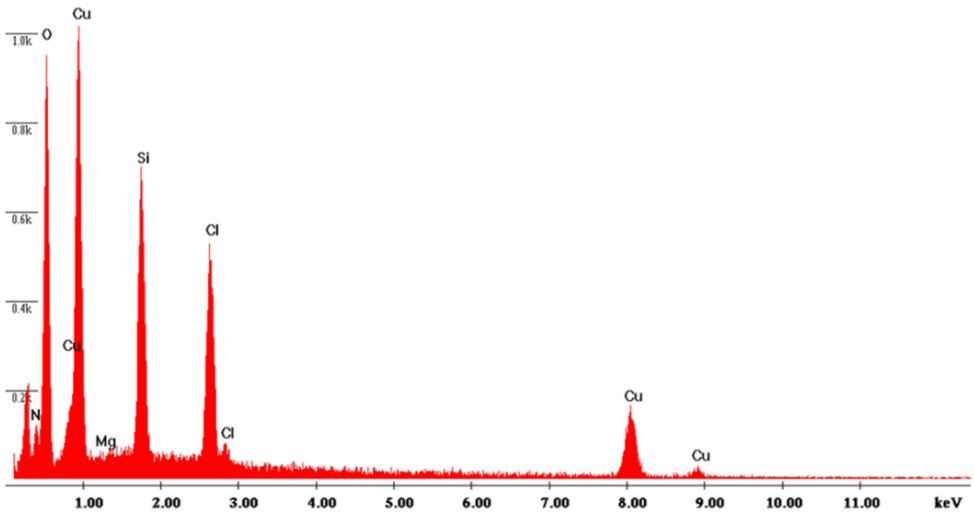

Figure 7. The EDX spectrum of Cu@AC solid showing shows the presence of Cu (from **F-MOF1** component) and Si, Mg (from AC).

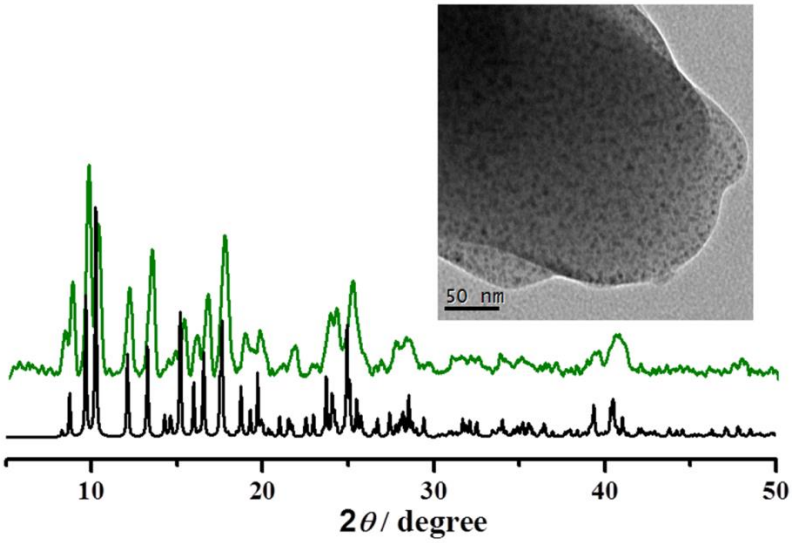

Figure 8. PXRD patterns of simulated **F-MOF-1** (black) and the solid (green) obtained from the reaction of Cu@AC and the ligand solution. Inset shows the TEM image.

The sorption isotherms of different gases were measured with the activated composites. The non-porous activated framework of **F-MOF1**[14] and densely stacked layered AC do not adsorb any N_2 at 77 K (Figure 9a). However, activated **F-MOF1@AC-1** shows considerable adsorption of N_2. Initially it shows smaller uptake at low pressure and the uptake gradually increases with increase in pressure with a type-IV like isotherm (Figure 9a). The pore size distribution plot of **F-MOF1@AC-1** calculated using non-local density functional theory (NLDFT) method shows wide distribution of micro (pore diameter ~16-18 Å) and mesopores (pore diameter ~24-40 Å). In **F-MOF1@AC-1**, the AC content is less and the MOF NPs are distributed on few layers of AC. The formation of the widely distributed micro and mesopores is attributed to the intercalation of MOF NPs between the AC layers and formation of voids at MOF NP-AC interface. With increase in non-porous AC loading, the N_2 adsorption uptake amount decreases significantly in **F-MOF1@AC-2**, and **F-MOF1@AC-3** does not adsorb any N_2. As the non-porous AC phase increases in the composites, the higher number of AC layers inhibit accessibility of guests thereby decreasing the adsorption uptake.

The activated framework of **F-MOF1** is reported to show guest-induced gate-opening behaviour for CO_2 adsorption at 195 K,[14] while AC does not adsorb any CO_2 (Figure 9b) due to difficulty in accessing active sites of $–NH_2$ groups within the layers. Interestingly, activated **F-MOF1@AC-1** shows a stepwise adsorption at 195 K with an initial uptake amount of 30 mL/g at P = 0.39 bar and after that a steep uptake observed which saturates at P = 1 bar with an uptake amount of 145 mL/g (Figure 9b). The total uptake at 1 bar

increases significantly (35%) compared to the activated **F-MOF1**. The initial CO_2 uptake is attributed to the presence of the micropores in the composite and the facile and steep uptake beyond P = 0.39 bar can be correlated to the open phase of the F-MOF1 NPs in the composite, similar to the activated F-MOF1. The higher adsorption uptake originates

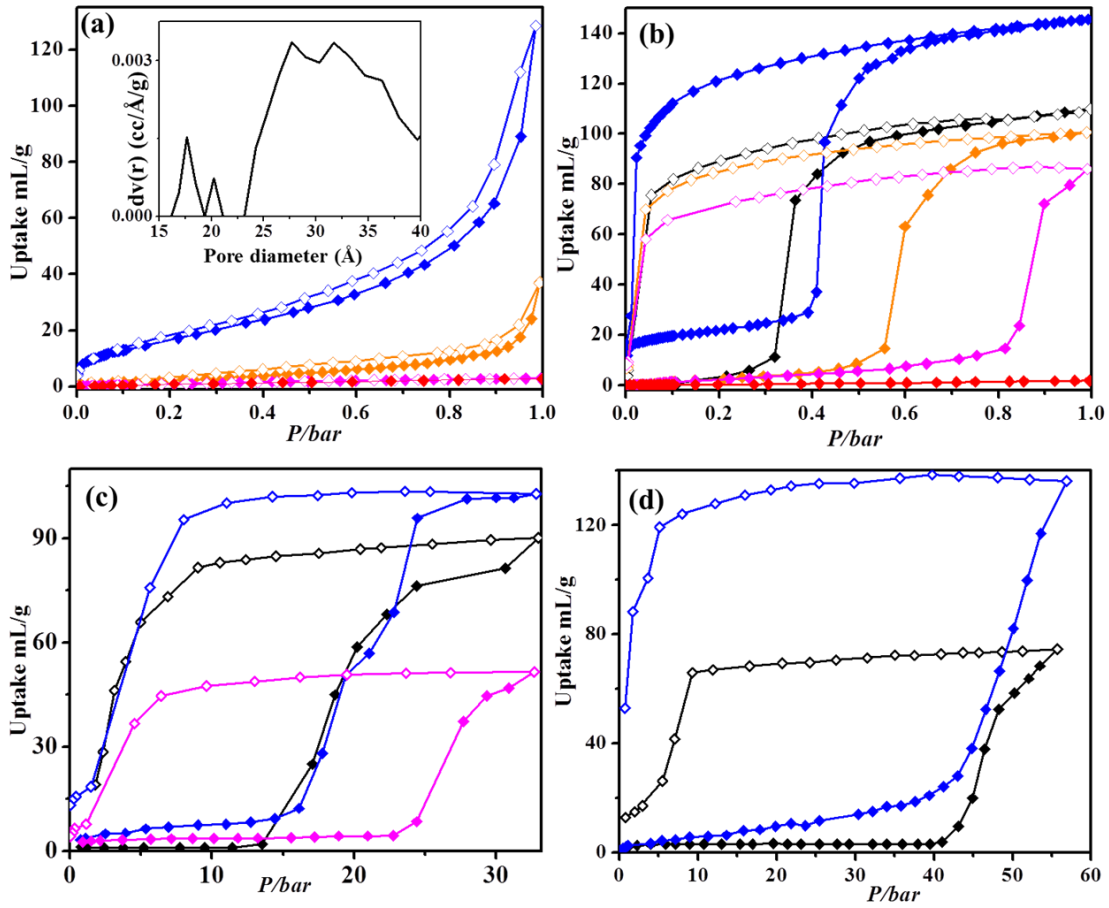

Figure 9. (a) N_2 adsorption isotherms at 77 K. Inset shows the pore size distribution of **F-MOF1@AC-1**. (b) CO_2 adsorption isotherms at 195 K. High pressure CO_2 adsorption isotherms at (c) 273 K and (d) 298 K. Color code: **F-MOF1:** black, **AC:** red, **F-MOF1@AC-1:** blue, **F-MOF1@AC-2:** orange, **F-MOF1@AC-3:** magenta. (Open and closed symbol denotes adsorption and desorption respectively).

from the initial low pressure adsorption**.** Furthermore, the well-dispersed MOF NPs allowing easy accessibility of CO_2 and active sites at MOF NP-AC interface can also contribute to enhance the total uptake. Unlike **F-MOF1@AC-1** the other composites show gated behaviour without any prominent step, which is attributed to the densely packed AC layers inhibiting the initial uptake. Interestingly, the step pressure (P = 0.39 bar) of **F-MOF1@AC-1** is higher than the gate-opening pressure than activated **F-MOF1** and the gate-opening pressure of CO_2 adsorption gradually moves to higher values from **F-MOF1@AC-2** to **F-MOF1@AC-3** (Figure 9b). It is proposed that the desolvated

frameworks become more stabilized on the AC template with increase in AC loading, as more amine groups are available to stabilize the desolvated phase through non-covalent interaction. Furthermore, with increase in AC loading, the relative amount of AC layers increases which inhibits easy accessibility of CO_2 molecules. Thus more adsorbate pressure is required to "open" the gate in the composites. In the report by Maji *et al*., the C_2H_2 adsorption isotherm was not measured for the activated **F-MOF1**.[14] In this work, the C_2H_2 adsorption isotherms of **F-MOF1**, **F-MOF1@AC-1** and **F-MOF1@AC-3** were measured at 195 K, which exhibit similar behaviour like CO_2 adsorption (Figure 10).

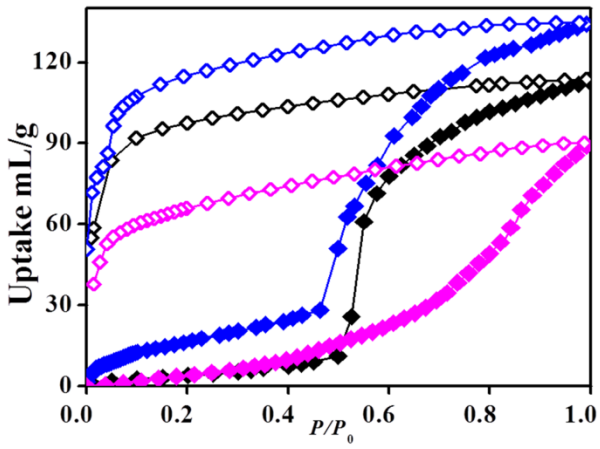

Figure 10. C_2H_2 adsorption isotherms at 195 K. Open and closed symbol denotes adsorption and desorption respectively. Color code: activated **F-MOF1** (black), **F-MOF1@AC-1** (blue), and **F-MOF1@AC-3** (pink).

The activated **F-MOF1** shows a gated isotherm with a gate-opening pressure at P = 0.5 bar followed by a sharp rise in the uptake which saturates at P = 1 bar with an uptake of 113 mL/g. In contrast, **F-MOF1@AC-1** shows a stepwise adsorption isotherm with initial uptake amount of 28 mL/g at P = 0.46 bar followed by a steeper uptake which saturates at P = 1 bar with an uptake amount of 135 mL/g. **F-MOF1@AC-3** exhibits lesser uptake than **F-MOF1@AC-1 and** F-MOF1which is attributed to the higher content of AC. To investigate the adsorption behaviour of the composites under ambient temperature and high pressure of the adsorbate, we further carried out CO_2 adsorption measurements of **F-MOF1** and the composites with minimum and maximum AC loading at high pressure. At 273 K and 298 K, the trend in the isotherms is similar to that at 195 K. At 273 K, activated **F-MOF1** shows gated adsorption with a gate-opening pressure at 13.6 bar and an uptake of 90 ml/g at P = 33 bar (Figure 9c). In contrast, activated **F-MOF1@AC-1** shows a stepwise uptake with a step pressure at 16 bar and the adsorption uptake is enhanced (103 ml/g at P = 33 bar) compared to the pristine **F-MOF1**. On the

other hand, **F-MOF1@AC-3** shows a lesser uptake (51 ml/g at P = 33 bar) with a higher gate-opening pressure (22.6 bar) compared to the **F-MOF1**, which is attributed to the high AC loading as explained before. At 298 K, the adsorption profile of **F-MOF1** shows an uptake of 74 ml/g at P = 55 bar with a gate-opening pressure at 41 bar (Figure 9d). The activated **F-MOF1@AC-1** shows a stepwise uptake with an uptake of 135 ml/g at P = 55 bar and the enhancement of adsorption uptake (45%) is remarkably high compared to the **F-MOF1**. However, **F-MOF1@AC-4** does not adsorb any CO_2 at 298 K upto P = 55 bar which is attributed to the high AC loading.

To verify whether AC can be used as a general scaffold to grow different types of F-MOF nanocrystals and to study the adsorption properties of such F-MOF composites, we tried to downsize another flexible 2D MOF, {[Cu(dhbc)$_2$(4,4'-bpy)]·5H$_2$O} (**F-MOF2**). **F-MOF2** contains linear 1D chains of Cu(II) ions connected by 4,4'-bpy ligand and the 1D chains are further linked by dhbc linker to give the 2D sheet. The π-π stacking interactions between nearest-neighbour dhbc linkers of the 2D networks create mutually interdigitated 3D framework with 1D channels (3.6 × 4.2 Å^2) along the *a* axis.[15]

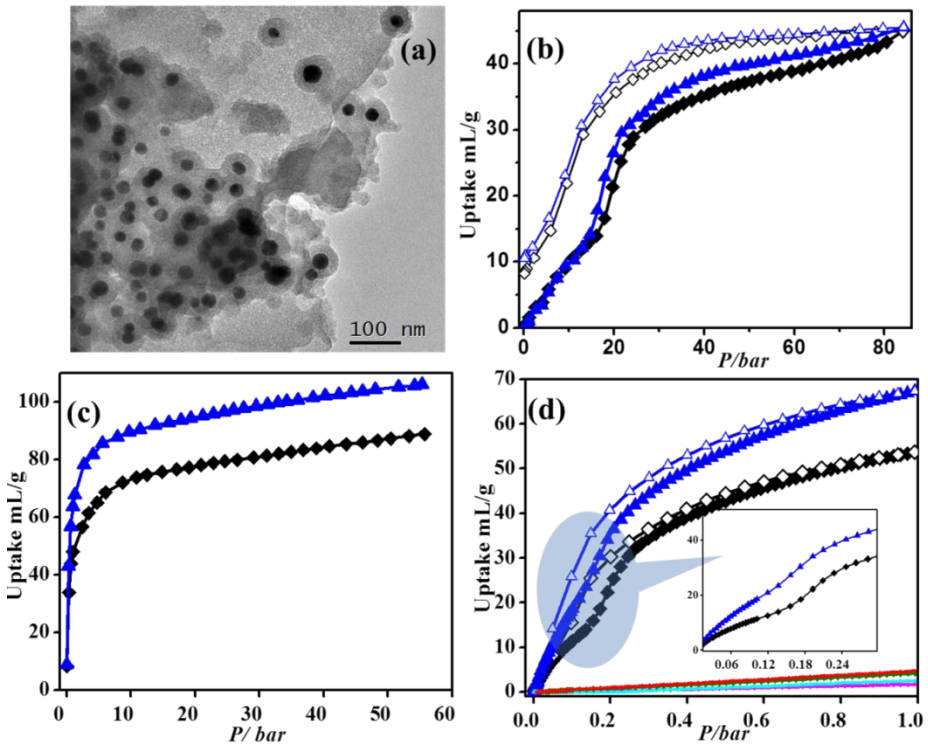

Figure 11. (a) TEM images of **F-MOF2@AC-1**. (b) High-pressure N_2 adsorption isotherms at 298 K. Color code: **F-MOF2** (black) and **F-MOF2@AC-1** (blue). (c) High-pressure CO_2 adsorption isotherms at 298 K. color code similar to Figure 11b. (d) CO_2, N_2 and CH_4 adsorption isotherms under ambient condition (upto 1 bar, at 298 K). Color code: CO_2: **F-MOF2** (black) and activated **F-MOF2@AC-1** (blue); N_2: **F-MOF2** (pink) and **F-MOF2@AC-1** (cyan); CH_4: **F-MOF2** (green) and **F-MOF2@AC-1** (red). The inset shows the variation at the low pressure of CO_2 adsorption isotherms.

Upon desolvation, the structural integrity of 2D motif is retained, but shrinking of the layers occurs along the *c* axis, which is attributed to a gliding motion of the two π-stacked rings (Scheme 1). Because of such structural contraction upon dehydration, only a type-II N_2 adsorption isotherm is obtained at 77 K.[15] However, **F-MOF2** was reported to show gated behaviour with different gases like N_2, CH_4 and O_2 at 298 K under high pressure based on structural expansion of a contracted interdigitated framework.[15] The structural re-expansion occurs with guest-inclusion at high pressure, which was reflected in the gated adsorption isotherms of various super-critical gases.[15] Two composites of **F-MOF2** with AC were synthesized employing similar synthetic strategy as of **F-MOF1** composites. ICP-AES analysis of the **F-MOF2@AC-1** and **F-MOF2@AC-2** composite shows that the AC contents are 14.6 and 21.2 wt%, respectively. TEM image of **F-MOF2@AC-1** shows homogeneous growth of **F-MOF2** nanocrystals with spherical morphology (diameter 25-40 nm) on the layered clay template (Figure 11a). The successful growth of **F-MOF2** nanocrystals suggests the potential of AC for growth and stabilization of different MOF NPs. To investigate the gas adsorption properties of the activated **F-MOF2@AC-1** composite under high pressure of adsorbates, CO_2, CH_4 and N_2 adsorption isotherms were measured under high pressure at 298 K (Figure 11, 12).

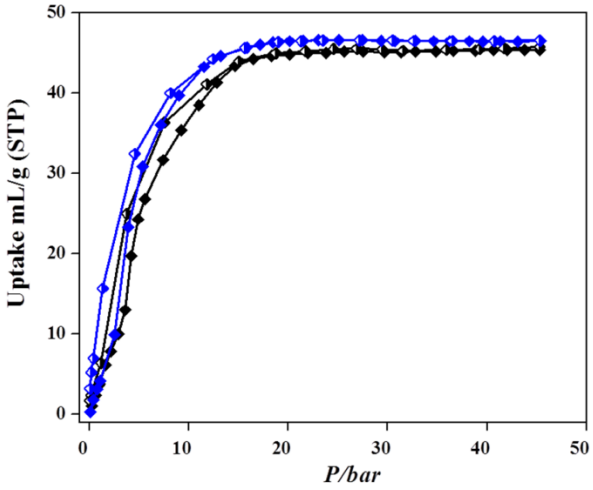

Figure 12. High-pressure CH_4 adsorption isotherms at 298 K. Color code: activated **F-MOF2** (black) and **F-MOF2@AC-1** (blue).

The N_2 adsorption isotherm of activated **F-MOF2** shows a stepwise and hysteretic profile with an uptake of 45 mL/g at P = 84 bar. The stepwise and hysteretic adsorption is attributed to the guest-induced structural expansion facilitating guest adsorption. Similar profile is observed for activated **F-MOF2@AC-1** composite (Figure 11b). The high-pressure CH_4 adsorption isotherms also reveal similar behaviour of **F-MOF2** and **F-**

MOF2@AC-1 (Figure 12). Interestingly, the high-pressure CO_2 adsorption isotherms at 298 K (Figure 11c) reveal type I profiles and the **F-MOF2@AC-1** composite exhibits an adsorption uptake of 106 mL/g at P = 55 bar, which is increased by 19% in compared to the uptake of **F-MOF2** (88 mL/g at P = 55 bar). Such enhanced uptake in the composite may be attributed to the easily accessible MOF NPs distributed homogeneously on AC and the facile interaction of the active sites at NP-AC interface with polar CO_2 molecules.

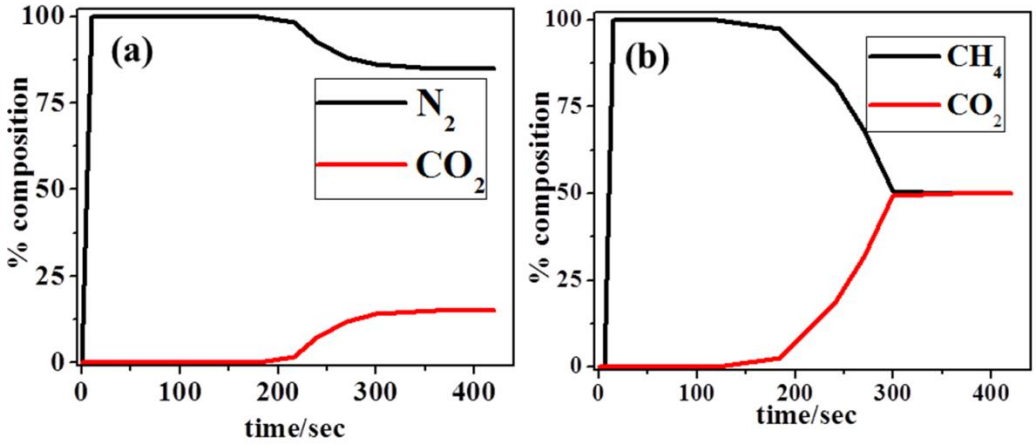

Figure 13. Breakthrough curves for binary mixture of (a) N_2 (black) /CO_2 (red) (0.85:0.15) and (b) CH_4 (black) /CO_2 (red) (0.5:0.5).

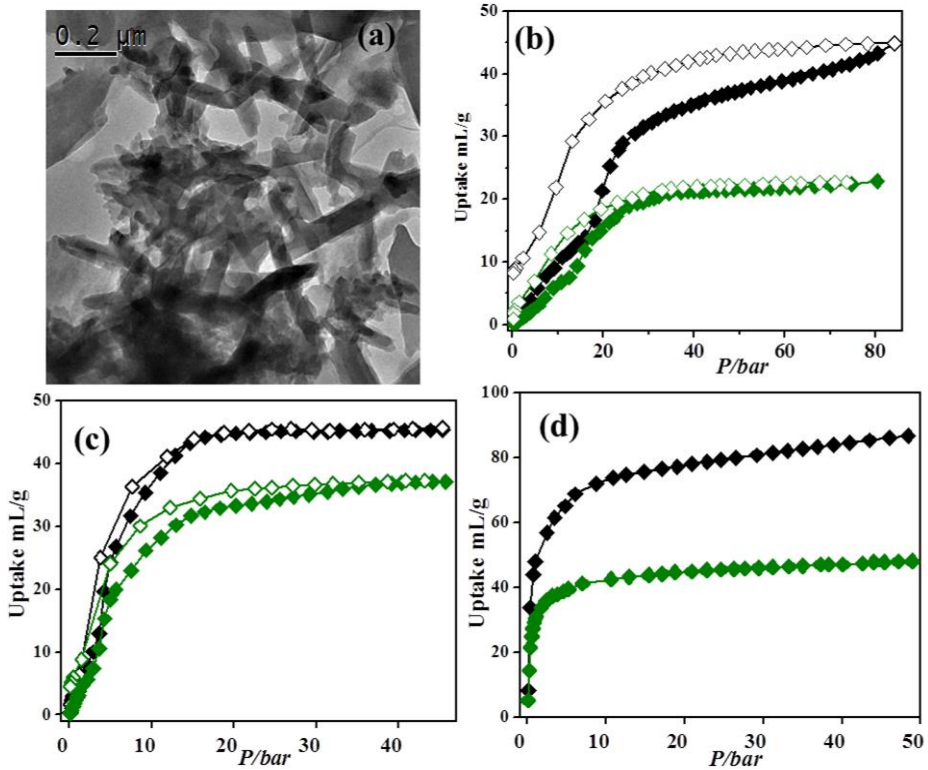

Figure 14. (a) TEM images of **F-MOF2@AC-2.** High-pressure isotherms at 298 K for (b) N_2 (c) CH_4 and (d) CO_2 adsorption. Color code of activated samples: **F-MOF2** (black) and **F-MOF2@AC-2** (green). Open and closed symbol denotes adsorption and desorption respectively.

A closer look into the CO_2, CH_4 and N_2 adsorption isotherms of activated **F-MOF2@AC-1** composite at the low pressure region (<1 bar) reveals the higher CO_2 adsorption uptake of the composite over the other gases (Figure 11b, 11c and 12), which motivated us to investigate the CO_2 selective nature of the composite framework. Single-component adsorption isotherms were measured for CO_2, N_2 and CH_4 gas (Figure 11d), which show that both **F-MOF2** and **F-MOF2@AC-1** do not adsorb N_2 or CH_4 gas significantly under ambient condition. Interestingly, **F-MOF2** shows a stepwise uptake (step pressure P = 0.16 bar) with a final uptake of 53 ml/g at P = 1 bar while **F-MOF2@AC-1** exhibits an adsorption uptake of 67 ml/g at P = 1 bar without a prominent step. Above results encouraged us to check the gas separation ability of the composite by breakthrough column experiments. Experiments were carried out using binary CO_2/N_2 (0.15:0.85) and CO_2/CH_4 (0.5:0.5) gas mixture at 298 K. A tightly packed column of the desolvated **F-MOF2@AC-1** composite sample (column length is 1 cm) was prepared and the rate of the gas flow was 1 ml/min (carrier He gas: binary gas mixture = 0.9: 0.1). Figure 13a represents the breakthrough curve of the binary mixture of CO_2/N_2 at 298 K, which shows a retention time of 216 seconds for CO_2 gas. This clearly advocates that **F-MOF2@CA-1** can really separate CO_2 gas from N_2. The breakthrough curve of CO_2/CH_4 binary mixture also shows similar separation capability, where the breakthrough occurs at 185 seconds (Figure 13b), indicating the CO_2/CH_4 separation efficiency of the composite. Thus **F-MOF2@AC-1** composite could be a potential candidate to selective separate CO_2 from gas mixtures under ambient condition. The **F-MOF2@AC-2** composite was also investigated and its TEM image shows different morphology than **F-MOF2@AC-1** (Figure 14). Nanorods (length and diameter are in the range of 200-300 nm and 35-60 nm respectively) are found to be present on the AC template. However, this composite shows decreased adsorption uptake capacity of different gases (Figure 14) compared to the **F-MOF2** compound, which is attributed to the higher AC loading and formation of an inhomogeneous composite.

5B.4 SUMMARY

In summary, F-MOF@AC nanocomposites were synthesized for the first time and their textural and adsorption properties were investigated. The results demonstrate that AC can be an effective template to assist growth and stabilization of versatile F-MOF NPs, thus ushering a new route of crystal downsizing towards new F-MOF composites. The studies also reflect that enhancement of gas uptake and tuning the gate/step pressure is possible in

such composites. By judicious integration of different functional materials towards nanocomposites would facilitate exciting outcomes such as stabilization of metastable phases, template directed assembly of nanocrystals, controlled drug delivery and enhanced adsorption and catalytic activity.

5B.5 REFERENCES

1. Themed Issue: Metal–organic Frameworks, *Chem. Rev*., 2012, **112**, 673.
2. (*a*) J. Jiang, J. Yu and A. Corma, *Angew. Chem., Int. Ed*., 2010, **49**, 3120; (*b*) P. Vanelderen, J. Vancauwenbergh, B. F. Sels and R. A. Schoonheydt, *Coord. Chem. Rev*., 2013, **257**, 483.
3. (*a*) A. Schneemann, V. Bon, I. Schwedler, I. Senkovska, S. Kaskel and R. A. Fischer, *Chem. Soc. Rev.*, 2014, **43**, 6062; (*b*) Z. Chang, D.-H. Yang, J. Xu, T.-Liang Hu and Xian-He Bu, *Adv. Mater*., 2015, **27**, 5432; (*c*) T. K. Maji, R. Matsuda and S. Kitagawa, *Nat. Mater*. 2007, **6**, 142; (*d*) N. Sikdar, A. Hazra and T. K. Maji, *Inorg. Chem.*, 2014, **53**, 5993.
4. (*a*) R. Haldar, S. K. Reddy, V. M. Suresh, S. Mohapatra, S. Balasubramanian and T. K. Maji, *Chem. Eur. J.,* 2014, **20**, 4347; (*b*) P. Kanoo, R. Matsuda, R. Kitaura, S. Kitagawa and T. K. Maji, *Inorg. Chem.*, **2012**, 51, 9141.
5. (*a*) S. Diring, S. Furukawa, Y. Takashima, T. Tsuruoka and S. Kitagawa, *Chem. Mater*., 2010, **22**, 4531; (*b*) A. Carne, C. Carbonell, I. Imaz and D. Maspoch, *Chem. Soc. Rev*., 2011, **40**, 291; (*c*) A. Umemura, S. Diring, S. Furukawa, H. Uehara, T. Tsuruoka, and S. Kitagawa, *J. Am. Chem. Soc*., 2011, **133**, 15506.
6. (*a*) D. Tanaka, A. Henke, K. Albrecht, M. Moeller, K. Nakagawa, S. Kitagawa and J. Groll, *Nat. Chem.*, 2010, **2**, 410; (*b*) Y. Sakata, S. Furukawa, M. Kondo, K. Hirai, N. Horike, Y. Takashima, H. Uehara, N. Louvain, M. Meilikhov, T. Tsuruoka, S. Isoda, W. Kosaka, O. Sakata and S. Kitagawa, *Science*, 2013, **339**, 193.
7. (*a*) Q-L. Zhu, Q. Xu, *Chem. Soc. Rev*., 2014, **43**, 5468; (*b*) A. Ranft, F. Niekiel, I. Pavlichenko, N. Stock and B.V. Lotsch, *Chem. Mater.*, 2015, **27**, 1961; (*c*) L. Li, X. Jiao, D. Chen, B.V. Lotsch and C. Li, *Chem. Mater.*, **2015**, ***27***, 7601; (*d*) J. E. Bachman, Z. P. Smith, T. Li, T. Xu and J. R. Long, *Nat. Mater.*, 2016, 15, 845.
8. (*a*) F. Hoffmann, M. Cornelius, J. Morell and M. Froba, *Angew. Chem. Int. Ed*., 2006, **45**, 3216; (*b*) D. Liu, R. C. Huxford and W. Lin, *Angew. Chem. Int. Ed*., 2011, **50**, 3696.

9. (*a*) P. Horcajada, T. Chalati, C. Serre, B. Gillet, C. Sebrie, T. Baati, J. F. Eubank, D. Heurtaux, P. Clayette, C. Kreuz, J.-S. Chang, Y. K. Hwang, V. Marsaud, P.-N. Bories, L. Cynober, S. Gil, G. Fe´rey, P. Couvreur and R. Gref, *Nat. Mater*., 2010, **9**, 172; (*b*) M. D. Rowe, C.-C. Chang, D. H. Thamm, S. L. Kraft, J. F. Harmon, A. P. Vogt, B. S. Sumerlin and S. G. Boyes, *Langmuir*, 2009, **25**, 9487; (*c*) M. G. Schwab, I. Senkovska, M. Rose, M. Koch, J. Pahnke, G. Jonschker and S. Kaskel, *Adv. Eng. Mater*., 2008, **10**, 1151.
10. (*a*) R. Kumar, K. Jayaramulu, T. K. Maji and C. N. R. Rao, *Chem. Commun*., 2013, **49**, 4947; (*b*) S. Liu, L. Sun, F. Xu, J. Zhang, C. Jiao, F. Li, Z. Li, S. Wang, Z. Wang, X. Jiang, H. Zhou, L. Yang and C. Schick, *Energy Environ. Sci*., 2013, **6**, 818.
11. K. R. Datta, A. Achari and M. Eswaramoorthy, *J. Mater. Chem. A*, 2013, **1**, 6707.
12. (*a*) S. Mann, S. L. Burkett, S. A. Davis, C. E. Fowler, N. H. Mendelson, S. D. Sims, D. Walsh and N. T. Whilton, *Chem. Mater*., 1997, **9**, 2300; (*b*) N. T. Whilton, S. L. Burkett and S. Mann, *J. Mater. Chem*., 1998, **8**, 1927; (*c*) J. E. Martin, A. J. Patil, M. F. Butler, S. Mann, *Adv. Funct. Mater*., 2011, **21**, 674; (*d*) A. J. Patil, E. Muthusamy and S. Mann, *Angew. Chem. Int. Ed*., 2004, **43**, 4928.
13. K. V. Rao, K. K. R. Datta, M. Eswaramoorthy and S. J. George, *Angew. Chem. Int. Ed*., 2011, **50**, 1179.
14. T. K. Maji, G. Mostafa, R. Matsuda and Susumu Kitagawa, *J. Am. Chem. Soc*., 2005, **127**, 17152-.
15. R. Kitaura, K.Seki, G. Akiyama, and S. Kitagawa, *Angew. Chem. Int. Ed*., 2003, **42**, 428.

Chapter 6A

Assembly of ZIF-8 Nanoparticles with Aminoclay Towards Nanocomposites Exhibiting Significant Enhancement in Adsorption Uptake

Abstract

This chapter reports the synthesis, characterization and adsorption studies of new ZIF-8-aminoclay nanocomposites. The composites are synthesized by adopting self-assembly approach and their formation is driven by the specific interaction between unsaturated Zn(II) sites of ZIF-8 nanoparticles and NH_2 groups of aminoclay. The composites exhibit significantly enhanced adsorption uptake compared to that of pristine ZIF-8 nanoparticles Best performance is achieved with one of the composites which exhibits 42% increase in BET surface area while CO_2 adsorption uptake is doubled compared to the ZIF-8 nanoparticles. Such enhancement is attributed to the formation of voids at the interfaces of ZIF-8 NP and aminoclay. Furthermore, the assembly of ZIF-8 nanoparticles through aminoclay increases the effective number of framework atoms in the composites, which also possibly contribute to facilitate gas adsorption.

Paper based on this study:

A. Chakraborty, M. Eswaramoorthy, T. K. Maji, *manuscript under preparation.*

6A.1 INTRODUCTION

The last two decades have witnessed tremendous growth in the synthesis, properties and versatile applications of metal-organic frameworks (MOFs) having intriguing structures.[1] A contemporary research on MOFs involves judicious integration of MOF and another active species (like metal nanoparticles, oxides, quantum dots, organic polymers, graphene oxide (GO), reduced graphene oxide (RGO), carbon nanotube, boron nitride (BN), biomolecules and silica) towards new composite materials having advanced functionalities.[2] Recently, a number of MOF composites have been synthesized by surface modifications of nanoscale MOFs (NMOFs) by coating the NMOFs with a suitable component for controlled drug delivery, improving *in vivo* performance or enhancing the mechanical properties.[3] However, coating of MOF nanoparticles (NPs) with a functional component towards new self-assembled composites exhibiting enhanced gas adsorption properties has not been explored. The self-assembly of the colloidal Janus particles into intriguing hierarchical structures have been well-studied, but the self-assembly of MOF particles is only recently explored by Granick's group where they have exploited attractive van der Waals interaction between the MOF facets or applied external electric field.[4] Self- assembly of MOF NPs with a suitable functional component towards self-assembled composites would be further interesting as the composites can exhibit novel and enhanced properties.

The prototypic ZIF-8 framework ($Zn[MeIm]_2$; MeIm = 2-methylimidazolate; ZIF= zeolitic imidazolate framework) has been well-studied for its high BET surface area (≈2000 m^2 g^{-1}), unimodal micropores and excellent thermal and chemical stability.[5] Nanosized ZIF-8 particles are particularly interesting as the nanoscale regime opens up the opportunity of diverse applications in microenvironments including drug delivery[6] due to better solution processibility. Room temperature syntheses of ZIF-8 NPs of various size and morphologies have already been reported[7-8]and few of the reports involve facile room temperature synthesis of NPs in aqueous medium. However, the ZIF-8 NPs (<100 nm) prepared at room temperature in general have significantly less surface area (≈800-1200 m^2 g^{-1}) than the bulk ZIF-8 frameworks,[7-10] which eventually limits the applications of ZIF-8 NPs. The reason behind such less surface area of ZIF-8 NPs is not very clear. Kida and co-workers suggested incomplete activation or the incorporation of a small amount of amorphous compounds can result in the smaller surface area in ZIF-8 NPs.[10] Recent experimental and simulation studies from Lively's group have demonstrated that

the N_2 adsorption uptake in the ZIF-8 NP is lower than that in the bulk, especially at the low pressure region.[11] In their calculations, they have partitioned the adsorption uptake in a NP into "bulk-like" and surface regions and observed preferential adsorption in the bulk-like region which was attributed to the increased number of neighboring framework atoms compared to the surface.Thus assembling ZIF-8 NPs with a suitable functional material may result in new nanocomposites with high gas uptake capacity and at the same time the nanocomposite would retain advantages of nanoscale, like enhanced solution processability. To synthesize such composites, the synthetic layered material aminoclay (AC), aminopropyl funtionalized magnesium (organo) phyllosilicate[12,13] was chosen (Scheme 1). AC has versatile applicability along with high water dispersibility, which makes it an attractive candidate to furnish better processable composites, compared to the conventional templates (like GO or RGO) which are poorly dispersible in water. In this chapter, synthesis and studies of self-assembled ZIF-8@AC nanocomposites are reported. The composites show significantly enhanced adsorption uptake compared to the ZIF-8 NPs. The formation of the composites is driven by the interaction between the amine groups of AC and unsaturated Zn^{II} coordination sites of ZIF-8 NPs which have high positive surface charge. Various composites are synthesized by varying the AC content and their textural and adsorption properties are studied. The best performance is achieved with the composite having AC content 18.3 wt%, which shows 42% increase in BET surface area while the CO_2 adsorption uptake is almost doubled, compared to the pristine ZIF-8 NPs. Such assembly of ZIF-8 NPs using the functional AC material towards new nanocomposites having improved adsorption behaviour is explored for the first time in this chapter.

6A.2 EXPERIMENTAL SECTION

6A.2.1 Materials

All the reagents and solvents employed are commercially available and used as supplied without further purification. $Zn(NO_3)_2.6H_2O$, 2-methylimidazole, $MgCl_2$ and 3-aminopropyltriethoxysilane were obtained from the Aldrich Chemical Co.

6A.2.2 Synthesis

ZIF-8 NPs (**1**): ZIF-8 NPs were synthesized at room temperature and aqueous solution following typical reaction conditions.[7] 0.117 g $Zn(NO_3)_2.6H_2O$ was taken in 0.8 mL

deionized water and then aqueous solution of 2-methylimidazole (22.7 g in 8 mL) was added to the Zn(II) solution under stirring. The reaction mixture was stirred for 5 minutes. The product was collected by centrifugation and washed with deionized water several times. A small portion of the product was re-dispersed in methanol to prepare samples for SEM study, and another part of the product was dried at 60 °C overnight in a drying oven. Yield, 77%, relative to Zn(II). The phase purity of the sample was checked by PXRD analysis (Figure 1).

Aminoclay: Aminoclay (AC) was prepared following typical reaction conditions reported by Mann and co-workers.[12d] 3-aminopropyltriethoxysilane (1.3 mL, 5.85 mmol) was added dropwise to an ethanolic solution of $MgCl_2$ (0.84 g, 3.62 mmol) in ethanol (20 g). The white slurry obtained was stirred overnight and the precipitate was isolated by centrifugation and then was washed with ethanol (50 mL) and dried at 40 °C. PXRD pattern (Figure 2) of the dried compound shows typical reflection corresponding to the d_{001} interlayer spacing of 1.6 nm originating from the bilayer arrangement of propylamine groups.

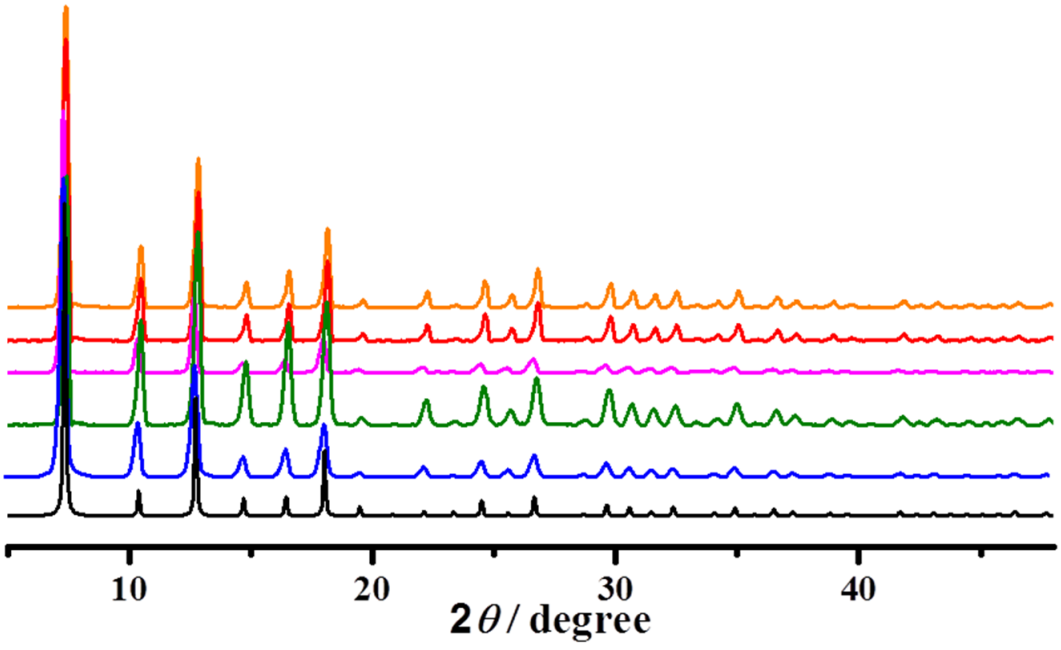

Figure 1. PXRD patterns of simulated plot (black) of ZIF-8, and experimental plots of ZIF-8 NP (blue), **ZIF-8@AC-1** (green), **ZIF-8@AC-2** (pink), **ZIF-8@AC-3** (red) and **ZIF-8@AC-4** (orange).

ZIF-8@AC composites: To prepare the composites, first 20 mg of AC was dispersed in 5 mL of water/ethanol (60: 40) mixture (pH= 7). To the dispersed solution of AC, the precursor solutions of ZIF-8 NPs were added at room temperature, as described above for

the synthesis of ZIF-8. The resulting solid was dried after repeatedly washing with water/ethanol, and is referred to as **ZIF-8@AC-1.** Similar procedure was repeated for the synthesis of **ZIF-8@AC-2, ZIF-8@AC-3** and **ZIF-8@AC-4** where 30 mg, 40 mg, 50 mg of AC were taken, respectively. The weight % of ZIF-8 in the composites were calculated through Inductively Coupled Plasma-Atomic Spectroscopy (ICP-AES) study based on the relative ratio of Zn(II) in the pristine ZIF-8 and the composites.

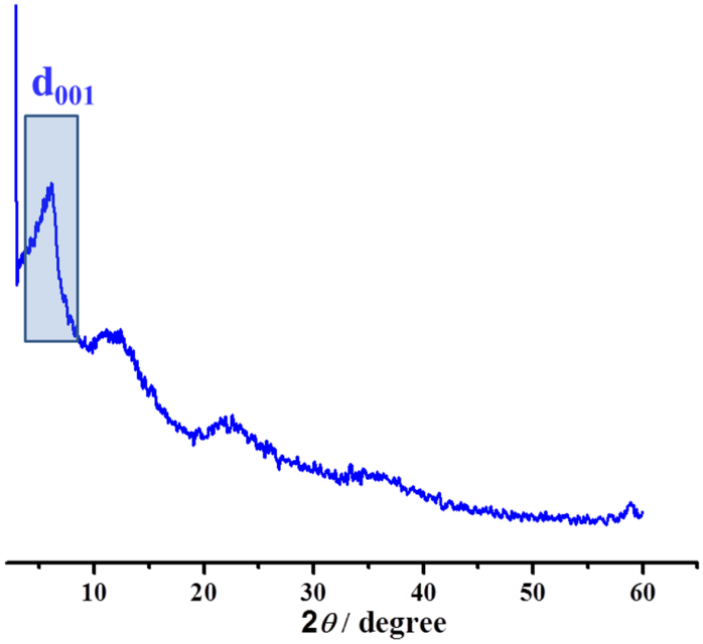

Figure 2. PXRD pattern of AC. The d_{001} peak is highlighted.

Control experiments and synthesis of Zn@AC solid:

30 mg of AC was dispersed in 5 mL of water/ethanol mixture (pH= 7). 0.117 g of $Zn(NO_3)_2.6H_2O$ was taken in 0.8 ml deionized water and was added to the above solution and the mixture was stirred for 10 minutes at room temperature. The colourless solid product (obtained after precipitation by adding ethanol to the reaction mixture) was washed several times with ethanol and dried. Elemental mapping and EDX analysis of the solid (referred as Zn@AC) were performed. Further room temperature stirring of Zn@AC and 2-methylimidazole in aqueous solution was performed. The resulting compound was collected by centrifugation and washed with deionized water several times.

6A.2.3 Physical Measurements

Powder X-ray diffraction (PXRD) patterns were recorded on a Bruker D8 Discover instrument using Cu–Kα radiation. Inductively Coupled Plasma-Atomic Emission

Spectroscopy (ICP-AES) measurements were recorded on Perkin Elmer Optima 7000dv ICP-AES instrument. Energy dispersive analysis of X-rays (EDX) was carried out using field emission scanning electron microscope. The scanning electron microscopy images were obtained using a Nova Nanosem 600 FEI field emission scanning electron microscope (FESEM). The samples were prepared by dispersing the sample in MeOH and then dropping 5 μL of the solution onto a small piece of silicon wafer and drying into air. Transmission electron microscopy (TEM) images were taken with a JEOL JEM-3010 transmission electron microscope operating at 200 kV. The samples were prepared in the same way as described above, but the drop cast was made onto a carbon-coated TEM grid. The zeta potential measurements were carried out using a NanoZS (Malvern UK) employing a 532 nm laser. Adsorption isotherms of N_2 (at 77 K) and CO_2 (at 298 K) were recorded with the desolvated samples using QUANTACHROME QUADRASORB-SI analyser and AUTOSORB IQ2 instrument. To prepare the desolvated samples of the ZIF-8 NPs (**1**) and the composites, approximately 70 mg of sample was degassed at 150 ºC under 10^{-1} pa vacuum for about 8 hours prior to the measurements. Dead volume of the sample cell was measured with helium gas of 99.999% purity.

6A.3 RESULTS AND DISCUSSION

The AC content in **ZIF-8@AC-1**, **ZIF-8@AC-2**, **ZIF-8@AC-3**, and **ZIF-8@AC-4** are 12.1, 18.3, 22.2, and 27.2 wt% as obtained from ICP-AES analyses. The good-correspondence of the PXRD patterns of ZIF-8 and the composites suggests existence of pure crystalline phase of ZIF-8 in the composites (Figure 1). The SEM image of as-synthesized ZIF-8 NPs (**1**) shows nanoparticles having size in the range of 70-100 nm (Figure 3), while the SEM image of pristine AC shows typical layered structure (Figure 4). All the composites are characterized by TEM analysis (Figure 5), which reveals that ZIF-8 NPs are coated with layered AC. TEM images of **ZIF-8@AC-1** shows that AC coated ZIF-8 NPs are assembled together. Such assembly of MOF NPs in a composite material is unprecedented. A magnified image of the edge of a single NP of **ZIF-8@AC-1** clearly shows presence of layers of AC (Figure 5a). A closer look into the TEM image reveals a contrast different in the particles where the darker contrast represents the ZIF NPs and lighter contrast having layered structure represents the AC (Figure 5a). To understand the mechanism of such coating of ZIF-8 NPs by AC in the composites, the zeta potential of pristine ZIF-8 NPs and the composite were measured. The as-synthesized pristine ZIF-8 NPs have a zeta potential of +55 mV. The high positive zeta

potential ZIF-8 NP arises from the unsaturated Zn^{II} sites at surfaces of the nanocrystals.[8] In contrast, the zeta potential of the composite reduced to ~+12 mV. Such reduction in the surface positive charge validates our conjecture that the amine functionality of the AC sheets can interact strongly with the unsaturated Zn(II) coordination sites of ZIF-8 NPs. Such facile interaction ensue the coating of ZIF-8 NP by AC. Once such coated particle is formed, some of the available unsaturated Zn(II) sites can further interact with the amine groups of AC which results in the assembly of the particles.

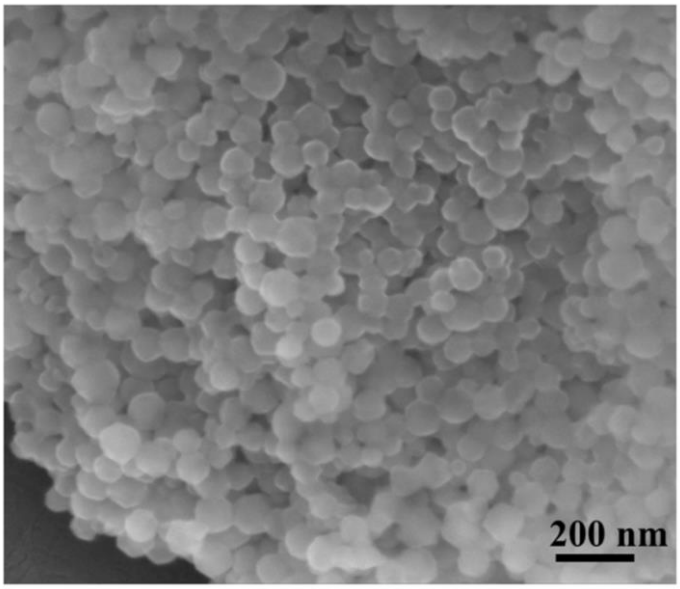

Figure 3. SEM images of the as-synthesized nanosized ZIF-8 (**1**).

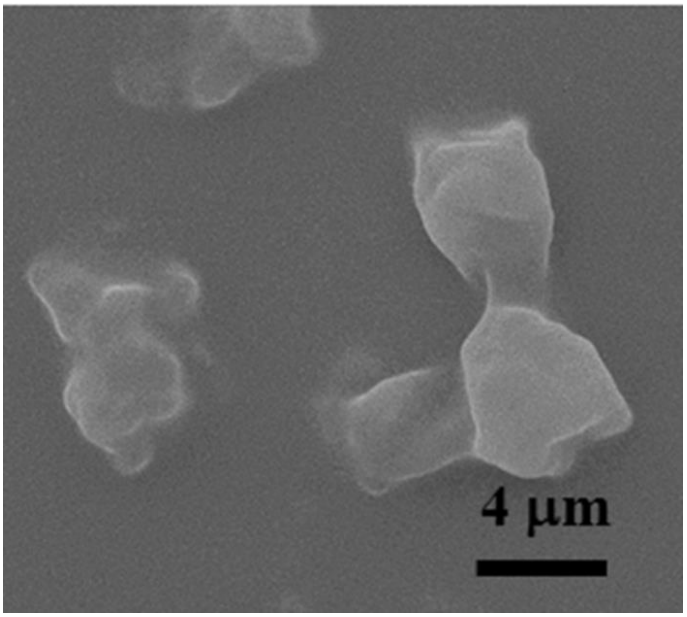

Figure 4. SEM images of the as-synthesized AC.

TEM images of different composites show that the sizes of the particles (70-120 nm) do not vary significantly, but the amount of AC increases from **ZIF-8@AC-1** to **ZIF-8@AC-4**. In **ZIF-8@AC-2** and **ZIF-8@AC-3**, with increase in AC loading, the ZIF-8 NPs are fused together by AC (Figure 5b) forming a well-connected network. In case of **ZIF-8@AC-2**, the contrast difference between ZIF-8 NP and AC is still observed but the two different components could not be distinguished clearly in **ZIF-8@AC-3**. This is

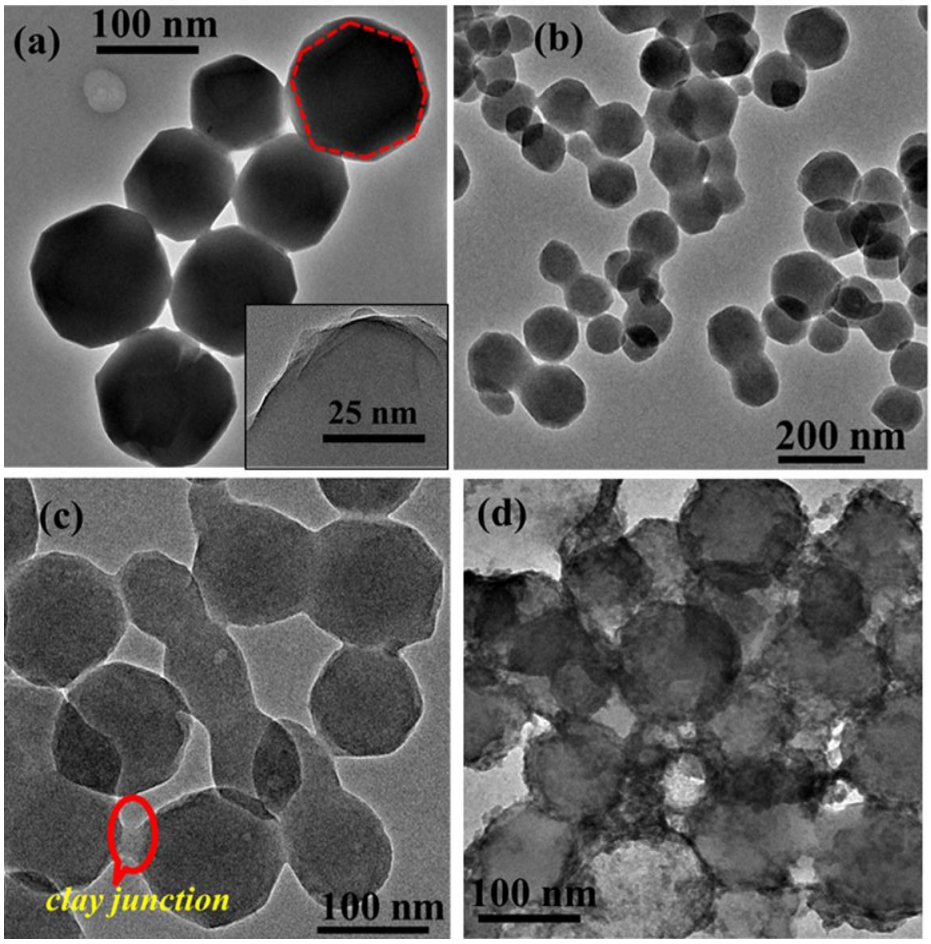

Figure 5. TEM images of (a) **ZIF-8@AC-1** (a ZIF-8 NP with darker contrast has been highlighted), (b) **ZIF-8@AC-2**, (c) **ZIF-8@AC-3** and (d) **ZIF-8@AC-4**. The AC junction between two NPs of **ZIF-8@AC-3** has been highlighted.

attributed to the more AC content and increased number of layers of AC in **ZIF-8@AC-3**. However, at the junctions of the coated NPs, a lighter contrast is observed which is attributed to the AC component (Figure 5c). Formation of such architecture may be ascribed to the fact that more number of ZIF-8 NPs can be wrapped simultaneously by the layers of AC, since the availability of AC layers is more in case of the composites having high AC content (like **ZIF-8@AC-3**) . To further investigate, FESEM images with point

EDX spectra were recorded for **ZIF-8@AC-3** (Figure 6). Point EDX study on a specific particle shows presence of both Zn (from ZIF-8) and Si (from AC); while a junction mostly contains Si instead of Zn. This proves that the layered junction consists of only AC and ZIF-8 is not present at the junctions. With 27.2 wt% AC content, **ZIF-8@AC-4** contains the highest amount of AC, where the ZIF-8 NPs are still fused together with AC but there are excess AC layers inhomogeneously present on the particles (Figure 5d). All the composites produce stable dispersions in water which are stable up to 1 hour. To elucidate the formation of such composites, control experiments were performed. Zn@AC solid was obtained after the addition of Zn(II) salt to the aqueous solution of AC followed by precipitation and washing, which shows presence of Zn distributed uniformly throughout AC, as seen by the EDX mapping (Figure 7). This observation indicates that the Zn(II) ions are strongly bound to the free amine groups of AC. Further reaction carried out with the Zn@AC and 2-methylimidazole resulted in a solid which shows formation of pure crystalline phase of ZIF-8 (Figure 8) as realized from PXRD measurement. TEM image suggest formation of ZIF-8-AC composites similar to **ZIF-8@AC-2** (Figure 8). The above experiments suggest that the amine groups of AC stabilize Zn(II) ions on its surface and then the ZIF-8-AC composites start forming rapidly when the solution of 2-methylimidazole is added. It is noteworthy that AC can

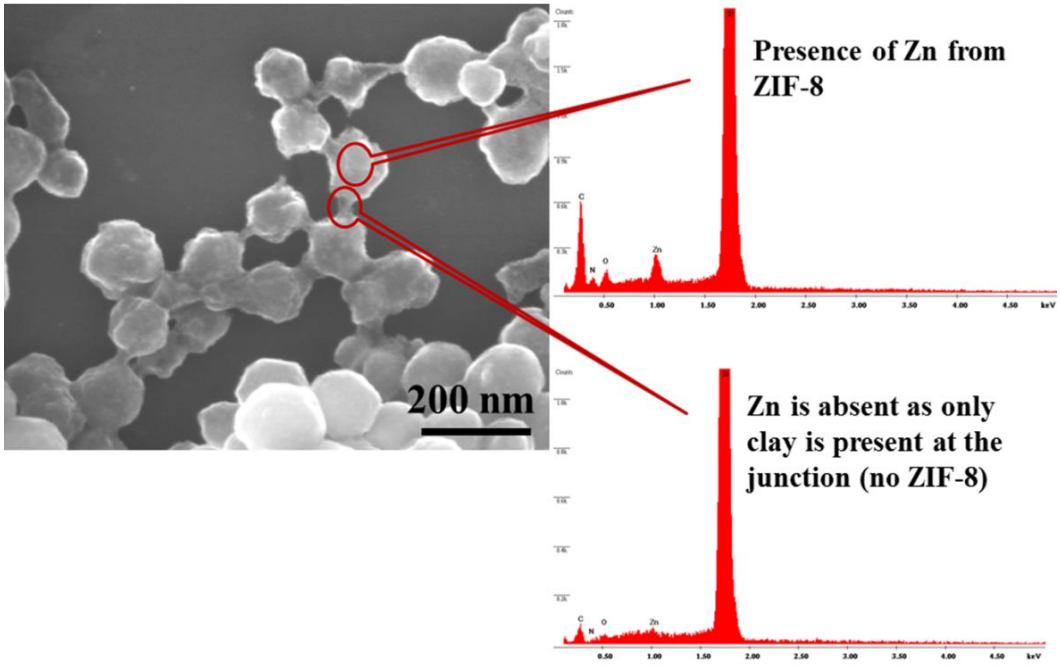

Figure 6. FESEM image and EDX study on **ZIF-8@AC-3**. Point EDX study on a specific particle shows presence of both Zn (from ZIF-8) and Si (from aminoclay); while a junction contains only Si and no Zn was found.

also act as a functional scaffold to support the nucleation and growth of different MOF NPs, as described in the previous chapter. In such cases, the kinetics of growth of CuBTC MOF NPs on AC is relatively slower. In contrast, formation of the nanocrystalline ZIF-8 discussed here occurs very rapidly (within ~ 5 minutes) in aqueous solution and a spontaneous self-assembly occurs to yield the assembly of ZIF-8 NPs. It may be noted that synthesis of the ZIF-8-AC composites adopting a post-synthetic approach was unsuccessful, where ZIF-8 NP were synthesized first following by stirring the dispersion of the NPs with AC solution.

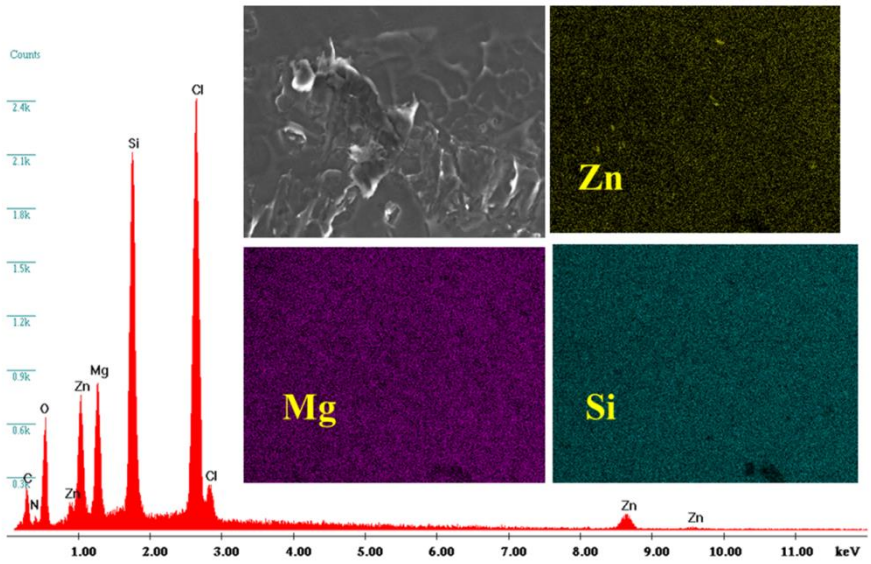

Figure 7. EDX spectrum of the Zn@AC solid showing the presence of Zn. Inset shows elemental mapping showing the homogeneous distribution of the elements (Zn, Mg and Si) throughout the sample.

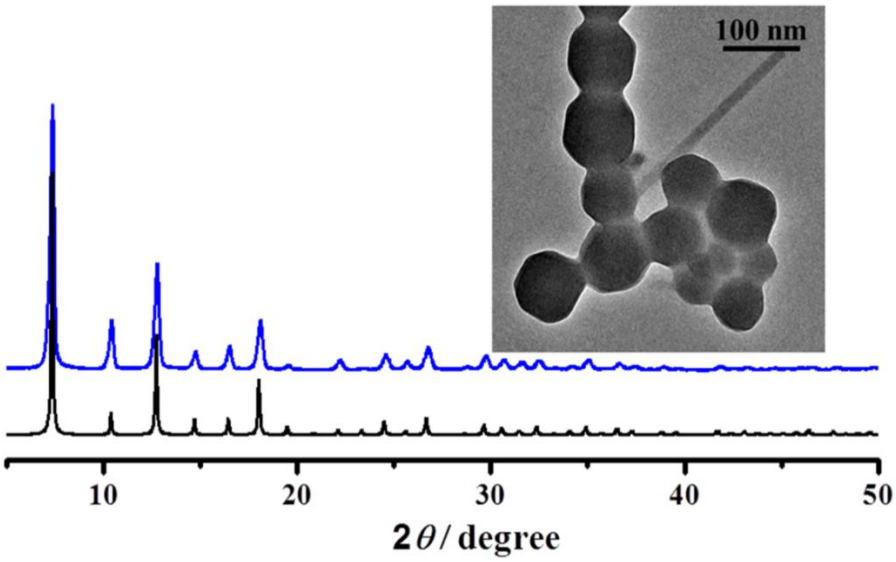

Figure 8. PXRD patterns of simulated ZIF-8 (black) and the solid (blue) obtained from the reaction of Zn@AC and 2-methylimidazole.Inset shows the TEM image.

The N_2 adsorption isotherms at 77 K of the activated compounds are shown in Figure 9. The ZIF-8 sample (**1**) shows a typical type-I adsorption profile with a surface area of 1030 m^2/g and a pore volume of 0.549 cc/g. The BET surface area is close to the value (1080 m^2/g) reported for the nano ZIF-8 samples prepared under the similar condition.[7] The densely stacked layered bulk AC do not adsorb any N_2 gas (Figure 9a). Interestingly, **ZIF-8@AC-1** shows significant adsorption of N_2 gas with a type-I profile and the BET surface area is increased by 21.6% compared to **1**. The enhancement in surface area is also accompanied with an increase in pore volume (0.625 cc/g). Similar type-I profiles are obtained for the other composites and the surface area and pore volume increase from **ZIF-8@AC-1** to **ZIF-8@AC-2** with increase in AC loading (Table 1) and **ZIF-8@AC-2** shows the highest surface area (1461 m^2/g) and pore volume (0.746 cc/g). However**,** with increase in non-porous AC loading the surface area starts decreases from **ZIF-8@AC-3**.

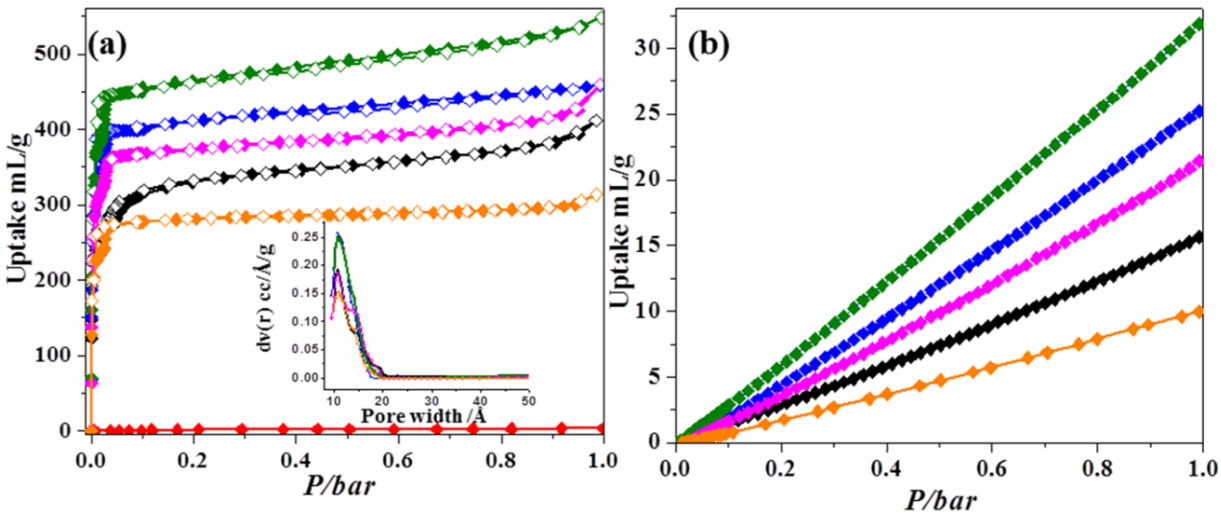

Figure 9. Adsorption isotherms of the activated samples. (a) N_2 adsorption isotherms at 77 K; Inset shows the pore size distribution plots (calculated using NLDFT method) for the composites. (b) CO_2 adsorption isotherms at 298 K. Color code: **1**: (black), AC: red, **ZIF-8@AC-1** (blue), **ZIF-8@AC-2** (green), **ZIF-8@AC-3** (magenta) and **ZIF-8@AC-4** (orange). Open and closed symbol denotes adsorption and desorption respectively.

Having excess AC loading, **ZIF-8@AC-4** shows a lesser surface area and pore volume compared to the other composites and **1**. The pore size distribution plot calculated using non-local density functional theory (NLDFT) method suggests maximum distribution at the pore diameter of 1.1 nm which corresponds to the typical micropore of ZIF-8 (Figure 9a, inset). The N_2 adsorption isotherm of the physical mixture of **1** and AC (ZIF-8: AC: 81.7: 18.3 wt%, similar to the composition of **ZIF-8@AC-2** exhibiting the highest surface area) shows that the adsorption uptake is much decreased compared to **1** (Figure

10), which is attributed to the presence of non-porous AC component. This clearly suggests that the effect of enhanced adsorption as shown by the composites could not be realized in a physical mixture. The increased surface area in the **ZIF-8@AC-1, ZIF-8@AC-2** and **ZIF-8@AC-3** can be attributed to the formation of some voids at the interface of ZIF-8 NPs and AC, which probably create some random micropores in the composites. Furthermore, the assembly of ZIF-8 NPs through AC in the composites result in a network of ZIF-8 NPs. In such a network, the effective number of neighbouring frameworks atoms is increased which can facilitate gas adsorptions, as proposed by Lively's *et al.*[11] With increase in AC content, the number of such neighbouring frameworks atoms increases increasing the gas uptake.

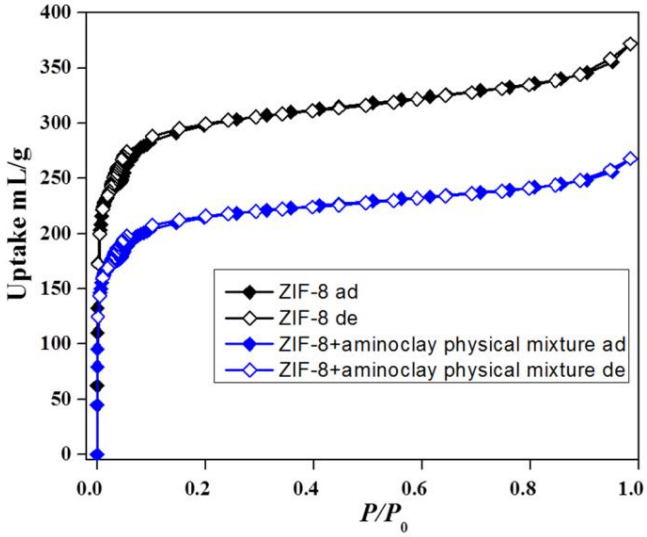

Figure 10. N_2 adsorption isotherms at 77 K of ZIF-8 NPs (black) and physical mixture of ZIF-8 and AC (blue).

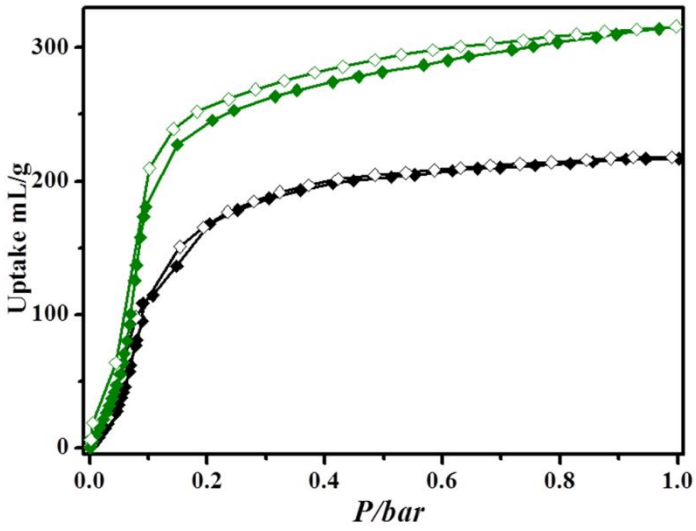

Figure 11. CO_2 adsorption isotherms at 195 K of ZIF-8 NP (black) and **ZIF-8@AC-2** (green).

The CO_2 adsorption isotherms at 298 K are shown in Figure 9b and the trend is similar to that of N_2 adsorption (Table 1). The ZIF-8 NP shows an uptake capacity of 15.6 mL at 1 bar, which is close to the values reported for the nano ZIF-8 samples in literature.[14] In contrast, **ZIF-8@AC-1** and **ZIF-8@AC-2** show enhanced CO_2 uptake of 25.2 and 31.9 mL/g at 1 bar, respectively. The **ZIF-8@AC-2** composite exhibits the highest uptake among the composite and the uptake is almost doubled compared to that of pristine nano ZIF-8 sample. The enhanced CO_2 uptake of the composites can be the result of the assembly of ZIF-8 NPs having increased number of neighbouring frameworks atoms and the formation of the voids at the interface of ZIF-8 NPs and AC. Furthermore, there could be some active sites at the ZIF-8 NP-AC interfaces having accessible amine groups coming from AC, which can interact well with polar CO_2 molecules. To understand the adsorbate-adsorbent interaction qualitatively, CO_2 adsorption isotherms were measured at 195 K for ZIF-8 NP (**1**) and **ZIF-8@AC-2** (Figure 11) and the profiles were further analyzed by the Dubinin-Radushkevich equation.[15] **ZIF-8@AC-2** exhibits an uptake amount of 316 mL/g at P = 1 bar which is 46% higher than the uptake amount of ZIF-8 NP (217 mL/g at P = 1 bar) and the $q_{st,\phi}$ value for **1** and **ZIF-8@AC-2** are found to be ~ 30.4 and ~ 31.6 kJ mol^{-1} respectively, suggesting strong interaction of CO_2 with the composite frameworks.

Table 1. Surface area, pore volume and CO_2 uptake of different compounds

Compound	**AC content (wt%)**	**BET surface area (m^2/g)**	**Pore volume (cc/g)**	**CO_2 uptake at 298 K at 1 bar (ml/g)**
ZIF-8 NPs(**1**)	0	1030	0.549	15.6
ZIF-8@AC-1	12.1	1253	0.625	25.2
ZIF-8@AC-2	18.3	1461	0.746	31.9
ZIF-8@AC-3	22.2	1150	0.591	21.4
ZIF-8@AC-4	27.2	842	0.418	9.9

6A.4 SUMMARY

In summary, new ZIF-8–aminoclay nanocomposites were developed exploiting the interaction between aminoclay and ZIF-8 NPs. The composites show significantly higher N_2 and CO_2 adsorption uptake compared to the pristine nano ZIF-8 framework. In the composites, the ZIF-8 NPs are assembled together by AC which assembles the NPs. Such assembly is expected to increase the effective number of neighbouring frameworks atoms

which eventually facilitates adsorption. The present work is expected to usher new routes towards novel composites with improved functions.

6A.5 REFERENCES

1. Themed Issue:Metal-organic Frameworks, *Chem. Rev.*, 2012, **112**, 673.
2. (*a*) Q-L. Zhu and Q. Xu, *Chem. Soc. Rev*., 2014, **43**, 5468; (*b*) J. E. Bachman, Z. P. Smith, T. Li, T. Xu and J. R. Long, *Nat. Mater.*, 2016, DOI: 10.1038/NMAT4621; (*c*) A. Ranft, F. Niekiel, I. Pavlichenko, N. Stock and B.V. Lotsch, *Chem. Mater.*, 2015, **27**, 1961; (*d*) L. Li, X. Jiao, D. Chen, B.V. Lotsch and C. Li, *Chem. Mater*., 2015, **27**, 7601.
3. (*a*) P. Horcajada, T. Chalati, C. Serre, B. Gillet, C. Sebrie,T. Baati, J. F. Eubank, D. Heurtaux, P. Clayette, C. Kreuz, J.-S. Chang, Y. K. Hwang, V. Marsaud, P.-N. Bories, L. Cynober, S. Gil, G. Ferey, P. Couvreur and R. Gref, *Nat. Mater*., 2010, **9**, 172; (*b*) M. D. Rowe, C.-C. Chang, D. H. Thamm, S. L. Kraft, J. F. Harmon Jr, A. P. Vogt, B. S. Sumerlin and S. G. Boyes, *Langmuir*, 2009, **25**, 9487; (*c*) M. D. Rowe, D. H. Thamm, S. L. Kraft and S. G. Boyes, *Biomacromolecules*, 2009, 10, 983; (*d*) W. J. Rieter, K. M. Pott, K. M. Taylor and W. Lin, *J. Am. Chem. Soc*., 2008, **130**, 11584.
4. (*a*) N. Yanai and S. Granick, *Angew. Chem. Int. Ed*., 2012, **51**, 5638; (*b*) N. Yanai, M. Sindoro, J. Yan and S. Granick, *J. Am. Chem. Soc*., 2013, **135**, 34.
5. (*a*) K. S. Park, Z. Ni, A. P. Cote, J. Y. Choi, R. Huang, F. J. Uribe-Romo, H. K. Chae, M. O'Keeffe and O. M. Yaghi, *Proc. Natl. Acad. Sci*., 2006, **103**, 10186; (*b*) X.-C. Huang, Y.-Y. Lin, J.-P. Zhang X-M. Chen, *Angew. Chem. Int. Ed*., 2006, **45**, 1557.
6. (*a*) C.-Y. Sun, C. Qin, X.-L. Wang, G.-S. Yang, K.-Z. Shao, Y.-Q. Lan, Z.M. Su, P. Huang, C.-G. Wang and E.-B. Wang, *Dalton Trans*., 2012, **41**, 6906; (*b*) H. Zheng, Y. Zhang, L. Liu, W. Wan, P. Guo, A. M. Nystrom and X. Zou, *J. Am. Chem. Soc*., 2016, **138**, 962.
7. Y. Pan, Y. Liu, G. Zeng, L. Zhao and Z. Lai, *Chem. Commun*., 2011, **47**, 2071.
8. J. Cravillon, S. Munzer, S.-J. Lohmeier, A. Feldhoff, K. Huber, and M. Wiebcke, *Chem. Mater.*, 2009, **21**, 1410.
9. S. K. Nune, P. K. Thallapally, A. Dohnalkova, C. M. Wang, J. Liu and G. J. Exarhos, *Chem. Commun*., 2010, **46**, 4878.

10. K. Kida, M. Okita, K. Fujita, S. Tanaka and Y. Miyake, *CrystEngComm*., 2013, **15**, 1794.
11. C. Zhang, J. A. Gee, D. S. Sholl and R. P. Lively, *J. Phys. Chem. C*, 2014, **118**, 20727.
12. (*a*) S. Mann, S. L. Burkett, S. A. Davis, C. E. Fowler, N. H. Mendelson, S. D. Sims, D. Walsh and N. T. Whilton, *Chem. Mater*., 1997, **9**, 2300; (*b*) S. L. Burkett, A. Press and S. Mann, *Chem. Mater*., 1997, **9**, 1071; (*c*) N. T. Whilton, S. L. Burkett and S. Mann, *J. Mater. Chem*., 1998, **8**, 1927; (*d*) A. J. Patil, E. Muthusamy and S. Mann, *Angew. Chem. Int. Ed*., 2004, **43**, 4928; (*e*) J. E. Martin, A. J. Patil, M. F. Butler and S. Mann, *Adv. Funct. Mater*., 2011, **21**, 674.
13. K. K. R. Datta, A. Achari and M. Eswaramoorthy, *J. Mater. Chem. A,* 2013, **1**, 6707.
14. S. Gadipelli, W. Travis, W. Zhou and Z. Guo, *Energy Environ. Sci*., 2014, 7, 2232.
15. M. M. Dubinin, *Chem. Rev*., 1960, **60**, 235.

Chapter 6B

Surface Coating of ZIF-8 NPs with Laponite Towards Hydrogel Composite for Controlled Drug Release

Abstract

This chapter reports the fabrication of a composite hydrogel from ZIF-8 nanoparticles and the layered nanoclay Laponite towards the controlled delivery of the anti-cancer drug 5-fluorouracil (FU). The hydrogel formation is driven by the electrostatic interaction between ZIF-8 nanoparticles having high surface positive charge and Laponite (Lp) particles having negatively charged surface. FU drug was encapsulated into ZIF-8 nanoparticles to obtain FU@ZIF-8 first and then gelation was performed with Laponite to obtain the hydrogel composite (FU@ZIF-8+Lp). In the hydrogel composite, FU@ZIF-8 nanoparticles are wrapped with layers of Laponite, which protect the FU drug molecules from undesired release under physiological condition (pH 7.4) and the undesired release is reduced significantly compared to that from FU@ZIF-8 particles. In contrast, rapid and facile release of FU occurs from FU@ZIF-8+Lp in acidic environment (pH 5). Thus the hydrogel composite could be an ideal pH-responsive drug-delivery system which would minimize release of anti-cancer drugs in normal cell (pH 7.4) and selectively deliver the drug molecules into acidic cancer cells.

Paper based on this study:

A. Chakraborty, M. Eswaramoorthy, T. K. Maji, *manuscript under preparation.*

6B.1 INTRODUCTION

A large number of drugs including small molecule inhibitors, antibodies, chemotherapeutics, and nucleic acid drugs are widely used as therapeutics for the treatment of several diseases including cancer. However, many of the drugs have significant drawbacks such as poor solubility and nonselective bio-distribution leading to the damage of healthy tissues[1] and adverse side effects.[2] These problems can be overcome by fabricating an efficient drug delivery system (DDS) which enhances drug solubility, inhibits premature release and trigger controlled release. Controlled release of drug molecules to target cells is very important for certain therapies such as cancer research to reduce the side effects of chemotherapy. The tumor cells (pH 5.0–6.0) are more acidic than the normal cells and a desirable drug delivery system should release the drug molecules only into the acidic cancer cells. Therefore, it is desirable to construct a pH-responsive drug delivery system that would minimize undesired drug release and selectively deliver the drugs into acidic cancer cells. The drug delivery system should also have bio-compatibility and high processablity. Hydrogels are hydrophilic polymer networks containing large quantities of water, have high processablity and have shown potential as drug delivery vehicles.[3] The fabrication of a pH-responsive drug-delivery hydrogel would be a highly demanding and challenging task.

Nanoscale metal-organic frameworks (NMOFs) have shown their potential to encapsulate and deliver drugs owing to the structural diversity and high porosity.[4-8] However, the processability and controlled release of drugs are the issues which need to be improved for the NMOF DDS. The performances of NMOF particles under physiological conditions have been improved through surface modification and such modifications have mostly been carried out using silica shell to coat the NMOFs.[9-11] Such surface functionalization encounters several disadvantages such as new toxicity issues due to the presence of exogenous silica. Highly processable bio-compatible hydrogels derived from NMOFs would be interesting in this respect. Although polymer gels derived from MOF by cross-linking of the organic linkers or SURGEL derived from SURMOF (surface-mounted MOF) have been reported recently,[12-13] fabrication of processable hydrogels from NMOFs for efficient drug delivery is yet to be documented. The zeolitic imidazolate frameworks (ZIFs) are one of the benchmark MOFs and are well-known for their high surface areas, high crystallinity, and excellent thermal and chemical stability.[14-16] The prototypic ZIF-8 framework ($Zn[MeIm]_2$; MeIm = 2-methylimidazolate) (Scheme 1) is

stable under physiological conditions but decomposes under acidic conditions and hence has been used to construct pH-sensitive drug delivery systems.[17] Certain small molecule anti-cancer drugs, such as 5-fluorouracil (FU) (Scheme 1), can be loaded into ZIF-8 framework with a high loading efficacy. At the same time, the small molecule drugs release significantly from the framework even under physiological conditions.[18] To minimize such undesired drug release and fabricate a superior drug delivery system, a new approach is reported in this chapter by coating FU encapsulated ZIF-8 NPs (FU@ZIF-8) with a suitable functional material towards a hydrogel composite. For such targeted synthesis, post-synthetic surface coating of FU@ZIF-8 was performed with the synthetic layered nanoclay, Laponite RD.[19-20]

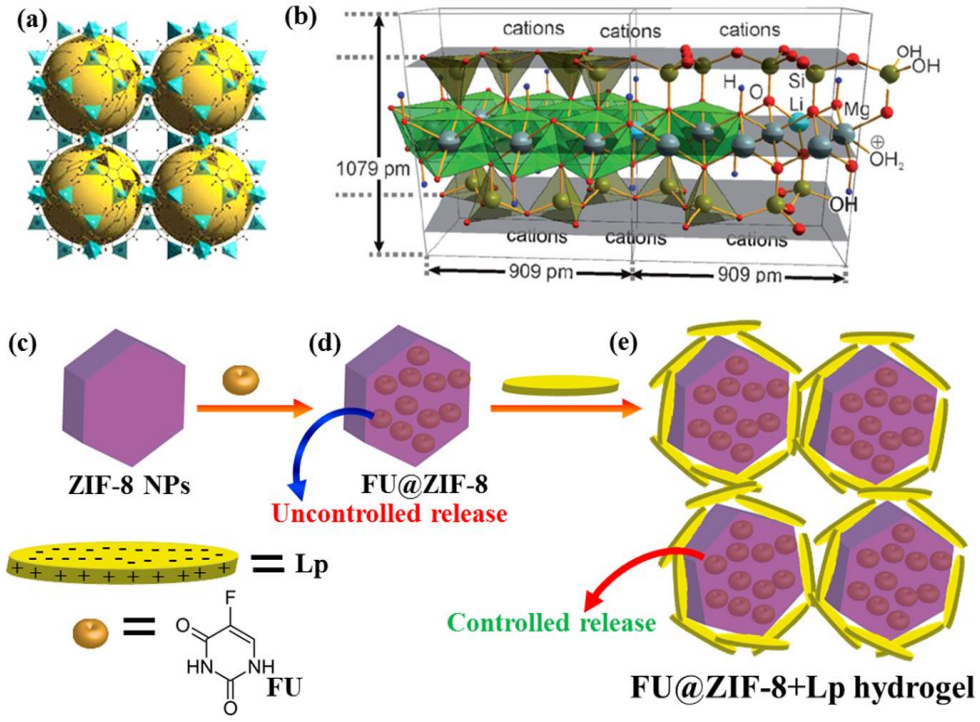

Scheme 1. (a) The structure of ZIF-8 having large cavity and narrow window. b) The structure of Laponite: side view of two unit cells, along (100) direction. Schematic of (c) ZIF-8 NPs, (d) drug loaded ZIF-8: FU@ZIF-8 and (f) hydrogel composite of Lp and FU@ZIF-8. The Lp wrapping in the composite triggers controlled release of FU molecules.

Laponite RD (Lp) (chemical composition of $Na_{0.7}[Mg_{5.5}Li_{0.3}Si_8O_{20}(OH)_4](H_2O)_n$) consists of layers of $[SiO_4]$ tetrahedra sandwiching sheets of Mg^{2+}, which fulfill their octahedral coordination by bridging OH groups (Scheme 1). The microstructure can be described as anisotropic platelets with primary particle diameter of approximately 25 nm, while the thickness of the platelets is less than 1 nm. Partial substitution of Mg^{2+} in the sheets by Li^+ makes the faces of the platelets negatively charged and hence cations are

accommodated on or between the faces of the platelets (interlayers) for charge compensation. It was anticipated that there would be facile formation of a self-assembled gel driven by the electrostatic interaction between ZIF-8 NP having unsaturated Zn^{2+} sites at surface and the Laponite particles having negatively charged faces. In this chapter, the synthesis of a hydrogel composite of FU@ZIF-8 and Lp and use of the composite as a pH-responsive efficient drug delivery vehicle are documented. The hydrogel composite shows significantly less undesired drug release in physiological pH (pH =7.4), compared to that from uncoated FU@ZIF-8 particles.

6B.2 EXPERIMENTAL SECTION

6B.2.1 Materials

All the reagents and solvents employed are commercially available and used as supplied without further purification. $Zn(NO_3)_2.6H_2O$, 2-methylimidazole, and Laponite RD were obtained from the Aldrich Chemical Co.

6B.2.2 Synthesis

ZIF-8 NPs: ZIF-8 NPs were synthesized in methanolic solution at room temperature following a reported procedure in literature.[16] 0.367 g (1.23375 mmol) $Zn(NO_3)_2.6H_2O$ was taken in 25 ml deionized water and then 25 mL of methanolic solution of 2-methylimidazole (0.811 g, 9.88 mmol) was rapidly added to the Zn(II) solution under stirring. The reaction mixture was stirred for one hour. The product was collected by centrifugation, washed with fresh methanol several times and dried in air. Yield, 47%, relative to Zn(II). The phase purity of the sample was checked by PXRD analysis (Figure 1).

ZIF-8+Lp hydrogel: To prepare the composites, first 5 mg of the ZIF-8 NPs was dispersed in 400 µL of methanol. 10 mg Lp was dispersed in 1 mL of water and the dispersed solution containing ZIF-8 NPs was added to it under sonication at room temperature. The mixture was sonicated for two minutes and left undisturbed. Stable hydrogel forms within 30 minutes. The PXRD pattern of the xerogel shows presnece of the crystalline phase of ZIF-8 (Figure 1).

FU@ZIF-8: FU encapsulation into ZIF-8 was carried out by impregnation method following the report by Wang and co-workers, where they obtained high FU loading

efficiency.[18] Approximately 100 mg of sample (as-synthesized ZIF-8 NPs) was desolvated at 150 ºC under 10^{-1} pa vacuum for about 8 hours. FU loading experiments were carried out by stirring the desolvated ZIF-8 in a methanolic solution of FU (6 mg mL^{-1}) for 2 days with a FU to ZIF-8 weight ratio of 3 : 2. The resulting compound (FU@ZIF-8) was washed with methanol repeatedly to remove any unreacted FU and then was dried in air. The incorporation of FU was confirmed from Fourier transformed infrared spectroscopy (FTIR) and the characteristic peaks of FU were observed at 1724 cm^{-1} and 1248 cm^{-1}, attributed to the stretching frequency of C=O, and C–N groups, respectively. The FU encapsulated ZIF-8 compound (FU@ZIF-8) retains crystallinity, as evident from PXRD pattern (Figure 1). The UV-Vis absorption spectroscopy has been used to determine the effective FU storage capacity. Seven different standard concentrations (2.537 mM, 1.2685 mM, 0.8457 mM, 0.72488 mM, 0.6343 mM, 0.5638 mM, 0.42285 mM) of FU were prepared and their UV-Vis spectra were recorded (Figure 2). The calibration curve was constructed to calculate unknown concentrations using Beer's law. To calculate the drug loading, 1 mg of the dried FU@ZIF-8 was taken in 2 mL concentrated HCl to decompose the ZIF-8 framework and to release the encapsulated drug. The amount of the released drug was calculated using the calibration curve and the loading amount is 0.54 g per g of ZIF-8.

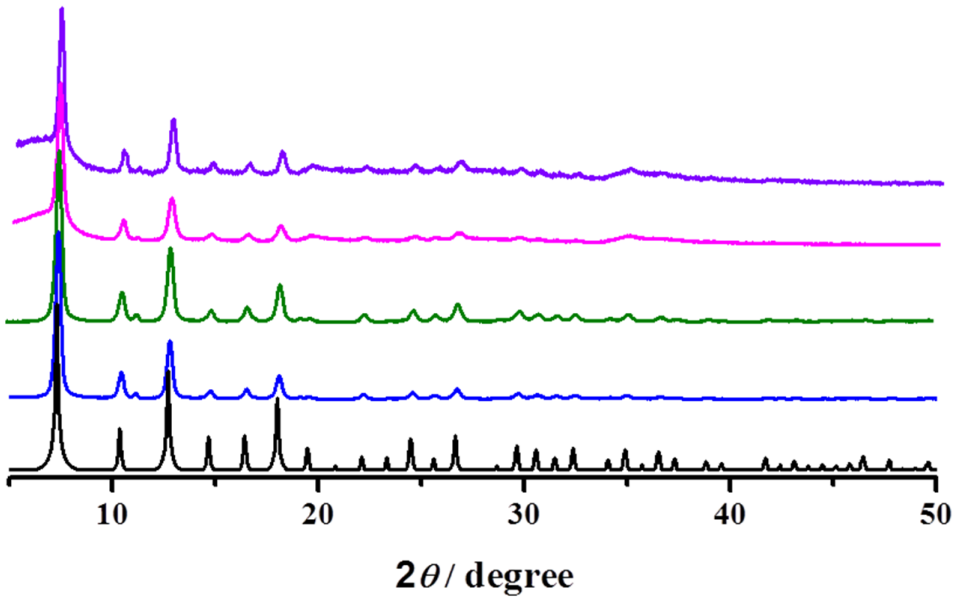

Figure 1. PXRD patterns of simulated plot (black) of ZIF-8, and experimental plots of ZIF-8 NP (blue), FU@ZIF-8 (green), ZIF-8+Lp xerogel (magenta) and FU@ZIF-8+Lp xerogel (violet).

FU@ZIF-8+Lp hydrogel: 7.7 mg of the FU@ZIF-8 compound was dispersed in 400 µL of methanol. 10 mg Lp was dispersed in 1 mL of water and the dispersed solution

containing FU@ZIF-8 NPs was added to it under sonication at room temperature. The mixture was sonicated for two minutes and left undisturbed. Stable hydrogel forms within 30 minutes. The PXRD pattern of the xerogel shows presnece of the crystalline phase of ZIF-8 (Figure 1).

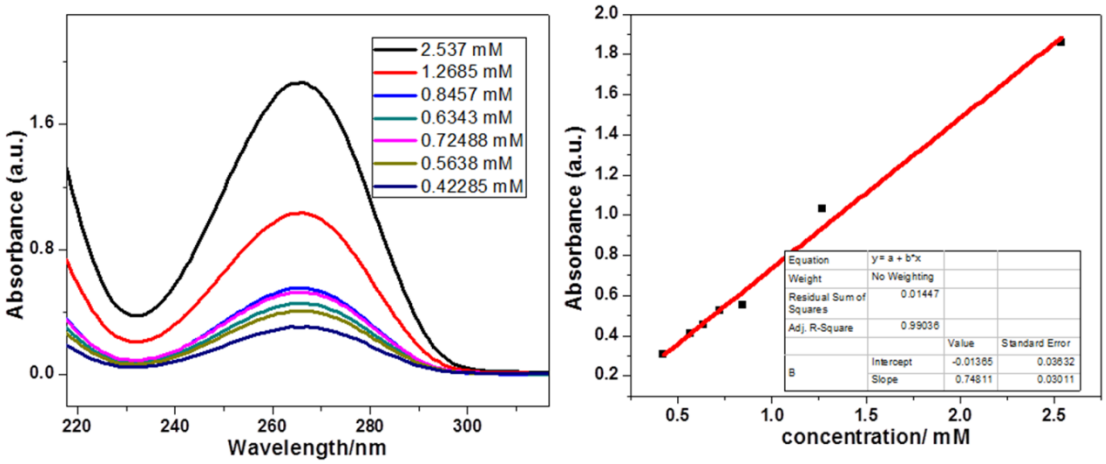

Figure 2. UV-Vis spectra of standard solution of FU and the calibration curve.

Drug Release Experiment

The release experiments were performed by taking the FU@ZIF-8 and the FU@ZIF-8+Lp samples in PBS (pH 7.4) and acetate buffer (pH 5.0) at 37 °C. The respective compound was dispersed in the release mediums and the solution was stirred mildly. At certain time intervals, FU concentration moved out into the solution was measured by UV-Vis absorption spectrophotometer using the calibration curve.

6B.2.3 Physical Measurements

Powder X-ray diffraction (PXRD) patterns were recorded on a Bruker D8 Discover instrument using Cu–Kα radiation. Energy dispersive analysis of X-rays (EDX) was carried out using field emission scanning electron microscope. Electronic absorption spectra were recorded on a Perkin Elmer Lambda 750 UV-VIS-NIR Spectrometer. IR spectra of the compounds were recorded on a Bruker IFS 66v/S spectrophotometer using the KBr pellets in the region 4000−400 cm^{-1}. The scanning electron microscopy images were obtained using a Nova Nanosem 600 FEI field emission scanning electron microscope (FESEM). The samples were prepared by dispersing the sample in MeOH and then dropping 5 μL of the solution onto a small piece of silicon wafer and drying into air. Transmission electron microscopy (TEM) images were taken with a JEOL JEM-3010 transmission electron microscope operating at 200 kV. The samples were prepared in the same way as described above, but the drop cast was made onto a carbon-coated TEM

grid. The zeta potential measurements were carried out using a NanoZS (Malvern UK) employing a 532 nm laser.

6B.3 RESULTS AND DISCUSSION

The as-synthesized ZIF-8 NPs show hexagonal NPs with average diameter of 50 nm (Figure 3a). The zeta potential of the as-synthesized ZIF-8 NPs and Lp particles were measured at pH = 7. ZIF-8 NPs have a zeta potential of +55 mV (Figure 3b) and such high positive zeta potential arises from the unsaturated Zn^{II} sites at surfaces of the nanocrystals.[16] On the other hand, Lp particles have zeta potential of ~-30 mV (Figure 3c) owing to the negative charge at its surface. Thus strong electrostatic interaction is expected between ZIF-8 NPs and Lp, which might result in a gel network. To investigate whether a facile gel-like structure can result from the self-assembly of ZIF-8 NP and Lp, gelation experiments were attempted at room temperature with different relative ratio of ZIF-8 and Lp. A stable hydrogel was achieved by adopting the reaction conditions as described in the synthesis part. It might be noted that Lp particles have a tendency to form hydrogel at a higher concentration in water by generating a "house of cards" structure.[20] However, such gelation by the interaction between the Lp particles is not possible at the concentration of Lp used for our study. Rapid gelation occurs when the dispersed ZIF-8 NPs were added to the aqueous solution of Lp resulting in an opaque hydrogel (ZIF-8+Lp) that remained stable upon inversion (Figure 4a).

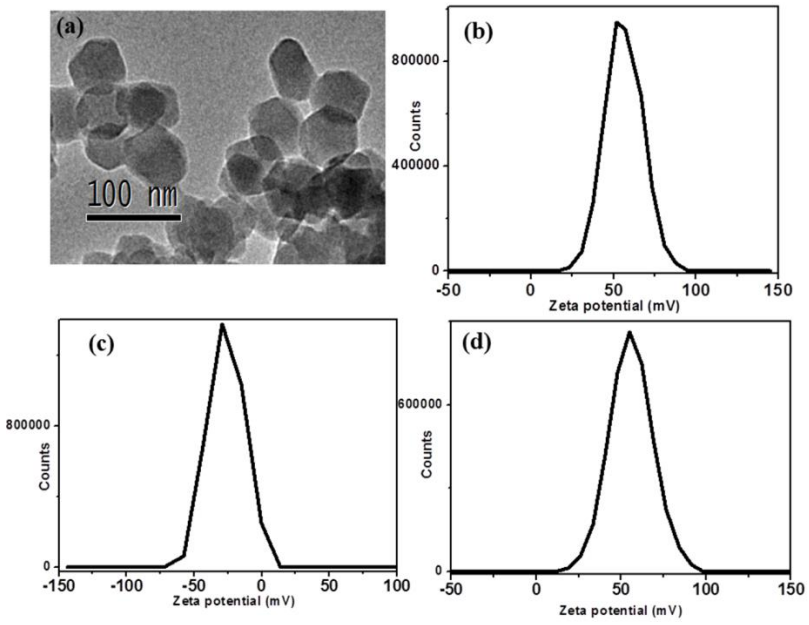

Figure 3. (a) TEM image of the as-synthesized ZIF-8 NP. Zeta potential plots of (b) ZIF-8 NP, (c) Lp and (d) FU@ZIF-8.

Scanning electron microscopy (SEM) image of the xerogel shows a porous network (Figure 4b). TEM images of the xerogel reveal that the hexagonal ZIF-8 NPs are wrapped with layered Lp particles (Figure 4c,d,e). The Lp layers are mainly found on the edges of ZIF-8 NPs, where the surfaces of Lp platelets surround ZIF-8 NPs. Formation of such architecture can be attributed to the presence of unsaturated Zn^{2+} sites at surface which interact well with negatively charged faces of Lp. If drug molecules are encapsulated into ZIF-8 NPs and then a composite hydrogel could be synthesized by wrapping the drug loaded ZIF-8 NPs with Lp, the undesired release of the drug molecules would be inhibited due to the Lp wrapping around the ZIF-8 NPs. Thus efforts were made to construct a hydrogel composite towards an effective DDS for controlled drug delivery.

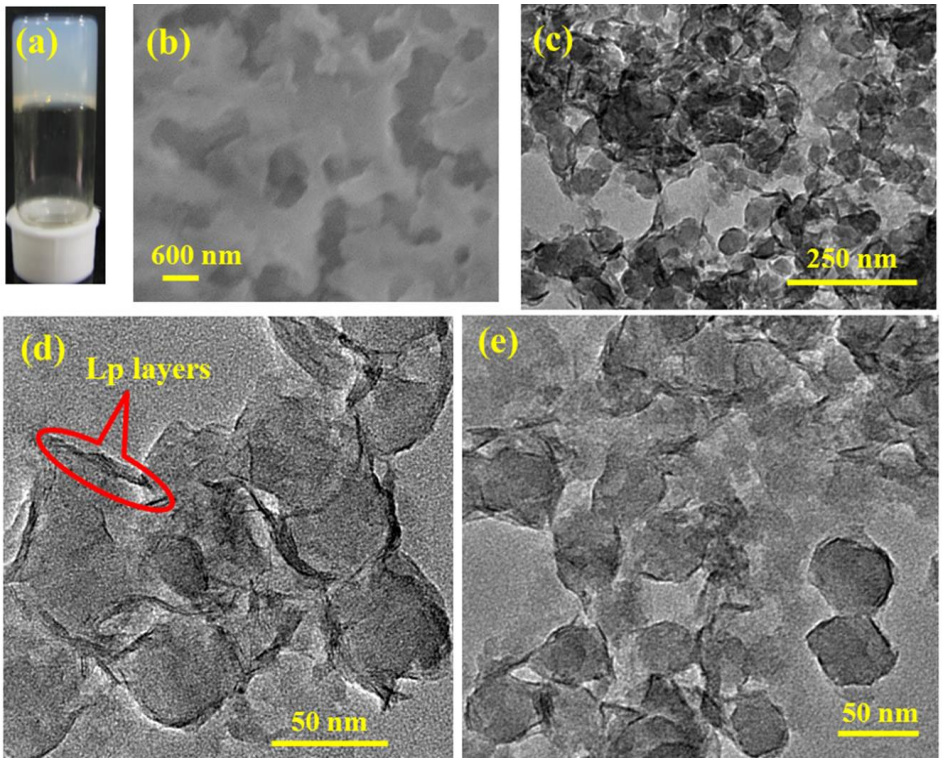

Figure 4. (a) Inverted image of the ZIF-8+Lp hydrogel. (b) SEM and (c), (d), (e) TEM images of the ZIF-8+Lp xerogel.

The FU@ZIF-8 particles have a zeta potential of +52 mV, similar to that of ZIF-8 NPs (Figure 3d). Thus the surface positive charge in FU@ZIF-8 particles does not decrease, suggesting that FU molecules are encapsulated into ZIF-8 NPs instead of getting adsorbed at surfaces. Owing to such high positive surface charge, further gelation of FU@ZIF-8 was successful with Lp resulting in a hydrogel (FU@ZIF-8+Lp) that remained stable upon inversion (Figure 5a inset). TEM images of FU@ZIF-8+Lp xerogel reveal that FU@ZIF-8 NPs are wrapped with Lp layers (Figure 5a, b. The Lp layers surround

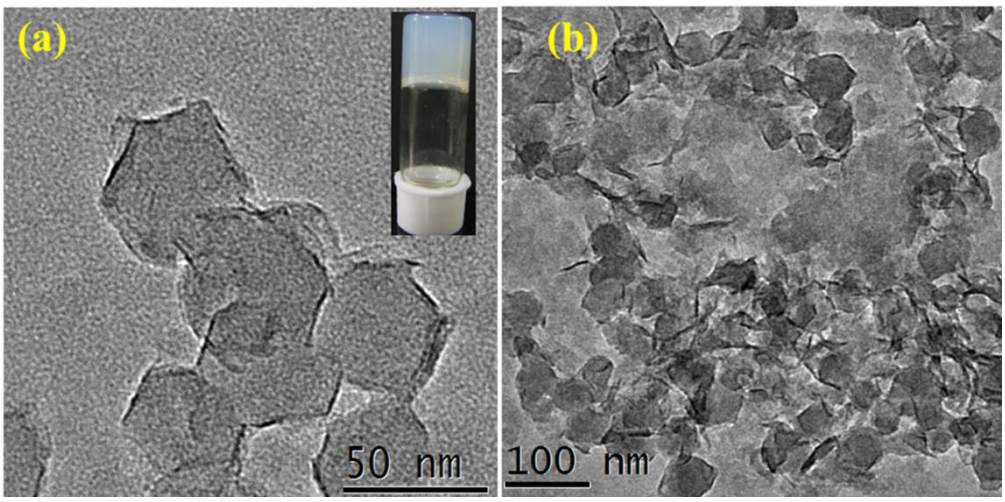

Figure 5. TEM images of the FU@ZIF-8+Lp xerogel. The inset shows the inverted image of the FU@ZIF-8+Lp hydrogel.

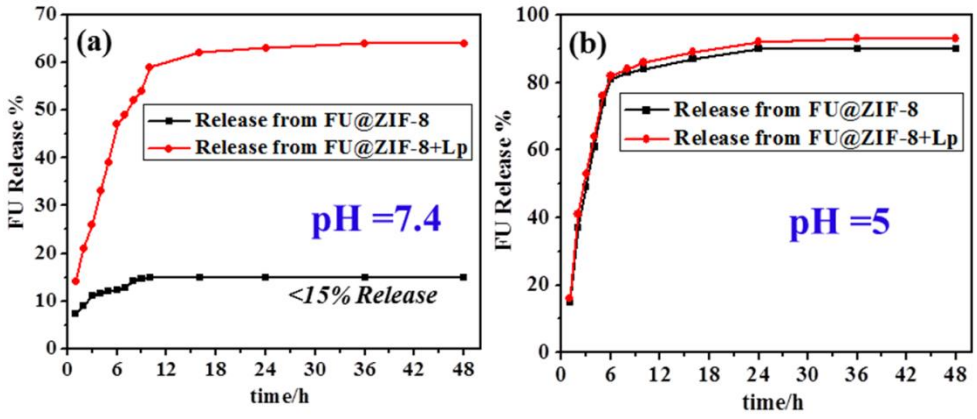

Figure 6. FU release from FU@ZIF-8 and FU@ZIF-8+Lp in (a) PBS buffer (pH = 7.4) and (b) acetate buffer (pH = 5).

FU@ZIF-8 NPs at the edges and thus the Lp layers are expected to inhibit uncontrolled release of the FU molecules from the wrapped FU@ZIF-8 NPs.

To investigate the pH-responsive drug release characteristics of the FU@ZIF-8 NPs and the FU@ZIF-8+Lp composite xerogel, release experiments were performed in PBS (pH 7.4) and acetate buffer (pH 5.0). The release experiments were monitored over a time period of 48 hours. In PBS solution, FU@ZIF-8 NPs exhibited a release of approximately 40% of the encapsulated FU drug within first 5 hours and more than 60% of the drug is released within 10 hours only (Figure 6a). Beyond 16 hours, a stable release was observed. In contrast, the release of FU drug is significantly reduced from FU@ZIF-8+Lp composite xerogel and the release is reduced to ~10% in first 5 hours. The FU release reaches to 15% within10 hours and then remains stable even over 2 days. Thus the

undesired release could be minimized in the composite xerogel DDS, which reduces the release by four times compared to that from uncoated FU@ZIF-8 NPs. In acetate buffer, FU release rate was significantly high from both FU@ZIF-8 and FU@ZIF-8+Lp and the release rates are comparable (Figure 6b). More than 80% of FU release from both FU@ZIF-8 and FU@ZIF-8+Lp within 10 hours. This is consistent with the expected decomposition of ZIF-8 framework in acidic environment and thus a burst release of FU occurs from both FU@ZIF-8 and FU@ZIF-8+Lp. The above results show that the undesired loss of FU could be reduced during blood circulation (pH 7.4) by furnishing a composite hydrogel DDS.

6B.4 SUMMARY

A composite hydrogel DDS was fabricated exploiting electrostatic interaction between ZIF-8 NPs having unsaturated Zn^{2+} sites at surface and the Laponite particles having negatively charged faces. In the hydrogel composite, FU encapsulated ZIF-8 NPs are wrapped with layers of Laponite particles. Such coating inhibits the undesired release of encapsulated drug molecules under physiological conditions (pH 7.4), while drug release is facile and rapid in acidic condition (pH 5. 0). Thus using the composite hydrogel drug-delivery systems, the encapsulated anti-cancer drug may be selectively delivered to cancer cells. Such hydrogel composites can be ideal pH-responsive drug-delivery systems which would mitigate the adverse side effects of chemotherapy.

6B.5 REFERENCES

1. L. Meng, X. Zhang, Q. Lu, Z. Fei and P. J. Dyson, *Biomaterials*, 2012, **33**, 1689.
2. K. Shan, A. M. Lincoff and J. B. Young, *Am. Coll. Physicians*, 1996, **125**, 47
3. (*a*) A. Vashist, A. Vashist, Y. K. Gupta and S. Ahmed, *J. Mater. Chem. B,* 2014, **2**, 147; (*b*) T. R. Hoare and Daniel S. Kohane, *Polymer*, 2008, **49**, 1993.
4. C. He, D. Liu, and W. Lin, *Chem. Rev.*, 2015, **115 (19)**, 11079.
5. P. Horcajada, R. Gref, T. Baati, P. K. Allan, G. Maurin, P. Couvreur, G. Ferey, R. E. Morris and C. Serre, *Chem. Rev*., 2012, **112**, 1232.
6. P. Horcajada, T. Chalati, C. Serre, B. Gillet, C. Sebrie, T. Baati, J. F.Eubank, D. Heurtaux, P. Clayette, C. Kreuz, J.-S. Chang, Y. K. Hwang, V. Marsaud, P.-N. Bories, L. Cynober, S. Gil, G. Fe´rey, P. Couvreur and R. Gref, *Nat. Mater*., 2010, **9**, 172.

7. M. C. Bernini, D. Fairen-Jimenez, M. Pasinetti, A. J. Ramirez-Pastor and R. Q. Snurr, *J. Mater. Chem. B*, 2014, **2**, 766.
8. A. C. McKinlay, B. Xiao, D. S. Wragg, P. S. Wheatley, I. L. Megson and R. E. Morris, *J. Am. Chem. Soc*., 2008, **130**, 10440.
9. (*a*) W. J. Rieter, K. M. L. Taylor and W. B. Lin, *J. Am. Chem. Soc*., 2007, **129**, 9852; (*b*) D. M. Liu, R. C. Huxford and W. B. Lin, *Angew. Chem., Int. Ed*., 2011, **50**, 3696.
10. W. J. Rieter, K. M. Pott, K. M. L. Taylor and W. Lin, *J. Am. Chem. Soc*. 2008, **130**, 11584.
11. K. M. Taylor-Pashow, J. Rocca, Z. Xie, S. Tran and W. Lin, *J. Am. Chem. Soc*., 2009, 131, 14261.
12. T. Ishiwata, Y.Furukawa, K. Sugikawa, K. Kokado and K. Sada, *J. Am. Chem. Soc*., 2013, **135**, 5427.
13. M. Tsotsalas, J. Liu, B. Tettmann, S. Grosjean, A. Shahnas, Z. Wang, C. Azucena, M. Addicoat, T. Heine, J. Lahann, J. Overhage, S. Bräse, H. Gliemann and C. Wöll, *J. Am. Chem. Soc*., 2014, **136**, 8.
14. K. S. Park, Z. Ni, A. P. Cote, J. Y. Choi, R. Huang, F. J. Uribe-Romo, H. K. Chae, M. O'Keeffe and O. M. Yaghi, *Proc. Natl. Acad. Sci*., 2006, **103**, 10186.
15. H. Zheng, Y. Zhang, L. Liu, W. Wan, P. Guo, A. M. Nystrom and X. Zou, *J. Am. Chem. Soc*., 2016, **138**, 962.
16. J. Cravillon, S. Munzer, S.-J. Lohmeier, A. Feldhoff, K. Huber, and M. Wiebcke, *Chem. Mater.*, 2009, **21**, 1410.
17. H. Zheng, Y. Zhang, L. Liu, W. Wan, P. Guo, A. M. Nystrom and X. Zou, *J. Am. Chem. Soc*., 2016, **138**, 962.
18. C.-Y. Sun, C. Qin, X.-L. Wang, G.-S. Yang, K.-Z. Shao, Y.-Q. Lan, Z.M. Su, P. Huang, C.-G. Wang and E.-B. Wang, *Dalton Trans*., 2012, **41**, 6906.
19. (*a*) G. Lagaly and S. Ziesmer, *Adv. Colloid Interface Sci*., 2003, **100 – 102**, 105; (*b*) A. Mourchid, A. Delville, J. Lambard, E. Lecolier and P. Levitz, *Langmuir*, 1995, **11**, 1942; (*c*) M. V. Martnez, F. L. Arbeloa, J. P. Prieto and I. L. Arbeloa, *J. Phys. Chem. B*, 2005, **109**, 7443; (*d*) M. M. Lezhnina, T. Grewe, H. Stoehr and U. Kynast, *Angew. Chem. Int. Ed*., 2012, **51**, 10652.
20. B. Ruzicka and E. Zaccarelli, *Soft Matter*, 2011, **7**, 1268.

Lists of Publications

1. **A. Chakraborty**, A. Achari, M. Eswaramoorthy, T. K. Maji, MOF-aminoclay composites for CO_2 capture, separation and enhanced catalytic activity in chemical fixation of CO_2, *Chem. Commun.*, 2016, DOI 10.1039/C6CC05289D.
2. **A. Chakraborty**, A. Escuer, J. Ribas, T. K. Maji, A discrete Cu^{II}_6 cluster and a 3D Mn^{II}-Cu^{II} framework based on assembly of Mn_2Cu_4 cluster: Synthesis, structure and magnetic properties, *Dalton Trans.*, 2016, DOI: 10.1039/C6DT03094G.
3. **A. Chakraborty**, S. Bhattacharyya, A. Hazra, A. C. Ghosh, T. K. Maji, Post-synthetic metalation in an anionic MOF for efficient catalytic activity and removal of heavy metal ions from aqueous solution, *Chem. Commun.*, 2016, 52, 2831-2834. (Highlighted in "Atlas of Science" in May 2016).
4. **A. Chakraborty**, S. R. Lingampalli, A. Kumari, J. Ribas, J. R. Arino, T. K. Maji, Structural and magnetic diversity based on different imidazolate linkers in Cu(II)-azido coordination compounds, *Inorg. Chem.*, 2014, 53, 11991-12001.
5. **A. Chakraborty**, T. K. Maji, Mg-MOF-74@SBA-15 hybrids: Synthesis, characterization and adsorption properties, *APL Mat.*, 2014, 2, 124107.
6. **A. Chakraborty**, K. K. Ramachandran, S.S.R.K.C. Yamijala, S. K. Pati, T. K. Maji, A hexanuclear Cu(I) cluster supported by cuprophilic interaction: Effects of aromatics on luminescence properties, *RSC Adv.*, 2014, 4, 35167-35170.
7. **A. Chakraborty**, T. K. Maji, Interpenetrated metal-organic frameworks with $[Ag(CN)_2]^-$ bridging ligand: synthesis, structural characterization and magnetic study, *Proc. Natl. Acad. Sci., Indian Section A*, 2014, 84, 243-249.
8. **A. Chakraborty**, T. K. Maji, Structural diversities in metal-organic coordination polymers based on flexibility in organic spacer, *Journal of the Indian Institute of Science*, 2014, 94, 1.
9. **A. Chakraborty**, R. Haldar, T. K. Maji, Bifunctional Co(II)-Ag(I) and Ni(II)-Ag(I) frameworks: Modulation of magnetic property and CO_2 uptake based on organic pillars, *Cryst. Growth Des.*, 2013, 13, 4968-4976.
10. **A. Chakraborty**, S. R. Lingampalli, A. K. Manna, S. K. Pati, J. Ribas, T. K. Maji, Discrete dinuclear complex to extended 2D compound in Cu-azido system by controlling coligand stoichiometry: Synthesis and magneto-structural

correlations, *Dalton Trans.*, 2013, 42, 10707-10714. (Highlighted in inside Cover Page of the journal).

11. **A. Chakraborty**, K. L. Gurunatha, A. Muthulakshmi, S. Dutta, S. K. Pati, T. K. Maji, Assembly of trinuclear and tetranuclear building units of Cu^{2+} towards two 1D magnetic systems: Synthesis and magneto-structural correlations, *Dalton Trans.*, 2012, 41, 5879-5888.
12. **A. Chakraborty**, B. K. Ghosh, J. R. Arino, J. Ribas, T. K. Maji, A heterometallic (Ni^{II}–Cu^{II}) decanuclear cluster containing two distorted cubane-like pentanuclear cores: Synthesis, structure, and magnetic properties, *Inorg. Chem.*, 2012, 51, 6440-6442.
13. S. Bhattacharyya, **A. Chakraborty**, K. Jayaramulu, A. Hazra, T. K. Maji, A bimodal anionic MOF: Turn-off sensing for Cu(II) and specific sensitization of Eu(III), *Chem. Commun.*, 2014, 50, 13567-13570.
14. S. Roy, **A. Chakraborty**, T. K. Maji, Lanthanide-organic frameworks for gas storage and as magneto-luminescent materials, *Coord. Chem. Rev.*, 2014, 273-274, 139-164. (*Equal contribution from the first two authors*).
15. S. Mohapatra, B. Rajeswaran, **A. Chakraborty**, A. Sundaresan, T. K.Maji, Bimodal magneto-luminescent dysprosium (Dy^{III})-potassium (K^{I})-oxalate framework: Magnetic switchability with high anisotropic barrier and solvent sensing, *Chem. Mater.*, 2013, 25, 1673-1679.
16. P. Ghorai, **A. Chakraborty**, A. Panja, T. K. Mondal, A. Saha, Mono- and di-nuclear nickel(II) complexes derived from NNO donor ligands: syntheses, crystal structures and magnetic studies of dinuclear analogues, *RSC Adv.*, 2016, 6, 36020-36030.
17. S. A. Adalikwu, **A. Chakraborty**, A. Hazra, D. Ghosh, S. K. Pati, T. K. Maji, 2D coordination polymer composed of 1D $\{Ni^{II}(\mu\text{-}O)(\mu\text{-}H_2O)Ni^{II}\}_n$ ferromagnetic chains: Modulation of magnetic properties based on dehydration and rehydration, *Polyhedron*, 2016, 115, 276-281.
18. P. Kanoo, R. Haldar, P. Sutar, **A. Chakraborty**, T. K. Maji, Gated and stepwise sorption processes in functional metal-organic frameworks, *RSC book chapter* on "Multifunctional Porous Organic Inorganic Hybrids for Storage and separation", under review (2016).